PhD Thesis

3D SILICA-GELATIN HYBRID SCAFFOLDS FOR TISSUE REGENERATION

Maria Nelson

May 2016

Department of Materials

Imperial College London

ABSTRACT

Cartilage defects affect millions of people worldwide however current treatment options do not provide the zonal organisation required to regenerate healthy hyaline cartilage. In particular, the regeneration of high density ECM and cells is required to provide the articular surface of the tissue. Developments in tissue scaffolds have typically focused on synthetic polymers with low bioactivity due to their ease of processing. Here, the silica-gelatin sol-gel hybrid system was further developed for 3D printing and electrospinning to generate a zonal, bioactive scaffold. GPTMS, (3-glycidyloxypropyl)trimethoxysilane, was used to couple the silicate network and gelatin molecules. A modified hybrid method was required to avoid rapid gelation but retain high levels of crosslinking and sol-gel network condensation. To produce the material, the gelatin and GPTMS were mixed for 3 h and 3D printed scaffolds were aged for 1 week at room temperature. The hybrid composition most compatible with the 3D printing process had a 78:22, gelatin to TEOS mass ratio, and C-factor of 500 (molar ratio of GPTMS to gelatin). When 3D printing the gels, a minimum strut separation of 1 mm was achievable. To dry the 3D printed scaffolds, freeze drying and critical point drying resulted in very different structures. Freeze drying produced very thin, <40 μm struts, and large ~700 μm channels. Critical point drying produced ~160 μm struts and ~200 μm channels which falls within the range hypothesised to be suitable for cartilage regeneration. Electrospinning required further adjustments to the hybrid method to improve the volatility of the solvent. Conformable cotton wool-like fibres with ~1.5 μm diameter were achieved using a 70:30 gelatin to TEOS mass ratio. The C-factors used: 250, 500, and 750, resulted in increasing silica network condensation: 64.3 %, 75.5 %, and 81.1 % respectively. To create the cotton wool-like fibre structure, hybrid solutions with 60-80 cP viscosity were electrospun in 55 % humidity and dried without contacting each other or the collector surface. Both 3D printed and electrospun fibres showed promising dissolution results. The structures were maintained as only ~3 % gelatin was released over a one month study (3D printed) and ~2 %gelatin over a one week study (fibres). The silicon release was ~25 % of the silica content for 3D printed scaffolds, and ~13 % for fibres (CF500 and CF750). The silica-gelatin hybrids were biocompatible and provided native attachment sites for both osteoblasts and chondrocytes. Over 28-days, chondrocytes appeared to regenerate uniform density hyaline cartilage throughout the 3D printed scaffolds *in vitro*.

DECLARATIONS

Declaration of Originality

I hereby certify that the work presented in this thesis is the result of my own investigations carried out at Imperial College during the period October 2012- March 2016, except where otherwise stated.

Maria Nelson

11/4/2016

ACKNOWLEDGEMENTS

The support and opportunities available during my PhD at Imperial has been incredible, and the advice and help from experts in many different areas of science was invaluable. Firstly, I would like to acknowledge the Engineering and Physical Science Research council for funding this research and my PhD supervisor, Prof. Julian Jones for accepting me into his group. My thanks go to Julian for his continuous support and for making confusing things simple. Particular thanks for the record thesis turnaround – what a rock star!

I would like to thank all the professors and academics who I have been honoured to work with; Prof. Peter Lee, for letting me loose on the beamline at Harwell; Prof. John Hanna and Sam Page for their help with NMR; and last but not least, Prof. Kasuga, from NITech, Japan. The opportunity to spend 3 months at NITech was fantastic for my research, but also an amazing experience. Thanks to the whole Kagusa research group, particularly Akiko, Qunqun, Susu and Yuki, for making me feel so welcome and being so efficient!

At Imperial, my PhD would not have been as enjoyable without the JRJ crew. Louise and Gowsh, thank you for welcoming me into the group and teaching me the ways of the sol-gel hybrid. Siwei, you are my cell hero, it has been excellent working with you and I promise we will publish soon. Amy, Sarah, Fra, Viv, Justin, conferences would have been boring without you – I'm so happy we worked together. To everyone else, good luck, you can do it!

Finally, I would like to thank my family for their support and encouragement during my PhD, and my proof readers to whom I am very grateful- you are all angles.

CONTENTS

LIST OF FIGURES

LIST OF TABLES

ABBREVIATIONS

3D	3 dimensional
ACI	Autologous chondrocyte implantation
MEM	Minimum Essential Medium
APTS	3-aminopropyltriethoxysilane
BG	Bioactive glass
BSA	Bovine serum albumin
CF	C-factor (molar ratio of GPTMS to gelatin)
CPD	Critical point dry
CT	Computed tomography
DABCO	1,4-diazabicyclo[2,2,2,]octane
DAPI	4',6-diamidino-2-phenylindole
DMEM	Dulbecco's modified eagle medium
DSC	Differential scanning calorimetry
ECM	Extracellular matrix
EDC	1-ethyl-3-(-3-dimethylaminopropyl)carbodiimide hydrochloride
FD	Freeze dry
FEG	Field emission gun
FDA	Food and Drug Administration
FTIR	Fourier transform infrared spectroscopy
G'	Storage modulus
G''	Loss modulus
GAG	Glycosaminoglycan
GPTMS	Glycidoxypropyl-trimethoxysilane
HA	Hydroxy apatite
HCA	Hydroxycarbonate apatite

HCl	Hydrochloric acid
HF	Hydrofluoric acid
ICP OES	Inductively coupled plasma optical emission spectroscopy
ICPTS	Isocyanatopropyl triethoxysilane
ID	Internal diameter
MAS NMR	Magic angle spinning nuclear magnetic resonance
MSC	Mesenchymal stem cells
MTT	3-(4,5-dimethylthiazol-2-yl)-2,5-diphenyltetrazolium bromide
NHS	N-hydroxysuccinimide
NITech	Nagoya Institute of Technology
NMR	Nuclear magnetic resonance
PBS	Phosphate buffered saline
PCL	Polycaprolactone
PDLA	Poly(D,L-lactide)
PE	Polyethylene
PFA	Paraformaldehyde
PGA	Polyglycolic acid
PGLA	Polyglycolic-lactic acid
PLA	Polylactic acid
PLLA	Poly(L-lactide)
PU	Polyurethane
PVA	Poly (vinyl alcohol)
RT	Room temperature
SBF	Simulated body fluid
SEM	Scanning electron microscopy
TEOS	Tetraethyl orthosilicate
TGA	Thermo gravimetric analysis
TRIS	Tris(hydroxymethyl)aminomethane
UV	Ultra-violet
XRD	X-ray diffraction
ZDEC	Zinc diethyldithiocarbamate

CHAPTER 1. INTRODUCTION

Cartilage defects

Cartilage defects affect millions of people across the world. Defects arise from degenerative diseases, general wear and tear, trauma and tumour removal (MMWR, 2007, Temenoff and Mikos, 2000). According to the NHS, in the UK alone, 70,000 knee replacement surgeries take place each year and the number is rising. Most naturally occurring joint problems begin with small lesions in the articular cartilage tissue (Orth *et al.*, 2014). Cartilage has almost no repair mechanisms due to its low cell density, low metabolism and absence of blood supply, so the damaged tissue progressively degrades until there is bone-on-bone contact (Muzzarelli *et al.*, 2012). This is known as an osteochondral defect, a defect that affects the full thickness of cartilage reaching subchondral bone and causes severe pain (Hunziker, 2002, Spiller *et al.*, 2011). Attempts by the body to repair the defect results in fibrocartilage, which has inferior mechanical and structural properties which cannot handle the loads required of it, leading to degeneration and more pain (Spiller *et al.*, 2011, Ahmed and Hincke, 2010).

Tissue engineering

Tissue engineering is a field combining the expertise of the life sciences and engineering. By understanding the materials and structural properties of organs and tissues, synthetic substitutes can restore or replace tissues that would otherwise require a donor. Langer and Vacanti (Langer and Vacanti, 1993) discussed three options for the future of tissue engineering. The first involves manipulating cells and implanting them without the need for open surgery. This is a simple and convenient solution, but the success rate is expected to be low due to the failure of the cells to retain function. The second option is based on supplying tissue inducing substances such as growth factors and signaling molecules to repair the tissue. This requires the development of delivery vehicles with mechanisms for targeted release. The third option, cells in a matrix (scaffold), was focused on in this work. By *in vitro* manipulation of cells in a host matrix, the idea is to replace damaged tissue with this implant. This option is particularly appropriate for cartilage tissue due to the extremely poor natural repair mechanisms (Knutsen *et al.*, 2007, Verzijl *et al.*, 2000). The time of culture of the cells *in vitro* on the scaffold depends upon the strategy chosen. Scaffolds can also be implanted to recruit cells from the *in vivo* environment.

The design of the host matrix is complex. It must provide a bioactive surface and act as a temporary template to guide tissue repair. The term bioactive refers to the material's capability to stimulate cell attachment and production of cartilage extracellular matrix, without fibrous encapsulation. The ideal scaffold would also degrade at the same rate at which the seeded cells form extracellular matrix and develop the native tissue structure (Solchaga *et al.*, 2005, Bryant and Anseth, 2003). This provides a transitional period without the loss of mechanical properties. The host matrix must also provide a low friction bearing surface compatible with cartilage in articular joints (Mow *et al.*, 1992).

Advances in processing

A three dimensional host scaffold is essential to support cell growth thicker than a few layers. The requirements include: bioactivity of the material; mechanical properties to match the host tissue; a degeneration rate to match the regeneration of the tissue; and channels for cells, nutrients and waste products. The channels/pores should be tailored to the tissue type, enabling cell-cell interactions. Matching mechanical properties to the host tissue and the degradation rate to tissue growth/remodelling rate would provide stability of the regenerating tissue. Matching the mechanical properties is also hypothesised to allow transduction of mechanical signals to cells growing on the scaffolds. Efficient diffusion channels are essential to allow for full thickness seeding of cells and avoid extracellular matrix and cytotoxic waste build-up (Vunjak-Novakovic *et al.*, 1998).

Traditional methods that produce sponge-like structures lack independent control of these requirements; however 3D printing is expected to overcome these limitations (Jakus *et al.*, 2016). 3D printing is generally a layer-by-layer fabrication technique which can provide accurate and reliable control of structures as dictated by computer software. The recent 3D printing boom has produced many printers with different mechanisms to build 3D structures and for use with different materials; metals, ceramics, polymers and cells all have various options for printing. Relating these capabilities to tissue scaffolds, the micro and the macro structure of the scaffold could therefore be tailored to fit a specific defect in a specific area in a specific patient. This tailoring can be achieved by creating computer simulations of the defect site to discover exact scaffold requirements (Semple *et al.*, 2005).

Hybrid materials

Alongside the advances in fabrication methods, bioactive materials have also been developing. Bioactive materials are defined here as materials which provide cell attachment sites and stimulate the formation of healthy native tissue. For bone and cartilage regeneration, composites are a common research focus. They provide strength from a ceramic and ductility

from a polymer, but degradation and bioactivity is inconsistent between phases. A bioactive phase can commonly be masked by the polymer and the interface between the polymer matrix and the reinforcing phase is usually poor, limiting the mechanical properties. Hybrids combine both organic and inorganic components at the molecular level. For cartilage regeneration, the organic component can provide toughness and bioactivity while the inorganic network provides strength. Due to the fine scale interactions between components, hybrids have the potential to degrade congruently and provide a fully bioactive surface for cells to attach (Mahony *et al.*, 2010). Hybrids are the focus of this PhD due to the tailorability of the material properties by variations in composition, making them suitable for adaption for 3D printing, electrospinning, and both cartilage and subchondral bone regeneration.

Aims

The aim of this thesis is to create a new cartilage regeneration construct through synthesis, 3D printing and electrospinning of sol-gel silica-gelatin hybrids. The variables of the synthesis and processing methods will be investigated with respect to pore morphology, mechanical properties, dissolution and cellular response.

CHAPTER 2. TISSUE REGENERATION, HYBRIDS AND 3D SCAFFOLDS

2.1 Hyaline cartilage

Anatomy and repair mechanisms

Hyaline cartilage, or articular cartilage, is a low friction wear-resistant tissue that coats the end of bones in the knees and other articular joints. It permits free movement of the joint and is able to distribute applied loads across its surface (Mow *et al.*, 1992). The multi-layered, fibre-reinforced structure has anisotropic and viscoelastic properties, and under stress, the pressurisation of the tissue is controlled though redistribution of interstitial fluid. The complex structure provides load support and a low friction surface in the presence of synovial fluid. When it is damaged, hyaline cartilage is challenging to regenerate to its original state and function, with many procedures producing inferior fibrocartilage (Kreuz *et al.*, 2006, Knutsen *et al.*, 2007, Gobbi *et al.*, 2005).

Cartilage is composed of ~5 % chondrocyte cells within a dense extracellular matrix (ECM) made up of ~72 % water, collagen, and proteoglycans. In cartilage, the main proteoglycan is aggrecan. Proteoglycans are proteins consisting of a core protein with a highly polar protein, glycosaminoglycan (GAG), covalently attached. GAG is a linear polymer of repeating amino sugars which have a prevalence of acidic groups leading to a negative charge. This attracts cations (e.g. Na^+) from the interstitial fluid and two important effects are observed: proteoglycan molecules electrostatically repel each other, and they attract water molecules. The hydrated aggrecan molecules are trapped within a network of Type-II collagen which reinforces the structure through stiffness and crosslinking. When under compression, the contact area is increased due to the reversible deformation that occurs when some of these water molecules are forced out. The load is supported through the majority of water molecules remaining in confinement and the trapped aggrecan molecules retaining their electrostatic repulsion (Muzzarelli *et al.*, 2012).

To complement the intricate interactions between aggrecan, collagen and interstitial fluid, the structure of the cartilage is equally complex. Hyaline cartilage is comprised of three zones as shown in Figure 1; superficial zone, middle zone and deep zone. Each zone varies in extracellular matrix (ECM) composition and organisation, cell morphology and metabolic activity (Klein *et al.*, 2009).

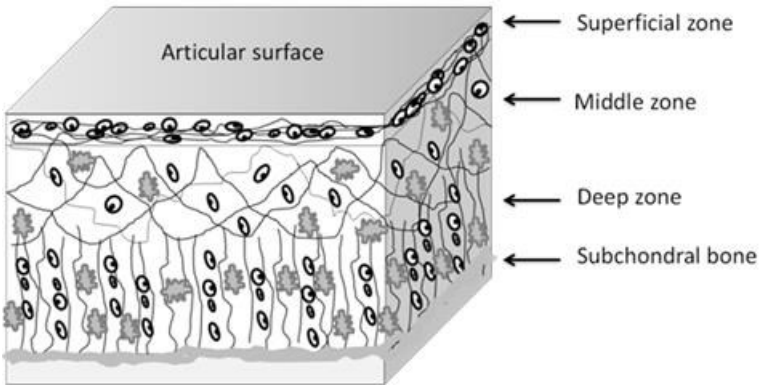

Figure 1. The zonal organisation of articular cartilage; the arrangement and distribution of cells collagen Type II, and proteoglycans.

The superficial zone provides the extremely low friction collagen surface and is 200 μm thick (Cui *et al.*, 2012). It has a high density of flattened chondrocytes and a parallel orientation of collagen fibres along the surface, which provides high lateral tensile strength to withstand shear stresses during loading (Akizuki *et al.*, 1986). The middle zone has randomly orientated fibres and higher aggrecan concentration, which gradually increases from the surface to the deep zone. High water levels provide high swelling pressure and impart compressive strength. Chondrocytes are spherical, randomly orientated, and present at a very low density. The deep zone allows for the transition from hyaline cartilage to calcified cartilage, subchondral bone. It consists of bundles of collagen fibres perpendicularly orientated to the calcified cartilage. The density of chondrocytes is low, but cells are large and well organised in vertical columns.

Natural repair mechanisms for healthy cartilage are limited due to the lack of a blood supply, transport mechanisms, and ability to recruit new cells. Additionally, chondrocytes have slow metabolism and are not active enough to provide effective repair (Verzijl *et al.*, 2000, Hidaka *et al.*, 2006). For an attempt at cartilage regeneration to occur, the defect must reach subchondral bone and stimulate the release of stem cells and signaling molecules from the bone marrow. The highly complex structure of hyaline cartilage is not achieved due to the lack of organisation and clear signaling to the cells in the defect. Instead of hyaline cartilage, fibrocartilage forms which has inferior mechanical properties and degrades under loading, often after 2-5 years (Furukawa *et al.*, 1980, Johnson, 1986).

The production of fibrocartilage rather than hyaline cartilage is due to whether the chondrocytes are in differentiated or dedifferentiated form. Hyaline cartilage is produced by differentiated chondrocytes, which have a spherical morphology and synthesise native ECM in a process known as differentiating. Fibrocartilage is formed by dedifferentiated chondrocytes, which do not have this capability to differentiate and have an elongated morphology (Stokes *et al.*, 2002).

Healthy hyaline cartilage markers

Specific proteins within cells can be stained to look for healthy hyaline markers. These markers include ECM components: aggrecan, GAG, and type II collagen, and proteins produced during differentiation such as Sox9. Negative markers include collagen Type I, an indicator of fibrocartilage, and collagen Type X, an indicator of calcified cartilage.

To determine cell attachment, cell filaments, actin and vimentin, are stained. Actin is a microfilament just inside the cell membrane involved in cell migration and adhesion, whereas vimentin filaments support and anchor organelles within the cell. When cells attach to the ECM, these internal filaments maintain cytoskeletal tension and cell shape (Langelier *et al.*, 2000).

Mechanical properties

Table 1 states the mechanical properties of hyaline cartilage tissue. These are the properties that the host matrix should provide in order to be compatible with host cartilage tissue and impart the stresses and strains to the cells that would be experienced in the native tissue.

Table 1. Mechanical properties of cartilage tissue.

Property	Cartilage
Ultimate Tensile Strength /MPa	0.8-25 (Little *et al.*, 2011)
Ultimate Tensile Strain /%	10-40 (Moutos *et al.*, 2007)
Compressive strength /MPa	22-37 (Kerin *et al.*, 1998, Repo and Finlay, 1977)
Young's Modulus /MPa	0.5-1.0 (unconstrained at sides) (Little *et al.*, 2011, Jurvelin *et al.*, 1997)
Compressive strain	0.3-0.8 (Jurvelin *et al.*, 1997, Boschetti *et al.*, 2004, Chen *et al.*, 2012)

2.2 Clinical treatments and developments

Current clinical treatments

For patients with full thickness cartilage damage and bone-on-bone contact, full knee replacements are required. Full knee replacements involve a huge loss of healthy cartilage and bone tissue and have a relatively short lifespan, an estimate of 20 years is given by the NHS. This eventuality is best avoided by repairing cartilage defects as soon as bone-on-bone is felt to prevent further damage. Before this point, defects go undetected due to the lack of nerves in the cartilage tissue. This is particularly important for young active patients who would require multiple implants over their lifetime. The surgery options currently available for cartilage defects are; microfracture, mosaicplasty, autologous chondrocyte implantation and scaffold-based techniques (Kreuz *et al.*, 2006, Knutsen *et al.*, 2007, Gobbi *et al.*, 2005, Ahmed and Hincke, 2010, Makris *et al.*, 2015).

In microfracture surgery, lesions are made into the bone marrow allowing cells and cell signaling molecules to enter the defect site and attempt to regenerate cartilage. The drawback of this technique is the lack of organisation and clear signaling given to the infiltrated cells (Gobbi *et al.*, 2005, Kreuz *et al.*, 2006).

Mosaicplasty is the placement of many small osteochondral autografts into the void from which the damaged cartilage was removed. The autografts are removed during a prior surgery from less critical loading areas, a very limited donor site. This has the clear drawback of being traumatic for the patient as two surgeries are required and healthy cartilage tissue is removed. This technique is also limited by the size of the defect, the amount of cartilage available for removal at the donor site, and the infiltration of unorganised cells entering from the exposed subchondral bone (Hunziker, 2002).

Autologous chondrocyte implantation (ACI) is an FDA approved cell-based cartilage regeneration strategy. In this surgery a sample of the patient's chondrocytes are removed and expanded *in vitro* to increase numbers for re-implantation at the damaged area, typically >12 million cells (Makris *et al.*, 2015). The number of chondrocytes that can be removed is limited to avoid damaging healthy tissue and very small compared to the number required for ACI. The primary drawback of this technique is again the lack of organisation and zonal distribution of the re-implanted cells, but also the high expense, long time frames, and high chance of dedifferentiation during cell expansion and once implanted (Knutsen *et al.*, 2007).

Matrix-induced autologous chondrocyte implantation (MACI) is another cell-based cartilage regeneration strategy which uses collagen or hyaluronic acid matrices to deliver cells to the defect. As with ACI, it involves two surgical procedures, the first to collect autologous tissue. After the cell population has been expanded *in vitro* and seeded on the matrix for 3 days, the seeded matrix is implanted in a second operation and fixed with fibrin glue. No mechanical support is provided by the matrices, and as yet, clinical studies do not show any clear benefit of MACI over ACI and it has not been FDA approved (Makris *et al.*, 2015).

All of these techniques aim to produce healthy hyaline cartilage, but the unfavourable mechanical conditions and unstructured organisation of cartilage cells often results in fibrocartilage which in the long term erodes away requiring a repeat operation in around 5 years (Knutsen *et al.*, 2007, Hunziker, 2002, Kreuz *et al.*, 2006). ACI also highlights the issues surrounding cell expansion. When large cell numbers are required and expansion periods are long, the flat surface tends to induce dedifferentiation to fibrocartilage due to signals from the internal filaments, actin and vimentin, to the cell nucleus (Stokes *et al.*, 2002, Allen *et al.*, 2012).

2.2.1 Developments in cartilage repair

Discussion of the current treatments available highlighted that cell organisation and low cell numbers are key to regenerating hyaline cartilage and avoiding fibrocartilage. To maintain cell organisation, a host matrix is necessary to provide zonal distribution during seeding and support under loading once implanted. This aligns with Langer and Vacanti's third option for tissue engineering (Langer and Vacanti, 1993), cells in a matrix.

Research into cartilage regeneration via cells in a matrix has three main focus points: cell source, cell stimulation and type of host matrix. The choice of cell type strongly affects the time frame to produce the implant, the chance of acceptance/rejection by the body, and the ease at which hyaline cartilage forms. Cell stimulation by mechanical or chemical signals can be used to aid the formation of hyaline cartilage, but the options when choosing the host matrix are many. The bioactivity, degradation rate, mechanical properties, pore/channel width, and fabrication method of the host matrix must all be considered.

Cell source

The ideal cell source would be easy to isolate and expand, and would synthesise cartilage specific ECM components such as aggrecan and type II collagen. Most research is focused on seeding chondrocytes or stem cells and extensive overviews of cell sources are available (Chung and Burdick, 2008, Reissis *et al.*, 2016).

Chondrocytes are the obvious choice as they are the native cartilage cell type and therefore produce, maintain and remodel cartilage ECM *in vitro*. Problems arise when harvesting due to low cell numbers, low expansion capacity, and the ease at which chondrocytes can switch between the differentiated and dedifferentiated phenotype. Despite being the natural cell source, chondrocytes also have low ability to form hyaline cartilage without additional stimulation and this ability reduces further with age of the patient (Hidaka *et al.*, 2006). A further disadvantage to all patients is the loss of healthy chondrocytes from the donor site.

Mesenchymal stem cells (MSCs) have the capacity for chondrogenic differentiation when exposed to cell signaling molecules which stimulate stem cells to form chondrocytes (chondrogenesis) and differentiate (Mackay *et al.*, 1998). As MSCs have the ability to self-renew, their extraction from bone marrow or adipose (fatty) tissue is not detrimental to the health of the patient (Huang *et al.*, 2005). The induction of chondrogenic differentiation by growth factors is an extensively researched area due to the complexity of regulating the proliferation of cells and ECM production. To complicate this further, different signals are

required for MSCs originating from different sources, however once tuned, growth factors can induce chondrogenesis in MSCs (Ahmed and Hincke, 2010, Chung and Burdick, 2008).

Cartilaginous matrix triggers

Stimulation of ECM production can be achieved by various triggers. Chemical stimulation, such as the application of growth factors (Fortier *et al.*, 2011, Ahmed and Hincke, 2010, Chung and Burdick, 2008), and mechanical stimulation of cell seeded constructs (Bian *et al.*, 2010, Wagner *et al.*, 2008, Kawanishi *et al.*, 2007) are both recognised as highly effective methods to produce high quality cartilaginous matrix. The induction of chondrogenic differentiation has been discussed in reference to MSCs, but can also enhance ECM production of chondrocytes. Mechanical stimulation of cells seeded in a host matrix also enhances hyaline tissue regeneration by exposing the differentiating chondrocytes to 'normal' loading conditions which leads to an increase in ECM production, proliferation of cells and improved compressive properties of the engineered tissue.

Both of these initial options are cell-focused and complex due to the huge number of combinations of growth factors and types of stimulation that can be applied. They tend to be used in combination with low bioactivity materials where the host matrix itself does not impart any signaling to the cells.

Cell-free biomaterials

Autologous matrix-induced chondrogenesis (AMIC) is a novel cartilage repair technique which avoids the need to pre-seed cells and is performed in a single surgery. Cells are released through microfracture immediately prior to implantation and fixation of the scaffold. Currently collagen scaffolds are the main focus of this technique (Makris *et al.*, 2015). To create a host matrix that stimulates chondrogenesis, the main two things to consider are the attachment sites and stiffness. Cell attachment to the matrix is essential to anchor cells in position. The use of ECM components in the matrix is well known to enhance cell attachment and increase ECM production due to the availability of native binding sites that are recognised by the cell surface (Fan *et al.*, 2006 , Chung *et al.*, 2009, Spiller *et al.*, 2011, Yamaoka *et al.*, 2006). Once attached to the matrix, the internal filaments of the cell maintain the cytoskeletal tension and detect the stiffness of the substrate. The stiffness of the attachment site has a strong influence on the efficiency of chondrocyte differentiation and can even induce dedifferentiation when conditions do not match native ECM (Allen *et al.*, 2012). This is the cause of dedifferentiation during chondrocyte expansion.

The cartilaginous matrix triggers of concern here are attachment sites and stiffness, which have a significant bearing on the material choice for the host matrix. A local 3D environment is also required to enable cell-cell interactions (Kohn and Rossello, 2010, Stokes *et al.*, 2002).

2.3 Cartilage host matrix options

There are various requirements of a host matrix for cartilage regeneration. Firstly, the material should be bioactive to provide attachment sites for cells and stimulate differentiation of cells to form healthy hyaline tissue. The mechanical properties of the matrix should also replicate the mechanical properties of hyaline cartilage, ideally on both the micro and macro scale. The degradation rate should be equal to the regeneration rate of the hyaline tissue to allow mechanical loads to transfer gradually from the matrix to the repaired tissue (Freed *et al.*, 1994, Bryant and Anseth, 2003). The pore/channel width should be carefully selected to allow for easy infiltration of cells, but provide a 3D local environment that cells can quickly populate, therefore reducing the number of cells required and regeneration rate. Finally, the fabrication method of the host matrix must be selected to incorporate all the elements of the matrix design. The following sections discuss candidate materials and fabrication methods for the scaffolds.

2.3.1 Polymers

Synthetic polymers

Polyesters such as polycaprolactone (PCL), polyglycolic acid (PGA), polylactic acid (PLA), as shown in Figure 2, and the copolymer polyglycolic-lactic acid (PGLA) are popular choices for tissue scaffold research. They are biocompatible and biodegradable polymers which are FDA approved (Huang *et al.*, 2013, Rezwan *et al.*, 2006) and already in use as sutures, tissue staples, stents, and many other devices. For the application of tissue regeneration, the degradation mechanism of polyesters is an issue. Polyesters degrade via hydrolytic chain scission which results in formation of carboxylic acid groups and reduces the local pH. Degradation continues rapidly in the self-catalysed acidic conditions and mechanical properties drop off sharply (Eglin *et al.*, 2009). This produces unstable scaffolds and a damaging acidic local environment that can be potentially cytotoxic (Hunziker, 2002).

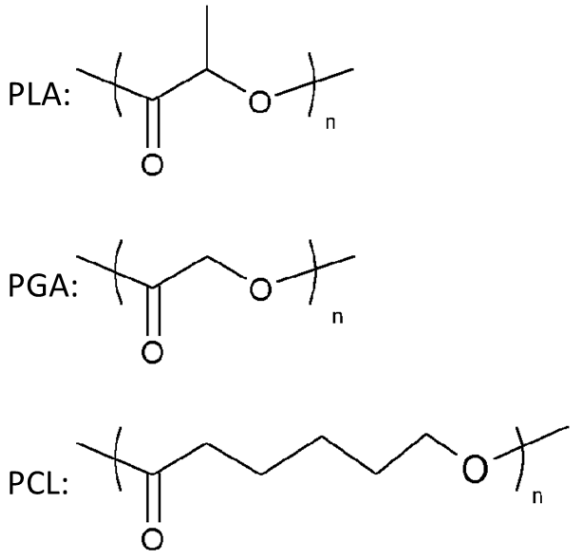

Figure 2. Chemical structure of PLA, PGA and PCL.

Of these polyesters, PCL and variations on PLA have the slowest degradation rate. PCL has the longest carbon backbone which reduces the prevalence of ester bonds. Both PCL and PLA are hydrophobic, which prevents water from permeating and hydrolysing the ester bonds (McCullen *et al.*, 2012). PLA has a central chiral carbon around which the methyl side chain is positioned to form poly(L-lactide) (PLLA) or poly(D,L-lactide) (PDLA) when the methyl side chain on the monomers alternates across the chiral centre. The regularity of PLLA results in a highly crystalline polymer that takes years to completely biodegrade.

Slower degrading scaffolds are preferable to fast degrading scaffolds as mechanical integrity is maintained throughout the healing process allowing thick, homogeneous ECM to be deposited (Chung *et al.*, 2009, Solchaga *et al.*, 2005), however, degradation cannot be infinitely slow. Scaffold degradation allows further integration and remodelling of the regenerated tissue (Bryant and Anseth, 2003, Chung *et al.*, 2009). Further negatives when considering polyesters are that for crosslinking, the active groups are the end groups, hence increased crosslinking can only be achieved by reducing the molecular weight, which increases degradation rate. Most importantly, despite FDA approval and biocompatibility, polyesters have low bioactivity in comparison to native ECM polymer (Cai *et al.*, 2013).

Native ECM polymers

As mentioned, polymers native to ECM can provide cell attachment sites and relay biological information to the cells to stimulate differentiation (Hunziker, 2002, Cai *et al.*, 2013, Spiller *et al.*, 2011, Yamaoka *et al.*, 2006, Fan *et al.*, 2006, Wang *et al.*, 2016). Collagen is therefore an obvious choice for cartilage tissue scaffolds as the structure of cartilage ECM is provided by collagen Type II and can be remodelled by chondrocytes. Collagen however is highly insoluble. It can only be dissolved in acetic acid at low concentrations due to the triple helix structure (O'Brien *et al.*, 2004), which limits the mechanical strength and degradation rate of collagen matrices. Furthermore, collagen has the potential to transfer diseases and may cause an immune response when sourced from other species.

Gelatin is hydrolysed collagen which means the complex conformation is lost, but biological signals from the amino acid sequences are retained (Lien *et al.*, 2009, Farris *et al.*, 2010). This allows for high solubility in water whilst still resembling the native ECM protein and providing native cell attachment sites. In this denatured form, concerns of immunogenicity and pathogen transmission are avoided and the ease of extraction from a number of different sources makes gelatin commercially available at low cost.

Gelatin has a gel transition temperature at 30°C so is soluble *in vivo* due to a thermo reversible conformational disorder-order transition of the gelatin chains stabilised by hydrogen bonds (Bigi *et al.*, 2002). Gelatin must therefore be crosslinked to prevent instability. Like collagen, gelatin is made up of amino acids which exhibit functional side groups: hydroxyl -OH, amine -NH_2 and carboxylic -COOH, which can be utilised for crosslinking. Polymers with functional side groups rather than functional end groups, have a distinct advantage as the degree of crosslinking is independent to the molecular weight (Valliant and Jones, 2011). In addition, crosslinked gelatin degrades linearly by enzyme action known as proteolysis, which avoids the sharp drop-off in stability typical of polyesters.

Different sources and extraction methods of gelatin produce different characteristics such as gel strength, viscosity, setting behaviour, ability to crosslink and susceptibility to protease attack. The two main gelatin types are Type-A (acid treated) and Type-B (alkali treated). Bovine and porcine sources are most commonly available. In a hydrogel study involving different gelatin types and methods of crosslinking, Type-A porcine crosslinked most readily and there was good correlation between the number of crosslinks and the degradation (Ozeki and Tabata, 2005). In a study comparing molecular weight of gelatin, higher weights resulted in stronger scaffolds, lower dissolution, and faster gel time of the crosslinked materials (Mahony *et al.*, 2014).

Gelatin is a low density polyelectrolyte. Depending on the pH, gelatin can have an overall positive or negative charge due to unequal distribution of carboxyl groups (negative charge) and amino groups (nitrogen containing bases, positive charge) along the gelatin chain. Porcine gelatin Type-A has an isoelectric point, pH_{iso}, between 7 and 9, at which the electric charge is neutral. Gelatin is soluble in polar solutions which provide counter-ions to the charges. Solvents with a low dielectric constant cannot provide sufficient counter-ions and instead facilitate ion-pairing between complementary ions along the gelatin chains, and therefore the gelatin precipitates.

One disadvantage of natural polymers such as collagen and gelatin is the non-uniform sequence of amino acids. It is not exactly known how many functional groups each polymer molecule will have so the number of covalent links formed between polymer and silica can only be estimated. For porcine Type-A gelatin, the proportion of each amino acid present was defined by Farris *et al.* (Farris *et al.*, 2010), however variation between batches can be large. Another consideration is that the market for products containing gelatin from porcine or bovine sources may be limited by refusal on religious and cultural grounds (Valliant and Jones, 2011). To avoid this, other natural polymers such as agarose or alginate are an option, however as plant based natural polymers, cell adhesion and degradation rates are an issue (Hunt and Grover, 2010). To ensure chondrocytes attach and differentiate on the host matrix, the implant developed here will be based on gelatin.

Crosslinking gelatin

To improve mechanical and dissolution properties, various options for covalent crosslinking are available due to the array of functional groups exhibited by amino acids along the gelatin chain: -OH, $-NH_2$, or -COOH. The most common gelatin crosslinking agents are: glutaraldehyde, EDC, GPTMS, and genipin. Each will briefly be discussed, however it must be

noted that crosslinking alone is not enough to provide the mechanical properties required of a cartilage scaffold.

Glutaraldehyde is the most common and efficient crosslinking agent for gelatin. 1 wt% glutaraldehyde results in 100 % crosslinking with a 20x increase in Young's modulus. It has an aldehyde, -CHO, group at both ends of the short chain polymer which covalently bonds to amine groups on the polymer chain. Glutaraldehyde is easily available, inexpensive and an efficient crosslinker, however if released due to biodegradation, is cytotoxic (Bigi *et al.*, 2001, Skotak *et al.*, 2010).

EDC, 1-ethyl-3-(-3-dimethylaminopropyl)carbodiimide hydrochloride, is water soluble and reacts with carboxyl groups on the polymer to form an active intermediate. This intermediate can easily be displaced by nucleophilic attack from amino groups on the polymer and EDC, a soluble urea derivative, is released as a by-product. To further improve efficiency, N-hydroxysuccinimide, NHS can be used to stabilise the intermediate against hydrolysis and allow for more efficient coupling at higher pH. To avoid cytotoxicity, remaining EDC and NHS must be removed by rinsing (Kim and Kim, 2013, Zhang *et al.*, 2009).

GPTMS, glycidoxypropyltrimethoxysilane is a short chain molecule with an oxirane group at one end and a trimethyloxysilane group at the other. It has been used to crosslink gelatin via nucleophilic attack of carboxylic groups on the gelatin molecule to form an ester bond. The trimethyloxysilane group hydrolyses under acidic conditions to form three silanol groups which condense to form a covalent bonded bridge between gelatin during solvent evaporation (Song *et al.*, 2008b, Ren *et al.*, 2001b, Tonda-Turo *et al.*, 2013).

Genipin is a natural plant-derived product that covalently bonds to amine groups, and although less effective than glutaraldehyde, it is the only non-cytotoxic alternative (Bigi *et al.*, 2002, Kirchmajer and Panhuis, 2014).

2.3.2 Cartilage scaffold requirements

To ensure healthy cartilage is produced, a zonal scaffold is required with various requirements as summarised in Table 2. Considering the material properties, it must be biocompatible, bioactive and degradable *in vivo*. To encompass all the requirements, polymers native to cartilage ECM are the most suitable as they provide binding sites for cell attachment and trigger differentiation of chondrocytes. Gelatin is the material of choice as it is a denatured form of collagen so can provide the native cell attachment sites and is highly abundant at low cost. Gelatin must be crosslinked to prevent the gel-liquid transition *in vivo* and ensure linear enzymatic degradation of the scaffold. The crosslinking agent method must also be biocompatible and improve the inherent mechanical properties of the gelatin.

Table 2. Requirements of a tissue scaffold for cartilage regeneration

Matrix property/variable	Biological response (Hunziker, 2002, Klein *et al.*, 2009, Allen *et al.*, 2012)
Biocompatibility	Induce no adverse immunological reactions: cytotoxic effects, inflammatory responses, foreign body giant cell reactions.
Bioactivity and adhesion	Promote cell attachment and proliferation, provide signals for chondrocyte differentiation and proliferation, ECM production and allow scaffold remodelling.
Biodegradability	Controlled degradation rate without cytotoxic or nephrotoxic (toxic to kidneys) by-products.
Mechanical properties	Support the engineered tissue with appropriate stiffness and volume stability even during degradation and remodelling.
Low friction surface	Provide a surface compatible with the extremely low friction surface of native hyaline cartilage in articular joints.
Interconnected porous structure	Allow efficient cell seeding, cell migration, ECM migration, diffusion of nutrients and waste products.
Structural anisotropy	Promote native anisotropic tissue organisation.
Fabrication	Tailorable to the patients' needs and up-scalable for mass production.

Considering the scaffold properties, the pores and channels should allow for efficient cell seeding, migration, and diffusion of ECM produced, nutrients and waste products. The

scaffold should also have a high surface to volume ratio for cell adhesion and be zonal to increase cell density and ECM production in the superficial layer. The compressive strength, Young's modulus, and ability to withstand cyclic loading of the scaffold should match the properties of native cartilage to share the loading of the body with the host tissue. To stabilise the scaffold in position, the lower portion of the scaffold must integrate with subchondral bone *in vivo*.

2.3.3 Scaffold fabrication options

Scaffolds can be fabricated in various ways depending on the type of host matrix in question i.e. a hydrogel or porous dehydrated scaffold. The processing options will be outlined briefly so that techniques are clear when discussing the host matrix options.

When discussing hydrogels, the main processing method is by forming the hydrogel *in situ*, however 3D printing can also be employed. 3D printing combines computer aided design with robotic layer-by-layer fabrication. In the case of hydrogels, a nozzle based extrusion system passes hydrogels chemically or thermally through a nozzle in droplets, or continuously, to deposit layers (Cui *et al.*, 2012, Hollister, 2005, Billiet *et al.*, 2013, Kundu *et al.*, 2015).

For the porous scaffolds, various options are discussed. Freeze casting, salt/porogen leaching and again 3D printing are the most popular options. Freeze casting is a process whereby ice crystals act as the template and the structure can be controlled/orientated by the direction of freezing, cooling rate, and freezing temperatures. The ice is later removed by sublimation (Ahmed and Hincke, 2010, Arora *et al.*, 2015). Salt/porogen leaching uses salt crystals or low melting point particles to act as a sacrificial template. Once the scaffold material has been infiltrated and solidified/dried, the sacrificial template is removed by dissolving or melting, leaving behind a porous network in place of the template (Steele *et al.*, 2014, Tanaka *et al.*, 2010). 3D printing of polymers to produce porous scaffolds often require temperature control to soften the polymers before extruding through a nozzle to build up the scaffold layer-by-layer (Woodfield *et al.*, 2004, Sobral *et al.*, 2011).

2.3.4 Host matrix: hydrogels

Cells can be encapsulated in hydrogels which provide a three dimensional environment similar to natural ECM. The high water content and crosslinked polymeric structure of hydrogels make them an important class of material for cartilage regeneration (Spiller *et al.*, 2011, Hunziker, 2002).

Benefits of hydrogels as a host matrix

The high water content means chondrocytes are more likely to maintain the hyaline spherical morphology rather than becoming elongated fibrocartilage cells (Benya and Shaffer, 1982, Rowley *et al.*, 1999). Although the differentiated phenotype is maintained, cell anchorage remains critical for cell survival to prevent sinking of the cells within the aqueous gel (Cui *et al.*, 2012). Native ECM polymers of collagen, gelatin, and hyaluronic acid have therefore shown increased production of cartilaginous matrix compared to other natural polymer hydrogels; chitosan, fibrin, agarose, alginate (Hunt and Grover, 2010).

Solutions of polymer and chondrocytes can be injected directly into the defect site to fill the defect volume, and form the hydrogel *in situ*. This provides a minimally invasive treatment option, however it provides no organisation to the cells (Spiller *et al.*, 2011). Other than lowering cell numbers required, it has little benefit over ACI. To overcome the issue of cellular organisation, steps have been taken to recreate the zonal structure of cartilage by creating multilayer hydrogel structures which separately encapsulate cells from the superficial, middle and deep zones (Kim *et al.*, 2003). To create zones and optimise the distribution of cells through the hydrogel, 3D printing has a lot to offer.

3D printing cells encapsulated in hydrogels

The most exciting development for hydrogels is that advances in 3D printing have allowed chondrocytes themselves to be 3D printed whilst contained within a hydrogel (Mannoor *et al.*, 2013, Cohen *et al.*, 2006, Cui *et al.*, 2012). This is an excellent breakthrough for regenerating whole organs such as the 3D printed bionic ear developed by Mannoor *et al.* which combined structurally supported cells with electronic elements (Mannoor *et al.*, 2013). Cells can be distributed across the scaffold as required which prevents inhomogeneous seeding issues in large scaffolds and allows the incorporation of different cells in different regions (Cui *et al.*, 2012). The stress exhibited when passing the cells through a nozzle is known to harm the cell viability (Schuurman *et al.*, 2011), though viability can be improved by reducing the dispensing pressure and using cylindrical rather than conical needles (Billiet *et al.*, 2013, Kundu *et al.*, 2015).

Despite the positive results of cell morphology maintenance and precise distribution of cells throughout the matrix, hydrogels come with their downsides. The concerns are mainly directed towards the mechanical properties and *in situ* crosslinking mechanisms for hydrogels.

Mechanical properties and crosslinking of hydrogels

Regardless of the natural polymer choice or crosslinking method, hydrogels typically have low mechanical strength, and low stiffness (Kuo and Ma, 2001). Hydrogels with dual polymer networks and both permanent and ionic crosslinks are shown to significantly improve these properties (Hong *et al.*, 2015, Norton *et al.*, 2014, Sun *et al.*, 2012b, Gong *et al.*, 2003, Kirchmajer and Panhuis, 2014). A gelatin based hydrogel was developed by Kirchmajer *et al.* with up to 1.1 MPa compressive strength and a Young's modulus of 0.4-0.9 MPa, through creating covalent crosslinks between gelatin using genipin, and creating a co-network with gellan gum, ionically crosslinked using $CaCl_2$. Considering the compressive strength of gellan gum is ~360 kPa and gelatin is ~20 kPa, the effects of combining the two and adding crosslinks was very effective, however compressive failure strength of 1.1 MPa is still well below that of hyaline cartilage. These hydrogels were produced without the inclusion of cells.

Crosslinking gelatin with cells encapsulated is a problem and many hydrogels discussed have either not encapsulated cells and just reported hydrogel properties, or have not reported on the cell viability after crosslinking (Kuo and Ma, 2001, Kim *et al.*, 2003). Covalent crosslinking agents are often toxic to cells and therefore not suitable *in situ* (Kuo and Ma, 2001), whereas ionic crosslinks cannot provide the necessary mechanical properties. Photopolymerisation using visible light or UV light results in cell death, as low as 26 % viability in some cases (Hoshikawa *et al.*, 2006). 3D printed hydrogels can improve the cell viability when UV exposure is applied in short bursts to the as-printed gel, rather than the required long exposure times to crosslink the entire bulk (Cui *et al.*, 2012).

Another issue with highly crosslinked hydrogels is that the diffusion of the ECM components and cells are affected by the mesh size of crosslinked polymer (Bryant and Anseth, 2003), therefore diffusion efficiency within the hydrogel is reduced by attempts to increase the mechanical properties and degradation rates.

3D printing PCL-hydrogel scaffolds

To avoid crosslinking while improving mechanical properties, cells encapsulated in hydrogels have been 3D printed alongside PCL 3D printed constructs (Kundu *et al.*, 2015, Kim *et al.*, 2016). PCL is a well-established 3D printing material and provides the strength, though

scaffold stiffness is considerably higher than hyaline cartilage at 6 MPa (Schuurman *et al.*, 2011).

Overall, there is a lot of interesting research into hydrogels for cartilage regeneration, particularly with the introduction of 3D printing to the field. As the key requirements are; bioactivity, mechanical properties, degradation rate and ease of infiltration and diffusion, hydrogels are unable to achieve these simultaneously. Using them inside structural scaffolds could be a viable strategy, however if the structural scaffold has suitable surface chemistry and the pore networks allow cell-material interactions, the need for the hydrogel component would be negated.

2.3.5 Host matrix: porous tissue scaffolds

Tissue scaffolds are defined here as un-hydrated implants which aid native tissue regeneration. Compared to hydrogels they can provide improved mechanical properties and diffusion channels. The porosity, interconnectivity, strut dimensions and stiffness all strongly affect the proliferation and morphology of chondrocytes, so designing a tissue scaffold is complex (Nuernberger *et al.*, 2011, Kelly and Prendergast, 2006, Genes *et al.*, 2004, Lien *et al.*, 2009). By varying the structure and composition of the scaffold, it is hoped the mechanical strength and degradation can be tuned.

Pore/channel size and interconnectivity

Traditionally 'sponge-like' cartilage tissue scaffolds have been made using porogen leaching techniques and freeze casting, so the first question when designing a scaffold is; what is the required pore size? A balance is required between large pores which allow easy infiltration of cells and diffusion of nutrients, waste, ECM components; and small pores which provide more cell attachment sites and promote differentiation due to the 3D environment provided (O'Brien *et al.*, 2005, Steele *et al.*, 2014). There is considerable contradiction in the literature as to the ideal pore size for cartilage scaffolds, due to the differences in interconnect size, which cannot easily be controlled independently of pore size.

There is strong support for cartilage tissue scaffolds with a 300-400 μm pore size. Salt leached PLLA scaffolds produced by Tanaka *et al.* with pores sizes of 300-900 μm and ~95 % porosity were compared and 300 μm found most effective (Tanaka *et al.*, 2010). 400 μm pore size scaffolds were again supported by Steele *et al.* (Steele *et al.*, 2014) who concluded 0.03 mm^3 porogen scaffolds (~400 μm pore size) yielded higher proteoglycan levels compared to 1 mm^3 porogen scaffolds (~1200 μm pore size) during *in vitro* culture of bovine chondrocytes. However interconnect size was not described. Lu *et al.* (Lu *et al.*, 2010) compared collagen sponges produced by ice particulate templates with the pore sizes: 180 μm, 400 μm, and 700 μm and varying interconnectivity. Overall, the 400 μm pore size scaffolds with large interconnects resulted in more homogenous cell adhesion and distribution than 180 μm and 700 μm pore size, however the 400 μm pore size scaffold with small interconnects resulted in the worst GAG/cell ratio. Even smaller pores, 60-80 μm have shown increased GAG/cell synthesis by Mandal *et al.* (Mandal *et al.*, 2011), however these pores can be considered as direct channels due to formation by a highly directional freeze drying. This confirms that the size of interconnects between pores is the limiting factor for cell infiltration and diffusion, and is therefore more important than pore size.

When developing sponge-like scaffolds, optimisation of the spherical pore size and interconnectivity to allow for a uniform distribution of attached cells is the main challenge. The tortuous path to reach the centre of the scaffold prevents full thickness regeneration due to pores being blocked with cells during seeding and build-up of toxic waste products (Malda *et al.*, 2005, Vunjak-Novakovic *et al.*, 1998). To overcome this, dynamic seeding (flowing or mixing of cell suspension) has been developed, however 3D printing offers an alternative solution.

3D printed scaffolds

Recent developments in 3D printing allow for greater control of the porosity. This is important as the switch from spherical pores with small interconnects to direct channels removes the tortuous path to reach the centre and improves cells seeding efficiency and ECM distribution.

Malda and Emans *et al.* compared 3D printed scaffolds to particulate leached sponges with the same composition and porosity (Malda *et al.*, 2005, Emans *et al.*, 2013). Both scaffolds were ~100 % interconnected, but the difference in interconnects gave very different cut-off values (pore size at which accessibility dropped below 90 %), ~120 µm for the leached sponges and ~680 µm for the 3D printed scaffold. Despite the large channel width of the 3D printed scaffold, the composition of the regenerated cartilage *in vitro* and *in vivo* was enhanced in comparison to the sponge-like scaffold, again proving the importance of large interconnects. Sobral *et al.* found that cell density was affected by gravity when PCL channel widths were large, 750 µm, but the effect was almost negligible when channel width was reduced to 100 µm (Sobral *et al.*, 2011). Therefore smaller pores encouraged cell retention, though the cell redistribution may have been enhanced by the low levels of cell attachment to the PCL scaffolds.

Conclusion on pore morphology

Spherical 300-400 µm pores allow good cell infiltration and ECM formation based on 'sponge-like' scaffolds where the pore size strongly affects the interconnect size and cell infiltration. Larger pores are unfavourable due to the reduced surface area and therefore reduced binding sites available (O'Brien *et al.*, 2005) which reduce cell attachment, so uniform distribution of ECM throughout the scaffold is not achieved. 3D printing can improve the diffusion efficiency and cell infiltration by providing direct channels throughout, which are shown to improve tissue regeneration in comparison to scaffolds synthesised by traditional routes with the same porosity and interconnectivity (Malda *et al.*, 2005). Therefore smaller, direct, 3D printed channels can be used to provide the 3D environment to the differentiating

cells without being limited by interconnect size. Though the literature is limited and contradictory, 200-300 μm channels of porosity seem appropriate for cartilage tissue regeneration when using a bioactive material.

Zonal scaffolds

To encourage a natural distribution of cells and generate high cell density in the superficial zone, the scaffold must be tailored for the regeneration of each hyaline cartilage zone.

The zonal organisation of cartilage has been mimicked by tissue scaffolds and proven to promote inhomogeneous, zonal distribution of cells, GAG, and collagen Type II. A variety of fabrication routes have been employed to achieve this: 3D printing (Woodfield *et al.*, 2005), freeze drying (Arora *et al.*, 2015), porogen leaching (Steele *et al.*, 2014), and electrospinning (McCullen *et al.*, 2012). For example, Woodfield *et al.* 3D printed scaffolds with an orthogonal array of struts but with decreasing spacing, from 2-0.5 mm, towards the top of the scaffold (Woodfield *et al.*, 2005). This increased ECM density in the smaller pores at the top of the scaffold mimicking the native ECM organisation, however as discussed, smaller channel widths are required to encourage the formation of a superficial zone with the cell and ECM densities native to hyaline cartilage.

Electrospinning

A combination of scaffold fabrication methods have been used to provide the requisite properties to each zone. Electrospinning is a cheap and easy fabrication method to produce sub-micron fibres (Chen *et al.*, 2008), and can provide a low friction surface and increase the density of cells by entrapment. The small contact points prevent cells from lying flat on a surface and instead the cells are suspended and attached to a number of fibres in the surrounding network. This mimics the natural morphology of collagenous extracellular matrix and discourages dedifferentiation (Stevens and George, 2005, Nuernberger *et al.*, 2011, Li *et al.*, 2006).

Electrospinning has been used to generate zonal scaffolds with depth-dependent fibre widths and pore sizes (McCullen *et al.*, 2012). Chondrocytes were seen to align on aligned fibres and spread on random fibre orientations. Collagen and GAG distribution was higher in the deep zone (5 μm fibres with 170 μm pore size) compared to the middle zone (1 μm fibres and 12 μm pore size). As 12 μm is similar to the size of a chondrocyte, ~20 μm, the cell migration and nutrient transport across the middle zone was poor, preventing hyaline tissue regeneration.

Steele *et al.* (Steele *et al.*, 2014) utilised a combination of scaffold fabrication methods; porogen leached scaffolds for the deep and middle zones, and aligned electrospun fibres for the

superficial zone. The aligned electrospun layer was designed to increase cell density, reduce friction, and improve tensile strength across the surface. Although the fibres successfully entrapped cells on the surface, infiltration into the fibre layer was limited. This is typical of electrospun fibres. The small spacing between fibres prevent cell infiltration, so cells and ECM tend to remain on the surface (Chen *et al.*, 2008, Ren *et al.*, 2010, Song *et al.*, 2008b, Gao *et al.*, 2013a, Zhang *et al.*, 2008). To avoid this, 3D cotton wool-like fibres were produced by Poologasundarampillai *et al.* and were shown to allow cell attachment and migration within the fibre network (Poologasundarampillai *et al.*, 2014a). For cartilage in particular, 3D electrospun fibres are of interest to provide a conformable cartilage surface.

Mechanical properties

Controlling the mechanical properties of the scaffolds produced using the traditional routes is difficult as strength is dependent on porosity, however Arora *et al.* were able to tailor mechanical properties through the alignment of freeze dried channels (Arora *et al.*, 2015). Channels aligned vertically in the deep and middle zones had ~3x the compressive strength of channels aligned horizontally in the superficial zone, however values were low, 2-7 kPa due to the very thin chitosan-gelatin walls.

3D printing can offer significant improvements to the mechanical properties through control of the strut width, channel width, and strut orientation (Giannitelli *et al.*, 2014). Combining these properties and 100 % accessible volume to cells, 3D printing is an excellent choice for tissue scaffolds, however the materials options available for 3D printing are limited. Currently in the literature, the materials being 3D printed for cartilage tissue scaffolds are synthetic polymers with high stiffness, slow degradation rates and low bioactivity (Woodfield *et al.*, 2005, Malda *et al.*, 2005, Emans *et al.*, 2013, Sobral *et al.*, 2011). The material must have an inherent stiffness between 0.5-1 MPa to retain the differentiated hyaline cartilage cells, as a higher or lower Young's modulus will invoke dedifferentiation to fibrocartilage (Allen *et al.*, 2012). Therefore, a new 3D printing ink based on gelatin will be developed here to make use of 3D printing technology in this field.

2.3.6 Hypothesised cartilage scaffold design

In this work, 3D printing and electrospinning were selected to generate a zonal cartilage tissue scaffold as seen in Figure 3 to regenerate mechanically stable and zonal hyaline cartilage *in vitro*. The electrospun layer aims to provide a conformable surface and increased cell density to mimic the superficial zone. Fibres must be small compared to cells, e.g. ~1 µm, and pore size must be greater than 50 µm to allow full infiltration of cells and ECM across the layer.

The 3D printed region aims to provide the mechanical properties and stability through integration with subchondral bone. A 90° mesh structure was selected to impart compressive strength by alignment of the struts and 200-300 µm channel width was selected to allow efficient cell seeding and diffusion, yet provide a 3D environment preferential to differentiating cells.

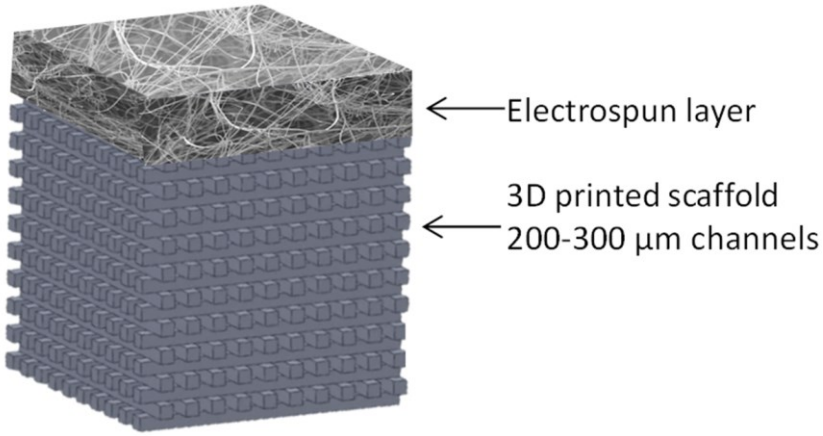

Figure 3. Cartilage tissue scaffolds made by 3D printing and electrospinning.

To combine all the materials properties with the scaffold design, a new gelatin ink is required for 3D printing mechanically strong and stable scaffolds. To reduce the dissolution rate of gelatin, crosslinking agents suffice, but to increase the mechanical strength up to the levels required, a secondary component is required.

2.4 Strengthening and controlling degradation using sol-gel hybrids

Hybrids can potentially improve mechanical properties by the incorporation of a silica network into the polymer using the sol-gel process. Unlike composites and nano-composites (Maquet *et al.*, 2004, Marelli *et al.*, 2011, Mozafari *et al.*, 2010), the components of a hybrid cannot be distinguished above the nanoscale and appear as a single material for cell attachment. This molecular level interaction allows control over the congruent degradation rate and mechanical properties by altering the composition (Mahony *et al.*, 2010, Novak, 1993).

There are two classes of hybrids that are made by incorporating a ready formed polymer, termed Class I and Class II. They are differentiated by the interactions between the inorganic and organic molecules as shown schematically in Figure 4. Class I hybrids use polymers to mechanically entangle with the inorganic, usually silica, network. Any strength comes from molecular entanglements, weak hydrogen bonds and Van de Waals forces (Allo *et al.*, 2010, Poologasundarampillai *et al.*, 2011). To improve strength and reduce dissolution rates, Class II hybrids were developed with covalent bonds linking the interpenetrating networks of inorganic and organic phases (Novak, 1993, Mahony *et al.*, 2010). This requires an additional stage of chemistry to functionalise the polymer by reacting it with a coupling agent.

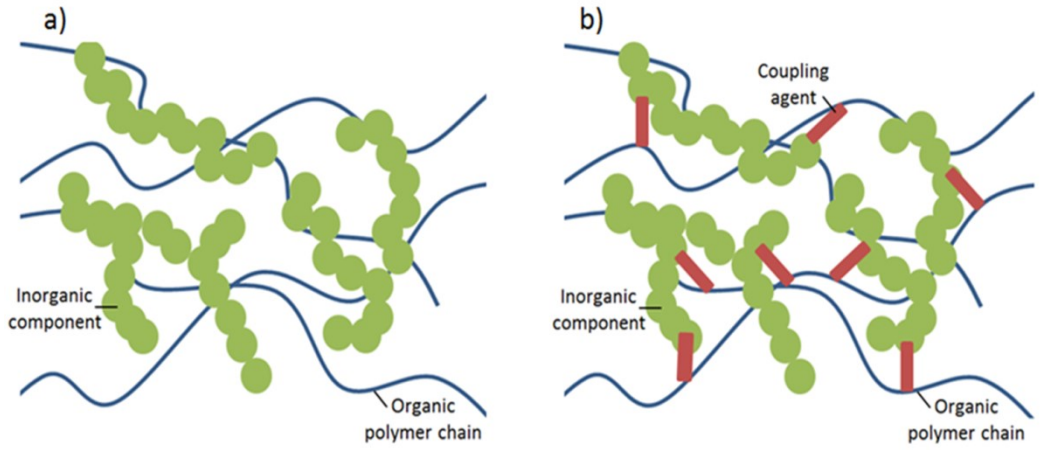

Figure 4. Schematics of a) Class I hybrids and b) Class II hybrids with organic and inorganic coupling.

Class II silica-gelatin hybrids developed by Mahony *et al.* showed very promising mechanical and dissolution results using GPTMS as the coupling agent (Mahony *et al.*, 2010), and

properties were adjustable depending on the ratio of organic to inorganic components and degree of coupling. The adjustable composition is also interesting for cartilage regeneration as the hybrid must be adapted for fabrication via 3D printing and electrospinning.

To fully understand the formation of hybrid materials and why GPTMS was kept as the coupling agent of choice, the sol-gel process and role of the coupling agents must be explained.

The hybrid sol-gel process

The hybrid sol-gel process is a room temperature chemical reaction that assembles silica nanoparticles to form an inorganic crosslinked structure, a sol-gel, which can incorporate polymers as the network forms. The polymer must therefore be soluble in the sol-gel process to form a hybrid, a requirement that gelatin fulfils.

The silicate precursor is tetraethylorthosilicate (TEOS) which can be hydrolysed to form $Si(OH)_4$. The hydrolysed TEOS molecules condense, as seen in Figure 5, and as the Si-O-Si bonds form and create a wet gel network, the polymer is introduced. As the sol-gel network develops, nanoparticles form and coalesce, trapping the polymer within the extending glass network (Mahony, 2010).

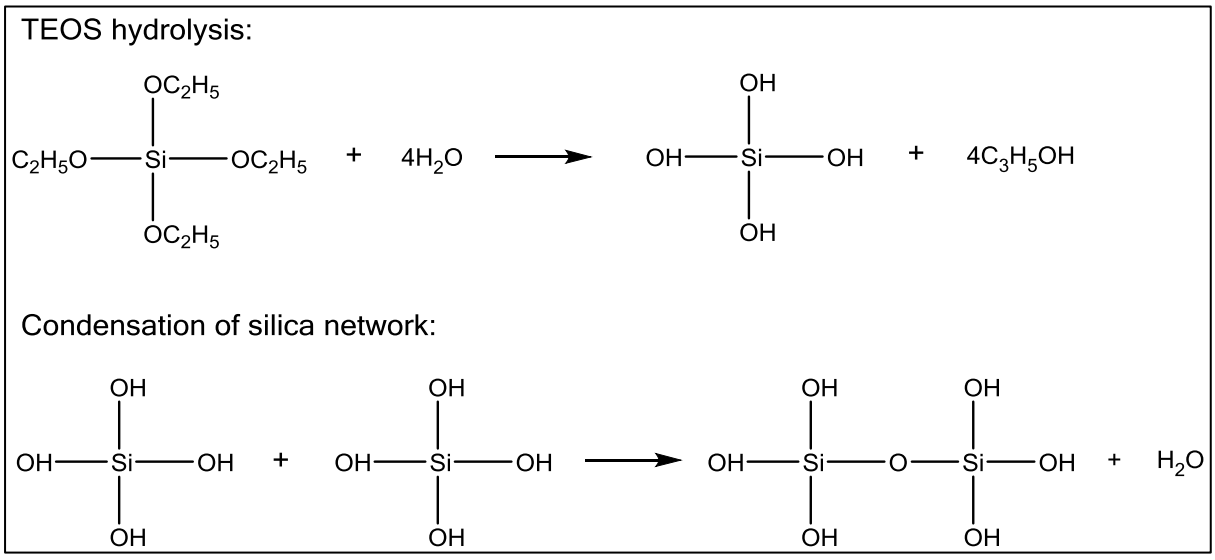

Figure 5. Formation of a silica sol-gel network

The rate of condensation of the sol-gel network can be controlled by the pH and additives such as HF which forms a complex and increases the coordination number of the silicon (Brinker, 1988, Mahony *et al.*, 2010). By controlling the rate of sol-gel condensation and hence gelation of the hybrid, 3D printing of sol-gel solutions is possible (Yun *et al.*, 2007, Gao *et al.*, 2013b).

Coupling agents

Coupling agents are covalent bridging molecules that bond between organic and inorganic components in Class II hybrids (Mahony *et al.*, 2010). They are typically short chain molecules containing alkoxysilane groups on one end to join the silica network, and a functional group on the other which is susceptible to nucleophilic attack from groups such as -OH, -COOH and $-NH_2$, all of which are present on gelatin molecules. The functionalised polymer can then covalently bond with the sol-gel network to form a hybrid.

GPTMS

The silica-gelatin Class II hybrids developed by Mahony *et al.* used GPTMS as the coupling agent. It has an oxirane ring and three methoxysilane groups at either end of the molecule. As shown in Figure 6, under acidic conditions, the C-O group in the epoxy ring becomes protonated and the negative -COOH groups on the polymer bond with the epoxy ring via nuceophillic attack. At the other end of the molecule, the methoxysilane groups hydrolyse and the GPTMS molecule can condense into the sol-gel network (Gabrielli *et al.*, 2013, Valliant and Jones, 2011, Mahony *et al.*, 2010, Ren *et al.*, 2002).

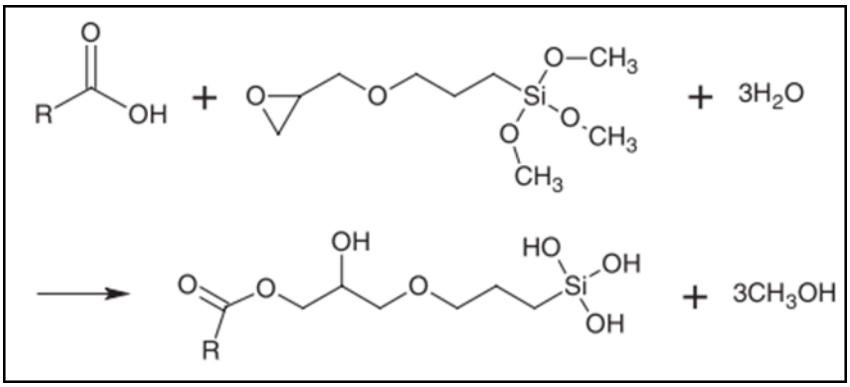

Figure 6. Functionalisation of a polymer with -COOH group using GPTMS.

The polymerisation of the organic and inorganic networks is a competitive process (Innocenzi *et al.*, 1999) and studies have shown that pH must be tightly controlled in order to control the kinetics of GPTMS (Gabrielli *et al.*, 2013). In basic conditions, e.g. pH 11, the methoxy hydrolysis is very slow but condensation is rapid once hydrolysis has occurred, whereas the remaining epoxide ring is unreactive. At low pH, e.g. pH 2, the silanol groups form rapidly and condensation begins within 30 minutes, resulting in oligomer formation. Hydrolysis of the oxirane is not prevalent until 3 h later, allowing time for functionalisation with gelatin to occur, however the degree of functionalisation is limited by the GPTMS position in an oligomer and hence less crosslinks can form. At neutral pH, the results are similar to the acidic case, however all reactions take place at a slower rate. The condensation reaction remains

dominant while the epoxide hydrolysis is almost negligible. It has been concluded that pH 5 is needed to functionalise polymers via nucleophilic attack to avoid oligomer formation before the hydrolysed TEOS is introduced. This pH is convenient when using GPTMS to functionalise a polymer, particularly those derived from natural sources, as a pH close to 7 is required to maintain the integrity of the polymer. It is important to note that the oxirane group of GPTMS is known to be cytotoxic and hence must be fully reacted with the polymer or hydrolysed for biological applications.

Alternative coupling agents

An alternative to GPTMS is ICPTS, (3-isocyanatopropyl)triethoxysilane, which when hydrolysed has three silanol groups and a isocyanate group, -NCO, to interact with hydroxyl groups of a polymer in the presence of a catalyst, DABCO, 1,4-diazabicyclo[2,2,2,]octane (Rhee *et al.*, 2002). The main disadvantage of ICPTS is that anhydrous solvents must be used, as ICPTS is preferentially reactive towards H_2O. Gelatin is not soluble in anhydrous solvents, hence this functionalisation method is unsuitable. Additionally, unreacted isocyanate groups are extremely dangerous and have the tendency to link with DNA molecules so careful purification is required, particularly for biomedical applications.

EDC, APTES and NHS have also been used in combination to functionalise polymers for hybrids (Hosoya *et al.*, 2004, Rowley *et al.*, 1999). As previously described for gelatin crosslinking, EDC, 1-ethyl-3-(-3-dimethylaminopropyl)carbodiimide hydrochloride, is water soluble and reacts with carboxyl groups on the polymer to form an active intermediate. The intermediate is displaced by nucleophilic attack from primary amino groups, $-NH_2$, and EDC and is released as a by-product. APTES, 3-aminopropyltriethoxysilane is added to provide these amino groups and form stable bonds with the 'activated' carboxylic groups on the polymer. APTES also provides the silanol groups at the other end of the molecule to condense into the sol-gel network. This crosslinking method is most efficient at pH 4.5 and must be performed in buffers. To further improve efficiency, N-hydroxysuccinimide, NHS can be used as it stabilises the intermediate against hydrolysing and allows for more efficient coupling at higher pH. This coupling agent has proved successful using PLLA (Maeda *et al.*, 2006), however when using gelatin, the hybrid formation becomes difficult to control as nucleophilic attack from primary amino groups is provided by both APTMS and from the gelatin itself. The degree of coupling, and therefore the control over mechanical and dissolution properties is therefore not entirely controllable.

2.5 Silica-gelatin hybrid scaffolds

The silica-gelatin hybrid developed by Mahony *et al.* showed excellent biocompatibility and bioactivity. The mechanical properties and dissolution rate of the hybrids were controlled by the amount of coupling and ratio of gelatin to sol-gel (Mahony *et al.*, 2010), and here composition adjustments can be further utilised to design inks for 3D printing and electrospinning.

HF Foaming method

The scaffolds developed by Mahony *et al.* were produced using a sol-gel foaming process followed by freeze-drying as seen in Figure 7. Firstly, the gelatin and GPTMS were mixed at 40°C, at pH 4.4 to allow functionalisation to occur through nucleophilic attack of the GPTMS oxirane by gelatin -COOH groups. The molar ratio of GPTMS to gelatin is described as the C-factor. A second solution was prepared to hydrolyse TEOS with a water/HCl volume ratio of 3 and R-ratio of 4. The R-ratio is the H_2O/TEOS molar ratio and 4 was selected to provide one water molecule to hydrolyse each ethoxy group (Brinker, 1988). To form the hybrid, these two solutions, functionalised gelatin and hydrolysed TEOS were combined and stirred on a hotplate at 40°C. Prior to foaming the scaffolds, surfactant and HF was added. HF initiated rapid condensation of the silica network and the surfactant stabilised the formation of bubbles in the liquid. After a few minutes the hybrid reached a critical stage in the condensation after which further foaming would cause collapse of the foams. Prior to this critical stage, the foams were poured into a container and sealed. The foams were then aged at 40°C to allow further condensation to take place and then freeze dried.

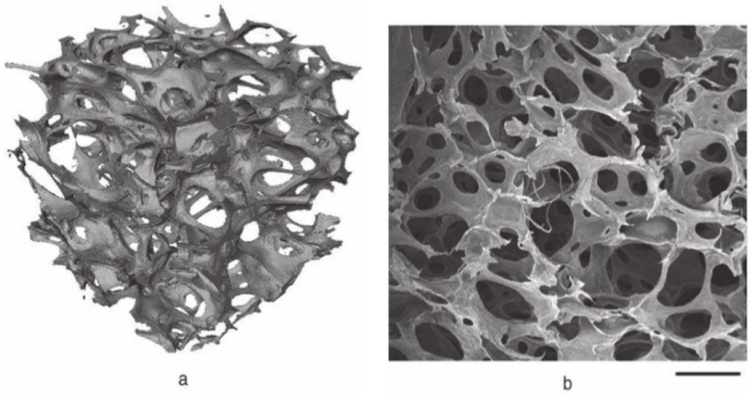

Figure 7. Hybrid silica-gelatin sol-gel hybrid (30 wt% gelatin with C-factor 1000) foamed scaffold for tissue regeneration; a) X-ray micro-computed tomography image, b) SEM image. Scale bar is 500 µm for both. Reprinted with permission (Mahony *et al.*, 2010).

Cell viability

As sol-gel hybrid synthesis occurs at low temperature, so as not to damage the organic components, cytotoxic by-products such as methanol, ethanol and unreacted oxirane were a concern as they must be removed by means other than burning out at high temperature. Freeze drying was expected to remove any remaining unreacted small molecules and solvents. To assess the cytotoxicity, human bone marrow derived mesenchymal stem cells (MSCs) were cultured on the foamed scaffolds. The LIVE/DEAD cytotoxicity assay showed that varying the wt% of gelatin and the C-factor had little effect on the viability of the cells after 7 days despite the presence of an oxirane peak in the FTIR data for C-factor 1500 foams. Cell attachment and morphology did vary with C-factor: 0, 500 and 1500. High C-factors induced the most cell attachment, better cell adhesion, and the most defined cellular organisation. Increased gelatin content, 60 wt% rather than 30 wt%, promoted cell proliferation over the 7 day culture period and demonstrated improved cell morphology. All the scaffold compositions were shown to be biocompatible and non-cytotoxic however, high C-factor and high gelatin content foams had the most promising cell results in terms of metabolic activity. However, the differentiation pathway of the MSCs was not investigated.

Mechanical properties and dissolution

The foaming process was able to incorporate up to 90 % porosity with the ultimate compressive stress ranging from 23 KPa to 60 KPa with increasing silica content. Increasing the C-factor also improved the compressive strength of the foams. For example, scaffolds with 60 wt% organic component showed a 360 % increase in stiffness by doubling the C-factor. However scaffolds with the same Young's modulus of cartilage, 0.5-1 MPa, had compressive strengths three orders of magnitude lower than cartilage. The dry mechanical properties of these hybrids were of interest for cartilage regeneration as they showed excellent properties under cyclic loading, but wet properties were not measured. The low strength was due to their high porosity, but it was not possible to reduce the porosity during the foaming process. An alternative scaffold process is needed, such as 3D printing.

A dissolution study revealed the total mass loss could be reduced from 15 % to less than 1 % by increasing the C-factor from CF250 to CF1500. It is hoped that by 3D printing, scaffolds with thicker struts and suitable C-factors will increase the compressive strength of the scaffolds and retain adequate properties during dissolution.

2.6 3D printing silica-gelatin hybrids

3D printing has recently come to the forefront of tissue scaffold fabrication as it allows unrivalled control of the scaffold architecture and can produce bespoke scaffolds. 3D printing provides the opportunity to generate 90° grid scaffolds with direct channels. This structure provides mechanical strength and efficient diffusion and cell infiltration channels due to the alignment of struts. The material of choice was silica-gelatin hybrids coupled by GPTMS due to the adjustable composition and excellent bioactivity (Mahony, 2010). To 3D print silica-gelatin hybrids, the condensation must be controllable and rapid gelation avoided.

The schematic in Figure 8 demonstrates how extrusion-based 3D printing (robocasting) operates schematically. The scaffold design is generated using computer software and from this a G code file is generated by the 3D printing deposition path software. The code dictates the motion of the 3D print head to achieve the structure designed. Signals are then sent to the motors controlling the x and y motion of the print head, and z motion of the deposition table. At the same time as the deposition path signals are sent to the x, y and z motors, signals are also sent to extrude the material. The extrusion/deposition rate is controlled by the force applied to the syringe plunger. The plunger is compressed at a particular rate to force the material out of the syringe and through the attached nozzle.

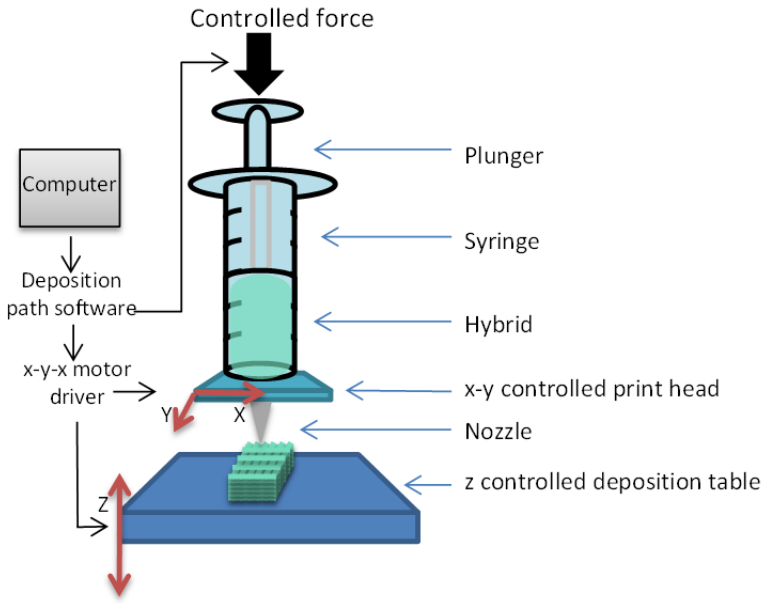

Figure 8. Schematic of a 3D printer (robocaster).

Materials parameters

To directly print silica-gelatin hybrids, the process is most similar to 3D printing hydrogels. It must be fluid enough to pass through the nozzle, yet retain the 3D structure deposited as layers are added. These printing properties can arise from viscoelasticity (Gao *et al.*, 2013b) or from gel strength (Mannoor *et al.*, 2013).

3D printing parameters

All the parameters involved in 3D printing affect each other. Nozzle size, deposition rate and print speed all affects strut width, and the achievable strut width affect the strut separation. The limitations in strut width affect the design of the scaffold, which in turn affects the mechanical properties. Larger struts and smaller channels maximise compressive strength, however this reduces porosity and diffusion/seeding efficiency, so a balance between strength and channel width must be found.

The strut width is limited by the material viscosity as higher viscosity materials cannot flow though the same nozzle diameter through which lower viscosity materials can flow. Viscosity also effects strut separation, the rigidity of the struts suspended on struts below dictates how far apart the struts can be to avoid sagging.

The print speed and deposition rate must allow for continuous flow of the printing material to avoid aggregation and breakage of struts.

2.6.1 3D printing silica-gelatin hybrids

In the literature, there has only been one attempt, by Gao *et al.,* to 3D print silica-gelatin hybrid materials. Gao *et al.* (Gao *et al.*, 2013b) used a different hybrid processing method to Mahony *et al.* (Mahony *et al.*, 2010). Rather than functionalising gelatin separately to hydrolysing the sol and combining the two once the separate reactions are complete, the gelatin was dissolved directly in the sol-gel precursor solution. The material was printed as a Class I hybrid after degassing and aged for 12 h at 37°C to achieve the required viscosity for printing. GPTMS was not used by Gao *et al.* as it caused rapid gelation which was incompatible with 3D printing.

3D printed 90° mesh scaffolds were fabricated by robocasting with a nozzle diameter of 510 μm. After forming, the scaffolds were dried in a vacuum then immersed for 12 h at 4°C in 95 % ethanol, EDC, NHS solution to crosslink the material. To hydrolyse any remaining EDC or NHS, the scaffolds were then immersed in sodium phosphate and following this, were washed. Gao *et al.* claimed to have 'crosslinked the gelatin and silicate BG chains', however it appears that in fact the gelatin was simply crosslinking around the bioactive glass as no APTES or any other organic-inorganic bridging molecule was added. This would explain the improvement in the dry compressive strength of scaffolds with crosslinking (5.5 MPa) and without crosslinking (3.75 MPa). However the huge degree of swelling, 440% of dry weight absorbed in 2 h, suggests the degree of crosslinking was low.

The resultant scaffold structure was re-immersed in aqueous medium to replicate *in vivo* conditions, and ~510 μm strut widths and ~1.2 mm channel width were measured. The compressive strength was found to be ~0.7 MPa which is two orders of magnitude lower than cartilage tissue. Overall this paper gave little information regarding the dissolution rates or degree of silica network connectivity of the hybrid. The large degree of swelling, drop in mechanical properties, and Class I nature, suggested the majority of the silica was lost from the scaffold when immersed in aqueous medium as it was not covalently bonded to the gelatin network and the open gel structure would have allowed for high release rates.

The main point to take from this paper by Gao *et al.* was that GPTMS, as well as HF, can induce rapid gelation of silica-gelatin hybrids. However, a Class II hybrid must be formed to retain the sol-gel network and mechanical properties of the scaffolds. A new hybrid method must be developed to avoid rapid condensation of the network before printing whilst retaining high network condensation, as this is ultimately going to improve the dissolution rate and compressive strength of the scaffolds *in vitro* and *in vivo*. Considering the incompatibility with

3D printing of the method used by Gao *et al.* when GPTMS was added, a HF-free version of the method used by Mahony *et al.* was expected to be a better starting point.

2.6.2 3D printing summary

A 3D printed scaffold structure to aim for has a strut separation of 200-300 μm, strut alignment of 90°, with the aim of providing compressive strength of ~30 MPa, and stiffness ~0.8 MPa.

In order to 3D print these scaffolds using silica-gelatin hybrids functionalised by GPTMS, the hybrid method and composition must be adapted from the method presented by Mahoney *et al.*, but avoiding rapid gelation of the hybrid induced by HF, and also GPTMS. Here, the condensation rate of the silica network and therefore viscosity increase over time is a very important parameter and designing a method and composition which allows for 3D printing whilst retaining a high degree of network condensation is essential.

2.7 Electrospinning silica-gelatin hybrids

Basic electrospinning apparatus is shown in Figure 9. The three main components are a high voltage power supply, a metal needle, and collector plate. To electrospin, solutions are contained within a syringe and a high voltage is applied to charge the solution within a metal needle. The polymer at the tip of the needle forms a Taylor cone. The cone shape forms due to the surface tension and electrostatic charging of the fluid due to the electric field (Cherney, 1999). The apex of the cone is where a single fluid jet is ejected when the electric field reaches a critical value to overcome the surface tension. The jet initially moves directly towards the collector but quickly becomes unstable due to surface charges on the jet interacting with each other and with the external electric field, causing elongation, thinning, and rapid whipping of the jet (Li and Xia, 2004, Tripatanasuwan *et al.*, 2007). The fibres deposited on the collector are randomly aligned due to the instability and rapid bending/whipping of the jet as it travels (Bhardwaj and Kundu, 2010, Hohman *et al.*, 2001). Aligned fibres can be produced by using a rotating collect drum. Once deposited on the collector, all solvent should have evaporated from the fibres in order to avoid fusion of fibres due to the plasticising effect of solvent when retained in the fibre.

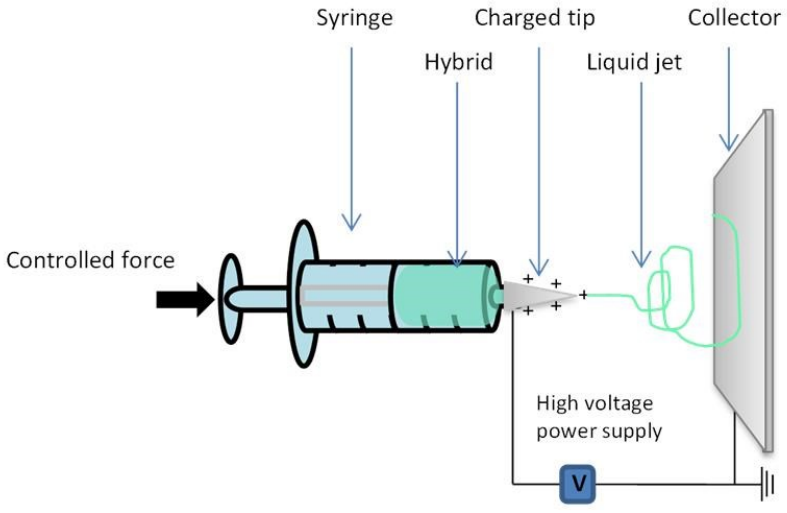

Figure 9. Schematic of electrospinning apparatus.

To electrospin, the material parameters and processing parameters must be adjusted according to the solution. The material parameters concern the viscosity, surface tension and conductivity of the solution whereas the process parameters concern the voltage, needle-collector separation, flow rate and ambient conditions, all of these parameters strongly effect the formation of the resultant fibres (Sun *et al.*, 2014).

Material parameters

When electrospinning a particular material, the material parameters focus on two things; viscosity and solvent choice, and even then, the solvent choice has an effect on viscosity.

The viscosity of the solution strongly effects the fibre formation. Low viscosity results in no continuous fibre formation and instead droplets reach the collector. At high viscosity it becomes difficult to eject jets of polymer at all. The optimum viscosity must therefore be determined. The viscosity is affected by the concentration of the polymer in solvent and molecular weight of the polymer (Bhardwaj and Kundu, 2010). In this case, the viscosity will also be affected by the degree of condensation within the network.

The surface tension is another important factor which can be controlled by the solvent choice. Low surface tension reduces the electric field required to produce fibres whereas high surface tension is unfavourable due to the instability of jets which results in spraying (Hohman *et al.*, 2001).

Competition between electric field, surface tension and viscoelastic force dictate whether smooth fibres or beads form. The surface tension drives to reduce surface energy by forming narrow fibre jets, however below a certain viscosity, the low degree of polymer entanglement is unable to stabilise the jet and beads or beaded fibres form. As the viscosity increases, the viscoelastic forces resist rapid changes in shape and smooth and uniform fibres form (Zhang *et al.*, 2005).

Surface charge density and conductivity is the final consideration. High conductivity of the polymer solutions results in smaller fibres whereas low conductivity solutions results in insufficient elongation of a jet to form a fibre which results in beading. Natural polymers such as gelatin have naturally occurring charged side groups which increase the charge carrying capacity and therefore require higher electric fields to form fibres (Zhang *et al.*, 2005).

Processing parameters

The applied voltage must overcome the forces of surface tension, however above this critical point, the effects of higher voltages are variable. In some cases, higher voltages cause higher polymer ejection producing larger fibre diameters. Others have reported narrowing of the fibres due to the increase in electrostatic charges and greater stretching of the solution (Bhardwaj and Kundu, 2010). The effects of applied voltage depend strongly on the solution being electrospun.

The needle-collector separation and solution flow rate are both dependent on the evaporation rate of the solvent. A minimum separation distance is required in order to allow fibres to dry

before reaching the collector (Ki *et al.*, 2005). The flow rate must be low enough to allow solvent to evaporate as otherwise fused fibres form.

The humidity is also known to have a strong effect on fibre formation. At higher humidity, the reduced evaporation rate of the solvent allows the charged jet to continue to elongate towards the collector and therefore smaller fibres are observed. This tends to come at the price of beading as the surface area and charge per unit area become unstable. The high humidity fibre elongation mechanism has a cut-off point above which fibres become fused as the solvent has not evaporated before reaching the collector (De Vrieze *et al.*, 2009). At higher humidity, greater bending of electrospun fibres has also been observed as opposed to straight fibres at low humidity (Tripatanasuwan *et al.*, 2007). At low humidity, the evaporation rate of the solvent is faster and therefore fibre jets are dried at larger diameters.

The temperature has two effects on electrospinning, firstly, the rigidity of the polymer chains (viscosity), and secondly the evaporation rate of the solvent. At high temperatures, when the electric field is applied, the low viscosity encourages stretching and thinning of the jet whereas the high evaporation rate of solvent opposes this (De Vrieze *et al.*, 2009). The opposing mechanisms are highly dependent on the material being electrospun and the choice of solvent.

2.7.1 Cotton wool-like fibres

Cotton wool-like electrospun fibres have a 3D voluminous nature which can overcome the problem of low cell penetration into the fibre network as proved by Poologasundarampillai *et al.,* at Nagoya Institute of Technology (NITech), who observed 3D fibre separation and improved infiltration (Poologasundarampillai *et al.*, 2014a). The solution being electrospun was calcium containing sol-gel and the cotton wool-like nature was obtained via fibre stretching due to Ca^{2+} ions travelling faster towards the collector than other charge carriers. A similar mechanism for generating cotton wool-like fibres was observed by Sun *et al.*, by the Fe^{3+} addition in polystyrene fibres (Sun *et al.*, 2012a).

At NITech, two further papers present cotton wool-like fibres with alternative mechanisms to generate the cotton wool-like nature of the fibres using PLA-vaterite (silica and calcium particles) composites using chloroform as the solvent. A fan method (Obata *et al.*, 2013) and ethanol stirring method (Kasuga *et al.*, 2012) were designed. The fan method worked by blowing air against the fibres to immediately evaporate the solvent and prevent fibres from sticking to each other. The ethanol stirring method required electrospinning jets to be directed into ethanol by grounding the ethanol bath. Once the fibres entered the bath the charge was neutralised and the solvent completely dissolved into the ethanol and fibres became entangled by stirring the fibre-ethanol mixture. In both cases, the solvent was chloroform. In both cases, the key was to avoid fibres from coming into contact before the solvent had fully evaporated.

To form cotton wool-like fibres from the silica-gelatin hybrids, the fibre elongation effects of high humidity will be investigated here, and to ensure fibres do not fuse together, a collector which allows fibres to dry without coming into contact with each other must be used.

2.7.2 Electrospinning highly crosslinked gelatin

Electrospun fibres of gelatin functionalised with GPTMS was reported by Tonda-Turo *et al.* (Tonda-Turo *et al.*, 2013), Song *et al.* (Song *et al.*, 2008b), Ren *et al.* (Ren *et al.*, 2010) and Gao *et al.* (Gao *et al.*, 2013a). The gelatin fibres were electrospun with GPTMS to reduce degeneration rate of the fibre, however the paper by Gao *et al.* also included a sol-gel bioactive glass component to create a hybrid material. A summary of the material and processing parameters reported in each paper is presented in Table 3.

Functionalised gelatin fibres

Gao *et al.*, Tonda-Turo *et al.* and Song *et al.* all electrospun solutions with C-factors comparable to those used by Mahony *et al.* in the foamed silica-gelatin hybrids (Mahony *et al.*, 2010). Ren *et al.* used a C-factor of 4 which is an almost negligible C-factor value and therefore shall not be discussed further due to the expected, though unreported, rapid dissolution and fibre instability.

First, considering the functionalised gelatin compositions, Tonda-Turo *et al.* electrospun functionalised gelatin with an equivalent C-Factor of 365. Electrospinning began 1 h after mixing GPTMS with the gelatin solution, 0.08-0.2 g mL^{-1} in water, and a high voltage of 30 kV was applied. Fibres with 200-500 nm diameters were achieved, however dissolution and fusion of the fibres after 168 h in PBS resulted in dense sheets with almost no fibre definition remaining. Song *et al.* (Song *et al.*, 2008b) also used GPTMS to crosslink gelatin with a co-solvent of acetic acid, ethyl acetate and water at a weight ratio of 4.2:2.8:2. Mass ratios of 2:1, 1:1 and 1:2 of siloxane to gelatin (equivalent to C-factors 740, 370 and 185 respectively) were examined. Solutions were aged at 37°C for 12-24 h and spun at 12 kV. Increasing the gelatin concentration from 0.05-0.1 g mL^{-1} led to increased fibre diameters, from 100 nm to 650 nm. Unfused fibres were achieved using a C-factor of 185 and 370, however 740 resulted in fused non-distinct fibres. After 7 days in PBS, the CF370 fibres showed considerable fusions and dissolution, whereas the CF740 fibres appeared unchanged, however this is unclear due to the initial fused structure. The before and after dissolution figure from the paper is shown in Figure 10. This suggested that increasing C-factor reduced dissolution rates, however a method to produce distinct fibres requires development.

In both of papers utilising high C-factors, the viscosity of the solutions during electrospinning were not reported, however a value was given by Ren *et al.*, 65,000 cP, comparable to castor oil. Tonda-Turo *et al.* stated that GPTMS addition did not increase the viscosity of the solutions and condensation was expected during solvent evaporation. Looking at the

electrospinning conditions, the evaporation rate would have been relatively slow as water was used as the solvent and the temperature was 50°C, not high enough to induce rapid evaporation. This would have allowed for considerable condensation of the GPTMS network, however dissolution properties were poor. Sol-gel-gelatin hybrids coupled with GPTMS have the advantage of higher silanol groups availability, hence more condensation reactions can occur and therefore more bridging and crosslinking of the hybrid network.

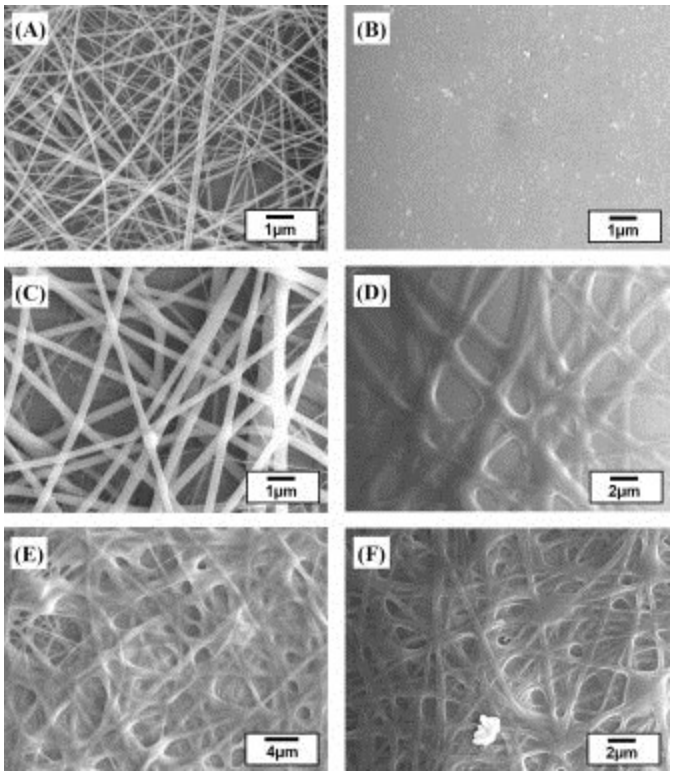

Figure 10. SEM morphologies of the nanofibres before (A,C,E) and after (B,E,F) 7 days of immersion in PBS at 37°C. The compositions of the nanofibres are (A,B) pure gelatin, (C,D) CF370 and (E,F) CF740. Reprinted with permission from (Song *et al.*, 2008b).

Silica-gelatin hybrid fibres

The only silica-gelatin hybrid electrospinning paper in the literature was reported by Gao *et al.,* and is developed for bone tissue regeneration purposes, using bioactive glass sol-gel ($70SiO_2$-$25CaO$-$5P_2O_5$) as the inorganic component. The compositions and synthesis method differs from the 3D printing paper reported by Gao *et al.* (Gao *et al.*, 2013b), and the foaming method developed by Mahony *et al.* (Mahony *et al.*, 2010). The electrospun scaffolds (Gao *et al.*, 2013a) were synthesised by dissolving the gelatin in a co-solvent of acetic acid and water, followed by the addition of the bioglass sol-gel precursor solution. GPTMS was added after 2 h, at pH 3.1 to give a C-factor of 370 and stirred for 4 h before electrospinning. The fibres obtained had diameters of ~192 nm and immersion in PBS resulted in fusion and webbing of

the fibres after only 12 h. The high degradation of the network may be due to the low pH, close to the pH_{iso} of silica, pH 2.5 which would induce a low silica network condensation rate (Brinker, 1988), or the calcium and phosphate additives which increase the degradation rate of silica network (Jones, 2013). The gelatin may also have been degraded in the low pH conditions which would increase the dissolution rate (Mahony *et al.*, 2014).

None of the papers presented a full dissolution study to examine the release of silica or gelatin, or characterised the viscosity of the electrospun solution, other than Ren *et al.* (Ren *et al.*, 2010). The main theme in the results was rapid dissolution using C-factors of 370 or below and fibre diameters around 200 nm.

Table 3. Summary of current literature of electrospun silica-gelatin hybrids or functionalised gelatin.

Author, composition	Material parameters and composition	Processing parameters	Properties
Gao *et al.* (Gao *et al.*, 2013a) BG-gelatin hybrid CF185	0.35 g mL^{-1} in co-solvent of acetic acid and water at a volume ratio of 6:4, pH 2.7 BG precursor sol ($70SiO_2$-$25CaO$-$5P_2O_5$) - stirred and aged for 48 h 30 wt% BG to gelatin stirred for 2 h GPTMS added (pH 3.1) and mixed for 4 h before electrospinning	12 kV 1.2 mm needle 25 µL min^{-1} flow rate 14 cm nozzle-collector distance Post electrospinning heat treatment for 6 h at 110°C	Fibre diameters if ~192 nm Fibre swelling and fusion observed after 12 h in PBS. HCA formation in SBF, however porosity lost after 5 days.
Tonda Turo *et al.* (Tonda-Turo *et al.*, 2013) Functionalised gelatin CF365	0.08-0.2 g mL^{-1} in water 1 h functionalisation before electrospinning	30 kV, 50°C 10 µL min^{-1} to 18 µL min^{-1} flow rate 7-19 cm nozzle-collector distance	Fibre diameters of 200-500 nm. Dissolution after 6 h resulted in non-distinct, fused fibres. After 168 h, individual fibres were non distinguishable.
Song *et al.* (Song *et al.*, 2008b) Functionalised gelatin CF740, CF370 and CF185	0.05-0.1 g mL^{-1} in co-solvent of acetic acid, ethyl acetate and water at a weight ratio of 4.2:2.8:2. CF740, CF370 and CF185 $CaCl_2$ (2.5 wt%) Solutions were aged at 37°C for 12-24 h before electrospinning	12 kV 500 micron needle 1.6 µL h^{-1} flow rate 8 cm nozzle-collector distance	No distinct fibres were produced using CF740. Fibre diameters of 150-550 nm, CF370 at 0.05 and 0.1 g mL^{-1} respectively. Loss of structure and fibre width after one week dissolution in PBS.
Ren *et al.* (Ren *et al.*, 2010) Functionalised gelatin CF4	15-25 wt% gelatin in 98 % formic acid 65,000 cP	30 kV 2 µL min^{-1} flow rate 30 cm nozzle-collector distance	Fibre diameters of ~2 µm BMSCs formed a thick layer on the surface of the fibre mats, no penetration.

Solvent options

The solvent has two functions, firstly to dissolve the polymer, and secondly to carry the dissolved material towards the collector when an electric field is applied. Table 3 presents the material variables as described in the literature, and each paper reported a different solvent choice. The solvent is a particular concern for gelatin as it has a polyelectrolytic nature due to the charged side groups on the gelatin molecule, which become ionised in acidic or basic conditions. In aqueous solutions, the water molecules interact with the charged groups and hinder fibre forming capacity due to the formation of a 3D network which greatly reduces the mobility of polymer chains. When a high DC voltage is applied, the applied electric field affects the gelatin charge generation and mobility of ions and therefore much higher voltages are required (Tonda-Turo *et al.*, 2013). Using alternative solvents to limit the ionisation is key to successfully electrospinning gelatin, however due to the strong polarity of gelatin, a highly polar solvent is required to dissolve it.

Silica-gelatin hybrids produced by Mahony *et al.* were produced using a water based method (Mahony, 2010). Even without considering the effect on the gelatin molecules, water has low volatility and high surface tension. Many papers have sought to increase volatility and reduce surface tension as this reduces beading and the applied voltage required (Fong *et al.*, 1999, Ki *et al.*, 2005).

To increase the volatility of solvents for electrospinning gelatin-based solutions, formic acid, acetic acid, ethyl acetate and ethanol are the most common additions. Formic acid and acetic acid have been used as alternative solvents for gelatin as they dissolve gelatin at room temperature without gelation, however both studies indicate gelatin degradation due to high acidity (Ki *et al.*, 2005, Song *et al.*, 2008b). Even when diluted, a composition of 60 vol% acetic acid, 40 vol% water and 0.35 g mL^{-1} gelatin has a pH of 2.7, very close to the pH_{iso} of silica (Gao *et al.*, 2013a). It is important to maintain a pH of ~pH 5 to optimise GPTMS reaction kinetics (Gabrielli *et al.*, 2013), allow condensation of the sol-gel network (Brinker, 1988), and avoid gelatin degradation.

Ethyl acetate has been shown to improve the electrospinnability of nanometre gelatin fibres without reducing the pH. It has a surface tension of ~23 mN m^{-1} compared to 74.2 mN m^{-1} for water, which therefore reduces beading, however as a solvent it is not often favoured as it is prone to hydrolysis. Gelatin in water/acetic acid/ethyl acetate solutions were electrospun with increasing ratio of acetic acid and ethyl acetate to water, however successful compositions had pH values less than 0.2 which again must have had considerable negative effects on the reaction chemistry of GPTMS with gelatin (Song *et al.*, 2008b), hence the plasticised and rapidly dissolving fibres.

Adding ethanol to water has various positive effects for electrospinning: higher volatility, lower gelatin solubility, reduced gelation temperature and reduced surface tension (Chen *et al.*, 2009, Fong *et al.*, 1999). Fong *et al.* found that by increasing the ethanol content in relation to water, up to 70 vol% ethanol, smooth, sub-micron fibres formed as opposed to beaded chains due to the decrease in surface tension and increase in viscosity.

1,1,1,3,3,3-hexafluoro-2-propanol and trifluoroacetic acid have also been considered in the literature as solvents for electrospinning organic polymers due to high solubility and high volatility (Song *et al.*, 2008b), however high toxicity prevents these solvents from being considered here.

Solvent choice

Here, the aim is to reduce the surface tension and volatility of the solvent when electrospinning highly crosslinked gelatin. It is fair to say that Tonda-Turo *et al.* were able to electrospin functionalised gelatin using water as the solvent, however elevated temperature and high applied voltages were required to compensate and the resultant fibres rapidly dissolved in PBS. The discussion into the solvent choices has led to a starting co-solvent of 60 vol% water, 40 vol% ethanol. This co-solvent combines the co-solvent ratio used by Song *et al.* to electrospin functionalised gelatin (Song *et al.*, 2008b) but replacing the acidic acetic acid and ethyl acetate portion of the co-solvent with ethanol which produced good results for Fong *et al.* and avoids strongly acidic solutions (Fong *et al.*, 1999).

Materials and processing parameters

The choice of solvent affects all material parameters related to electrospinning: viscosity, surface tension and conductivity. Of these parameters, the viscosity is the only remaining variable once the concentration of the solution and the choice of solvent are fixed. The paper by Fong *et al.* suggested 1250 cP to be appropriate for solutions with a water-ethanol co-solvent (Fong *et al.*, 1999), Ren *et al.* suggested 65,000 cP for gelatin functionalised by GPTMS at C-factor 4 (Ren *et al.*, 2010), and Poologasundarampillai *et al.* suggested ~500 cP to electrospin cotton wool-like fibres from sol-gel (Poologasundarampillai *et al.*, 2014a). As the viscosity strongly influences the processing variables (Fong *et al.*, 1999) they cannot be predetermined, though the reviewed literature can be used as a guide. The combination of silica-gelatin hybrid solution and water-ethanol co-solvent has not been previously investigated. The viscosity and parameters required for electrospinning silica-gelatin hybrids coupled by GPTMS in a water-ethanol co-solvent must be developed here. To add to complexity, the silica-gelatin solution will be increasing in viscosity as the sol-gel network condenses.

2.7.3 Electrospinning summary

The electrospun fibres are required to provide a conformable surface layer, and enhance cell density in the superficial zone. A key requirement of the electrospun fibres is that they allow cells to infiltrate and produce ECM throughout the electrospun scaffold. To achieve this, the fibres must have a cotton wool-like voluminous 3D nature, and be stable *in vivo* until the tissue is regenerated.

Highly crosslinked gelatin compositions are required to ensure fibres are stable during cartilage regeneration. The use of C-factors above 740 appeared to show improved dissolution characteristics, however this was not entirely clear due to the pre-fused structure. A method to produce distinct fibres with a high degree of crosslinking must be developed. The incorporation of sol-gel into a functionalised gelatin solution is expected to improve the degree of crosslinking between gelatin molecules by providing additional molecules to condense with GPTMS and form bridging linkages.

To generate a 3D structure from the silica-gelatin hybrids functionalised by GPTMS, a high humidity environment will be used to produce highly elongated fibres, and fibre collection must prevent fibres from coming into contact. The solvent option selected is 60 wt% water and 40 wt% ethanol to allow the gelatin to dissolve, but increase the volatility of the solvent during electrospinning.

2.8 Objectives

Having reviewed the literature, the objectives are to develop a new tissue scaffold for cartilage repair using silica-gelatin Class II sol-gel hybrids and a combination of 3D printing and electrospinning. 3D printing was selected to impart the mechanical properties through the design of the scaffold, without affecting the cell seeding and diffusion efficiency within the scaffold. Electrospinning was selected to provide a conformable layer and increase the cell density in the superficial layer.

Silica-gelatin hybrids functionalised by GPTMS were selected due to the high bioactivity and adjustable composition which allow dissolution rate and mechanical properties to be adjusted. A new method to produce the silica-gelatin hybrids must be developed to avoid rapid condensation and allow for 3D printing and electrospinning, whilst retaining a highly condensed sol-gel network. Specifically, HF addition must be omitted, and the method must be developed to avoid rapid condensation when GPTMS is added. In order to produce the tissue scaffold designed in Figure 11, the adjustable composition of the hybrid material must also be investigated to develop rheologically suitable inks for 3D printing and electrospinning.

The silica-gelatin hybrid will be printed in a gel-state, so a suitable drying method must be established and the mechanical properties must be investigated *in vivo* conditions. The dissolution properties and bioactivity of the 3D printed and electrospun silica-gelatin hybrids must also be assessed.

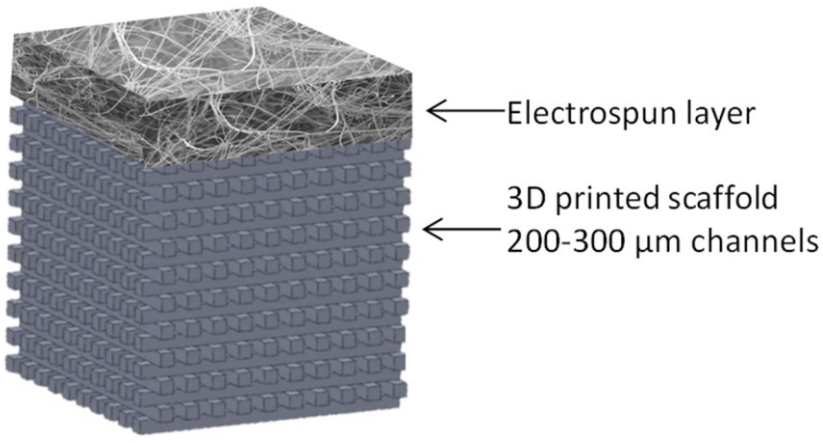

Figure 11. Schematic of proposed cartilage tissue scaffolds made by 3D printing and electrospinning. The printed component has 200-300 µm porosity channels, and 3D electrospun fibres have diameters of ~1 µm.

CHAPTER 3. CHARACTERISATION TECHNIQUES

3.1 Imaging techniques

Scanning Electron Microscopy

In scanning electron microscopy (SEM), electrons are emitted from a filament via thermionic emission and accelerated towards a sample by the application of a bias voltage between the electron source and target. The sample must be conductive or coated with a conductive layer. The scanning beam irradiates the sample and electrons interact with the surface to produce a variety of signals: primary backscattered electrons, secondary electrons, Auger electrons and X-rays. Primary backscattered electrons, Auger electrons, and X-rays are useful when trying to understand material composition, whereas secondary electrons produce images of the surface. Secondary electrons are ejected by ionisation arising from the impact of the primary electron beam. The secondary electrons are attracted to the detector by a positive bias and undergo elastic and inelastic collisions to reach the surface of the material. Information regarding the topography of the surface is obtained as secondary electrons released from surfaces closer or tilted towards the detector, travel less distance and loose less energy to reach the detector. The detector accelerates the secondary electrons into a scintillator which converts the electron signal to a light signal, and a photomultiplier converts the photons into a pulse of electrons. This pulse is amplified and used to modulate the intensity of the image on the computer display.

Field Emission Gun Scanning Electron Microscopy

High resolution surface images were acquired using a field emission gun scanning electron microscope (FEGSEM). The principles are similar to SEM however electrons are emitted via field emission from a much smaller area than thermionic emission by the application of a large electrical potential gradient. The resultant beam is more coherent, the energy spread is smaller, and the electron spot size is reduced resulting in higher resolution imaging. Images were taken using the InLens detector rather than the conventional secondary electron detector. The InLens detector is located inside the electron beam column. This allows for higher efficiency of electron beam collection particularly at small working distances.

X-ray Micro-Computed Tomography

X-ray micro-computed tomography, micro-CT, uses X-rays to image a sample and generate a 3D image. To achieve this, images (radiographs) must be taken as the sample rotates at incremental angles from 0° to 360°, then reconstructed to create the 3D image. To generate each radiograph, x-rays leave the source, pass through the sample and hit the detector. The

density and thickness of the sample effects the amount of x-rays absorbed and this is measured by the greyscale value of each pixel in the collected radiograph. The energy of the x-rays must be carefully selected for the material being observed in order to obtain good contrast. In the case of natural tissue or low-density materials, low beam energy, 12 keV, is required.

3.2 Composition and bonding analysis

Fourier transform infrared spectroscopy

Fourier transform infrared spectroscopy (FTIR) is a technique used to investigate the interaction of infrared light with a sample. Covalent bonds with a dipole moment can be excited by particular frequencies of light. In FTIR, a beam containing many frequencies of light is shone at the sample. The bonds absorb particular frequencies of light and the total absorbance is measured by the change in intensity of the beam before and after passing though the sample. Further data points are generated by shining different combinations of frequencies at the sample. Once all measurements have been taken, a Fourier transform is performed to convert the raw absorbance data into the amount of energy absorbed at each wavelength. The resultant spectrum is used to identify the bonding present within the material.

^{29}Si MAS NMR

The degree of condensation of a silica network is evaluated by ^{29}Si magnetic angle scattering nuclear magnetic resonance (^{29}Si MAS NMR). The technique detects the characteristic spin of atoms when a magnetic field is applied. The characteristic spin is affected by shielding of the external magnetic field by electrons in the bonds surrounding the nucleus. Therefore the same atom in different environments can be distinguished.

Si atoms bonded to four oxygen atoms are known as the Q species. Si atoms bonded to one bridging-oxygen and three -OH groups are known as Q^1, and can be distinguished from a Si atom bonded to two bridging-oxygens and two -OH groups, Q^2. The same can be said for Si atoms bonded to a carbon atom and three oxygen atoms, such as in GPTMS, however these species are known as the T species. As with the Q species, the order of the T species relates to the number of bridging-oxygen, Si-O-Si, bonds made by the central Si atom.

In the solid state, atoms cannot move or naturally rearrange as is possible in the liquid state. To prevent anisotropy issue, samples are ground to a powder, orientated at 54.74° to the static magnetic field, and spun faster than the magnitude of dipolar coupling (the interaction between magnetic moments of two nuclei). This allows for orientation averaging as a collective orientation is imposed on all molecules around the axis. Any anisotropic interactions are suppressed so peaks can be identified. NMR measures the chemical shift of the species, which describes the resonant frequency of the characteristic spin relative to a standard.

X-ray diffraction

X-ray diffraction (XRD) is used to analyse crystal phases in a material. X-ray diffractometers consist of three elements: an X-ray tube, a sample holder, and an X-ray detector. Within the X-ray tube, a filament is heated to produce electrons which are accelerated by application of a voltage to bombard a target material, typically copper. The electrons displace inner shell electrons and release characteristic X-rays which are filtered to produce a monochromatic X-ray source and concentrated towards the sample.

The X-ray source and detector are rotated around the sample though a range of 2θ angles. The interaction between incident X-rays and sample produces constructive interference and the diffracted X-rays are detected when conditions satisfy Bragg's law, presented as Equation 1, where n is an integer, λ is the wavelength, d is the interplanar spacing, and θ is the angle of rotation.

Equation 1: $$n\lambda = 2d\sin\theta$$

All possible angles of constructive interference can be obtained by using a powdered sample, as crystals are randomly orientated allowing many crystallographic planes to be detected. Bragg's law links the wavelength of the X-rays to the diffraction angles and therefore the unique d-spacings of the crystals are found. By comparing the peaks observed in the diffraction pattern with standard reference patterns, the crystal phase can be identified.

Amorphous materials do not have characteristic d-spacings and instead give rise to an amorphous halo, a diffuse pattern due to the broad distribution of atomic spacing.

The materials are analysed using a single crystal silicon holder, cut along an obscure lattice plane that would diffract at an angle outside the measurable 2 theta range. Therefore no amorphous response or peaks are generated from the holder.

Thermal analysis

Thermo-gravimetric analysis (TGA) and differential scanning calorimetry (DSC) are two thermal analysis techniques used in this study. The physical properties, mass and heat flow, were measured whilst subject to a controlled, elevating, temperature program. The change in mass is detected by an electronic balance which is kept away from the high temperatures by suspending the sample and alumina reference material in platinum crucibles on an alumina rod. DSC measures the heat flow between the sample and a reference to detect exothermic and endothermic reactions occurring in the sample as the temperature increases.

ICP OES

Inductively coupled plasma optical emission spectroscopy (ICP OES) detects the concentration of particular elements in a solution. In the ICP, argon gas is ionized in an intense electromagnetic field to form the plasma and a peristaltic pump delivers the liquid sample to a nebuliser which converts the liquid to a fine mist. Any larger droplets are removed by a spray chamber while smaller droplets pass through to the plasma. The solvent is evaporated and the remaining sample collides with electrons and charged particles in the plasma. The sample decomposes to atoms which repeatedly lose and recombine with electrons and emit light of a characteristic wavelength. In the optical chamber, the emitted light is separated into different characteristic wavelengths and measured to give an in intensity value. This value can be compared to previously analysed standards to give the concentration of each element tested in the sample.

BCA assay

The Thermo Scientific™ Pierce™ BCA protein assay uses bicinchoninic acid (BCA) for the colorimetric detection and quantitation of total protein. Cu^{+2} reduces to Cu^{+1} in the presence of protein in an alkaline medium (the biuret reaction). In this assay, the BCA in the reagent provides sensitive and selective colorimetric detection of the Cu^{+1} cation. A purple-coloured reaction product forms by the bonding of two BCA molecules with one Cu^{+1} cation. The absorbance of the complex is measured at 562 nm and is linear with increasing protein concentration. The protein concentration of the samples is determined with reference to standards prepared from the protein and assayed alongside the unknown samples to create a standard curve.

3.3 Mechanical properties and scaffold structure

Compression testing

Compression testing evaluates the compressive stress, compressive strain, and Young's modulus of a material by applying a constant rate of displacement to the material. Samples being tested must be accurately measured in order to calculate the stress and strain, according to equations below.

To determine the strain, Equation 2 is used, where l is the original thickness and Δl is the change in thickness.

$$\textbf{Equation 2:} \qquad \varepsilon = \frac{\Delta l}{l}$$

To determine the stress, σ, Equation 3 is used, where F is the force applied and A is the cross sectional area measured prior to testing.

$$\textbf{Equation 3:} \qquad \sigma = \frac{F}{A}$$

Young's modulus can be found using Equation 4, where ε is strain, or by measuring the linear gradient of the stress-strain curve.

$$\textbf{Equation 4:} \qquad E = \frac{\sigma}{\varepsilon}$$

Rheology

Rheology is the science of deformation and flow. A sample is typically held between two plates, the top of which can rotate.

A viscosity measurement measures the resistance of a fluid to flow. The top plate rotates on the sample at a constant shear rate, and the shear stress, τ, is measured to calculate the viscosity, η, according to Equation 5.

$$\textbf{Equation 5:} \qquad \eta = \frac{\text{shear stress },\tau}{\text{shear rate}}$$

A deformation measurement measures how a viscoelastic material behaves before flow occurs. Instead of applying a constant shear rate, the top plate oscillates back and forth imparting a sinusoidal strain. The stiffness of the material is measured by the complex modulus, G^*, according to Equation 6, where γ is the shear strain. The higher the modulus, the tougher the material.

Equation 6: $$G^* = \frac{\tau}{\gamma}$$

As demonstrated in Figure 12, the phase angle, δ, measures the lag between the sinusoidal oscillatory strain and stress response of the material, due to the extra time required for molecules to flow and relaxations to occur. A purely elastic material has δ = 0, whereas a purely viscous material has δ = 90°.

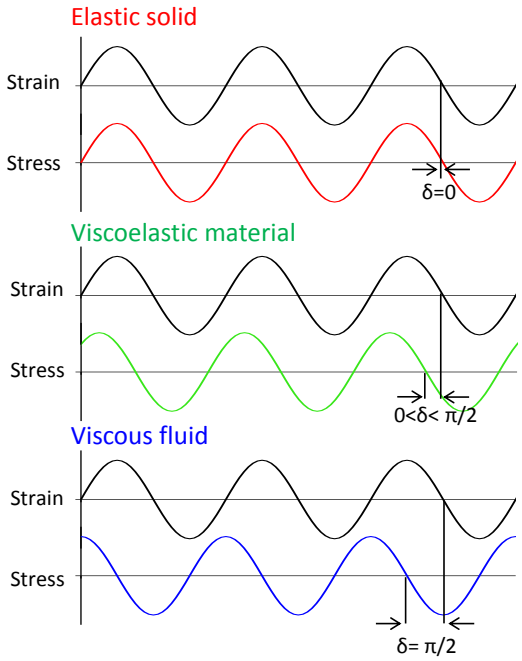

Figure 12. Schematic of strain response to applied oscillatory stress for an elastic solid, viscous fluid and viscoelastic material.

For viscoelastic materials, G^* and δ properties are combined to give the storage modulus (G', the elastic component) and loss modulus (G'', the viscous component). The elasticity of the material arises from crosslinking and molecular constrictions, whereas the viscosity arises from the ability of the material to flow. The material is said to be solid-like when G' > G'' and δ < 45°, and vice versa for a liquid-like material.

G', G'' and δ are defined according to Equation 7, Equation 8, Equation 9 respectively.

Equation 7: $$G' = \frac{\tau}{\gamma} \times \cos\delta$$

Equation 8: $$G'' = \frac{\tau}{\gamma} \times \sin\delta$$

Equation 9: $$\tan\delta = \frac{G''}{G'}$$

Helium Pycnometer

Helium pycnometry (Quantachrome, Pycnometer) uses gas displacement to measure the skeletal volume and hence skeletal density of porous materials. By infiltrating helium gas into a chamber of known volume containing scaffolds with known mass, the skeletal volume and density can be calculated. The skeletal volume is defined as the volume of the scaffold excluding all pores larger than one molecule of helium gas. The technique is based around the ideal gas law, as shown in Equation 10, where P is the pressure, V is the volume, n is the number of moles, R is the gas constant and T is the temperature. The temperature must be carefully controlled at 25 °C.

Equation 10: $$PV = nRT$$

CHAPTER 4. 3D PRINTING OF SILICA-GELATIN HYBRIDS

4.1 Introduction

Previous 3D printing attempts of silica-gelatin hybrids have avoided the addition of any crosslinking agent before the 3D printing process which resulted in a two stage process with a low degree of crosslinking (Gao *et al.*, 2013b). Here, the aim was to 3D print highly stable cartilage scaffolds from silica-gelatin Class II hybrids functionalised by GPTMS in a one stage process, directly from sol.

To achieve this, the silica-gelatin hybrid material and 3D printing process was investigated in terms of: reaction times of the hybrid method, suitable printing composition, and 3D printing parameters.

The scaffold structure

Tissue scaffolds require high interconnectivity for cell migration and nutrient transport (Malda *et al.*, 2005). 3D printing of 3D grid scaffolds with 90° layers allows for high interconnectivity but low porosity. Unlike traditional foaming or leaching methods, 3D printing allows mechanical strength and interconnectivity to be designed into the scaffold and removes the dependency on pore width and porosity. An example of such a structure is shown in Figure 13. This structure is simple yet promises to provide direct transportation channels, adjustable micro and macro structure, and ultimately improved cellular interaction and mechanical properties.

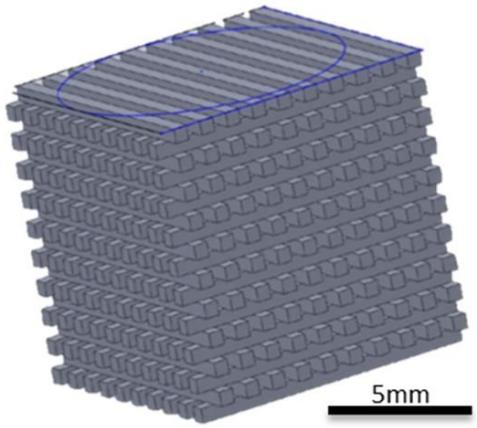

Figure 13. Schematic of the 90° mesh 3D printed scaffold design.

It was necessary to create 3D scaffolds with a channel width that allowed easy infiltration of cells, yet once seeded, cells must be hosted in an environment where native ECM can be produced to fill the porosity in order to achieve full thickness regeneration (Malda *et al.*, 2005,

Emans *et al.*, 2013, Lu *et al.*, 2010). The literature suggests 300-400 μm as a suitable spherical pore width for particulate leached scaffolds (Steele *et al.*, 2014, Lu *et al.*, 2010, Tanaka *et al.*, 2010). Smaller pores have also shown success, 80 μm (Mandal *et al.*, 2011), and considering the high interconnectivity of 3D printed scaffolds, the target channel width may be smaller than a target pore width. The work on 3D printing host scaffolds for cartilage is limited, many using synthetic polymers with low bioactivity, however 525 μm channel width was shown to achieve full osteochondral defect repair *in vivo* (Malda *et al.*, 2005, Emans *et al.*, 2013). Comparing 750 μm and 100 μm channel width showed that smaller channels were more capable of retaining cells in even distribution throughout the scaffold (Sobral *et al.*, 2011). As the exact value of the ideal channel width is unknown, the target channel width for cartilage regeneration was deemed to be 200-300 μm to allow for easy infiltration but allow cells to quickly fill the surrounding porosity with ECM.

The scaffold must also provide anchorage in the subchondral bone as well as providing a suitable host environment for cartilage regeneration. Silica-gelatin hybrids with high silica content have previously stimulated the formation of a hydroxycarbonate apatite layer in simulated body fluid, and hence show compatibility with bone tissue regeneration (Mahony *et al.*, 2010). A gradient of hybrid composition with high silica content in the integration region to form HCA is therefore an option.

Material processing variables

The foaming method for silica-gelatin hybrids was developed by Mahony *et al.* (Mahony *et al.*, 2010) using HF as a key addition to induce rapid gelation of the silica network. This aided scaffold formation by preventing foam collapse as well as inducing a highly condensed network. When developing a material for 3D printing, rapid gelation is undesirable as it reduces the window of opportunity to print the hybrid directly from sol.

To produce silica-gelatin hybrids that were suitable for 3D printing, the foaming method was adapted to compensate for the removal of the HF network condensation stage, but also to avoid rapid gelation due to GPTMS, which was seen as a barrier to 3D printing by Gao *et al.* (Gao *et al.*, 2013b). The material processing variables investigated were: the gelatin and GPTMS reaction time prior to sol addition (functionalisation time), and the aging time and temperature of the 3D printed hybrid scaffold. Once determined, this revised hybrid method was known as the HF-free hybrid method.

Identifying the printing composition

The composition for 3D printing cartilage scaffolds required high crosslinking to avoid degradation. The rate of gelation due to silica and GPTMS network condensation was an important factor to monitor to ensure compatibility with 3D printing despite the removal of HF from the method (Gao *et al.*, 2013b).

The amount of GPTMS added, C-factor, suited to the newly developed HF-free hybrid method, was identified through investigation of the relationship between GPTMS added and the resultant degree of crosslinking. The gelatin to silica ratio was determined by monitoring the gelation behaviour of various hybrid compositions with the same C-factor. As the silica-gelatin hybrids were 3D printed directly from sol, identifying the time frame within which the hybrid gels could be printed- the 'printing window'- was key to this study. The final composition selected was the composition which allowed for the most efficient 3D printing method in terms of time and chemicals used.

Printing variables

The printing variables were defined in order to generate scaffolds using the adapted HF-free hybrid method and the selected composition. To 3D print, there are numerous variables to consider: deposition rate, nozzle size, speed of print head, and temperature. The variables must all align along with the printing ink, the silica-gelatin hybrid, to create the desired structure. By systematic trial and error, suitable settings were determined for this system.

The printer

Two different robocasters were used over the course of this project. A Fab@home printer was initially used. However, the mechanism for extrusion was not robust enough, so an Ultimaker Original, as seen in Figure 14, was adapted for robocasting. A nozzle and tubing were connected to the print head and the hybrid was extruded from a syringe along the tubing to the printing nozzle using a syringe pump, Harvard Apparatus PHD Ultra, which controlled the material deposition. The adapted Ultimaker 3D printed all the 3D printed scaffold characterised and analysed in this thesis.

Figure 14. Image of the Ultimaker Original, before adaptation for sol-gel hybrid printing (www.ultimaker.com).

4.2 Methods

A series of monoliths, foams, and eventually 3D printed scaffolds were produced in this study to examine the chemistry of the hybrids and develop a new HF-free hybrid method for 3D printing. The most compatible composition was determined for use with the new method and a 3D printing process was established.

The silica-gelatin hybrids are named depending on their gelatin to silica (from TEOS) ratio and C-factor. The gelatin to silica ratio, e.g. 70G:30SiO_2, shortened further to 70G, is defined as the mass ratio of gelatin to SiO_2, under the assumption that 1 mole of TEOS forms 1 mole of SiO_2. Any silica contributions from GPTMS are ignored in this ratio. The C-factor, CF, is defined as the molecular ratio of GPTMS to gelatin when the molecular weight of gelatin is 87.5 kDa (Mahony, 2010).

4.2.1 Preliminary sol-gel hybrid method

All reagents were supplied by Sigma Aldrich UK unless otherwise specified. For all hybrids, the first stage was to dissolve gelatin (Porcine skin, gel strength 300, Type A) in 10 µM hydrochloric acid (HCl), to give a concentration of 50 mg mL^{-1}, in a covered beaker at 40°C for 1 h. This solution was functionalised by the addition of GPTMS, the amount of which was dependent on the C-factor. The time allowed for functionalisation was investigated. Depending on the study, the functionalisation was either: 3 h, 14 h or 22 h.

The functionalisation of gelatin and the hydrolysis of the sol are separate reactions which were timed to be complete at the same time. 1 h before the end of the functionalisation of gelation, the sol was prepared. In the following order: deionized water, 1 M HCl and tetraethyl orthosilicate (TEOS) were combined. The quantities of each depended on the molar ratio of water/TEOS (R-ratio) and the volume ratio of water/HCl. An R-ratio of 4 was chosen to hydrolyse TEOS so as to provide one water molecule for each silanol-forming ethoxy group. HCl was added to catalyse TEOS hydrolysis, and the volume ratio of water/HCl used was 3 based on the work by Mahony *et al.* (Mahony *et al.*, 2010). The solution was stirred for 1 h at 400 rpm to hydrolyse TEOS.

Both reactions were complete at the same time and the functionalised gelatin and hydrolysed TEOS were mixed and returned to the hotplate at 40°C at 400 rpm. The amount of each solution added was dependent on the gelatin to silica ratio of the hybrid composition being made. Aging was defined here as the condensation period of the sol-gel hybrid over time, therefore from the onset of mixing the hybrid, the solution had begun aging. Before the hybrid was formed into a monolith, foam or 3D printed scaffold, this aging period was named 'solution-aging'.

For the preliminary work, the hybrid solutions could go down one of two processing routes: monolith method or foaming method. After the monolith or foam generation, a second aging stage followed. The second aging stage provided an additional window for further functionalisation and network condensation whilst the hybrid gels were formed yet still aqueous. Depending on the study, the temperatures used were 5°C, 21°C (RT), or 40°C, and the aging time was either 5 days, 7 days or 14 days. When aging was complete, samples were frozen at -4°C overnight then placed in a freeze dryer for 24 h. Conditions are: -96°C, pressure 0.13 mbar (Thermo Scientific Heto PowerDry LL1500).

3D printed scaffolds were also produced, the method of which is discussed later in section 4.2.3.

Monolith route

To form a monolith, the solution was stirred until it raised up above the stirrer bar rather than forming a vortex. At this point, 3 mL samples of the gel were placed in airtight wide mouth polycarbonate screw cap containers (Nalgene, 60 mL volume) for the second aging stage, conditions were dependent on the study. The samples were then freeze dried as described above.

Foaming route

Foams were produced using the method described by Mahony *et al.* (Mahony *et al.*, 2010). After 1 h of mixing the hybrid, 50 mL of the solution was transferred to a 600 mL polypropylene beaker. 1 mL of HF and 1.5 mL of a surfactant, Triton X-100, were added immediately before vigorous whisking using a hand held blender (Morphy Richards, speed setting 1). After approximately 4 minutes of whisking, the foams reached the point of gelling. They were then poured into wide mouth polycarbonate screw cap containers and samples were separated into two sets for aging at 40°C or 21°C for 1 week. The samples were then freeze dried as described above.

4.2.2 Functionalisation and aging study

The parameters of functionalisation and aging were varied in this study to assess the effect on the hybrid chemistry as expressed in FTIR analysis. The aim was to determine the functionalisation time, aging temperature and aging time for the new HF-free hybrid method which would be compatible with robocasting. The investigated parameters are displayed schematically in Figure 15, along with the reaction chemistry of the silica-gelatin hybrid system.

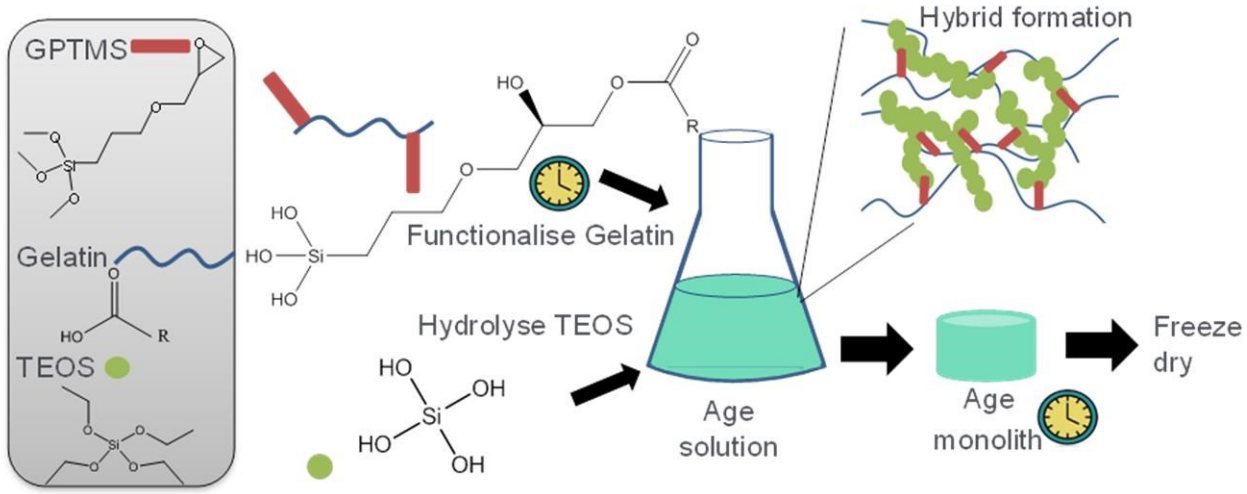

Figure 15. Schematic of hybrid chemistry and monolith method.

GPTMS hydrolysis

A preliminary investigation into the chemical structure of GPTMS and hydrolysed GPTMS was performed in order to determine the FTIR bands associated with GPTMS. The GPTMS was hydrolysed in the same way as TEOS would be hydrolysed according to the preliminary method, however the R-ratio was 3 rather than 4 as GPTMS has just 3 silanol-forming methoxy groups to hydrolyse.

Functionalisation study

The effect of functionalisation time on the bonding observed in the hybrids was investigated to determine the most effective functionalisation time for the new HF-free hybrid method. One composition was studied, 78G CF750, due to high gelatin content and high C-factor hybrids producing the best cell compatibility results according to Mahony *et al.* (Mahony *et al.*, 2010).

The preliminary method was followed up to the functionalisation stage to produce 40 mL of functionalised gelatin. During the functionalisation stage, 3 mL samples (n = 3) were taken at

particular time points. The 3 mL samples were placed in airtight containers and freeze dried as described previously. Samples were taken for analysis at three time points: 3, 14 and 22 h. At 22 h, functionalised gelatin had gelled, i.e. the solution rose up above the stirrer bar rather than forming a vortex. 14 h was selected as it was the functionalisation time used by Mahony *at al.* (Mahony, 2010) to create the foamed scaffold, and 3 h was selected as a shorter functionalisation time to compare to 14 h.

A shorter functionalisation time of 3 h was of interest because lengthy functionalisation times are known to be detrimental to the hybrid formation (Mahony, 2010). When functionalising for long periods of time, it was possible that hydrolysed silanol end groups of GPTMS react with each other through condensation (Gabrielli *et al.*, 2013). Condensation between GPTMS molecules to form oligomers is expected to be detrimental to hybrid formation as it is predicted to limit further functionalisation and interaction with the sol when added later (Gabrielli *et al.*, 2013).

Aging study

The aging study was conducted on monoliths of 78G CF750 hybrid in order to determine the most effective time and temperature for silica-gelatin hybrid aging without the use of HF. The hybrid solutions were functionalised for 3 h due to the results obtained in the functionalisation study. Aging was performed at: 40°C, 21°C (room temperature), 5°C, and the aging times investigated were: 5 days, 7 days and 14 days. The aging conditions of 40°C and 1 week were the aging conditions used on the silica-gelatin hybrid foams produced by Mahony *et al.* (Mahony *et al.*, 2010). For the HF-free hybrid method, lower temperatures were investigated due to the unknown effects of elevated temperature on the hybrid material. A longer aging time period (14 days) was tested to potentially compensate for the reduced temperature. A shorter time period (5 days) was tested to ensure the same results cannot be achieved in a shorter time period.

Characterisation

FTIR was used to analyse the chemical bonding of: GPTMS before and after hydrolysis, the functionalised gelatin samples, and the aging study samples. From observing the changes in the chemical bonding, the most effective functionalisation time, aging temperature, and aging time were selected for the new HF-free hybrid method.

FTIR, Perkin Elmer Spectrum 100, was run in absorption mode between 600-4000 cm^{-1}, 50 scans, at a resolution of 4 cm^{-1}. 5 spectra were obtained per sample. The FTIR samples were prepared by crushing the dry samples using a pestle and mortar. Once background analysis

was complete, the sample was placed over the beam and secured in place for testing. Between samples, the surface is cleaned with ethanol.

4.2.3 Silica-gelatin HF-free hybrid method

To be suitable for 3D printing, the silica-gelatin hybrid solutions were produced according to the HF-free hybrid method as determined by the results of the functionalisation and aging studies. To continue the methods section, the HF-free hybrid method and 3D printing route must be introduced here as the method is used in all future investigations. A schematic of the method is shown in Figure 16.

HF-free hybrid method

All reagents were supplied by Sigma Aldrich UK unless otherwise specified. For all hybrids, the first stage was to dissolve gelatin (Porcine skin, gel strength 300, Type A) in 10 µM hydrochloric acid (HCl), to give a concentration of 50 mg mL^{-1}, in a covered beaker at 40°C for 1 h. This solution was functionalised by the addition of GPTMS, the amount of which was dependent on the C-factor. The time allowed for functionalisation was 3 h.

The sol was prepared separately. Hydrolysis of TEOS started 2 h after the start of the gelatin functionalisation, i.e. 1 h before the end of gelatin functionalisation. It was prepared by combining the components in the following order: deionized water, 1 M HCl and tetraethyl orthosilicate (TEOS). The R-ratio was 4 and the volume ratio of water/HCl was 3. The solution was stirred for 1 h at 400 rpm to allow hydrolysis of TEOS.

Both reactions were complete at the same time. The functionalised gelatin and hydrolysed TEOS were mixed and returned to the hotplate at 40°C at 400 rpm. The amount of each solution added was dependent on the gelatin to silica ratio of hybrid composition being made.

As with the preliminary methods, the solution-aging (the aging period of the solution before processing into a monolith/foam/3D printed scaffold) of the hybrids began with mixing on a hotplate at 40°C at 400 rpm. The solution-aging time of the hybrid varied between 4 h and 30 h depending on the composition. When necessary, the hybrid solutions were mixed on the hotplate for a maximum of 5 h then transferred to a 20 mL syringe and placed in a -18 °C freezer. When required for further aging, the syringes were placed in a 40°C oven where solution-aging was resumed.

Monolith route

When solution-aging was complete and 3D printed scaffolds were not required, samples of the hybrid solutions or gels could be separated into monoliths once solution-aging was complete. The samples were placed into wide mouth polycarbonate screw cap containers and were aged

for a further 1 week at 21°C. The samples were frozen at -4°C overnight then placed in a freeze dryer for 24 h. Conditions are: -96°C, pressure 0.13 mbar (Thermo Scientific Heto PowerDry LL1500).

3D printing route

Figure 16 presents a schematic of the HF-free hybrid method and 3D printing route. Once solution-aging was complete, the gel reached the 'printing window', the period of time within which the gel could be printed. The required solution-aging time and 'printing window' was determined for different compositions (see Table 4) in the composition compatibility study to follow. The printing window identified the period of time within which the hybrid gel could flow through the tubing and nozzle and hold its shape once printed. The exact 3D printing parameters used are discussed in the later section 4.2.5: printing parameters, and the set-up is shown in Figure 17.

The 3D printed scaffolds were placed into sealed containers and aged at 21°C for 1 week. The samples in this chapter were all frozen at -4°C overnight then placed in a freeze dryer for 24 h. Conditions are: -96°C, pressure 0.13 mbar (Thermo Scientific Heto PowerDry LL1500).

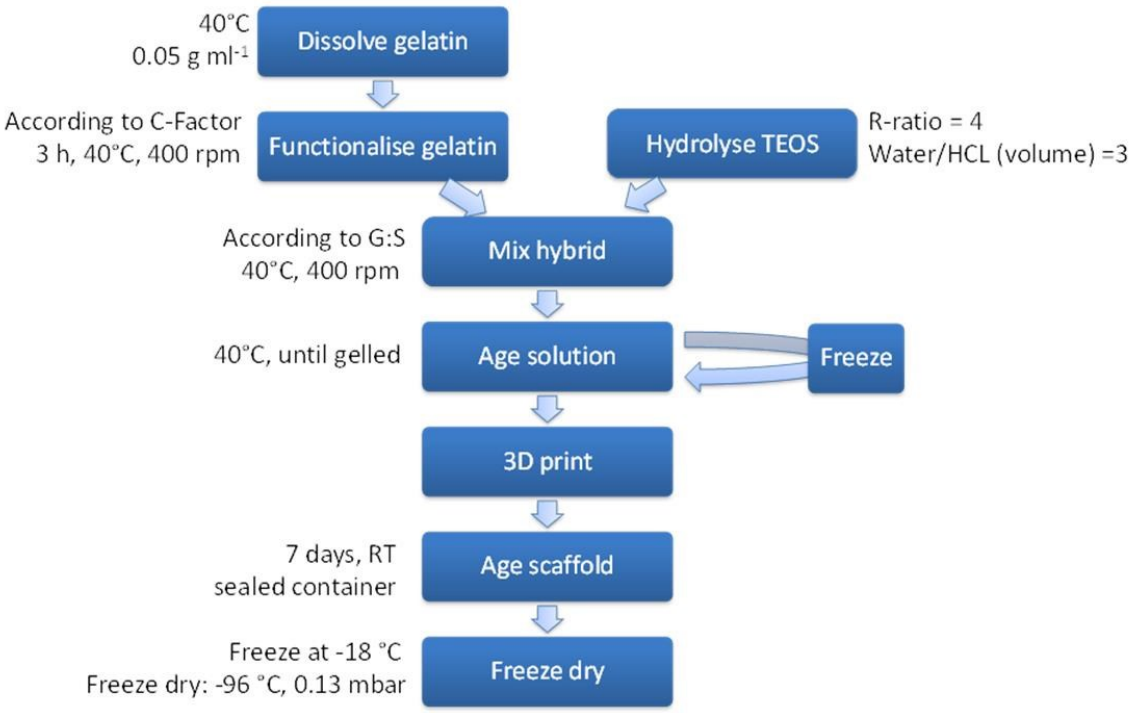

Figure 16. Schematic of the HF-free hybrid method for 3D printing silica-gelatin hybrids: 3D printing route.

4.2.4 Crosslinking effects of C-factor

The effect of C-factor on the degree of crosslinking of the final hybrid material was assessed. This was conducted in order to determine which C-factor provided the highest degree of crosslinking without being in excess when producing hybrids using the new HF-free method.

The crosslinking index was determined by measuring how the concentration of detectable primary and secondary amino acids changed as the C-Factor of hybrids increased from 0 to 1000. The epoxide ring of GPTMS reacted with gelatin due to nucleophilic attack from -COOH groups present in amino acid groups on the gelatin chain. The number of primary and secondary amino acids on the gelatin chain was therefore reduced when functionalised with GPTMS due to steric hindrance (Gabrielli *et al.*, 2013, Shirazi *et al.*, 2016).

Ninhydrin reagent (1,2,3-triketo-hydrindene hydrate, Sigma Aldrich) is commonly used to determine the concentration of primary and secondary amines and amino acids (Lai *et al.*, 2013). Ninhydrin reagent and free, unreacted amino acids interact to form an intense purple colour, known as Ruhemann's purple.

To assess the crosslinking, 78G hybrids with C-factors of CF0, CF100, CF250, CF500, CF750 and CF1000, and gelatin standards at concentration: 0.01, 0.02, 0.04, 0.05, 0.09 g mL^{-1}, were reacted with ninhydrin reagent (1,2,3-triketo-hydrindene hydrate). The hybrids were produced in accordance with the HF-free hybrid method following the monolith route. For each hybrid composition, after 5 h of solution-aging, 2 mL samples (n = 3) were placed in a covered glass test tube where the monoliths were aged and later freeze-dried.

Once all samples and standards were prepared, 2 mL of DI water was added to the dried hybrids and held in a water bath for 1 h at 80°C to allow any unreacted gelatin to dissolve. 1 mL of Ninhydrin reagent was then added to each sample and standard and left for a further 30 minutes. The samples and standards were then cooled to room temperature and 5 mL of 95 % ethanol was added to each sample. A further dilution of 1:49 sample and standard volume to additional ethanol volume was required to bring the absorbance readings below a value of 1. Samples and standards were read using a microplate reader (SpectraMax M5) at 570 nm from a 48 well plate. From the calibration curve, the presence of free amino acids and hence unreacted protein was quantified (Lai *et al.*, 2013).

The amount of free amino groups in the gelatin was proportional to the optical absorbance of the solution. To calculate the crosslinking index (the degree of crosslinking in the hybrid),

Equation 11 was used, where respectively; C_i and C_f are the optical absorbance of the gelatin solution before and after cross-linking.

Equation 11: $$\boldsymbol{Crosslinking\ Index}\ (\%) = \frac{C_i + C_f}{C_i} \times \mathbf{100}$$

4.2.5 3D printing parameters and composition compatibility

To develop a process for 3D printing, the printing parameters and properties of the silica-gelatin hybrid printing ink were closely tied. As the silica network in the hybrid solutions condensed over time, it was important to characterise this condensation which was causing gelation and work out the stage of gelation at which the hybrids could be 3D printed.

The aim here was to determine the most compatible composition for 3D printing and the most suitable parameters for 3D printing. The 3D printing parameters and composition compatibility study are presented here as two separate studies; however, in practice they were highly dependent on each other.

3D printing parameters

Developing the process to 3D printing silica-gelatin hybrids started with printing pure gelatin solutions of 50 mg mL^{-1}. This gave a basic understanding of how the aqueous gel would flow and at what levels of observable gelation the solutions held their shape when printed. With this basic information, the 3D printing process for silica-gelatin hybrids was developed through systematic trial and error.

The printing process was developed using an adapted Ultimaker Original, as shown schematically in Figure 17. The gels to be printed were held within a 10 mL luer lock BD Plastipak™ syringe and the syringe plunger had a controlled force applied by a Harvard Apparatus PHD Ultra syringe pump. The force applied by the syringe pump controlled the deposition rate of the hybrid gel. As the main component of the hybrid was gelatin, during the printing process, the hybrid gel required heating to ensure that any viscosity increase of the hybrid was due to network condensation and crosslinking of the hybrid rather than gelatin transitioning from the liquid to solid state. Therefore, a heat jacket was used to warm the hybrid-containing syringe and the applied temperature was investigated.

On exiting the syringe, the gels then flowed along tubing towards the printing tip. The tubing used was Harvard Apparatus' PolyE polyethylene tubing with an internal diameter (ID) of 1.78 mm. It was chosen due to the flexibility and hydrophobic surface which allowed smooth flow of the hybrids. The tubing ID was compatible with Nordson EFD stainless steel dispensing tips (outer diameter of 1.83 mm) which connected the syringe to the tubing, and the Ibidi male luer connectors which connected the tubing to the printing tip. Tapered and stainless steel Nordson EFD tips were tested with decreasing ID from 0.41-0.2 mm (gauge 22-27).

On exiting the nozzle, the gels were required to hold their shape and be built upon layer-by-layer without collapse. If this was achieved, then the material was deemed to be within its printing window.

The 3D printing parameters investigated were: material deposition rate, nozzle size, speed of print head, and scaffold structure (strut separation and layer height). Due to the limitation of the deposited strut width, which is discussed in the results, the aim was to 3D print scaffolds with the smallest strut separation possible without collapse during processing or densification of pores during aging.

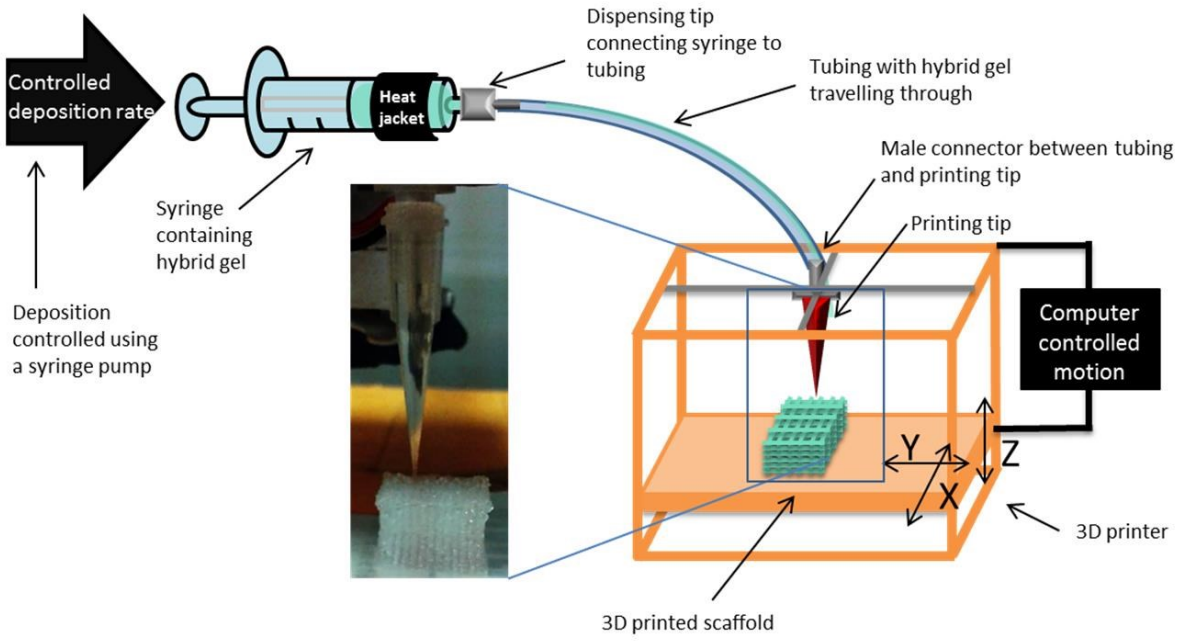

Figure 17. Schematic of the 3D printing set-up including an image of scaffold being 3D printed.

A printing set up for scaffolds with 1 mm strut separation and 1.5 mm strut separation was developed.

Composition compatibility study

The most suitable C-factor, CF500, was determined in section 4.2.4: crosslinking effects of C-factor, and the aim in this section was to determine the mass ratio of gelatin to silica (from TEOS contributions only) by assessing the gelation rate of the hybrids and finalise the 3D printing composition. Due to the condensation of the gel over time, the gelation stage where the hybrid could be printed, the printing window, had to be determined in order to successfully 3D print using the gel. The effect of the gelatin to silica mass ratio on the gelation rate of the hybrid was examined to determine the composition most compatible with the 3D printing process. The mass ratio of gelatin and silica was selected in order to allow the most

3D printed scaffolds to be printed per batch of hybrid. The solution-aging time and printing window were determined for compositions with increasing wt% gelatin at CF500 where wt% is calculated from gelatin/(gelatin + silica from TEOS).

Evaluating the gelation

The hybrid solutions progressed through 3 stages after the two components were mixed: not gelled enough for printing, printable, then too gelled for printing. The stages were named: solution-aging, printing window, and over-gelled.

The time frame for each stage was investigated for the compositions in Table 4. To conduct the study, the solutions and later the gels were monitored and 3D printing was attempted regularly (~1 h intervals) as the condensation of the solution increased over time. As the study was based on trial and error, new solutions were repeated to ensure the reliability of the printing window.

Table 4. Silica-gelatin hybrid compositions for printing compatibility study.

Hybrid description	Gelatin: Silica mass ratio	C-Factor
60G CF500	60:40	500
70G CF500	70:30	500
78G CF500	78:22	500
84G CF500	84:16	500
89G CF500	89:11	500
95G CF500	95:5	500

To understand the change in gel strength, and how this related to whether the gel could be 3D printed or not, the rheological properties of the composition found most suitable were investigated.

Rheology

The rheological properties of the hybrid composition most compatible with 3D printing, 78G CF500, were measured over time to assess how the rheology of the hybrid gels affected the ability to print the material. Direct viscosity measurements were not possible due to the high degree of crosslinking preventing viscous flow of the hybrid gel. Instead, oscillatory viscosity

was employed to monitor the storage and loss moduli of the gels with increasing solution-aging time (increasing condensation of the silica network).

To measure the storage and loss modulus a Discovery Hybrid Rheometer, TA instruments was used in oscillatory mode. Firstly, a suitable strain rate was found by determining the Linear Viscoelastic Region (LVR) of the material and selecting a strain rate value within this region. To do this, an oscillation-amplitude test (0.1-100 % strain rate) was performed under the conditions: 1 mm gap, 40 mm stainless steel plate, 40°C, 30 s soak time, 10 rad s^{-1} frequency using a solvent trap. 10 % strain was found to be within the LVR. G' and G'' were then measured using an oscillation-frequency test (0.1-100 Hz) with conditions: 1 mm gap, 40 mm stainless steel plate, 40°C, 30 s soak time, 10 % strain. This oscillation-frequency test was performed at: 7, 9, 11, 13, 15 h of solution-aging.

4.2.6 Silica network condensation

The chapter has so far investigated and established: a new HF-free hybrid method, that the 78G CF500 hybrid composition was most compatible with 3D printing, and the parameters for 3D printing. Here, solid state NMR was employed to assess how the network connectivity of the HF-free hybrid method compared to that of the original foaming method (Mahony *et al.*, 2010).

The silica network connectivity of four 78G CF500 hybrids with different hybrid methods and processing parameters were compared. Functionalisation time, aging time, aging temperature, and use of HF were investigated. The 78G CF500 hybrid composition was selected due to the results of the two composition studies. All monoliths and scaffolds were freeze-dried.

The variations in the silica-gelatin hybrid methods are presented in Table 5. Method A is the new HF-free hybrid method which followed the 3D printing route. Method D is the foaming method by Mahony *et al.* (Mahony *et al.*, 2010). Methods B and C are intermediary control methods allowing the effects of the long functionalisation time, HF addition, and 40°C aging to be observed individually. Functionalisation time is compared by methods A and B as they are both 3D printing methods, however method B had a 14 h functionalisation rather than 3 h. Methods B and C differed through the addition of HF. Method C used HF which allowed for foaming rather than 3D printing. Methods C and D were both foamed using HF however method C retained room temperature aging whereas method D used an aging temperature of 40°C.

Table 5. Variations on the silica-gelatin hybrid method, 78G CF500.

Method	Description	Functionalisation time /h	Hybrid solution-aging time /h	HF addition	Processing route	Aging temperature /°C
A	HF-free 3D printing method	3	Until suitable for printing	No	3D printing	21
B	Method A + increased functionalisation time	14	Until suitable for printing	No	3D printing	21
C	Method B + HF addition	14	1 h	Yes	Foaming	21
D	Foaming method	14	1 h	Yes	Foaming	40

^{29}Si MAS NMR

All ^{29}Si MAS NMR measurements were performed at the University of Warwick at 7.0 T using a Varian/Chemagnetics InfinityPlus spectrometer operating at a Larmor frequency of 69.62 MHz. These experiments were performed using a Bruker 7 mm HX probe which enabled a MAS frequency of 5 kHz to be implemented. For ^{29}Si single pulse measurements a flip angle calibration was performed on kaolinite from which a $\pi/2$ pulse time of 5.5 μs was measured. All measurements were undertaken with a $\pi/2$ tip angle along with a delay between subsequent pulses of 240 s.

From the ^{29}Si MAS NMR spectra, the relative peak areas were resolved by deconvolution using OriginPro software and the network condensation was calculated using Equation 12, where Q^n is the % abundance of Q^n species and T^n is the abundance of T^n species.

Equation 12:

$$D_c = \left(\left[\frac{4Q^4 + 3Q^3 + 2Q^2}{4} \right] + \left[\frac{3T^3 + 2T^2 + T^1}{3} \right] \right)$$

4.3 Results and discussion

The results present the journey taken to adapt the silica-gelatin hybrid method to 3D printing. Firstly the hybrid process was investigated to determine the new HF-free hybrid method. The C-factor of the hybrid was then chosen to maximize crosslinking and following this, the 3D printing parameters and gelatin wt% were established. The HF-free hybrid 3D printing method was then probed structurally to assess the connectivity of the silica network and the final composition of the hybrid scaffolds was analysed.

4.3.1 Functionalisation study

The mechanism of functionalising gelatin with GPTMS has been proved possible by Gabrielli *et al.* and Ren *et al.*, however the reaction is difficult to control (Gabrielli *et al.*, 2013, Ren *et al.*, 2001b). It was therefore necessary to monitor the extent of the reaction through observing the epoxy ring opening and silanol formation at increasing time points. Using FTIR these developments were observed and the functionalisation time which produced a material with the lowest epoxy ring (oxirane) presence was chosen. A low oxirane presence indicated that the oxirane ring had either opened by hydrolysis or reacted through nucleophilic attack by a -COOH group on the gelatin to create a permanent bond. As oxirane is cytotoxic, a low oxirane presence is highly desirable for tissue scaffolds. Here, FTIR spectra of CF750 functionalised gelatin samples functionalised for 3 h, 14 h, and 22 h were compared in order to determine the functionalisation time for the HF-free hybrid method.

To identify the vibrational bands associated with GPTMS in the functionalisation study, FTIR spectra of GPTMS before and after hydrolysis was obtained. FTIR spectra of GPTMS obtained by Mahony *et al.* (Mahony, 2010) could not be used as a reference as the relative strengths of the vibrational bands were very different to the spectra obtained here. The hydrolysed GPTMS spectra produced by Mahony *et al.* observed Si-CH_2, Si-O-Si (1020 cm^{-1}), and oxirane vibrational bands to have a similar intensity. Here, the FTIR spectra of GPTMS before and after hydrolysis was repeated, as seen in Figure 18, and the Si-CH_2 band was weaker. To identify the vibrational bands associated with GPTMS in the functionalised gelatin spectra, the revised FTIR spectra of GPTMS before and after hydrolysis was used.

Figure 18 shows the FTIR spectra of GPTMS before and after hydrolysis with all bands normalised to Si-C band at 1200 cm^{-1}. The strongest vibrational band in non-hydrolysed GPTMS was Si-OCH_3 (1075 cm^{-1}), and both Oxirane (910 cm^{-1}) and methyl (850 cm^{-1}) groups were also observed. In the hydrolysed GPTMS spectra; two bands between 1020 cm^{-1} and 1150 cm^{-1} developed which assigned to the asymmetrical Si-O-Si vibrations, the methyl group was lost, and the band at 910 cm^{-1} increased. The increase at 910 cm^{-1} was not due to oxirane as the relative amount of oxirane cannot increase with hydrolysis, only decrease. There is conflict in the literature as to where the Si-OH bond is seen; 900 cm^{-1}, 920 cm^{-1} or 958 cm^{-1} (Tonda-Turo *et al.*, 2013, Gao *et al.*, 2013a, Jerman *et al.*, 2011, Liu *et al.*, 2004) and here the results suggest the GPTMS Si-OH stretching band is assigned to 910 cm^{-1}. The broad band at 1650 cm^{-1} is assigned to the bending mode of adsorbed water molecules. (Tonda-Turo *et al.*, 2011, Liu *et al.*, 2004, Gao *et al.*, 2013a, Duran *et al.*, 1986).

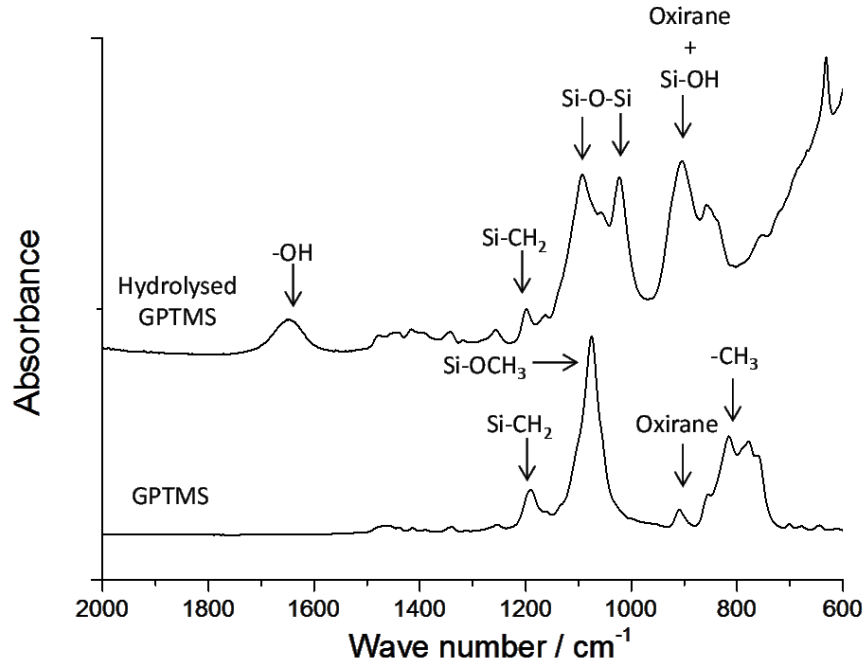

Figure 18. FTIR spectra of GPTMS before and after hydrolysis

With the GPTMS bands assigned, FTIR spectra of gelatin functionalised by GPTMS at CF750 was analysed. Figure 19 shows the spectra for three functionalisation times: 3 h, 14 h and 22 h. Bands at 1640 cm^{-1} (Amide I), 1540 cm^{-1} (Amide II), 1450 cm^{-1} (Amide III) arose from the presence of gelatin.

At 22 h, the functionalised gelatin was gelled; it rose above the stirrer bar when being mixed rather than forming a vortex so was not suitable to mix with the sol-gel to form a hybrid. The reduction in Oxirane/Si-OH band at 910 cm^{-1} corresponds to a more condensed, gelled network. The increase in intensity of the asymmetrical Si-O-Si band between 1020-1150 cm^{-1} and the symmetric Si-O-Si vibrational band at 790 cm^{-1} confirm this increase in network condensation.

Comparing 14 h and 3 h, there is no observable difference in FTIR spectra. For this reason, 3 h was selected as the functionalisation time for the new HF-free hybrid method as the additional time spent functionalised appeared to add no benefit to the bonding in the material.

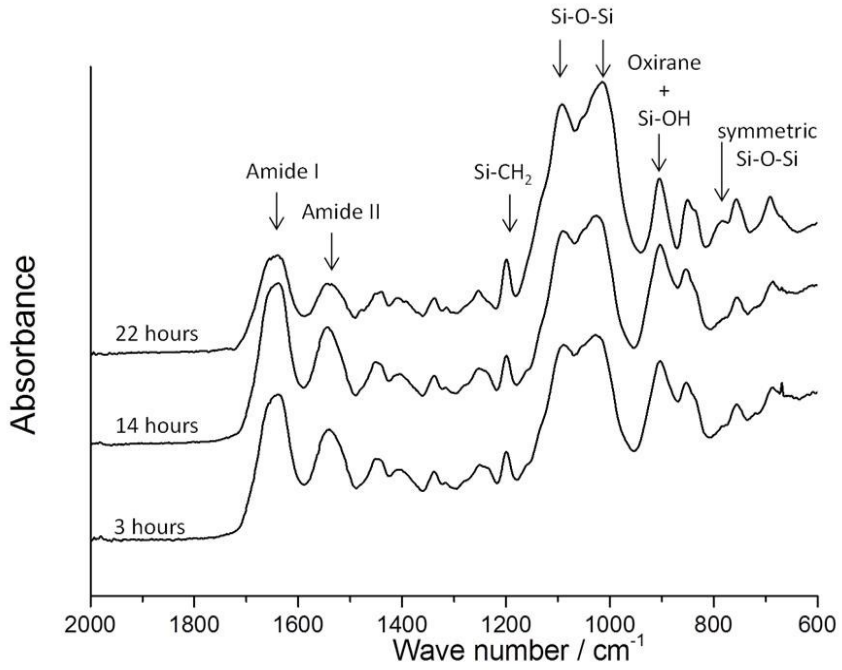

Figure 19. FTIR spectra of gelatin functionalised with GPTMS, CF750, for increasing lengths of time.

4.3.2 Aging study

Aging of the monolith was the last stage in the formation of a silica-gelatin before drying. In practice, it would occur after the hybrid gel had been 3D printed. Here, the aging stage was investigated by examining how 9 different aging conditions affect the bonding seen in 78G CF750 monoliths. Increasing temperatures: 5°C, 21°C (RT) and 40°C, and increasing times: 5, 7 and 14 days, were studied.

The aging stage allowed further condensation of the silica network and hydrolysis or bonding of the epoxy ring whilst the hybrid remained aqueous (i.e. before drying). The change in the material chemistry due to the aging conditions experienced was observed by FTIR. When aging glass samples, elevated temperatures are used to further improve the silica network (Hench and Wilson, 1993), but in the case of silica-gelatin hybrids, temperatures are limited by gelatin. Gelatin alone has a gel transition at 30°C, however in a hybrid material gelatin can withstand higher temperatures due to crosslinking (Mahony *et al.*, 2010).

Figure 20 presents FTIR spectra obtained for the aging study. The 40°C data has been removed as it induced drying of the hybrid monolith surface after 5 days. 14 days at 21°C was also void as bacteria was seen growing on the surface.

The oxirane/Si-OH band in FTIR spectra at 910 cm^{-1} is a good indicator of whether reactions are taking place as a reduction in this vibrational band relates to both GPTMS and TEOS incorporation. This band appeared with equally low intensity for the 21°C, 7 day condition and 5°C, 14 day condition. Hence, the main benefit of increased temperature was that condensation happened faster, as expected (Hench and Wilson, 1993). The 21°C, 7 day condition was the most efficient and effective time frame for scaffold-aging so was taken forward as the aging time and temperature for the HF-free hybrid method.

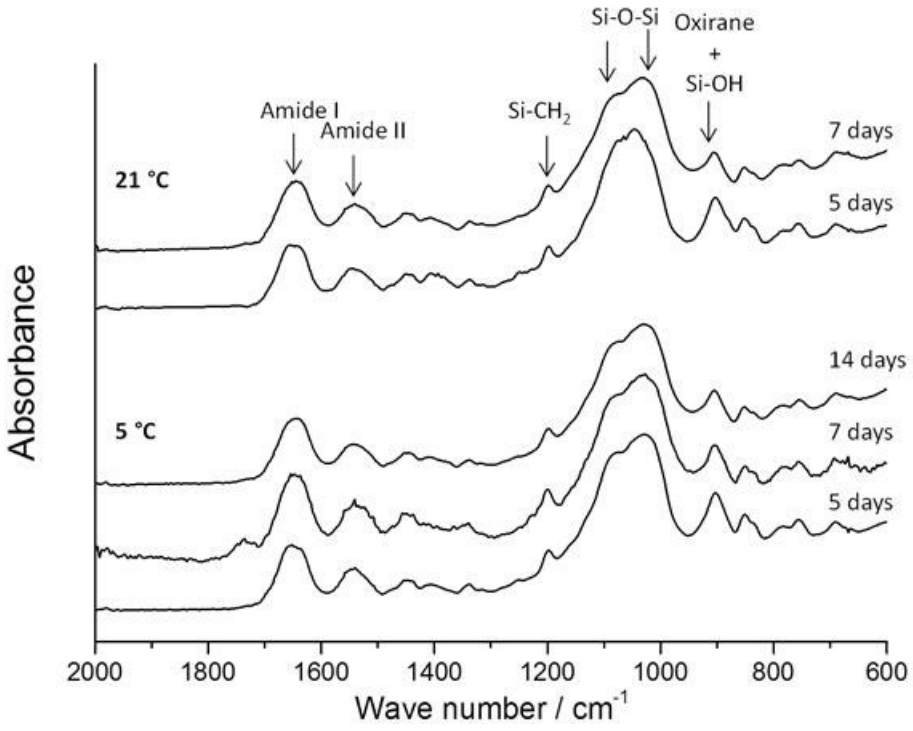

Figure 20. FTIR spectra of 78G CF750 hybrid monoliths aged at 5°C and room temperature for up to 14 days.

At this stage, the HF-free hybrid method conditions are a functionalisation time of 3 h and post monolith/scaffold forming aging conditions of 21°C for 7 days.

4.3.3 Crosslinking effects of C-factor

Understanding how the C-factor affected the degree of crosslinking of the hybrids was important to determine which composition to focus on for 3D printing. Theoretically, the molar ratio of GPTMS to the highly reactive amino acids containing -COOH groups on the gelatin molecule can be calculated. Farris *et al.* determined the percentage of amino acids in Type A pigskin gelatin (Farris *et al.*, 2010), and unpublished work by Connell *et al.* determined that glutamic acid (7.1 %) and aspartic acid (4.42 %) were the two most important amino acids involved in gelatin functionalisation with GPTMS based on abundance and reactivity. The number of moles of gelatin was used to calculate the number of amino acids, by multiplying by the mean number of amino acids per gelatin molecule (porcine skin, Type A). The number of moles of glutamic acid and aspartic acid were calculated as 11.52 % of the total. Dividing the number of moles of GPTMS by this number of moles of amino acids, CF250 gave a result of 0.14, CF500 gave 0.27, CF750 gave 0.41 and CF1000 gave 0.55. Therefore theoretically, none of the C-factors investigated should have excess GPTMS.

Here, ninhydrin reagent was used to assess the crosslinking index of 78G hybrids prepared using the HF-free hybrid method. Hybrids with increasing C-factor, from CF0 to CF1000 were investigated as shown in Figure 21. With increasing C-Factor from 0 to 500, the crosslinking index and C-factor had a linear relationship. Above CF500, the crosslinking index reached a plateau which suggested that additional GPTMS was not improving the crosslinking in the hybrid further. This lack of further crosslinking is unlikely to be due to saturation due to the theoretical ratio of GPTMS to functionalising amino acids calculated. More likely, the kinetics of the reaction slows over time due to reduced availability of binding sites and oligomer formation.

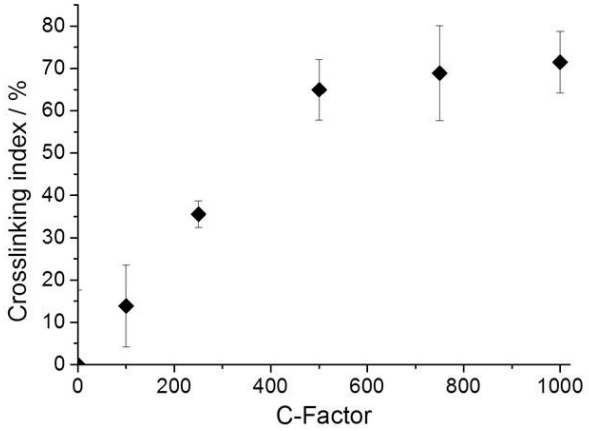

Figure 21. Crosslinking index determined by optical absorbance at 570 nm of 78G hybrids reacted with ninhydrin reagent.

In the optical absorbance experiments conducted by Mahony *et al.* (Mahony, 2010), the results showed that above CF500, the silica-gelatin components were fully integrated. This information alongside the ninhydrin reaction data in Figure 21 indicates that CF500 is the most effective C-factor as the GPTMS has bonded with the gelatin but is not yet in excess.

4.3.4 3D printing parameters

Alongside the composition compatibility study, the 3D printing parameters were investigated and determined. Hybrid gels that held their shape on exiting the nozzle were required for 3D printing. The degree of gelation was initially determined by systematic trial and error by working repeatedly with the material.

To develop the 3D printing process, the parameters investigated were: temperature of syringe warmer, deposition rate, nozzle size, speed of print head, and design of the print file (strut separation and layer height). The aim was to print 3D grid scaffolds with 90° layers which had channel widths of 200-300 μm when dry.

All the 3D printing parameters were dependent on each other and Table 6 summarises the parameter values investigated and general notes on the effects of increasing or decreasing each parameter. Two 3D printing set ups were developed: one with a 1 mm strut spacing, and another with 1.5 mm strut spacing. The 1.5 mm strut spacing scaffold was determined first then parameters were tweaked to obtain the 1 mm strut spacing. The 1 mm parameters are shown alongside the 3D printing process schematic in Figure 22.

A **strut spacing** of less than 1 mm was not possible with the hybrids gels. Due to the aqueous nature of the gel, a nozzle ID of 0.2 mm generated a strut width of 0.5 mm as the gel expanded on exiting the nozzle. This was the limiting factor during 3D printing as the gels would not flow through smaller nozzles and reducing the deposition rate to obtain a thinner strut led to inconsistent flow. Struts could not be printed closer together as when attempted, the struts condensed to neighbouring struts and vertical channels were not retained after 1 week of aging.

The **layer height** was selected by finding a layer separation height where the layers were in contact with the layer below, but not being printed into it. A height of 0.3 and 0.4 was selected for the 1 mm and 1.5 mm strut separation scaffolds respectively. If a larger layer height was used, the subsequent layer would not be in contact with the layer below during printing resulting in poor accuracy in layer deposition.

The **syringe temperature** was maintained at 40°C to ensure any unreacted gelatin remained soluble and did not set or increase the viscosity of the gel. Higher temperatures had the effect of increasing the gelation rate and reducing the time frame for 3D printing.

The **deposition rate** was closely linked to the **nozzle size** and **speed of the print head.** For the 1 mm strut separation scaffold, the values were 0.1 mL min^{-1}, 0.2 mm (ID) smooth flow tapered

tip, and 500 respectively. For the 1.5 mm strut separation scaffold, the values were 0.12 mL min^{-1}, 0.25 mm smooth flow tapered tip, and 400 respectively. This combination resulted in smooth flow through the nozzle without any breaks in the extruded gel.

Table 6. 3D printing parameters, the investigated range and values selected.

Parameter	Investigated range and findings	1 mm strut separation scaffold	1.5 mm strut separation scaffold
Strut separation	1.5-0.5 mm The strut separation is limited by the width of the extruded gel. This value was determined alongside deposition rate and nozzle size.	1 mm	1.5 mm
Layer height	0.2-0.6 mm The gel needed to be touching the previous layer when 3D printing. If separation is too small the layer is printed into the previous layer and if too large the material is not deposited accurately.	0.3 mm	0.4 mm
Syringe temperature	RT-60°C Temp too low- gelatin transitions from liquid to solid, too high- the hybrid gelation rate increased which reduced the 3D printing window.	40°C	40°C
Deposition rate	0.14-0.07 mL min^{-1}using BP plastic 10 mL syringe. Deposition rate is dependent on the nozzle size. Higher rate needed for larger nozzles	0.1 mL min^{-1}	0.12 mL min^{-1}
Nozzle size (ID)	Tapered tips vs. stainless steel nozzles from EFD Nordson: 0.41 mm, 0.25 mm, 0.2 mm nozzle sizes (gauge 22, 25, 27) Larger nozzle sizes are suitable for larger prints with wider strut separation	0.2 mm smooth flow tapered tip	0.25 mm smooth flow tapered tip
Speed of print head	Feed rate (FR) 200-800. Lower speeds lead to more accurate prints but reduce the number of prints possible within the 3D printing window.	Feed rate 500	Feed rate 400

As already mentioned, the scaffolds are aqueous when they are being printed. To be used, they required a drying stage. The drying options: critical point drying and freeze drying, are evaluated in the following chapter.

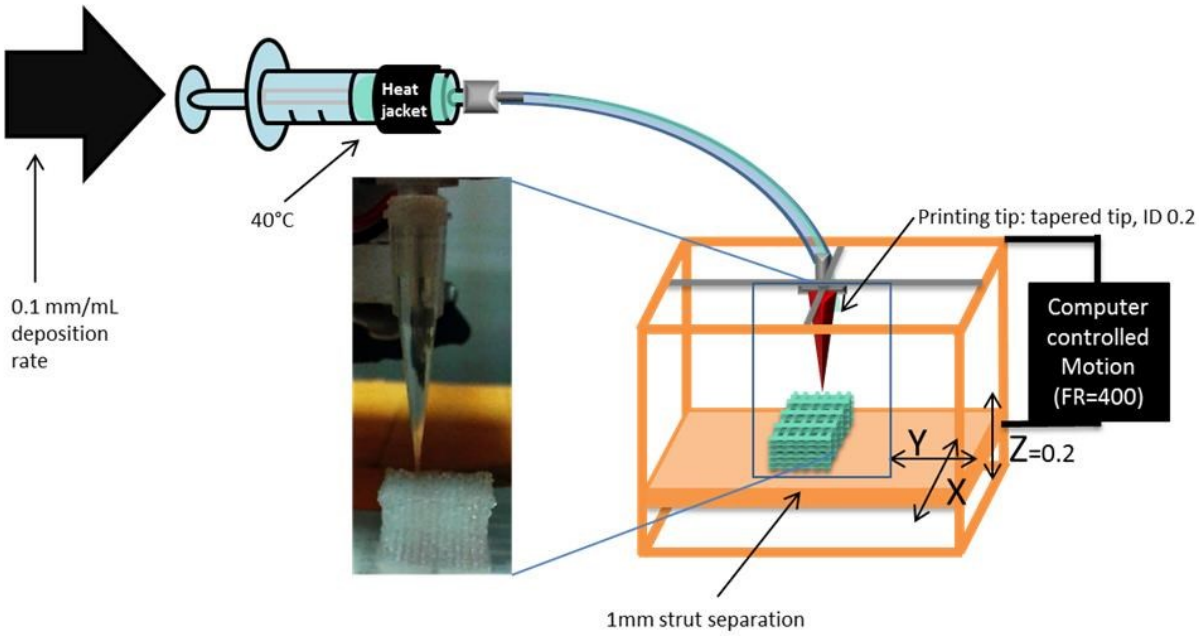

Figure 22. Schematic of the 3D printing set-up including an image of scaffold being 3D printed showing the printing parameters required for a 1 mm strut separation scaffold.

4.3.5 Composition compatibility study

This study compared the gelation over time of silica-gelatin hybrids with 60 - 95 wt% gelatin. This high gelatin content range was investigated to avoid formation of hydroxycarbonate apatite (HCA) on the scaffold surface when *in vitro* or *in vivo*, as seen on 30G foamed hybrids (Mahony *et al.*, 2014). The hybrids were prepared with a C-factor of 500 due to the results of the crosslinking study. By comparing the time frame over which the hybrids gelled, due to the continued sol-gel network condensation and GPTMS functionalisation, the most suitable composition for 3D printing was chosen. The ideal composition would have had a very short time period for solution-aging and a large time period where the gel is compatible with 3D printing. This 3D compatibility period was named the printing window and the aim was to select a composition that would maximize the number of scaffolds that could be printed per batch of hybrid but with a reasonable solution-aging period.

Figure 23 graphically shows the time frames for solution-aging and the printing windows for hybrids with increasing gelatin content. The 89G and 95G compositions did not form printable solutions within 30 h of solution-aging and as the idea was to determine the most efficient composition for 3D printing, these compositions were not studied further.

As shown in Figure 23, the solution-aging time and 3D printing window increased with increased gelatin content. The increase in solution-aging time indicated slower condensation of the sol-gel network. As the C-factor was maintained at CF500, the amount of GPTMS increased in proportion to the gelatin increase due to C-factor being a molar ratio. As the wt% of gelatin in the hybrids was increased, the amount of TEOS in the system was decreased. Condensation rate was strongly affected by the changes in composition and the slower condensation indicated that the increase in GPTMS content could not compensate for the reduction in TEOS content in terms of network formation and hence crosslinking.

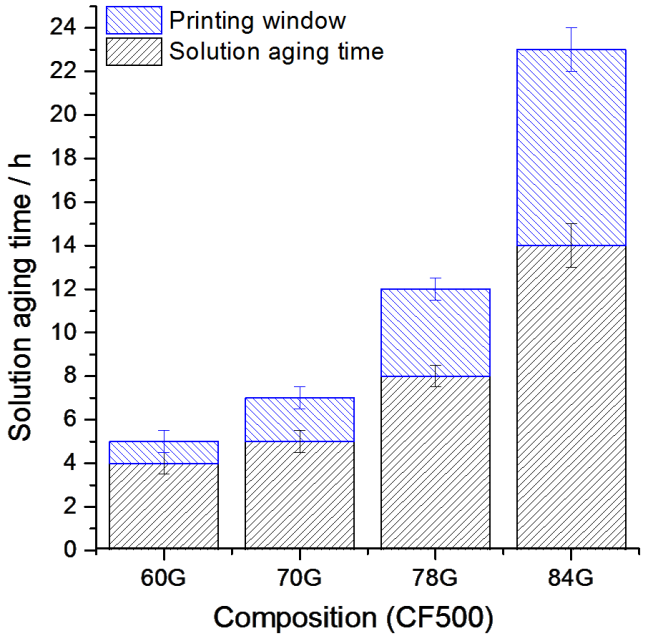

Figure 23. Graphical representation of solution-aging and printing window times for printable compositions with increasing wt% gelatin and C-factor of 500.

The study identified 78G CF500 to be the most compatible hybrid composition for 3D printing using the method developed. This was due to the convenient solution-aging time period and large printing window. To 3D print 78G CF500, the whole process from dissolving the gelatin to 3D printing took 2 days. The hybrid was frozen in batches of 20 mL, which is approximately the amount of hybrid that could be printed in the 4 h period. This made scaffold synthesis convenient and efficient as the 20 mL batches could be stored in the freezer until required.

The timeline for making the hybrid and 3D printing was:

Day 1 - Dissolve and functionalise gelatin, hydrolyse TEOS, mix the components and solution-age for 5 hours. Place 78G CF500 hybrid in 20 mL syringes and freeze.

Day 2 - Place syringe containing frozen hybrid in the oven for 3 h to further solution-aging the hybrid network. 3D print the 78G CF500 hybrid for 4 hours.

The 3D printing method is discussed in the previous section of this chapter.

Rheology

The rheological properties of 78G CF500 were examined to demonstrate the development of the viscoelastic properties of the gel over time.

Usually when robocasting, the shear thinning properties of 3D printing inks are tightly monitored and controlled to produce accurate prints (Fu *et al.*, 2011, Gao *et al.*, 2013b). Shear thinning inks are designed to flow through the nozzle when a force is applied but hold their shape once extruded out of the printing nozzle. In a plot of storage modulus (G', elastic properties) and loss modulus (G'', viscous properties) for a shear thinning ink, G' would decrease with increasing frequency and G'' would increase. At a certain frequency the lines plotting G' and G'' would cross indicating predominantly 'liquid-like' behaviour at higher frequencies. The shear thinning hybrid inks printed by Gao *et al.* gained their properties by being uncrosslinked during 3D printing and therefore a two stage process was required to chemically link the gelatin however inorganic and organic crosslinking was not achieved (Gao *et al.*, 2013b).

In Figure 24, G' and G'' of the 78G CF500 silica-gelatin hybrid gels were plotted against increasing frequency over 15 h. Figure 24 shows that G' increased with frequency at each time point. Also, at every time points other than 7 h, G' was an order of magnitude larger than G''. The silica-gelatin hybrid gels were therefore not shear thinning inks, and the G' and G'' plots resemble those of highly crosslinked polymers (Hoch *et al.*, 2012). The large elastic component is due to the large degree of crosslinking caused by silica network condensation and functionalisation of the gelatin with GPTMS. The time-dependent crosslinking of the silica-gelatin hybrids made the gels difficult to characterise, but here, the hybrids were 3D printed directly from sol in a one stage process to achieve highly crosslinked scaffolds.

When measuring the oscillatory rheology response, the gel was stored in bulk in a 40°C oven and samples were removed at each time point. The hybrid gels were measured as a 1 mm layer and despite using a solvent trap and applied temperature of 40°C this did not fully replicate the conditions of 3D printing where the hybrid flowed gradually from the syringe to the nozzle with no loss of solvent. Therefore, due to the difference in conditions between 3D printing and the process of measuring the rheological properties, the exact values at a time point and rate of increase of G' and G'' is likely to be slightly different, however the general trend is the same.

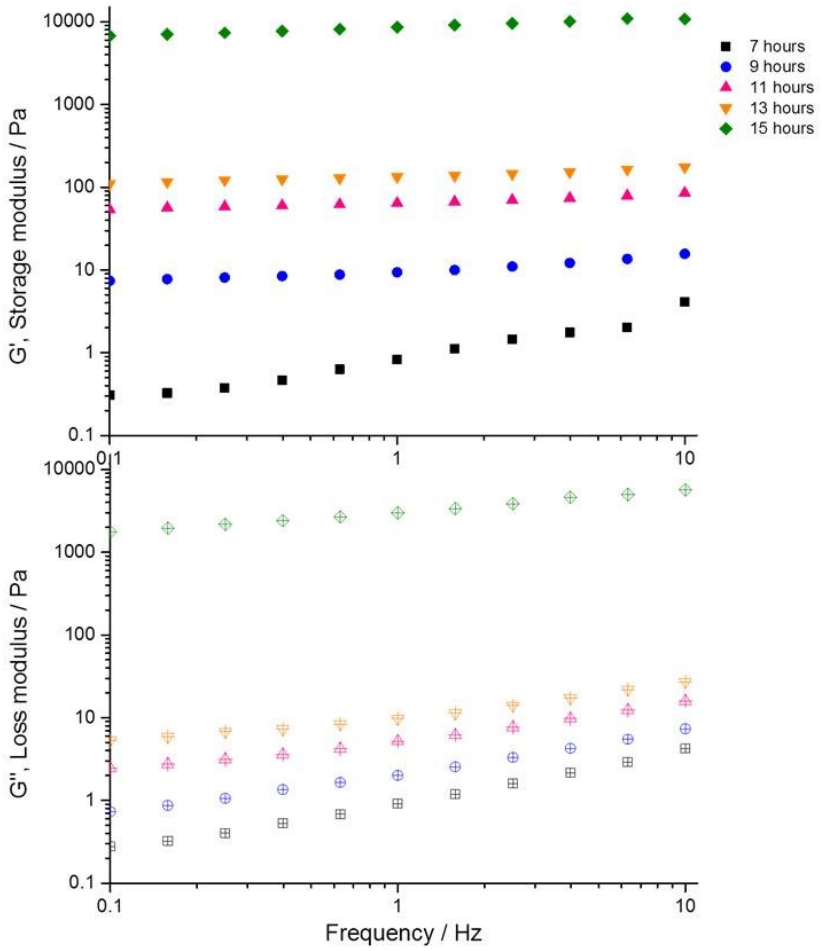

Figure 24. The frequency dependence of storage and loss moduli of 78G CF500 hybrid gels increasing solution-aging time.

To 3D print silica-gelatin hybrids functionalised by GPTMS using a robocasting method, the ability to print did not come from shear thinning properties however 3D printing was still possible. Rather than flowing through the tubing and nozzle, the highly crosslinked hybrid gel was forced along the tubing and on exiting the nozzle was able to hold its shape. The composition found most suitable for 3D printing via this extrusion method was 78G CF500 due to the convenient gelation rate and large printing window. To 3D print this hybrid composition, a solution-aging time of 8 hours was required after which the hybrid gel was able to be 3D printed for 4 hours.

4.3.6 Silica network condensation

The silica network connectivity of the 78G CF500 silica-gelatin hybrid scaffolds produced using the HF-free hybrid method, following the 3D printing route, were investigated by ^{29}Si MAS NMR. The new method was compared to the foaming method by Mahony *et al.* (Mahony *et al.*, 2010). The GPTMS connectivity and TEOS connectivity, respectively the T and Q structure, were measured.

Table 7 compares the T and Q structure of 78G CF500 hybrids, the hybrid composition found to be most suitable for 3D printing. The 78G CF500 hybrid was produced using 4 different methods. Method A was the newly developed HF-free hybrid method: 3 h functionalisation, no HF addition and room temperature aging. Method D was the foaming method: 14 h functionalisation, HF addition and 40°C aging. Comparing the degree of condensation, D_c as calculated using Equation 12, method A had a D_c of 90.4 % whereas method D had a D_c of 94.2 %. Method D had various differences: longer functionalisation, HF addition, and higher temperature aging. To clarify how each of these parameters improved the network connectivity, the parameters were adjusted individually. These intermediary control methods were method B, longer functionalisation time, and method C, longer functionalisation time plus HF addition.

Comparing method A to B, the only difference in method was functionalisation time. Method A was functionalised for 3 h whereas B was functionalised for 14 h. The result of longer functionalisation time was a D_c 0.6 % lower than the HF-free hybrid method. Method B showed an overall decrease in connectivity of the T structure as T^1 increased from 1.3 % to 1.8 % and T^3 decreased from 39.0 % to 34.3 % for methods A and B respectively. The condensation of TEOS in method B showed a slightly higher percentage of Q^2, increased from 0.7 % to 1.1 %, and a positive increase in Q^4 from 31.8 % to 35.1 % for methods A and B respectively. The overall change in D_c was small, however the shorter functionalisation time improved the T structure and reduced the Q^2 contribution to the silica network. This aligned with FTIR data that suggested longer functionalisation times for GPTMS and gelatin were not beneficial to the hybrid synthesis.

Table 7. T structure, Q structure, and degree of condensation quantified by ^{29}Si MAS NMR for hybrids synthesised using four different methods: A, B, C, and D. The composition of all hybrid are 78G CF500.

				Method A	Method B	Method C	Method D
				HF-free 3D printing method	A + increased functionalisation time	B + HF addition	Foaming method
Parameters	Functionalisation time /h			3	14	14	14
	Solution-aging /h			Until gelled	Until gelled	1	1
	HF addition			No	No	Yes	Yes
	Aging temperature /°C			21	21	21	40
T^1	δ_{iso}	[ppm]]		-48.6	-49.3	-48.3	-51.6
	I	[%]		1.3	1.8	0.7	0.7
T^2	δ_{iso}	[ppm]		-58.4	-58.0	-58.7	-58.4
	I	[%]		19.0	18.8	11.8	9.4
T^3	δ_{iso}	[ppm]		-66.8	-66.6	-66.8	-66.9
	I	[%]		39.0	34.3	44.5	45.5
Q^2	δ_{iso}	[ppm]		-96.7	-95.9	-	-97.0
	I	[%]		0.7	1.1	-	0.3
Q^3	δ_{iso}	[ppm]		-102.1	-1017	-102.5	-102.5
	I	[%]		8.2	9.0	11.0	8.1
Q^4	δ_{iso}	[ppm]		-111.3	-111.0	-111.5	-111.7
	I	[%]		31.8	35.1	32.0	35.9
D_c	**[%]**			**90.4**	**89.8**	**92.8**	**94.2**

Comparing method B to method C allowed the effect of HF addition to be observed whilst retaining the same functionalisation and aging temperature. In method C, gelling was induced rapidly (minutes) by HF addition whereas in method B gelation occurred gradually (hours). HF addition caused a 3 % increase in D_c, the most substantial increase of all the parameters investigated. The most prominent improvement was in the T structure as T^1 more than halved and T^2 decreased from 18.8 % to 11.8 %, while T^3 increased from 34.3 % to 44.5 % when

HF was added. The lower species of the Q structure improved as Q^2 was no longer present, and Q^3 increased from 9.0 % to 11.0 %, however Q^4 decreased from 35.1 % to 32.0 %. Overall, the T structure showed greater improvement than the Q species when HF was added.

Method D showed that 40°C aging provided a less pronounced improvement on D_c compared to the effects of HF addition, just 1.4 % increase in connectivity compared to method C. The increased aging temperature induced further improvement to both the T and Q structure as T^2 reduced from 11.8 % to 9.4 % while Q^4 increased from 32.0 % to 35.9 %.

Methods C and D were interesting to evaluate against the HF-free 3D printing method, however neither HF nor a 40°C aging temperature were compatible with 3D printing. A visual summary of the data is displayed in Figure 25. The results confirmed that the HF-free hybrid method produced a hybrid material with a D_c comparable to that of the foaming method. The shorter functionalisation time of 3 h compared to 14 h slightly improved the condensation of the T structure as well as speeding up the hybrid method.

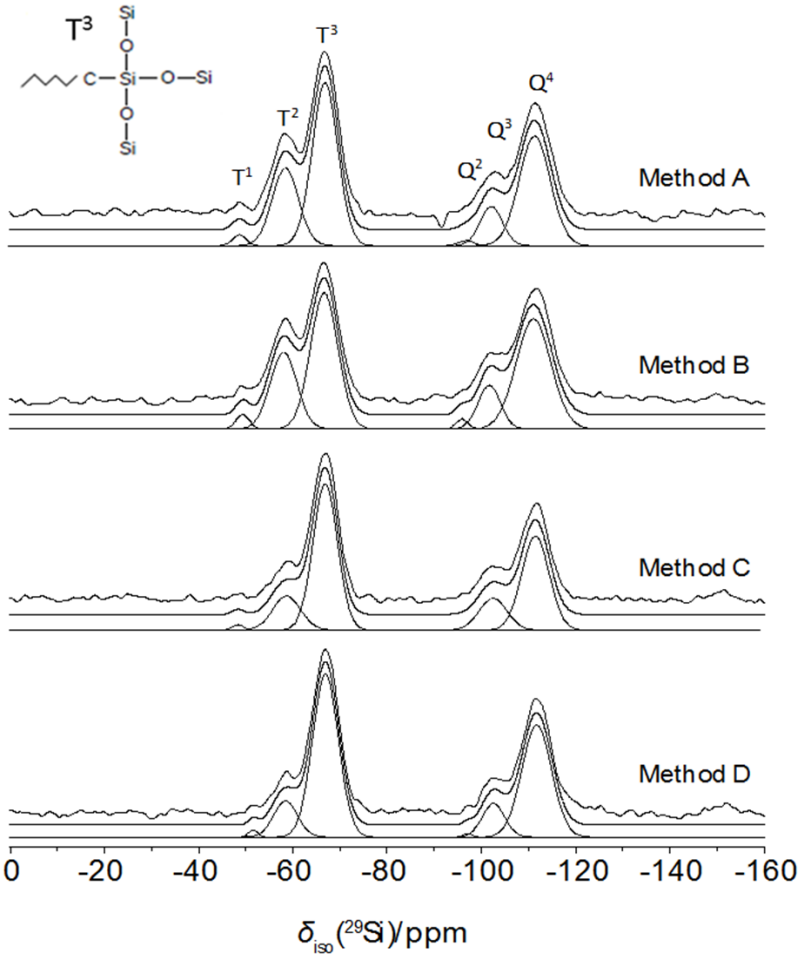

Figure 25. ^{29}Si MAS NMR spectra for Methods A, B, C, and D plus a schematic of the T^3 structure.

4.4 Summary

A method to 3D print silica-gelatin hybrids functionalised by GPTMS was developed. The reaction times and composition were tailored to avoid rapid gelation yet still produce a highly crosslinked and condensed material. To 3D print this gradually gelling material, the gelation period compatible with 3D printing was determined and printing parameters were defined.

The HF-free hybrid method was determined by observing the changes in bonding in FTIR spectra whilst varying the functionalisation time and aging conditions. The functionalisation time was selected to be 3 h as 14 h showed no improvement to the bonding. The aging time was chosen to be 7 days at 21°C due to the conditions being the most effective and compatible with the HF-free method.

Taking the HF-free hybrid method forward, the effect of C-factor on the degree of crosslinking of the hybrid material was investigated. The most efficient C-factor to crosslink the hybrid using the HF-free method was CF500. It resulted in maximum crosslinking to the 78G hybrid without being in excess.

The 3D printing parameters and composition compatibility studies were closely linked and conducted in parallel. To 3D print the hybrid, the condensation of the sol-gel network which caused crosslinking and hence gelation of the hybrid gel, had to reach a critical point in order for the material to hold its shape once printed. This gelation period where printing was possible was named the 'printing window' and was determined for various compositions, but to know when the hybrid was in this window, it was necessary to have some knowledge of how to 3D print the hybrid gel. The printing parameters were determined for the production of two types of scaffolds, one with a strut separation of 1 mm, and another with strut separation of 1.5 mm. 1 mm was found to be the minimum strut separation achievable due to the aqueous nature of the sol. A smaller separation lead to fusion of the struts during aging, and thinner struts could not be obtained by a lower deposition rate as it resulted in inconsistent flow. Smaller nozzles were also incompatible as the gels could not flow though. The limiting factor to the resolution of the 3D printed scaffolds was therefore the width of the gel deposited when extruded through the smallest compatible nozzle with the lowest compatible deposition rate.

The composition with the most convenient and efficient solution-aging time and printing window was 78G CF500 as determined by the composition compatibility study. It had a

solution-aging time of 8 h and printing window of 4 h which allowed hybrid production on day 1 and 3D printing on day 2. This counteracts the claim by Gao *et al.* that silica-gelatin hybrids functionalised by GPTMS were incompatible with 3D printing due to rapid gelation (Gao *et al.*, 2013b).

With the composition and method decided upon for 3D printing the silica-gelatin hybrid, the network condensation of the 78G CF500 scaffolds were compared to 78F CF500 foams using ^{29}Si MAS NMR. The overall degree of network condensation, D_c, of the 3D printed scaffolds was 90.4 %, just 3.8% less than the D_c when using the foaming method. As HF nor aging at 40°C were compatible with 3D printing, the only adjustable variable before 3D printing was the functionalisation time. When using the shorter functionalisation time selected for the HF-free method, 3 h, the results showed a slight increase in the degree of condensation compared to 14 h, in particular for the T species connectivity. This confirmed 3 h to be the right selection for functionalisation time.

CHAPTER 5. 3D PRINTED SCAFFOLD PERFORMANCE

5.1 Introduction

3D printing 78G CF500 silica-gelatin hybrid solutions has been proved possible through careful selection of the hybrid reaction parameters and composition as determined in the previous chapter. Here, different drying methods were investigated: freeze-drying and critical point drying, to assess the effect on materials properties and scaffold structure. The difference in properties led to a change in mechanical properties under compression and cell attachment.

Scaffold drying options

Freeze-drying (FD) was the initial method used to dry scaffolds as it was the drying method used by Mahony *et al.* to produce the silica-gelatin hybrid foams (Mahony and Jones, 2008). FD is a technique whereby the transition from liquid to gas is avoided when removing aqueous solvent from a material, however capillary stresses are experienced (Koebel, 2011). The material is frozen and by applying controlled temperature (-96°C) and pressure (0.13 mbar), the water present as ice is removed from the scaffold by sublimation.

The second drying method tested was critical point drying (CPD). CPD is a drying technique which eliminates capillary stresses by avoiding the effects of liquid surface tension (Weibel and Ober, 2003, Koebel, 2011).

To dry a gel using CPD, the sample solvent must be a pure ethanol. The drying method works by replacing the ethanol in the samples with liquid carbon dioxide and elevating the temperature (31.1°C) and pressure (1170 psi). At this critical point, the CO_2 liquid and vapour states are indistinguishable and in this super-critical state have the same density and surface tension. The liquid is then heated to convert the liquid to the gas phase without any distortion of the morphology.

Gelatin is typically non-compatible with this process due to precipitation in ethanol, however in a hybrid system with chemical crosslinks, shrinkage rather than precipitation was predicted due to reduced electric charge interactions between the gelatin and solvent.

Porcine gelatin Type A is a low density polyelectrolyte with a pH_{iso} between 7 and 9, arising from charged amino acids due to unequal distribution of carboxyl groups (negative charge) and amino groups (nitrogen containing bases, positive charge) along the gelatin chain. During synthesis, the pH is 4.4 and therefore lower than pH_{iso}, resulting in a polycation. In aqueous solvent, swelling of gelatin gels is observed. The polar solution is mobile within the gel

providing counter-ions and causing swelling. Ethanol however has a low dielectric constant compared to water, 24.3 Å versus 78.5 Å, so instead facilitates ion-pairing between complementary ions along the gelatin chains, causing shrinkage. As the concentration of ethanol in the solvent was increased during the solvent exchange, the hydrated gelation gel began to de-swell and hence shrinkage was observed (Boral *et al.*, 2006).

The hypothesis was that the 3D printed scaffolds dried by CPD would result in smaller channel widths, compared to FD scaffolds due to the large shrinkage effects caused by the solvent exchange required to perform CPD. As discussed in the previous chapter, the 3D printed scaffolds are limited to a strut separation of 1 mm, hence a large degree of shrinkage was required to achieve the channel width, 200-300 µm, desired for cartilage regeneration.

5.2 Methods

The 3D printed scaffolds required characterisation in various forms. Firstly the composition of CPD scaffolds was compared to that of FD scaffolds using TGA and DSC. The shrinkage of the overall scaffold was measured and skeletal density measurements taken to calculate the porosity. The degree of swelling of the scaffolds in TRIS was also measured to finalise the characterisation of the materials properties.

SEM and micro-CT imaging was used to assess the channel width, strut width and internal channels within the dried scaffold. The change in structure and materials properties induced by FD and CPD led to the comparative study of mechanical, dissolution and cell testing of the scaffolds.

The compressive strength of the scaffolds was determined to assess whether any of the scaffolds produced matched the compressive properties of cartilage. Dissolution studies measured the gelatin and silica release to give further insight into the hybrid structure on a molecular level, and a second dissolution study assessed whether a detrimental HCA layer would form on the scaffold surface.

Finally, various cell studies were performed by Dr Siwei Li on the FD and CPD scaffolds. Firstly the cytotoxicity of the dissolution products was analysed and the compatibility of preosteoblast and chondrogenic cell lines on the FD scaffolds printed with 1 mm pore channels were observed. Secondly, the effects of channel width and cell seeding density on cartilage matrix formation were investigated.

5.2.1 3D printed scaffold drying methods

The scaffolds were generated using the HF-free hybrid method and 3D printing parameters as described in the previous chapter in Figure 16 and Table 6. Scaffolds with 1 mm and 1.5 mm strut separation were produced. The hybrid composition used for all scaffolds was 78G CF500. This was the composition determined to be most compatible with 3D printing from the results of the crosslinking study and compatibility study in the previous chapter.

Freeze drying method

To FD the scaffolds, samples were first placed in the freezer overnight at -18°C, then in the freeze-dryer for 2 days at -96°C, pressure 0.13 mbar (Thermo Scientific Heto PowerDry LL1500).

Critical point drying method

To CPD the scaffolds, firstly, a solvent exchange was required to replace any water with ethanol. The water was replaced gradually by soaking the scaffolds in a water-ethanol co-solvent, starting with 10 % ethanol. After a minimum of 3 h, the solvent was replaced with a 20 % ethanol solvent and repeated with 10 % increments up to 100 % ethanol. After 3 h the solution was replaced with fresh 100 % ethanol and left overnight.

The CPD (Tousimis 931 Series, 2.5 in I.D Chamber) was used in Stasis Mode, which means the samples were held in the chamber with liquid CO_2 for an increased amount of time to ensure all ethanol was removed before drying. The time of the stasis cycle was chosen to be 8 h after consultation with Tousimis advisors. The stages of the CPD drying method are shown in Figure 26: slow fill of 1.5 minutes, fill of 2.5 minutes, purge of 10 minutes and stasis of 8 h. 'Cool' refers to the chamber temperature, 'fill' refers to the introduction of liquid CO_2 into the chamber, 'purge' is the removal of the alcohol-LCO_2 mixture and replacement of pure LCO_2. At this point the CPD enters stasis mode and after 8 h the earlier processes are repeated. The critical point is achieved during 'heat', where the chamber warms to the critical point and maintains a critical temperature and pressure of 31°C and 1072 psi/173.9 bar for 2 minutes. After this, the chamber was decompressed during 'bleed' and 'vent'.

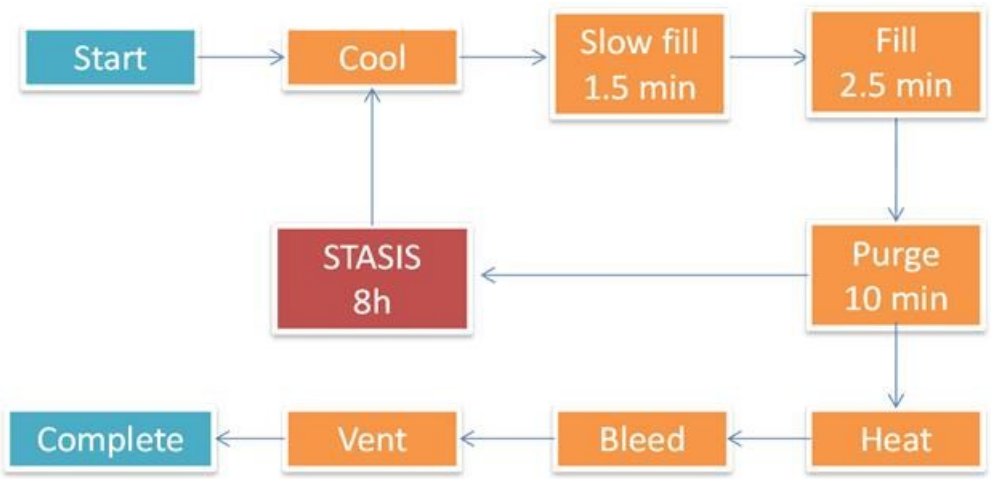

Figure 26. Schematic of CPD stages including stasis mode.

5.2.2 Structure of dried scaffolds

The shrinkage effects, materials properties and structure induced by FD and CPD were compared here. Scaffolds printed with 1 mm and 1.5 mm strut separation were dried using FD or CPD after 1 week of scaffold-aging.

Firstly, the organic contents of the CPD and FD scaffolds were measured using TGA and DSC analysis to ensure the ratio of inorganic to organic was not affected by the solvent exchange in ethanol. To analyse the materials, TGA and DSC were performed using a Netzsch STA 449C under the following conditions: 21°C to 800°C, ramp rate of 10 K min^{-1}, air flow rate 50 mL min^{-1}, in an alumina crucible (n=3).

The shrinkage induced by the FD and CPD process was calculated by measuring scaffold dimensions using digital calipers (+/- 0.01 mm) (n > 7) at the following stages: after aging of the 3D printed scaffold; after solvent exchange; after drying.

To assess the strut and channel structure of the dried scaffolds, the porosity of the scaffolds, φ, was calculated using skeletal density values obtained by helium pycnometry (Quantachrome Ultrapycnometer, n = 20). To ensure results were stable, a control sample of known volume was measured before and after sample analysis (n > 7). Porosity was calculated according to Equation 13, where ρ_t is the total scaffold density and ρ_s is the skeletal density.

$$\textbf{Equation 13:} \quad \textbf{Porosity}, \Phi = \left(1 - \frac{\rho_t}{\rho_s}\right) \times 100$$

The porosity is calculated from the division of ρ_t by ρ_s, which is effectively the division of the skeletal volume by total volume, as they use the same mass. This gives the vol% occupied by the hybrid material in the porous scaffold. The porosity is defined as the vol% not occupied by material, i.e. the volume of pores.

A swelling study in TRIS was performed on FD and CPD scaffolds printed with 1 mm strut separation to assess the effect of drying method on water uptake. Each scaffold was immersed in 5 ml of TRIS for 24 h (n = 6), the scaffold dimensions were measured using digital calipers (+/- 0.01 mm) before and after immersion.

To measure the strut and channel width of the scaffolds, 2D images were obtained using SEM. To prepare the scaffold samples for SEM, scaffolds were cut parallel (x,y cross section) and perpendicular (z,y cross section) to 3D printed layers, and attached to a metal SEM stub using carbon tape. As the scaffolds are non-conductive, silver paint was used as a contact from the base to the surface and scaffolds were coated in chromium to allow a voltage to be applied

across the surface. This is done using a sputter coater (Quorum, Q150T) set to a 5 nm coating. Secondary electron imaging was achieved using a JEOL JSM 6010 SEM in normal scanning mode with an accelerating voltage of 20 kV, working distance of 19 cm, spot size of 50 and x50 magnification. To measure channel width and strut width, x30 magnification images were analysed using ImageJ software (n = 30 horizontal measurements).

High resolution FEGSEM images were taken to compare the difference in surface texture. The samples were prepared as described above for SEM, however the Zeiss Auriga Cross Beam SEM was used. The FEGSEM was used InLens with an accelerating voltage of 5 kV, working distance of 5.4 mm.

3D reconstructions of the scaffolds were generated from micro-CT tomographs to compare the structures formed by FD and CPD drying methods. The Diamond Manchester Imaging Branchline I13 was under the conditions of 0.1° intervals, 1 s exposure, 12 keV beam energy. The tomographs obtained were then layered and rendered using Avizo software to generate the 3D reconstructions of the scaffolds and the internal pores.

5.2.3 Dissolution characteristics

Dissolution testing was performed in both SBF and TRIS over a one-month period. The SBF test was a preliminary experiment to assess HCA formation on the surface of the silica-gelatin hybrid FD scaffolds. The dissolution study in TRIS assessed the silica and gelatin release of both FD and CPD 78G CF500 scaffolds produced by 3D printing with 1 mm strut separation.

Dissolution

150 mg of dried scaffold was immersed in 100 mL of solution (SBF or TRIS) and stored in an incubator shaker for the duration of the study (n = 3). Time points were performed at the following hours: 0, 1, 2, 4, 8, 24, 48, 72, 168 (1 week), 336 (2 weeks), 504 (3 weeks), 672 (4 weeks). At the 12 given time points, the pH was measured and solution was removed for inductively coupled plasma optical emission spectroscopy (ICP) and gelatin detection by BCA assay. The removed solution was replenished with fresh solution.

ICP samples were examined at the end of the dissolution study whereas BCA was done immediately after the time point.

The ICP used was a Thermo Scientific iCAP 6300 Duo inductively coupled plasma optical spectrometer (ICP-AES) with an auto sampler (ASX-520) (n = 3). To prepare the samples, 1 mL of solution was removed and added to 9 mL of 1 M HNO_3 at each time point. Before ICP analysis, the solutions were filtered using a Minisat 0.2 µm syringe filter (Satorius stedim biotech, Germany) to remove gelatin from the solutions as polymers are not compatible with ICP analysis. When using SBF, phosphorous and calcium ion concentrations were measured. When using TRIS, only silicon was measured. Standards were prepared for the relevant ions: 0, 2, 5, 20, 40 µg mL^{-1}, used for the calibration curve which was measured at the beginning of each sequence.

For the BCA assay (Pierce BCA Protein Assay kit) in the TRIS study, 25 µl aliquots (n = 3) were placed into 96-well plates for each sample. 200 µl of working reagent (bicinchoninic acid) was added to each well and shaken for 30 s. The microplate was then incubated for 4 h before reading the absorption values at 562 nm using a microplate reader (SpectraMax M5). The assay was less sensitive to gelatin than to the protein it is designed to work with, albumin, so to lower the minimum detection range of the assay the microplate incubation time was increased to 4 h. BCA standards: 0, 2.5, 5, 26, 62.5, 125, 250 µg ml^{-1}, were produced using 1mg mL^{-1} gelatin solution and measured alongside each time point.

Post dissolution analysis

To complete the dissolution study in SBF, XRD was performed on the FD scaffolds after the 4 week study. Samples were rinsed 3x in DI water and dried in a 40°C oven overnight before grinding to a powder for XRD analysis. The diffraction was measured with a PANalytical X'Pert Pro MPD XRD between 5° and 80° 2θ, with a 0.03° step size and a total counting time of 15 minutes.

5.2.4 Compressive strength

The compressive strength of FD scaffolds (700 µm channels) were compared whilst dry and wet, after 1 week soaking in TRIS. CPD scaffolds (200 µm channels) were only tested wet. The scaffolds were filed into cubes with equal height and width before testing. When testing wet scaffolds, the filing was done before immersion into TRIS. The diameters and height of the samples were measured before compressive testing began in order to calculate the stress and strain values. The compression testing unit used was a Bose ElectroForce® 3200 Series III Extended Stroke. It was used with a 440 N load cell and compression rate of 0.5 mm min^{-1}. The scaffold was placed between the testing plates and the compression extension value zeroed on contact with the scaffold. In each sample set, 8 scaffolds were tested.

To probe the failure mechanism of the scaffolds, micro-CT was used to image a FD scaffold (700 µm channels) under increasing compressive stress: 0 MPa, 0.56 MPa, 0.71 MPa and 0.76 MPa applied by the P2P rig. The set-up is shown in Figure 27. The scaffold was held under static load whilst being scanned after a relaxation time of 20 minutes. The Diamond Manchester Imaging Branchline I13 was used to collect the micro-CT data. Parameters were 0.1° interval, 1 s exposure, 12 keV beam energy.

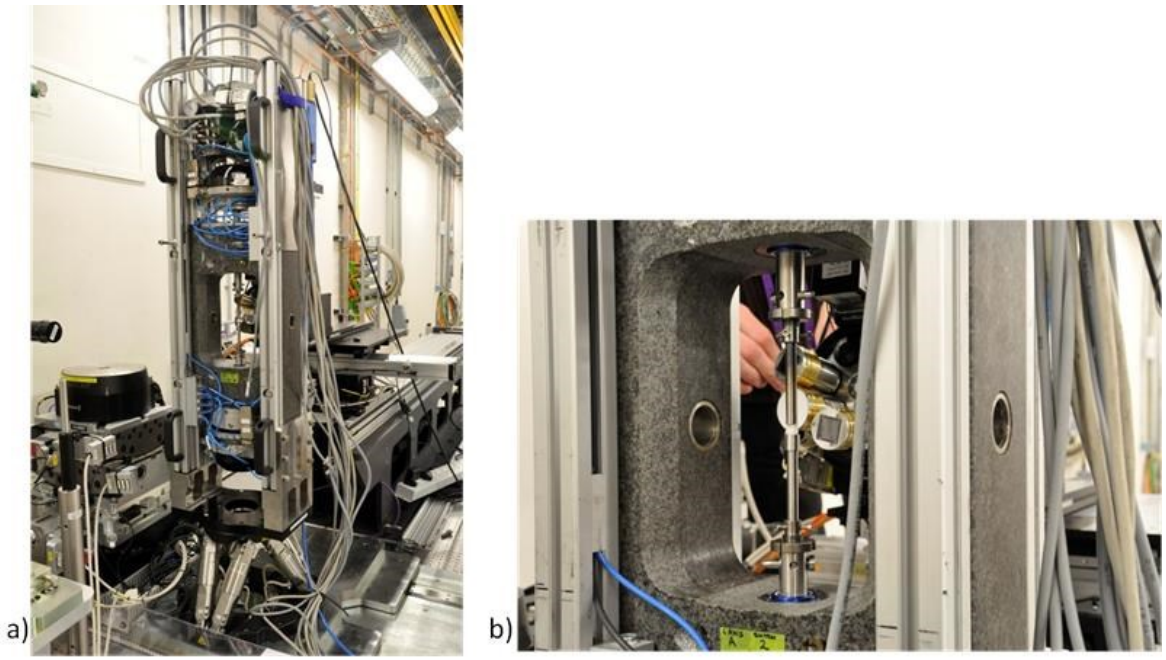

Figure 27. Diamond beamline compression testing rig. Images demonstate a) the P2P rig and b) the scaffold placed within the compression unit.

5.2.5 Cell Interactions

Cell work was performed by Dr Siwei Li on silica-gelatin hybrid 3D printed scaffolds with composition 78G CF500. All cell culture reagents were obtained from Invitrogen and Sigma-Aldrich UK unless specified otherwise. ATDC5 murine chondrogenic cell line (ATCC, UK) was culture expanded in basal DMEM supplemented with 5 % (v/v) FCS (foetal calf serum), 100 unit mL^{-1} penicillin, 100 µg mL^{-1} streptomycin and 1× ITS liquid supplement (10 µg mL^{-1} insulin, 5.5 µg mL^{-1} transferrin and 5 ng mL^{-1} selenite premix). Pre-osteoblast cell line MCT3T3 cells were culture expanded in basal α-MEM supplemented with 10 % (v/v) FCS, 100 unit mL^{-1} penicillin and 100 µg mL^{-1} streptomycin. Cultures were maintained in humidified atmosphere at 37°C, 5 % CO_2 and 21 % O_2. Upon confluence, cells were passaged using 500 µg mL^{-1} trypsin-EDTA (ethylene diamine tetra-acetic acid).

Cell viability

To begin, the *in vitro* cytotoxicity of the material was examined by assessing the metabolic activity of ATDC5 and MCT3T3 cells after exposure to the dissolution products of the 78G CF500 scaffolds, in accordance to ISO 10993-5 and ISO 10993-12 (Standardization, 2009). Dissolution products released by the powder form of the 78G CF500 scaffolds (0.2 g mL^{-1} in DMEM and α-MEM at 37°C) over a 72 h period were prepared. Medical grade polyethylene (PE) was used as non-cytotoxic negative control and polyurethane (PU) containing 0.1 % (w/w) zinc diethyldithiocarbamate (ZDEC) was used as positive control, which induces reproducible cytotoxic response. The dissolution products were filter sterilised and dilution series (25 %, 50 %, 75 % and 100 %) were prepared and supplemented with 10 % (v/v) FCS prior to use in cell viability assays.

Cell viability was assessed by a calorimetric cell metabolic activity assay based on the conversion of 3-(4,5-dimethylthiazol-2-yl)-2,5-diphenyltetrazolium bromide (MTT) into formazan. The cells were seeded at 1×10^4 cells per well on 96-well plates and left to grow in respective basal media for 24 h until a sub-confluent monolayer was formed. The culture media was removed and cells were then incubated with fresh basal media, dissolution products of 78G CF500 scaffolds or controls for a further 24 h. The culture media was removed and MTT diluted in serum-free media at a concentration of 1 mg mL^{-1} was added. Following an incubation period of 2 h, the MTT solution was removed and each well was filled with 100 µL DMSO and shaken briefly to dissolve the formazan derivatives. The optical density was measured spectrophotometrically at 570 nm using a microplate reader (SpectraMax M5).

Cell attachment

A 3-day cell attachment study was performed using the two cell lines: ATDC5 and MCT3T3, on the FD 700 µm channel scaffolds. The cells were stained for cytoskeletal protein actin, vimentin and nuclei. The abundance of these dictated how well attached the cells were to the surface and their likelihood of proliferation and survival.

For cell attachment studies, 78G CF500 3D printed scaffolds (approximately 5×5×2 mm^3) were sterilised with 70 % ethanol for 1 minute. Following washing with a copious amount of PBS, each sample was preconditioned for 30 minutes in respective serum-free media for each cell type in humidified atmosphere at 37°C, 5 % CO_2 and 21 % O_2. Each sample was transferred to a sterile 50 mL centrifuge tube fitted with a filter cap.

Cells were harvested and suspended in basal media. 5 mL of cell suspension containing 3×10^6 cells was added to each centrifuge tube containing the 78G CF500 scaffold and incubated in a humidified atmosphere at 37°C, 5 % CO_2 and 21 % O_2 for 2 h, with gentle agitation every 30 minutes to allow for diffusion and well-distributed cell adhesion. Cell-seeded scaffolds were collected on day 3 and analysed for cell attachment by immunohistochemistry staining and confocal microscopy.

Cartilaginous matrix formation

The results of mechanical testing and the cell attachment study indicated the scaffolds to be more suitable for cartilage regeneration. Therefore, a 28 day cartilaginous matrix formation study of ATDC5 cells was performed on scaffolds with 200 µm (CPD) and 700 µm (FD) channel width to assess how channel width and cell seeding density affected the cell and matrix distribution throughout the scaffold.

For cartilaginous matrix formation, the 3×10^6 or 10×10^6 (for 700 µm channel width scaffolds) cells were seeded as described above. On day 3, basal DMEM was replaced by chondrogenic media and cultured for further 21 days with media change every 3-4 days. The chondrogenic media was made up of DMEM supplemented with 10 ng mL^{-1} rhTGF-β3 (100-36E, PeproTech, UK), 100 µM (28.95 µg mL^{-1}) L- Ascorbic acid 2-phosphate, 10 nM (3.92 ng mL^{-1}) dexamethasone and 1× ITS liquid supplement, a modification of the media described in previous studies (Mackay *et al.*, 1998). After 28 days, the seeded scaffolds were analysed by immunohistochemistry staining and confocal microscopy.

Evaluating cell behaviour

Immunohistochemistry staining

Cell-seeded constructs were fixed with 4 % paraformaldehyde (PFA) and used for immunohistochemical analysis of cell attachment and cartilaginous matrix formation. Following permeabilisation with buffered 0.5 % Triton X-100 in PBS (300 mM sucrose, 50 mM NaCl, 3 mM $MgCl_2$, 20 mM Hepes and pH 7.2) and blocking with 10 mg mL^{-1} BSA in PBS, samples were incubated with relevant primary antiserum at 4°C overnight. This was followed by hour-long incubation with Alexa Fluor® 488-conjugated secondary antibody. Negative controls (omission of the primary antisera) were performed in all immunohistochemistry procedures. No staining was observed in the samples used as negative controls.

Cytoskeletal marker anti-Vimentin antibody (rabbit polyclonal, IgG, Abcam, Cambridge, UK) was used at a dilution of 1:500 dilution in 10 mg mL^{-1} BSA. Chondrogenic differentiation and cartilaginous matrix markers, anti- Sox9, aggrecan, collagen Type II, collagen Type I and collagen Type X antibodies were used at dilutions of 1:150, 1:500, 1:500, 1:1000 and 1:100 respectively in 10 mg mL^{-1} BSA.

F-actin was labelled using CytoPainter F-actin staining kit (Abcam, Cambridge, UK) following the manufacture's instruction. Briefly, Alexa Fluor® 568-conjugated phalloidin (1:1000 dilution in labelling buffer) was added simultaneously with the secondary antibody during the incubation period. All samples were counter-stained with DAPI (0.1 µg mL^{-1} in PBS).

Confocal microscopy

The samples were imaged under confocal microscopy (Leica SP5 MP laser scanning confocal microscope and software, Leica Microsystems, Wetzlar, Germany).

5.3 Results and discussion

To characterise the 3D printed scaffolds, firstly the effects of freeze drying and critical point drying on the inherent materials properties and scaffold structure were measured.

The scaffolds now characterised by their channel width and drying method, were tested under compressive loads and the failure mechanism analysed. Dissolution testing and cell studies were performed to assess the compatibility of the scaffolds *in vitro*.

5.3.1 Dried 3D printed scaffolds

Once a method had been established for 3D printing the silica-gelatin hybrid, FD and CPD were used to dry the scaffolds. As the smallest strut spacing that could be achieved by 3D printing was 1 mm, the aim was to utilise uniform shrinkage induced by the drying method to create scaffolds with the desired channel width of 200-300 µm. Due to the solvent exchange stage required for CPD, CPD was expected to result in smaller scaffolds compared to FD. This was achieved as shown below in Figure 28.

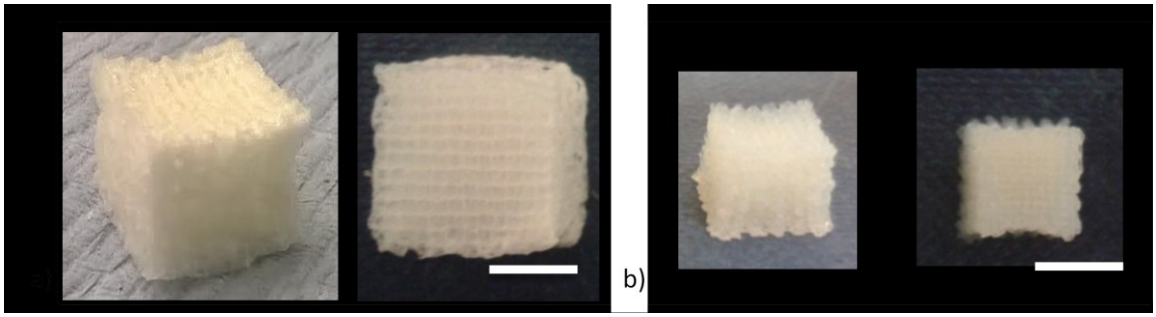

Figure 28. Photo of 3D printed 78G CF500 scaffolds printed with 1 mm strut separation dried by a) freeze drying and b) critical point drying. The scaffolds are imaged from the side and from above to show the difference in size of the scaffolds after drying. Scale bar 0.5 cm.

Thermal analysis

As gelatin is known to precipitate in ethanol, compositional analysis was performed to ensure gelatin was not lost from the hybrid system during the required solvent exchange stage of CPD. TGA and DSC were used to compare the silica-gelatin composition of the 78G CF500 scaffolds dried by FD and CPD in Figure 29. For CPD scaffolds, the remaining mass after heating to 750°C was 27 % versus 28 % for FD which corresponded to the remaining inorganic.

The TGA curve of the functionalised gelatin samples showed initial mass loss of solvent and unreacted components before 250°C. Above this temperature, there were two stages of mass loss. A sharp loss of mass at 340°C is attributed to the thermal degradation of GPTMS organic chains. Here, the mass loss was not steep as GPTMS chains were bonded to the gelatin. The shallow peak at ~370°C was attributed to the helical structure breakage and degradation of proteins, predominantly proline (Correia *et al.*, 2013, Cesario *et al.*, 2011, Ren *et al.*, 2010). At 620°C, a second peak was seen in the DSC which corresponded to the oxidation of glycine, the smallest amino acid, which completed the thermal decomposition of the organic component of the hybrid (Cesario *et al.*, 2011).

By removing the mass loss due to solvent, the organic:inorganic ratio for CPD and FD scaffolds were 72:28 and 70:30. The very similar plots and organic:inorganic ratio indicated that little of the gelatin content was lost during solvent exchange of CPD compared to FD, however a small amount of silica appears to be lost, potentially due to the 24 h soaking in ethanol.

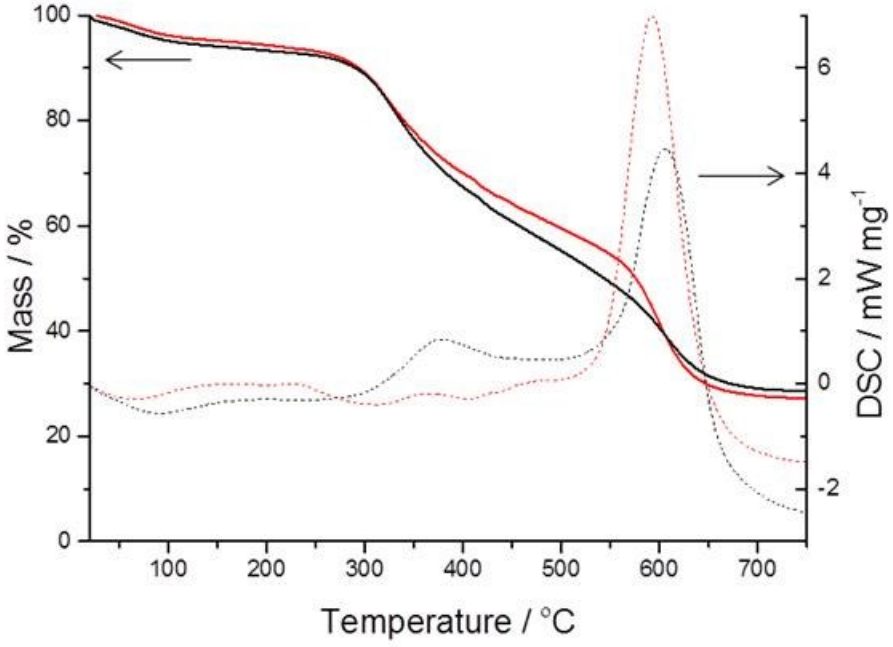

Figure 29. TGA and DSC analysis comparing 78G CF500 scaffolds dried via FD (black lines) and CPD (red lines).

Shrinkage and porosity

FD and CPD induced different amounts of shrinkage to the scaffolds as evident from the photographs in Figure 28. Table 8 summarises the shrinkage and porosity of the scaffolds printed with 1 mm strut separation.

Both drying methods induced shrinkage. To dry scaffolds using CPD, the replacement of water with ethanol induced additional shrinkage to the gelatin-based gel as the reduced dielectric constant of ethanol encouraged ion-pairing between gelatin molecules. As a result, 52 ± 3 % shrinkage occurred as the number of counter-ions in the solvent was reduced. After the drying process, the volume reduced by a further 57 ± 3 % for CPD scaffolds, to a total of 80 ± 1 % shrinkage. FD scaffolds incurred 42 % shrinkage due to capillary stresses. In total, the shrinkage for CPD scaffolds was approximately double the shrinkage of the FD scaffolds.

Despite the large decrease in overall volume of CPD scaffolds, the skeletal density increased only slightly, from 1.5 g cc^{-1} (FD) to 1.7 g cc^{-1} (CPD). To understand this, the shrinkage of the

individual struts must be considered as seen in Figure 31 and Figure 32 and measured in Table 9. Despite the reduced shrinkage of the FD scaffolds overall, the FD struts were an order of magnitude smaller than the CPD struts and overall volume was maintained by the larger channel width. Therefore, the FD and CPD drying methods had little effect on skeletal density but strongly effected channel width.

The skeletal density was used to calculate porosity using Equation 13. The porosity was 88 % and 72 % for FD and CPD scaffolds respectively. Both are comparable to the porosity of cancellous bone, the typical benchmark for tissue scaffolds (Renders *et al.*, 2007).

Table 8. Summary of shrinkage, skeletal density and porosity of FD and CPD scaffolds printed with 1 mm strut separation.

Drying Method	Shrinkage after solvent exchange /%	Shrinkage after drying /%	ρ_s, Skeletal density /g cc^{-1}	φ, Porosity /%
FD	-	42 ± 0	1.5	88 ± 1
CPD	52 ± 3	80 ± 1	1.7	72 ± 0

Channels and Struts

Scaffolds printed with a strut separation of 1.5 mm were achieved first and the preliminary SEM images of these FD scaffolds, an example of which is shown in Figure 30, indicated channels in all 3 directions, X, Y and Z.

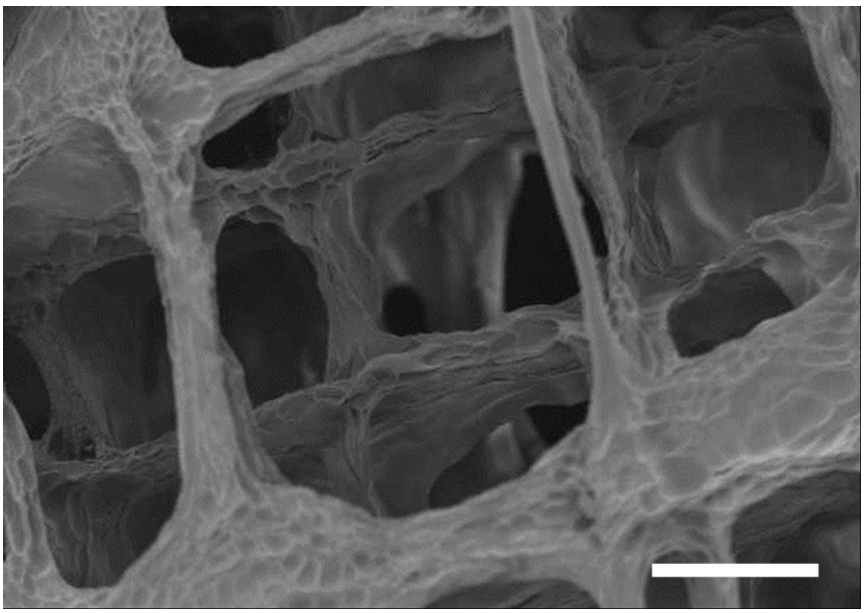

Figure 30. SEM of preliminary 3D printed 78G CF500 FD scaffolds with 15° tilt along Z axis, 20 kV. Scale bar is 500 µm.

Later results showed a different structure of the scaffolds printed with the same parameters. The SEM images of 1.5 mm and 1 mm strut separation scaffolds in Figure 31 and Figure 32 respectively, show direct, vertical channels in the XY cross section, and reduced interconnects in ZY directions due to collapse of struts which fused with the layer below to form an almost solid wall. The structure was seen for all further scaffolds regardless of drying method or strut separation.

In both Figure 31 and Figure 32, images a and c of the XY cross section show direct channels in the Z direction, however images b and d show solid walls rather than open channels in the X and Y directions. The printing parameters had not changed, however initial results were obtained in the winter months while the majority of the scaffolds produced in the summer months. Between these seasons there was an approximately 5°C temperature increase in the lab so the collapse of layered struts to form the scaffold walls may have been due to the increase in ambient temperature.

Despite the reduced interconnectivity in the X and Y directions, the walls now present in the scaffolds had potential to improve compressive strength. The very open channels in the Z direction potentially allow for faster migration of cells and nutrients compared to foamed structures and although the number of interconnects across the walls is small, they are large compared to the size of chondrocytes which are ~20 μm in diameter.

The CPD scaffolds had a more similar morphological appearance to the 3D printed scaffolds by Gao *et al.* (Gao *et al.*, 2013b) than the FD scaffolds, as cylindrical struts were retained during CPD, despite being fused. The post-printing crosslinking treatment used by Gao *et al.* had similarities to the CPD process. To crosslink the scaffolds, they were immersed in 95 % ethanol for 12 h followed by vacuum drying which would have had similar effects on the scaffold as the solvent exchange followed by CPD method used here.

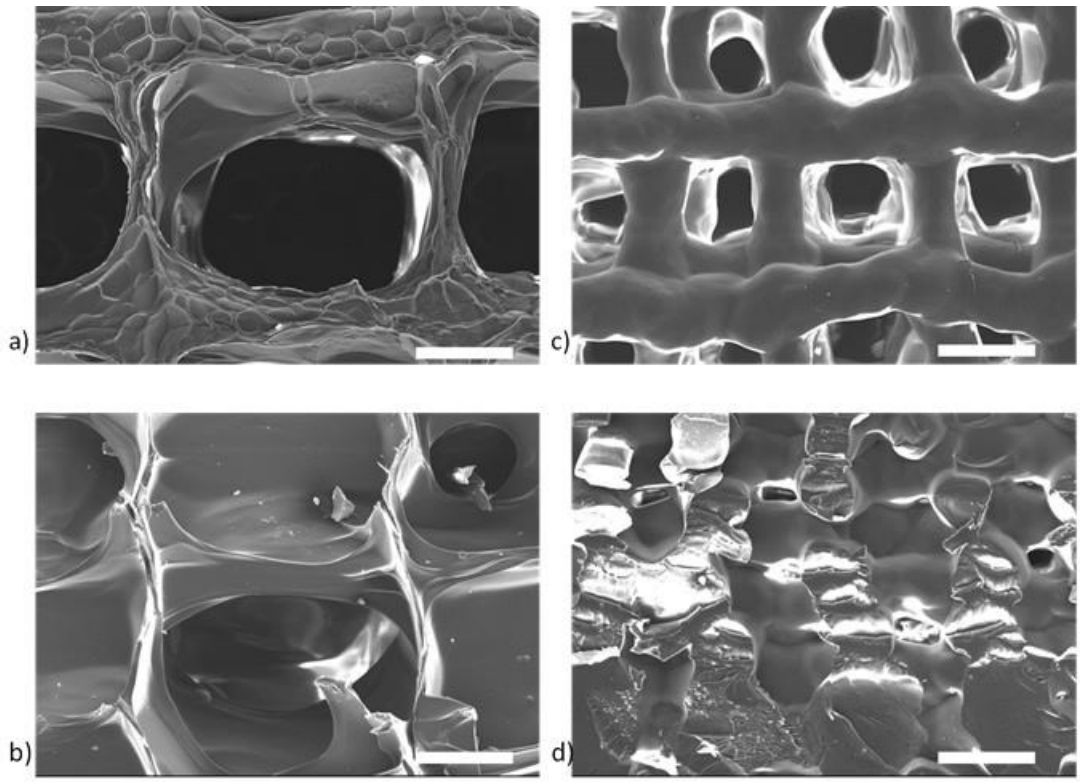

Figure 31. SEM images a,b) FD and c,d) CPD 78G CF500 scaffolds printed with 1.5 mm printed strut separation, 20 kV. Images show a,c) XY cross section and b,d) ZY cross section. Scale bar is 500 µm.

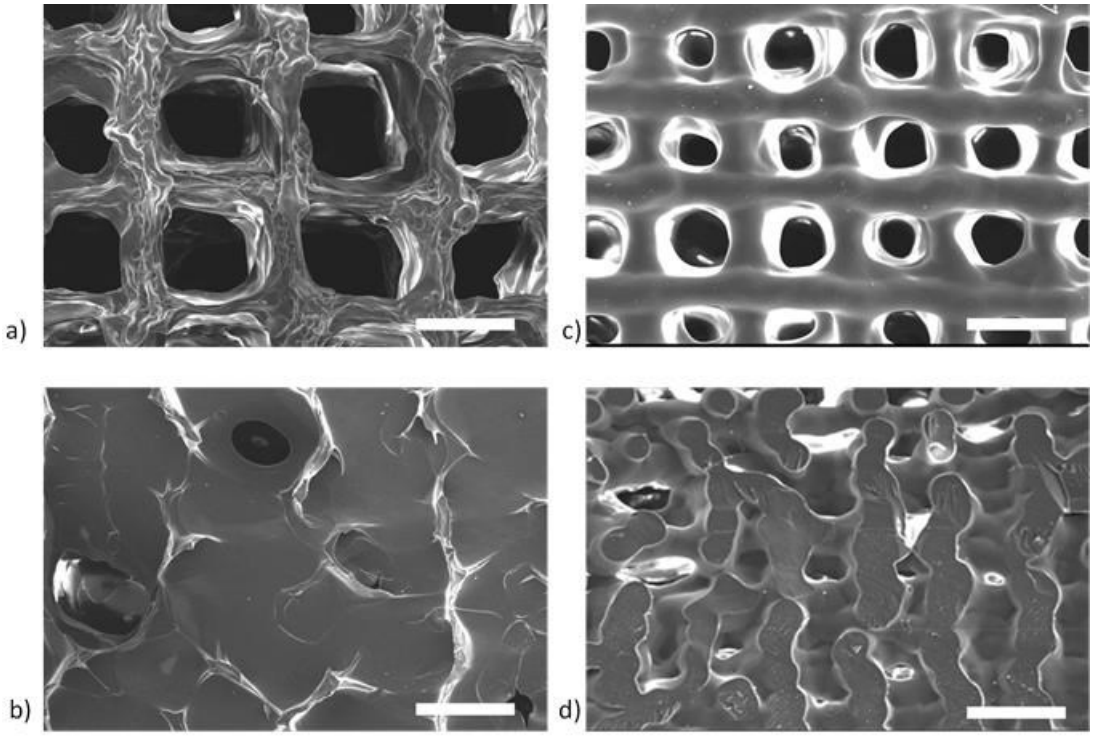

Figure 32. SEM images a,b) FD and c,d) CPD 78G CF500 scaffolds printed with 1 mm printed strut separation, 20 kV. Images show a,c) XY cross section and b,d) ZY cross section. Scale bar is 500 µm.

To obtain a clear picture of the internal structure of the scaffolds, micro-CT images were reconstructed, as shown in Figure 33. Images a, b and c show the FD scaffolds viewed in three orientations: YZ, XY, XZ. Images d and e show the CPD scaffolds in two orientations, YZ and XY. The third orientation, XZ looked similar to YZ. Due to the small pore width compared to strut width of the CPD scaffolds, interconnectivity and channels were not clear so 3D renders of the pores (with the scaffold material removed) were also generated as seen in images f and g.

The most prominent difference between these images and SEM are that channels in the Z axis are not direct channels. There is only one set of walls formed by fused struts within the bulk of the scaffolds.

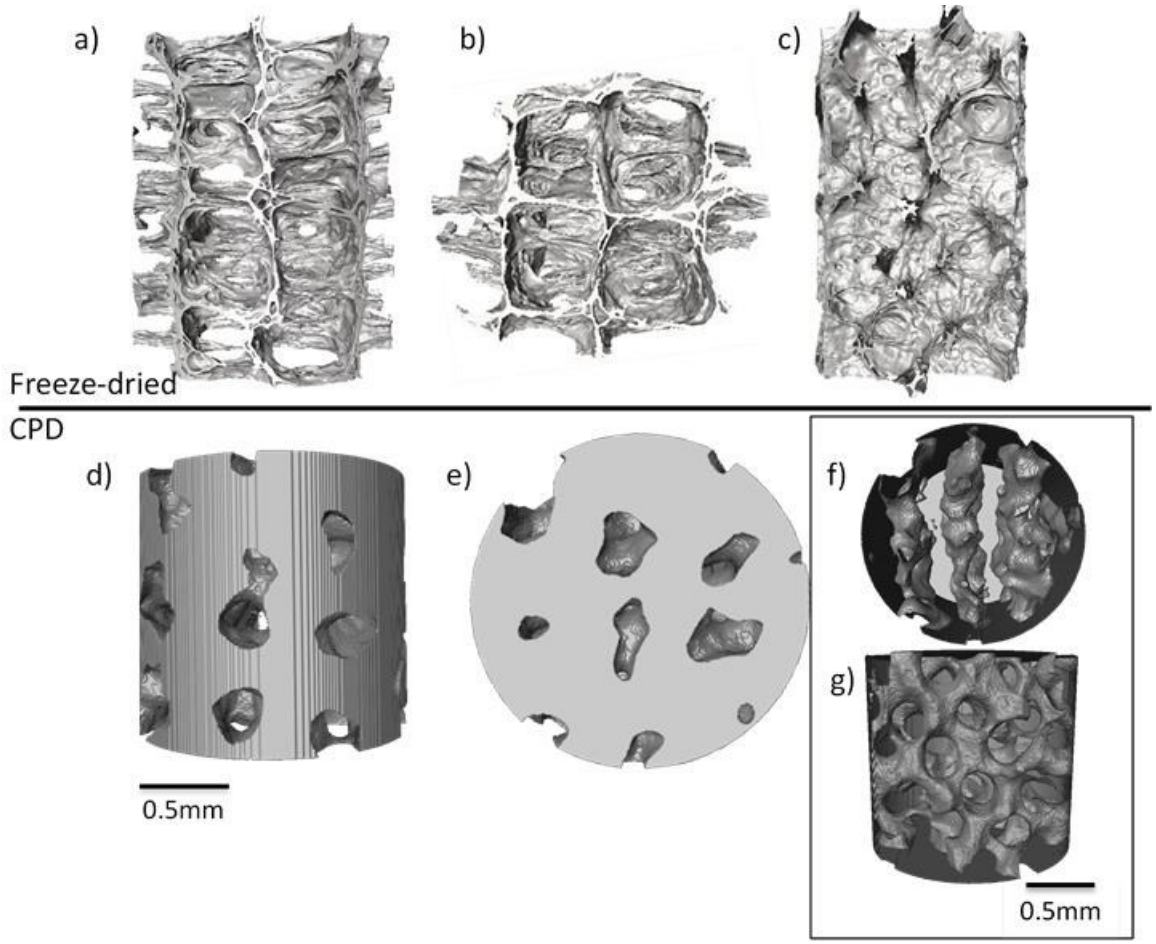

Figure 33. 3D reconstructions of FD scaffolds (a,b,c) and CPD scaffolds (d,e) and the pore channels within the CPD scaffolds (f,g). The images are of scaffolds are viewed in the a,d) YZ, b,e,f) XY and c,g) XZ plane (micro-CT, Diamond Light Source) (Figures d,e,f,g courtesy of Xiaomeng Shi).

In the X-direction as defined by Figure 33, the struts had merged resulting in dense walls, clearly seen in the FD scaffolds (Figure 33c) and inferred from the lack of porosity in one plane for the CPD scaffolds (Figure 33f). Perpendicular to these dense walls, Y-direction, the struts

were not aligned and therefore the dense walls did not form after aging and drying. The individual struts were seen in all the FD micro-CT images and can be visualised from the porosity of the CPD scaffolds in Figure 33g.

My prediction is that the shift in struts occurred after printing rather than during as the struts appear misaligned in the micro-CT images but aligned in SEM. There is a chance the struts shifted during scaffold-aging to accommodate the weight of the struts above resulting in this structure and therefore the porosity and channels changed depending on the location within the printed scaffold and the loads experienced locally during aging. This was not ideal in terms of mechanical properties as it was expected to induce variation to a scaffold generation method that was hoped to minimise variation, however, the dense walls had potential to improve compressive strength.

Channel width and strut width

The mean channel and pore width were measured from ZY cross section SEM images using Image J software and summarised in Table 9.

The channel width of CPD scaffolds printed with 1 mm strut separation had a mean value of 210 ± 53 µm whereas FD scaffolds had a mean channel width of 682 ± 92 µm. The 1 mm strut separation CPD scaffolds had a channel width 69 % smaller than the FD scaffolds. Similarly for the 1.5 mm printed strut separation scaffolds, the CPD channels were 74 % smaller than the FD scaffolds. The values were 319 ± 80 µm for CPD channels rather than 1229 ± 124 µm for FD channels. The increase in channel width of the CPD scaffolds correlated to the increase in strut separation from 3D printed strut separation, 1 mm to 1.5 mm (50 % increase) as the channel width increased by 52% for CPD scaffolds whereas FD scaffold channels increased by 81 %.

The FD scaffold struts/wall thickness was difficult to measure accurately using the Image J software, however in both cases the thickness was below 40 µm due to the shrinkage and distortion caused by the freeze drying method (Eisenback, 1986). The CPD scaffolds had rounded, distinguishable struts despite fusion with the upper and lower layers. The strut widths were measured horizontally to avoid any increase in size due to fusion, and 162 ± 27 µm and 299 ± 41 µm strut widths were measured for 1 mm and 1.5 mm strut separation scaffolds respectively. The mean strut width for 1 mm strut separation scaffolds was 54 % the strut width of the 1.5 mm strut separation scaffolds. This increase in strut width was due to the increased deposition rate and slower print speed used to print the 1.5 mm strut separation scaffolds as opposed to 1 mm scaffolds.

To simplify the scaffold descriptions going forward, the scaffolds 3D printed with 1 mm strut separation will be referred to as FD 700 µm, and CPD 200 µm. The scaffolds 3D printed with 1.5 mm strut separation will be referred to as FD 1200 µm, and CPD 300 µm, where the number in microns represents the approximate channel width of the scaffold.

Table 9. The mean pore width for FD and CPD scaffolds with 1 mm and 1.5 mm printed strut separation. Errors represent the standard deviation of the set of measurements (n > 20).

Printed strut separation /mm	Scaffold drying method	Mean channel width /µm	Mean strut width /µm	Scaffold identity
1	FD	682 ± 92	<40	FD700
1	CPD	210 ± 53	162 ± 27	CPD200
1.5	FD	1229 ± 124	<40	FD1200
1.5	CPD	319 ± 80	299 ± 41	CPD300

Overall, the channel width and pore width measurements indicated the gelatin-hybrid 3D printed scaffolds to be considerably more compatible with CPD than FD, as the structure can be more accurately controlled despite the shrinkage induced by solvent exchange. Compared to silica-gelatin hybrids printed by Gao *et al.*, the strut and channel widths here are similar; Gao *et al.* 3D printed scaffolds with ~350 µm strut width and ~550 µm channel width.

Surface texture

Overall, the surface texture of the CPD scaffolds appeared much smoother than the surface of the FD scaffolds which appeared shrivelled. This is seen in images a and c, in both Figure 31 and Figure 32. The shrivelled appearance of FD scaffolds is due to the sublimation of the ice crystals and is known to produce distortion in samples (Eisenback, 1986). The CPD scaffolds appear smooth as the effects of surface tension are avoided during the drying stage.

To further probe the surface of the scaffolds dried by both FD and CPD, higher magnification images were taken and presented in Figure 34. The CPD scaffold surface showed spherical nanoparticles embedded within a polymeric matrix. The formation of spherical sol-gel nanoparticles is characteristic of sol-gel derived mesoporous silica (Lin *et al.*, 2009) and the formation of spherical sol-gel nanoparticles embedded with a polymeric matrix as previously seen by Mahony *et al.* in ground silica-gelatin samples (Mahony, 2010). The mechanism for gelation is the same in the hybrids as for sol-gel derived mesoporous silica, however in hybrids, the polymeric matrix of GPTMS functionalised gelatin embeds and chemically binds to the particles. The FD scaffold had a smooth, uncharacteristic surface, however the image captured

shows an area damaged by over exposure of the beam and directly beneath the surface, the typical sol-gel hybrid texture was visible.

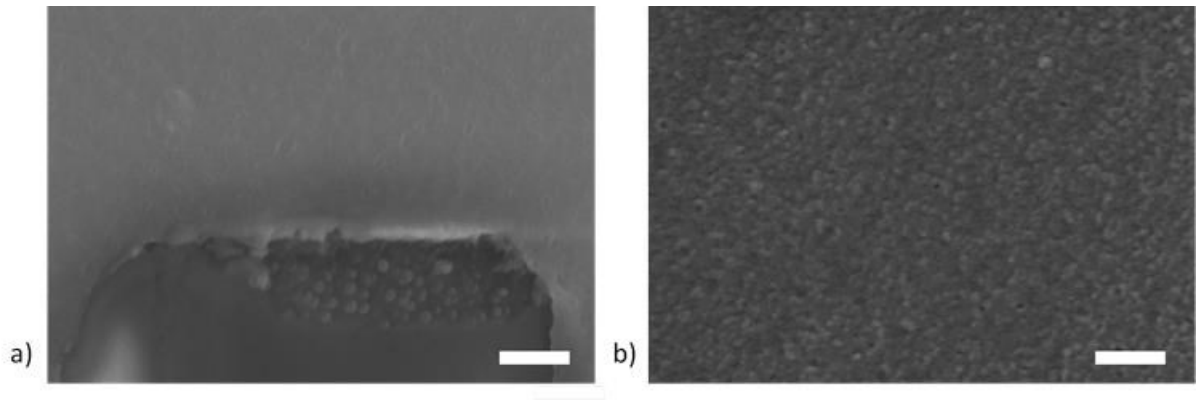

Figure 34. SEM inLens images of 78G CF500 scaffolds a) electron beam damaged FD scaffold surface and b) CPD scaffold surface. Scale bar is 400 nm.

The smooth surface of FD scaffolds is likely to be an effect of the capillary stresses experienced during freeze drying or the long scaffold-aging times during which the gelatin outer layer may have formed to reduce surface tension. CPD scaffolds were prepared using the same scaffold-aging conditions, however the solvent exchange caused shrinkage of the gelatin network and CPD avoided capillary stresses. One or both of these factors is predicted to be the cause of the revealed sol-gel particles.

Swelling effects

The swelling of the scaffolds after 24 h in TRIS was found to be higher for CPD scaffolds than FD scaffolds, 156 ± 7 % versus 112 ± 3 % respectively. The result is an improvement on silica-gelatin hybrid scaffolds produced by Gao *et al.* which showed 440 % swelling in just 2 h. Swelling is caused by water breaking gelatin-gelatin hydrogen bonds and forming gelatin-water hydrogen bonds. The increase in CPD scaffold swelling is predicted to be due to slight mesoporosity of the organic network due to the removal of capillary stresses during drying. Mesopores in the CPD scaffolds would allow for easier infiltration of water into the network compared to FD scaffolds.

Overall, swelling values were low which suggests the scaffolds produced here had higher crosslinking compared to Gao *et al.*, as crosslinks prevent water from entering the gelatin network (Ren *et al.*, 2001a). Comparing the strut dimensions and separations, scaffolds by Gao *et al.* swelled from ~550 µm to ~1.2 mm strut separation and strut width increased from ~350 µm to ~510 µm in just two hours. In this case, assuming uniform swelling of struts and channels (116 % swelling in terms of length for CPD scaffolds), the CPD 200 µm scaffolds

swelled to approximately 190 µm strut width with 240 µm channel width, which is still within the desired channel width for cartilage regeneration.

The CPD 200 µm and CPD 300 µm scaffolds achieved the desired channel width for cartilage tissue scaffolds. The FD scaffolds both have a channel width larger than desired, however taking the scaffolds forward it was considered more interesting to compare CPD scaffolds to FD scaffolds and future work will focus on scaffolds printed with 1 mm strut separation: FD 700 µm, and CPD 200 µm.

5.3.2 Dissolution properties of scaffolds

Hydroxycarbonate apatite formation

HCA formation on a material is triggered by the release of cations, such as calcium, and formation of silanol groups on the surface, which can nucleate calcium phosphate rich layer formation (Hench and Polak, 2002). HCA formation is detrimental to the regeneration of cartilage, as the increase in surface stiffness, and presence of calcium phosphate mineral, triggers dedifferentiation of chondrocytes, reducing the amount of hyaline cartilage and increasing the amount of fibrocartilage (Allen *et al.*, 2012, Maldonado and Nam, 2013). The dissolution study conducted by Mahony *et al.* (Mahony *et al.*, 2014) indicated HCA formation for 30G scaffolds with CF0, CF100 and CF500, however HCA did not form on 30G CF1500 foams. To avoid HCA formation on the 3D printed scaffolds designed for cartilage tissue, a high ratio of gelatin to silica and crosslinking was used as it is the silica surface which plays a role in HCA formation. To assess the scaffold HCA formation, a dissolution study was performed in SBF.

During the SBF study, the solutions were analysed to measure the levels of calcium and phosphorus in the SBF. When HCA forms on the surface of scaffolds, calcium and phosphorus from the solution are depleted to form the surface layer. Figure 35a, plots the calcium and phosphorus levels in the solution. The steady calcium and phosphorus levels suggest that HCA did not form on the surface. The slight deviation from the control is likely to be due to homogeneous precipitation. Figure 35b shows the XRD pattern of the scaffold post dissolution after rinsing in DI water. The amorphous halo is observed due to the short range order of the amorphous material, and no HCA peaks were observed. The scaffolds are therefore unlikely to form HCA *in vivo,* a positive result.

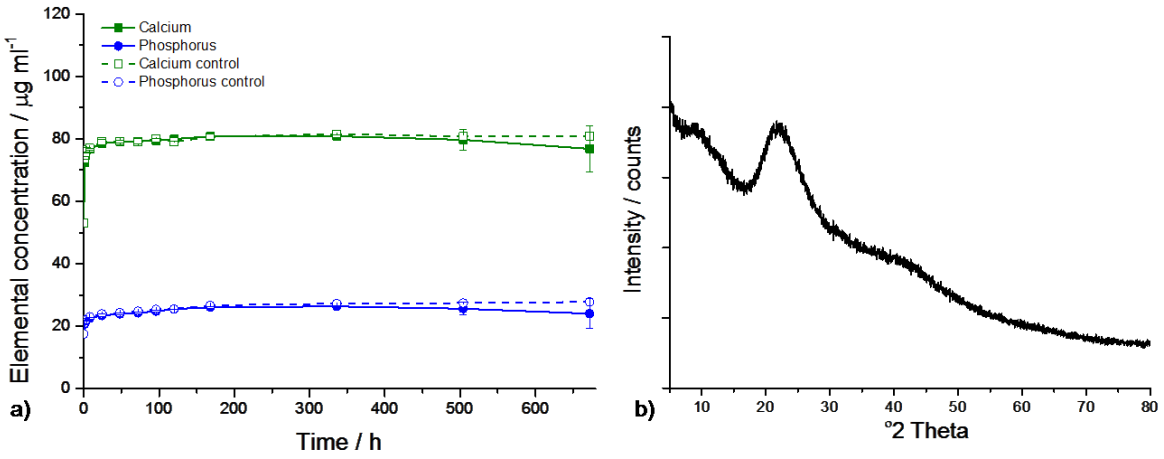

Figure 35. a) Elemental concentration of calcium and phosphorus in SBF following the immersion of FD 700 µm 78G CF500 scaffolds over a one month period; b) XRD pattern of scaffold post dissolution study in SBF.

Dissolution in TRIS

The dissolution profiles of CPD and FD scaffolds were monitored over a 4 week study in TRIS. TRIS was used rather than SBF as HCA formation was no longer a concern. CPD 200 µm scaffolds and FD 700 µm scaffolds were compared, the two scaffolds printed with 1 mm strut separation.

The release of gelatin and silicon in the form of soluble silica was measured over the four week study. The results are presented in Figure 36a and b for silicon and gelatin release respectively. The silicon release for both scaffolds had a very similar profile in the first 72 h, however the total silicon release was less for CPD scaffolds (105 µm mL^{-1}) than for FD scaffolds (117 µm mL^{-1}). The gelatin release was consistent independent of drying method, a mean of 32 µm mL^{-1} of gelatin was released over the 4 week study.

Compared to the 30G CF500 foams produced by Mahony *et al.* the release of gelatin from the 3D printed scaffolds was very low, but silicon release was high (Mahony *et al.*, 2010). The amount of material added to the solution for dissolution testing was greater in the study by Mahony *et al.*, 200 mg in 100 ml, compared to 150 mg in 100 ml used here, so quoted values have been adjusted to make the values comparable. The 30G CF500 foams released ~56 µm mL^{-1}, so despite the higher gelatin content, the gelatin release from the 3D printed scaffolds was lower. The silicon release of the foams levelled off at ~45 µm mL^{-1}, less than half the release observed in the 3D printed scaffolds, despite the lower silica content.

The solid state NMR results of the HF-free 3D printing method versus the foaming method (section 4.3.6), indicated similarly condensed materials; the Q structure in particular had

negligible differences. However, the dissolution results suggest otherwise and the 3D printed hybrids appear to have a more highly crosslinked functionalised gelatin network whereas the silica is released more readily compared to the foams. Looking at the percentages of the T species, there is approximately double the percentage of T^1 and T^2 in the 3D printed hybrids compared to the foams. This suggests the increase in silicon release could be from GPTMS molecules released by hydrolysis of the ester bond. Another consideration is surface area. The direct channels in the 3D printed scaffold are expected to have reduced the surface area compared to the foams, which may be the cause for higher gelatin release in the foams. It is also likely that the addition of HF used by Mahoney *et al.* broke down the gelatin chains which would have caused faster release (Gore, 1869, Mahony *et al.*, 2014).

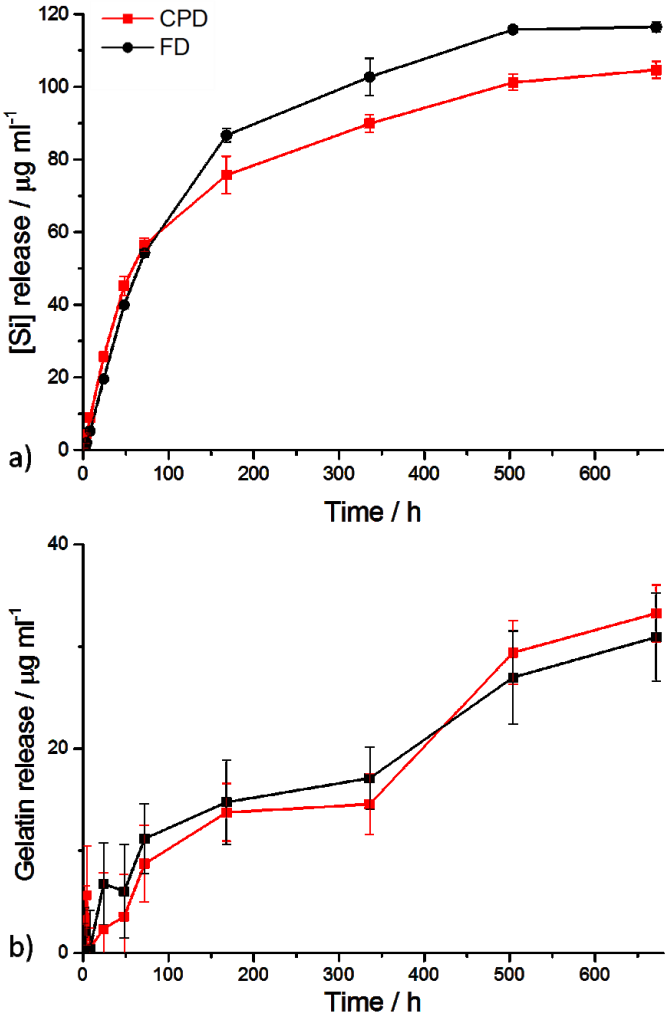

Figure 36. Dissolution profile of a) silicon and b) gelatin over a one month period in TRIS. 78G CF500 CPD 200 µm were compared to FD 700 µm scaffolds, both printed with 1 mm strut separation.

The silicon and gelatin release can be calculated as a percentage of the initial inorganic and organic mass. From the TGA of the organic:inorganic ratio for CPD and FD scaffolds were

72:28 and 70:30 respectively. Considering FD scaffolds first, of the 150 mg of scaffold used for dissolution, 45 mg was silica and 105 mg was organic. Therefore, the 117 μm mL^{-1} silicon release of the FD scaffolds after 4 weeks, 11.7 mg, was 26 % of the total inorganic. The 31 μm mL^{-1} gelatin release, 3.1 mg, was 3 % or the total organic. For CPD scaffolds, the inorganic release was 25 % and organic release was 3 %. After the one month study, the scaffolds had not changed in appearance as the low gelatin release resulted in volume stability of the scaffolds. Considering the silicon loss is measured here, the soluble silica loss is approximately 3.4x greater if the silicon is lost in the form of $Si(OH)_4$ and the mass is greater if Si is lost though cleavage of the GPTMS ester bond.

5.3.3 Mechanical properties of scaffolds

Compression testing of 78G CF500 scaffolds: FD 700 µm and CPD 200 µm were compared when wet, after one week soaking in TRIS. The FD 700 µm properties were also characterised when dry. Table 10 gives the mean values obtained from compressive testing. The porosity values, the highest strength foams produced by Mahony *et al.* (40G CF1000) (Mahony *et al.*, 2010), and cartilage tissue values are included for reference. Figure 37 shows representative plots of the stress strain curve for each type of scaffold tested.

Table 10. Mechanical properties of dry and wet (one week soaking in TRIS) 78G CF500 3D printed scaffolds (n = >6), 40G CF1000 foams (Mahony, 2010) and hyaline cartilage.

Sample		Compressive strength /MPa	Young's modulus, E /MPa	Compressive Strain	Porosity, φ /%
FD 700 µm	Dry	1.0 ± 0.1	7.1 ± 0.9	0.1 ± 0.02	87.5 ± 0.8
FD 700 µm	Wet	0.1 ± 0.02	0.7 ± 0.1	0.2 ± 0.03	87.5 ± 0.8
CPD 200 µm	Wet	1.3 ± 0.04		0.5 ± 0.04	71.9 ± 0.1
Foamed 40G CF1000 (Mahony, 2010)	Dry	0.06 ± 0.1	1.3 ± 0.1	0.05 +/- 0.00	50
Hyaline cartilage		22-37 (Kerin *et al.*, 1998, Repo and Finlay, 1977)	0.5 - 1.0 (Jurvelin *et al.*, 1997, Allen *et al.*, 2012)	0.24-0.85 (unconstrained at sides)(Little et al., 2011, Jurvelin et al., 1997)	0

The FD 700 µm scaffolds showed a significant change in properties from dry to wet as seen in Figure 37a. Compressive strength and Young's modulus reduced by ~90 % and compressive strain doubled. Compared to hyaline cartilage properties, the wet properties of the scaffolds were in the same range for the Young's modulus and compressive stain, however the compressive strength was two orders of magnitude smaller. This loss of strength was due to the reduction of silica after one week in TRIS and the swelling of the scaffolds which increased the water content and reduced the scaffold density.

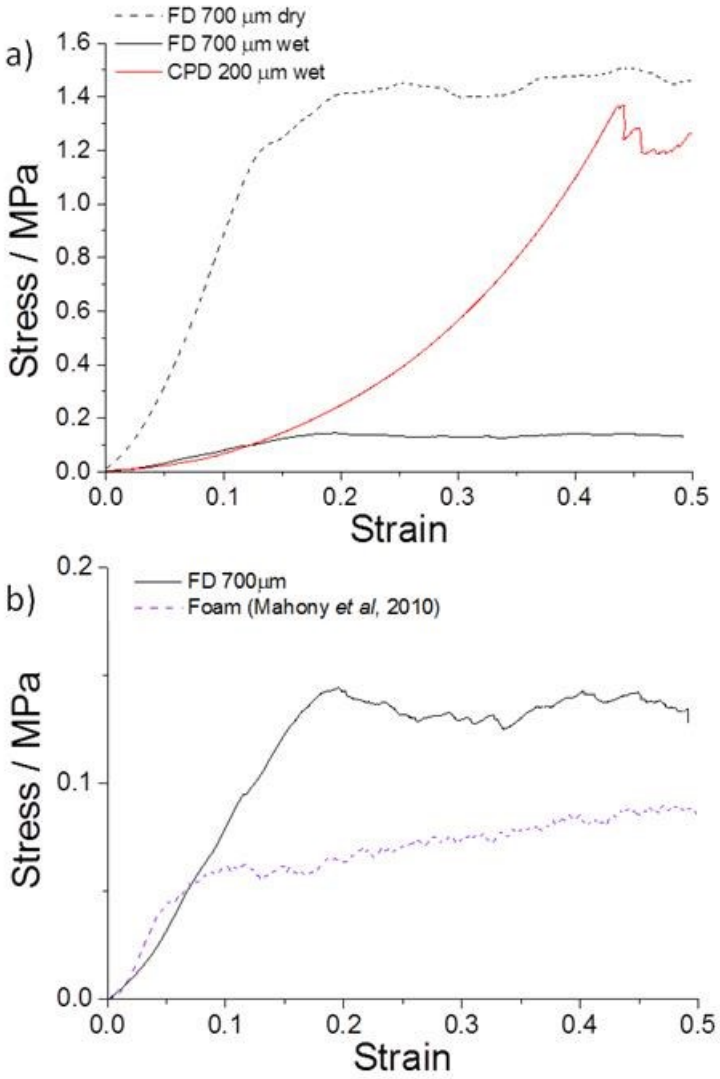

Figure 37. Example stress-strain plots of compression testing 3D printed 78G CF500 scaffolds dried via FD and CPD methods. Solid-lines indicate wet samples (1 week soaking in TRIS), dashed lines indicate dry samples. Graph a) FD 700 µm scaffolds wet and dry compared to wet CPD 200 µm scaffolds, and b) FD 700 µm wet sample and the highest strength dry foam (40G CF1000) produced by Mahony *et al.* (Mahony, 2010).

The behaviour of the FD 700 µm and CPD 200 µm scaffolds under compressive loading was very different. The FD scaffold exhibited a brittle elastic response before reaching the ultimate compressive strength, whereas the CPD scaffolds exhibited a non-linear response as stiffness increased with increased applied load and had a stress-strain curve similar to hyaline cartilage (Edelsten *et al.*, 2010, Little *et al.*, 2011). The higher degree of swelling of the CPD scaffolds in aqueous solution and larger strut width was predicted to be the cause, as the inclusion of water molecules in the gelatin network would have allowed for densification of the material during compression. Overall, the compressive strength of the CPD 200 µm scaffolds was over

10 times greater than that of the FD 700 µm scaffolds due to the increased strut/wall width and reduced porosity.

The compressive strain is not directly comparable as hyaline cartilage is a viscoelastic tissue and strain is therefore dependent on the strain rate. For example, when a 0.025 MPa stress is applied to hyaline cartilage, biomechanical models have shown that the compressive strain is dependent on time and does not reach the maximum, 0.08 compressive strain until 200-400 s after application of the stress (Boschetti *et al.*, 2004). The stress required to achieve 0.08 strain can be calculated from the Young's modulus for FD scaffolds, resulting in 0.056 MPa and the value for CPD scaffolds would be less due to the non-linear response, though from looking at the stress-strain plots, the value would not be less than 0.025. This is a positive result particularly for CPD scaffolds, as the scaffolds would deform with the same response as the native cartilage surrounding the implant.

The stiffness of the attachment sites of the cell, the ECM, is one of the most important mechanical properties to consider when regenerating cartilage *in vitro*. When cells attach to the ECM, in this case the scaffold surface, internal filaments, actin and vimentin, are produced which maintain cytoskeletal tension. The stiffness of the substrate is detected and can increase or decrease the efficiency of chondrocyte differentiation or induce dedifferentiation (Allen *et al.*, 2012). The Young's modulus of hyaline cartilage is within the range of 0.5-1.0 MPa, and the wet FD scaffolds fall within this range at 0.7 ± 0.1 MPa, an extremely positive result considering the drastic change in properties from dry to wet. CPD scaffolds behave non-linearly but when comparing the plots in Figure 37, deformation up to 0.15 strain was very similar for CPD and FD scaffolds, hence the cellular response induced is likely to be similar. To assess the stiffness of the CPD scaffolds, shear loading would provide information regarding the complex modulus, G^*, however the number of CPD scaffold was limited to compression testing.

The wet compression testing indicated the compressive strengths of the scaffolds were lower than that of cartilage tissue, which has a compressive strength ~30 MPa. Wet FD 700 µm scaffolds had a compressive strength of 0.1 MPa whereas CPD 200 µm scaffold had a compressive strength of 1.3 MPa. Depending on the defect size, the low compressive strength may initially limit the patient from normal activity, however as the cartilage tissue regenerated, the natural ECM would take over the mechanical properties.

In Figure 37b, the wet FD 700 µm scaffold was compared to the highest strength foam when dry produced by Mahony *et al.* This foam had a composition of 40G CF1000 and modal pore interconnect diameter of ~200 µm (Mahony *et al.*, 2010). The foams were not tested wet. The

compressive strength of the 3D printed scaffold was approximately three times larger than that of the foam, despite having been soaked in TRIS for one week, having increased gelatin content, and reduced C-factor. This proved that 3D printing can impart definite improvements to the mechanical properties of silica-gelatin hybrid scaffolds when compared to foaming. This was improved by the dense walls within the structure, and the variation in properties between scaffolds was still low despite the misalignment of struts. The foams would not be able to perform *in situ* whereas the 3D printed scaffolds retained their structure and the required strength over the one week period.

Failure mechanism

From the compression tests, the CPD scaffolds were shown to deform non-linearly up to ~0.5 strain after which unrecoverable failure occurred. For FD scaffolds, Figure 37 allows the compression profile of the wet and dry scaffolds to be compared due to adjustment in scale. The mechanism by which the scaffolds withstood the compressive force appears similar. Reaching the ultimate compressive strength did not result in instant failure, the compressive stress that the scaffolds are able to withstand was maintained until the end of measurement at 0.5 strain. This suggested a failure mechanism where individual struts were fractured at a time. To confirm this mechanism, a FD 700 µm scaffold was tested under compression and micro-CT to capture the failure mechanism of the scaffold. Figure 38 presents the 3D renders generated from micro-CT imaging. At 0 MPa, the scaffold is yet to be deformed. At 0.81 MPa, the scaffold was seen to be compressed in the lower section, however no collapse was observed. As the force increased from 1.02 MPa to 1.12 MPa, the majority of the scaffold in the field of view kept the original structure, however the lower section showed increasing levels of damage. This supports the idea that stress was locatised in particular layers which lead to the failure of the individual layers. This mechanism of failure allowed the compressive strength to be maintained for high levels of strain.

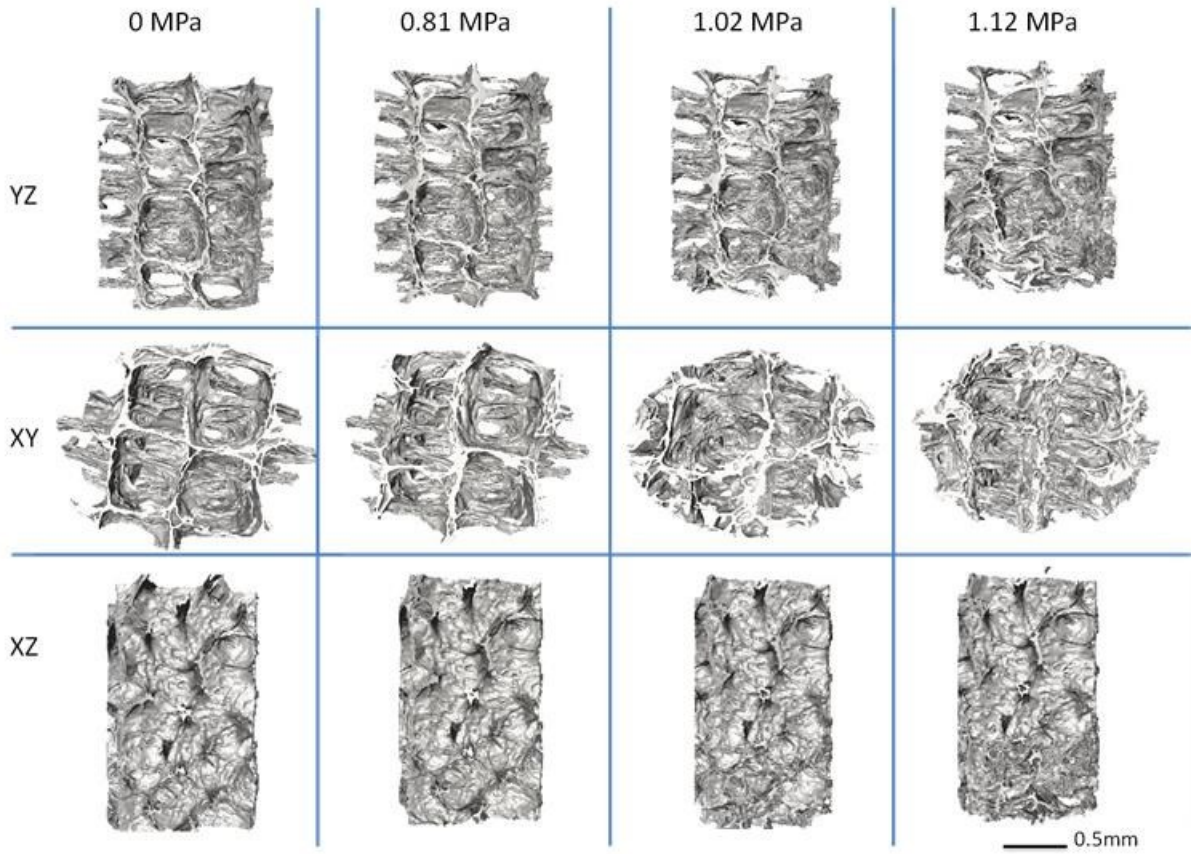

Figure 38. 3D reconstructions of a FD700 scaffold under increasing stress: 0 MPa, 0.81 MPa, 1.02 MPa and 1.12 MPa in the YZ, XY and XZ plane (micro-CT, Diamond Light Source).

5.3.4 Cell interactions

Cell viability

The 78G CF500 3D printed scaffolds were developed for regeneration cartilage tissue. In terms of cell work, the initial test was whether the scaffold would release cytotoxic dissolution products and hence reduce cell viability. Cell viability was a concern due to the potential release of GPTMS with an unreacted oxirane end group which is known to be cytotoxic. The viability of MC3T3 osteoblast precursor cells, and ATDC5 chondrogenic cells were assessed using as MTT assay as the scaffold required integration with bone to anchor the scaffold as well as regenerate hyaline cartilage.

Figure 39 shows the results of the MTT assay for ATDC5 chondrogenic cells and MCT3T3 preosteoblast cells after exposure to the dissolution products of the 78G CF500 scaffolds and positive and negative controls. Metabolically active cells will interact with MTT and produce purple coloured formazan crystals. An absorbance value of the dissolved crystals less than the control/standard culture conditions suggest a reduction in the rate of cell proliferation. The ISO-10993 standard states that a reduction of less than 30% at the tested concentration is regarded as non-cytotoxic. The results presented here indicate that the 78G CF500 scaffolds can pass ISO standard of biological device evaluation and be used in potential future *in vivo* studies.

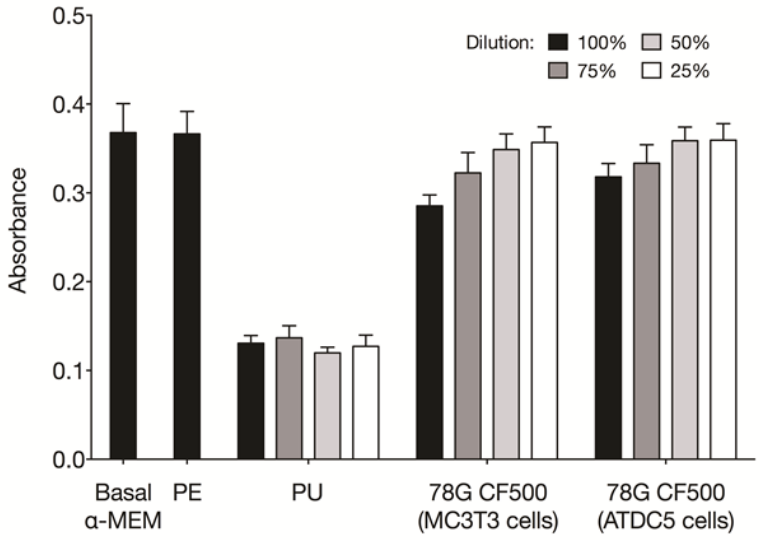

Figure 39. MTT metabolic activity assay according to the ISO standard 10993-5 and 10993-12. Dilution % values are vol% concentrations in PBS buffer, for a) for ATDC5 chondrogenic cells and MCT3T3 osteoblast cells.

Cell attachment

MC3T3 and ATDC5 cells were seeded on FD 700 µm 3D printed scaffolds to assess the cellular attachment after 3 days. Figure 40 shows confocal images of the cells on the scaffold. The staining indicates the presence of cytoskeletal proteins actin (red) and vimentin (green), and nuclei (blue).

Figure 40a presents the attachment of chondrocytes on the scaffold. The well organised actin and well defined vimentin markers indicate well attached cells which had spread across the surface. The result was similar for the preosteoblast cells in Figure 40b, however the actin and vimentin appear less defined. Comparing the nuclei presence, the chondrocytes appeared to be higher in number than the preosteoblasts.

The reduced number of preosteoblasts observed on the scaffold surface is predicted to be because cells can detect a stiffness lower than native bone ECM and have changed behaviour accordingly (Allen *et al.*, 2012, Geiger *et al.*, 2001). The chondrocytes responded well to the inherent stiffness, whereas the bone cells showed reduced spreading and potential subsequent proliferation. As the lower portion of the 3D printed scaffold is required to provide an anchor in bone, this result suggests a dual composition scaffold is required with increased surface stiffness to support bone growth.

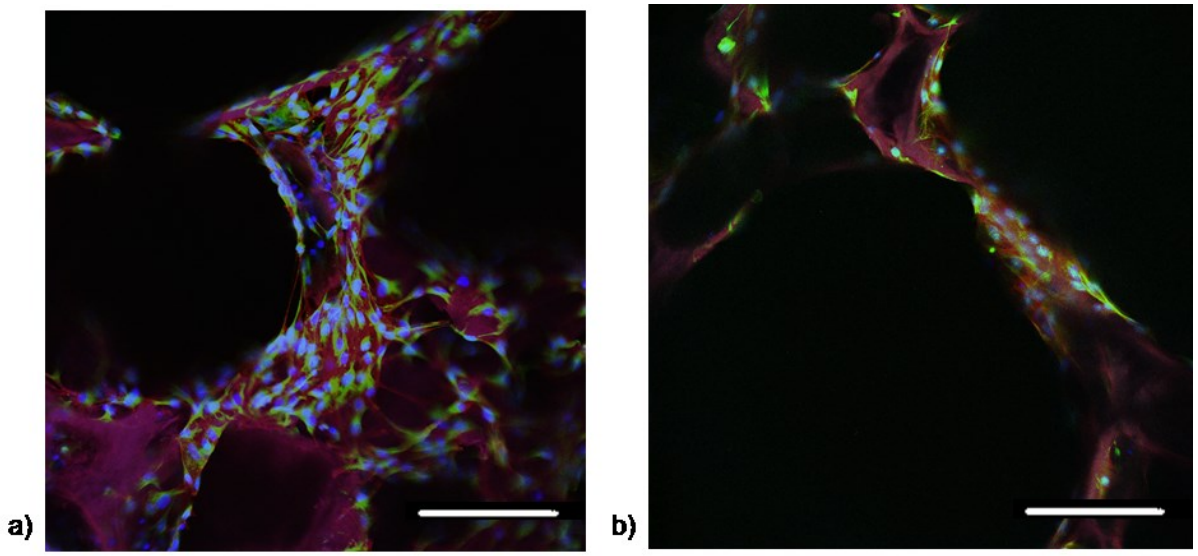

Figure 40. Confocal images of (b) ATDC5 and (c) MCT3T3 cells on the 3D printed scaffolds stained for cytoskeletal protein actin (red), vimentin (green) and nuclei (blue). Scale bar is 200 µm.

Cartilaginous matrix formation

A 28 day cell study of ATDC5 was conducted to see whether hyaline cartilage, healthy knee cartilage, would form on the scaffolds. Figure 41 shows the results of staining for positive

chondrogenic differentiation and hyaline cartilage markers: Sox9, aggrecan, and collagen Type II, and negative markers: collagen Type I and collagen Type X. The markers were stained green and the nuclei were stained blue. Three conditions were compared, FD 700 µm scaffold with 3×10^6 cells, FD 700 µm scaffold with 10×10^6, and CPD 200 µm scaffold with 3×10^6 cells.

The positive hyaline cartilage markers are all proteins expected to be present in hyaline cartilage. Aggrecan and collagen Type II are the main components of hyaline cartilage ECM (excluding water) and Sox9 is a protein that indicates chondrogenic differentiation. The negative markers indicate the formation of fibrocartilage (collagen Type I) and calcified cartilage (collagen Type X). The results in Figure 41 show all the positive markers to be expressed and all the negative markers to be negligible.

When 3×10^6 cells were seeded, the FD 700 µm scaffold showed poor cell and ECM distribution compared to the uniform distribution throughout the pores observed for the CPD 200 µm scaffold. Despite the larger pore width, it was possible to achieve similar results with the FD 700 µm scaffold when using 10×10^6 cells. Therefore, both scaffolds were capable of support tissue regeneration of hyaline cartilage, however in practice, 10×10^6 cells is inconveniently large. The cells used in this study are immortalised cartilage mouse cells, an effective model for the proof of concept experiment here, but they expand considerably faster than primary cells from patients.

Lower cell numbers required for seeding has various benefits to the patient as in practice the cells would be autologous and therefore would be harvested from the patient. A patient has limited number of healthy cells that can be removed and proliferation rates of cartilage cells are very slow and rates reduce further with age and/or other underlying diseases (Hidaka *et al.*, 2006). Alternatively, stem cells can be harvested however numbers of bone marrow cells reduce with age. Regardless of the cell source, $>10^6$ cells is a lot for seeding onto the implant, similar to the numbers needed for ACI. To obtain this number, first the cells harvested from the patient must be cultured *in vitro* which is very costly and labour intensive. Additional issues arise during cell culture as expansion takes place on a flat surface which tends to induce dedifferentiation. Overall, it is more convenient and there is higher chance of avoiding fibrocartilage formation when the number of cells required is small.

The smaller pore width of CPD 200 µm scaffolds therefore allows for faster, cheaper cartilage, and potentially more effective hyaline cartilage regeneration with one quarter of the cells required for ACI (Klein *et al.*, 2009).

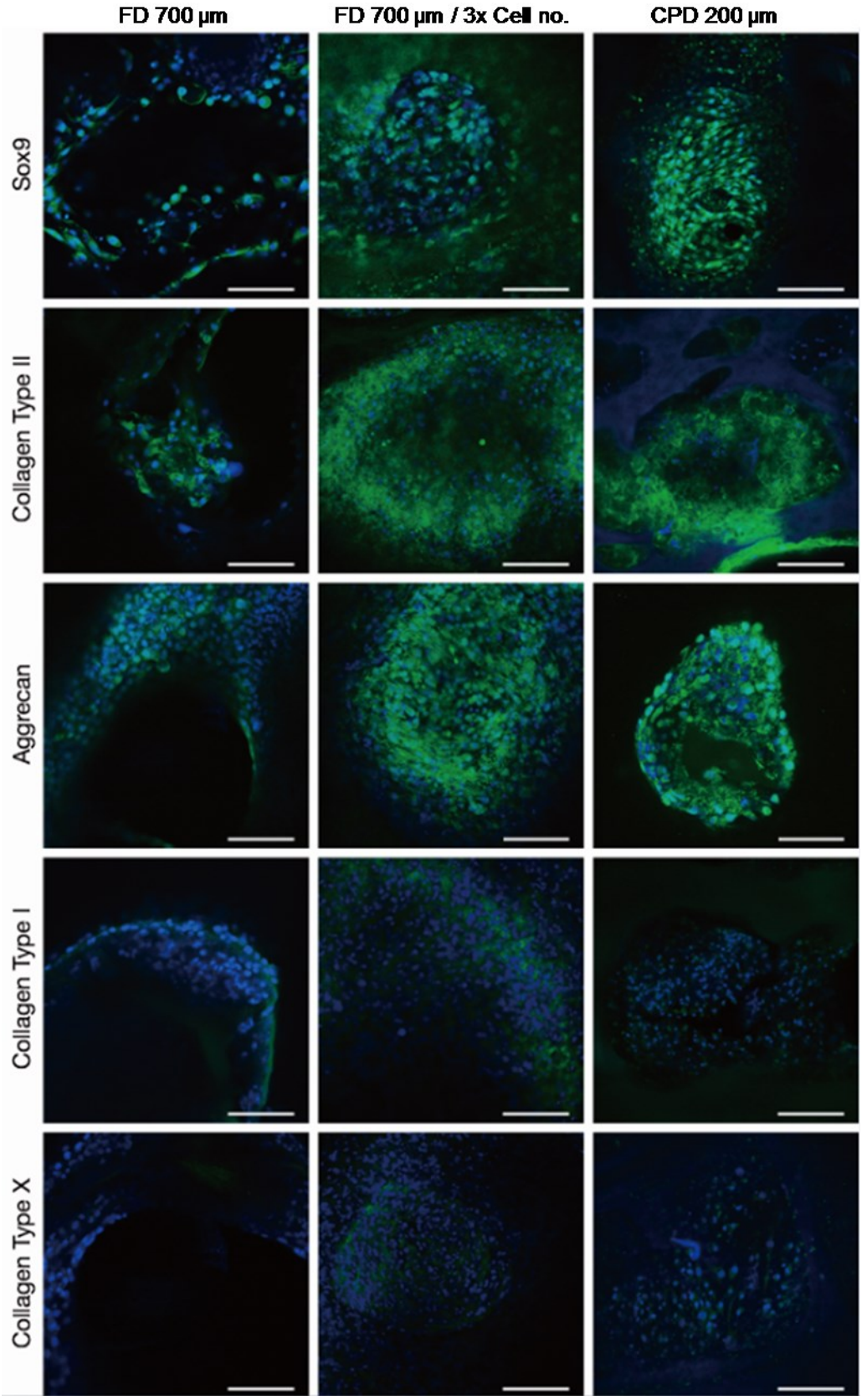

Figure 41. Confocal images of ATDC5 cells on the 3D printed scaffolds stained for cytoskeletal proteins: Sox9, collagen Type II, aggrecan, collagen Type I, collagen Type X (all green) and nuclei (blue). Scale bar is 200 µm.

5.3.5 Summary

3D printed scaffolds dried using CPD resulted in scaffolds with the desired channel width, similar mechanical properties to cartilage in compression, volume stability in TRIS, and well distributed hyaline ECM after 28 days in culture. FD and CPD were shown to induce very different structures from scaffolds printed in exactly the same way and the scaffolds properties were compared.

CPD induced considerably more overall shrinkage to the scaffolds than FD, 80 % rather than 42 %. Despite this, variation was low, the porosity remained high, 72 % for CPD, and 88 % for FD, and the composition of the hybrid material was not affected. Imaging of the internal structure of the scaffolds showed that the struts collapsed after printing. This caused dense walls to be formed within the scaffolds irrespective of drying method. This was not the desired result however the scaffold retained open channels and the walls contributed to the compressive strength of the scaffolds.

The main difference caused by the drying method was the strut structure. Scaffolds printed with 1 mm strut separation resulted in <40 µm struts width and 682 µm channels width when dried by FD (FD 700 µm), or 162 µm struts with 210 µm separation when dried by CPD (CPD 200 µm). Scaffolds printed with 1.5 mm strut separation resulted in <40 µm struts and 1229 µm channels when dried by FD (FD 1200 µm), or 299 µm struts with 319 µm separation when dried by CPD (CPD 300 µm). The increase is 3D printed strut separation from 1-1.5 mm, a 50 % increase, resulted in approximately 50 % increase of the strut separation using CPD and the strut width increased as expected. This was not the case for FD as the struts were reduced to thin walls or needle-like struts and the channel width increased by 81 %. CPD drying was therefore more compatible with 3D printing as the resultant strut and channel dimensions could be more reliably controlled.

Slight mesoporosity of the CPD scaffolds was predicted to be the cause of the increased swelling, 156 %, for CPD scaffolds compared to 112 % for FD scaffolds. Compared to scaffolds printed by Gao *et al.* (440 % swelling in 2 h) the swelling was small for both scaffold types which indicated a high degree of crosslinking.

The dissolution testing and compression testing compared the two scaffolds printed with 1 mm strut separation: CPD 200 µm and FD 700 µm. The CPD 200 µm was selected as it fit the desirable channel width for cartilage regeneration: 200-300 µm. The FD 700 µm was selected to compare the drying methods. The dissolution results were the similar for both scaffolds, but showed reduced gelatin release and increased silicon release compared to foams produced by

Mahony *et al.* (Mahony *et al.*, 2010). The low gelatin release of ~3 % resulted in a stable scaffold volume. Rapid release of soluble silica from FD and CPD scaffolds was observed. Of the total inorganic content, 26 % and 25 % silicon was released from FD and CPD scaffolds respectively. Considering a $Si(OH)_4$ molecule of soluble silica has a mass 3.4x that of silicon, the loss of silica, and swelling, were predicted to be the cause of the compressive strength reduction when tested wet compared to dry. Despite this large release of silicon, no HCA was seen to form on the surface of the scaffolds after one month in SBF.

After one week soaking in TRIS, the compressive strength and Young's modulus of the FD scaffolds reduced by 90 %, and the strain doubled. The stiffness of the scaffolds after soaking was found to be within the range of native hyaline ECM, 0.5-1 MPa. This was an excellent result and the importance of stiffness was confirmed in the cell attachment study. Chondrocytes thrived on the surface with native stiffness whereas the osteoblasts showed a less defined actin and vimentin structure and were lower in number.

The mean compressive strength of the wet scaffolds was 1.3 MPa for CPD 200 μm and 0.1 MPa for FD 700 μm, both of which showed improvement in compressive strength compared to the highest strength dry foam produced by Mahony *et al.*, but were below the compressive strength of hyaline cartilage (22-37 MPa). The stronger CPD scaffolds had a non-linear compressive response with increasing stiffness, whereas the FD scaffolds showed an elastic stress-strain plot up to the point of fracture at which the maximum stress was maintained due to fracture of individual layers. The non-linear response of the CPD scaffolds due to larger strut width and increased water content was closer to the stress-stain response typical of viscoelastic cartilage tissue than the FD response.

Cell viability tests showed the 78G CF500 silica-gelatin hybrid was biocompatible with both preosteoblasts and chondrocytes. The last test, the cartilaginous matrix formation, showed uniformly distributed ECM across the channels of the CPD and FD scaffolds, however the number of cells required was 3 $x10^6$ for the CPD 200 μm scaffolds and 10 $x10^6$ for the FD 700 μm, which is comparable to the cell number required for ACI (~12 $x10^6$). Therefore CPD 200 μm scaffolds were determined to be the most suitable scaffold for cartilage tissue regeneration.

CHAPTER 6. ELECTROSPINNING SILICA-GELATIN HYBRIDS

6.1 Introduction

To regenerate cartilage tissue, zonal organisation of cells is required to encourage the formation of the superficial zone where cells are in high density. The top zone of the scaffolds should provide a conformable surface to prevent further damage to healthy tissue when implanted, and provide a template for chondrocytes to produce the superficial zone.

So far, 3D printed silica-gelatin hybrid scaffold with adjustable channel width has been achieved, resulting in improved mechanical properties and dissolution properties compared to foams. The material has been shown to support cartilage regeneration, however the superficial zone and conformable layer is yet to be formed. Electrospinning of the silica-gelatin hybrid was the technique chosen to generate this cartilage surface regeneration layer.

Electrospinning produces nano to micrometer fibres through the application of a high electric field between a solution in a needle to a collector. The high surface to volume ratio of electrospun fibres provides multiple contact points for cells to attach hence mimicking the three dimensional and nanoscale features of cartilage ECM (Nuernberger *et al.*, 2011, Li *et al.*, 2006). This has been shown to encourage the spherical morphology of differentiated chondrocytres and ECM production.

Cotton wool-like scaffolds

This chapter explores the possibility of electrospinning the silica-gelatin hybrid solutions to create fibres with a cotton wool-like 3D nature. The hypothesis was that the 3D nature of the fibre structure was important to allow for cells and ECM to infiltrate across the full thickness of the layer as this is often not the case for 2D fibres (Chen *et al.*, 2008, Ren *et al.*, 2010, Song *et al.*, 2008b, Gao *et al.*, 2013a, Zhang *et al.*, 2008).

Cotton wool-like structures have previously been electrospun directly from bioactive sol-gel solutions by using Ca^{+2} or Fe^{+3} charged ions to accelerate portions of the electrospun fibres and produce the 3D morphology (Poologasundarampillai *et al.*, 2014a, Sun *et al.*, 2012a). Cotton wool-like fibres were first produced by Poologasundarampillai *et al.* at Nagoya Institute of Technology (NITech). Their hypothesis was that the positively charged calcium ions in the sol caused a whipping of the sol. Since, other methods have been developed at NITech. Cotton wool-like fibres have been achieved via a fan method (Obata *et al.*, 2013) and ethanol stirring method (Kasuga *et al.*, 2012). Both techniques rely on fibres avoiding contact with each other and any surfaces before drying to obtain the 3D nature. The previous work

into electrospun was developed for bone tissue regeneration, whereas here the focus was on cartilage. To avoid using highly charged ions, the 3D cotton wool-like structure was hoped to be achieve by generating long, unfused, fibres using a high humidity environment and highly crosslinked solutions (De Vrieze *et al.*, 2009, Tripatanasuwan *et al.*, 2007). All research into electrospinning silica-gelatin hybrids in this thesis was conducted on placement at NITech.

Material variables

Gelatin crosslinked by GPTMS has been electrospun by various research groups for tissue regeneration purposes due to the biocompatibility and bioactivity of gelatin (Ren *et al.*, 2010, Song *et al.*, 2008b, Song *et al.*, 2008a, Tonda-Turo *et al.*, 2013). Silica-gelatin hybrids using bioactive glass and gelatin functionalised by GPTMS have also been electrospun for bone tissue regeneration purposes (Gao *et al.*, 2013a). All the methods for electrospinning are different in terms of solvent and electrospinning parameters, however none of the literature reports unfused fibres that are stable after one week soaking in PBS. The BG-gelatin hybrid fibres, 70G CF185, produced by Gao *et al.* displayed degradation after just 12 h in PBS and although Song *et al.* made functionalised gelatin CF740 fibres that show little dissolution, the initial fibre structure was fused.

As high C-factor,functionalised gelatin fibres had been shown to form fused fibre mats, the aim here was to use 70G hybrid solutions like Gao *et al.* to produce distinct fibres with high crosslinking.

Electrospinning variables

The electrospinning variables were defined to generate distinct unfused fibres using the adapted materials processing method and compositions identified. There were numerous parameters to consider: flow rate, needle size, temperature, humidity, applied voltage, and needle-collector separation (Bhardwaj and Kundu, 2010). All variables had to work in unison to create the unfused fibres, and the aim was to create cotton wool-like fibre structures by electrospinning in high humidity environments.

Desired properties and requirements

This work was hoped to be distinguished by the production of distinct unfused fibres using high GPTMS composition, little or no fibre dissolution after one week soaking, and a 3D cotton wool-like fibre structure. A 3D fibre structure has so far only been obtained from sol gel glasses, not functionalised gelatin or hybrid materials.

To electrospin the silica-gelatin hybrid; a new electrospinning hybrid method was required. Compatible compositions also needed to be identified and the time frame within which the hybrid solutions could be electrospun, the 'electrospinning viscosity range', had to be determined.

6.2 Methods

To electrospin the silica-gelatin hybrid, changes were required to the HF-free hybrid method and suitable silica-gelatin hybrid compositions and electrospinning parameters had to be identified. A starting composition with low C-factor was initially investigated then higher C-factor fibres were electrospun and characterised by imaging, evaluating the degree of condensation of the fibres, a dissolution study, and cell studies.

As before, hybrids were named depending on their gelatin to silica ratio and C-factor. The gelatin to silica (from TEOS) ratio, e.g. 70G:30SiO_2, shortened further to 70G, was defined as the mass ratio of gelatin to SiO_2, under the assumption that 1 mole of TEOS forms 1 mole of SiO_2. Any silica contributions from GPTMS are ignored in this ratio. The C-Factor, CF, was defined as the molecular ratio of GPTMS to gelatin when the molecular weight of gelatin is 87.5 kDa (Mahony, 2010).

6.2.1 Silica-gelatin electrospinning hybrid method

It was known that the choice of solvent had considerable effect on the feasibility of electrospinning. The HF-free hybrid method established for 3D printing was water based with low concentrations of gelatin at 0.05 g mL^{-1}. To electrospin the hybrid, the method required adaptation as water was not a suitable solvent for electrospinning gelatin due to its low volatility (Ki *et al.*, 2005) and electrostatic interactions with the charged side groups of gelatin. The electrospinning hybrid method was defined to decrease surface tension and increase volatility of the solvent. The functionalisation stage of the HF-free hybrid method was adapted to increase gelatin concentration and replace water with ethanol. The revised functionalisation method was based on methods by Song *et al.* (Song *et al.*, 2008b) and Fong *et al.* (Fong *et al.*, 1999). By combining the principles of these methods, here 0.1 g mL^{-1} gelatin was electrospun using a 60 wt% water and 40 wt% ethanol co-solvent. The composition was based on work by Gao *et al.* (Gao *et al.*, 2013a) which electrospun sol-gel hybrids functionalised by GPTMS equivalent to 70G CF185.

The electrospinning hybrid method is summarised in Figure 42 for 70G CF185 hybrids. Other than functionalisation, other reaction stages remained the same as the HF-free hybrid method, however due to the change in experimental location, room temperature in Japan was defined as 25°C and solution-aging, when in an oven, was performed at 37°C due to the equipment available. At this stage, the solution-aging time, electrospinning viscosity range and electrospinning parameters were yet to be determined.

Electrospinning hybrid method

All reagents were supplied by Sigma Aldrich UK unless otherwise specified. For all hybrids, the first stage was to dissolve gelatin (Porcine skin, gel strength 300, Type A) at a concentration of 0.1 g mL^{-1} in a co-solvent of 60 vol% water, 40 vol% ethanol. The solution was stirred at 400 rpm in a covered beaker at 40°C for 1 h. The pH of the gelatin solution was adjusted to pH 4.4 by the addition of 1 M HCl to replicate the pH conditions in the HF-free hybrid method (accounted for in the 60 % aqueous volume). The gelatin solution was functionalised by the addition of GPTMS, the amount of which was dependent on the C-factor. The time allowed for functionalisation was 3 h.

The sol was prepared separately. Hydrolysis of TEOS started 2 h after the start of the gelatin functionalisation, i.e. 1 h before the end of gelatin functionalisation. It was prepared by combining the components in the following order: deionized water, 1 M HCl and tetraethyl

orthosilicate (TEOS). The R-ratio was 4 and the volume ratio of water/HCl was 3. The solution was stirred for 1 h at 400 rpm to allow hydrolysis of TEOS.

Both reactions were complete at the same time. The functionalised gelatin and hydrolysed TEOS were mixed and returned to the hotplate at 40°C at 400 rpm. The amount of each solution added was dependent on the gelatin to silica mass ratio of hybrid composition being made.

As with the HF-free hybrid method, the solution-aging of the hybrids began with mixing on a hotplate at 40°C at 400 rpm. After 3 h of solution-aging on a hot plate, the hybrid solutions were transferred to a sealed container and into a 37°C oven where solution-aging was resumed. The solution-aging time varied depending on the composition. If solution-aging was not complete by the end of the day, the sealed containers were placed in a -18°C freezer. When required for further aging, the containers were placed in a 37°C oven where solution-aging was resumed.

Electrospinning

Once solution-aging was complete, the hybrid reached the 'electrospinning viscosity range', the viscosity range within which the hybrid solution could be electrospun to form distinct, fused fibres. The required solution-aging time and 'electrospinning viscosity range' was determined for different compositions in this study. After electrospinning, the 3D printed scaffolds were left to dry over night at room temperature, 25°C. The exact electrospinning parameters used are discussed in the electrospinning parameters section.

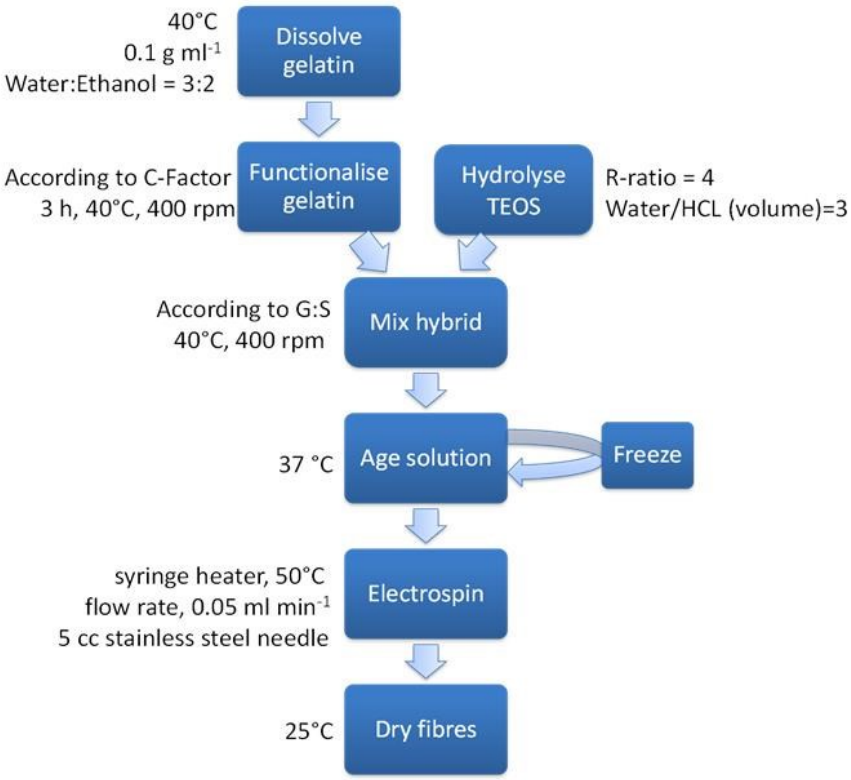

Figure 42. Electrospinning hybrid method for silica-gelatin hybrids. Solution-aging time, electrospinning viscosity window and electrospinning parameters were initially unknowns.

6.2.2 Electrospinning parameters

All electrospinning was conducted at NITech using the apparatus shown in Figure 43. The pre-determined variables were: humidity, needle diameter, syringe temperature, and flow rate. These were values suggested by NITech research staff and adjusted following preliminary trials. A 22 gauge stainless steel 18-8 hypodermic needle was used and flow rate was controlled by a syringe pump (FP-W-100, Melquest, Japan) at 0.05 mL min^{-1}. The humidity of the electrospinning environment can strongly effect the electrospun fibre structure (Tripatanasuwan *et al.*, 2007, De Vrieze *et al.*, 2009), hence all electrospinning was conducted in a humidity controlled chamber which contained silica beads to absorb moisture and maintain a high humidity of 55 %. As with 3D printing, it was necessary to raise the temperature of the hybrid solution above the gelation temperature of gelatin. To achieve this, a heat jacket was wrapped around the syringe at 50°C to prevent cooling across the metal needle which caused the solution to gel in the nozzle.

The investigated electrospinning apparatus variables were: needle-collector distance and applied voltage.

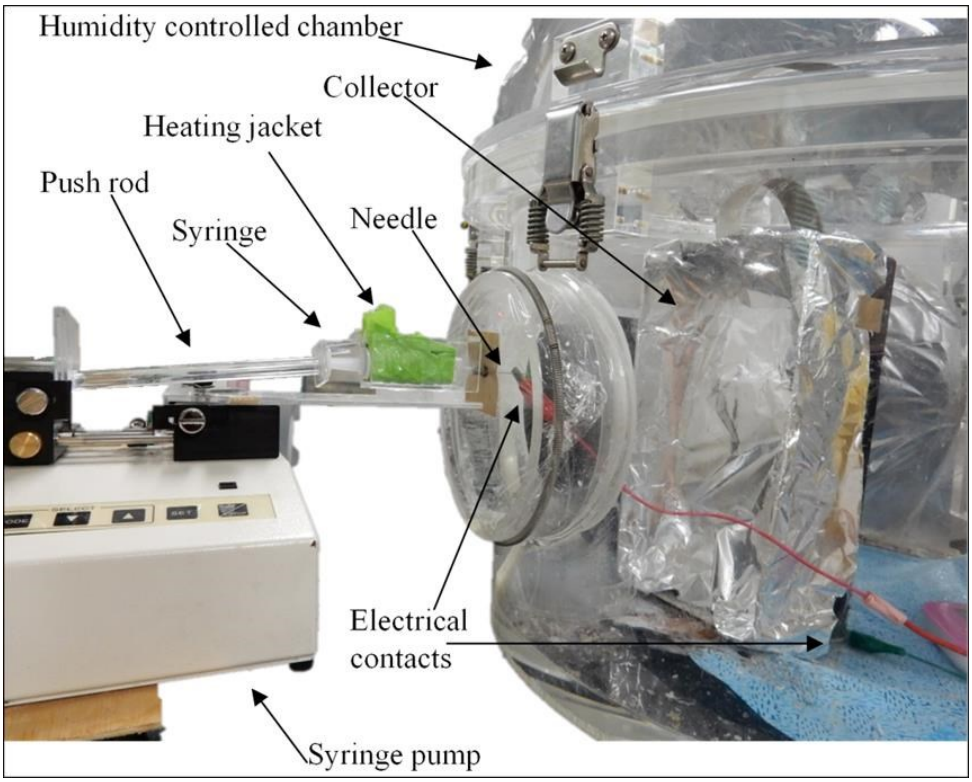

Figure 43. Electrospinning apparatus at NITech, Nagoya, Japan.

6.2.3 CF185 electrospinning study

70G CF185 was expected to be a good starting point for electrospinning as it was the gelatin to silica ratio and C-factor used by Gao *et al.* when electrospinning BG-gelatin hybrids to form smooth nanofibres (Gao *et al.*, 2013a), and close to the composition used for 3D printing. To electrospin the silica-gelatin hybrid, the solution viscosities compatible with electrospinning needed to be determined. For 3D printing, the degree of crosslinking was high and the material was in the form of a gel rather than a viscous solution, so viscosity measurement could not be taken directly. Compared to 3D printing, the viscosities expected to be compatible with electrospinning were considerably lower. For electrospinning CF4 functionalised gelatin, Ren *et al.* suggested a viscosity less than 65000 cP (equivalent to ketchup) (Ren *et al.*, 2010). For electrospinning cotton wool-like sol-gel fibres, the solution viscosity was lower, 560 - 950 cP (equivalent to caster oil)(Poologasundarampillai *et al.*, 2014b), however the viscosity of the BG-gelatin hybrids electrospun by Gao *et al.* (Gao *et al.*, 2013a) were not reported.

The viscosity of the solutions was dependent on the crosslinking induced by condensation of the silica-gelatin hybrid network which developed over time. To monitor how this evolution of viscosity affected electrospinning, the 70G CF185 electrospinning study aimed to determine:

1- The solution viscosity dependence on time of 70G CF185 solution compared to 100G CF185 solutions;
2- The viscosity range compatible with electrospinning;
3- The needle-collector distance required for successful electrospinning at each viscosity;
4- The applied voltage required for successful electrospinning at each viscosity.

Successful electrospinning was defined as electrospinning where fibre formation from needle to collector was continuous and fibres were distinct, i.e. they were not fused together at the collector.

The viscosity was directly measured over time and the solution was electrospun at increasing viscosities to determine the electrospinning viscosity range. Analysis of the electrospun fibres by rheology, FTIR and SEM, provided information regarding the fibre structure and chemical bonding as viscosities increased. It was also necessary to determine a suitable voltage for electrospinning at each viscosity tested: 7 kV, 9.5 kV and 12 kV. These values were selected after initial experiments showed 5 kV to be too low to induce fibre formation and 15 kV to be too high.

Hybrid preparation

The 70G CF185 hybrid composition was prepared following the electrospinning hybrid method as presented in Figure 42. The 100G CF185 functionalised gelatin composition was prepared following the electrospinning hybrid method however the TEOS hydrolysis and TEOS addition was omitted.

Time point protocol

The time point protocol was designed to determine the electrospinning viscosity range, the most suitable needle-collector separation, and most suitable applied voltage for each composition.

During the solution-aging period, 3 mL samples of the 70G and 100G solutions were removed at ~1 h intervals and placed in a 5 mL syringe. The viscosity of the solutions were measured using an Anton Paar Modular Compact Rheometer, MCR 102 (NITech). Conditions were: solvent trap, 40°C, 50 points, 2 second intervals, frequency 20 rad s^{-1}. The mean viscosity was calculated and standard deviations were negligible.

The 70G CF185 solutions were then electrospun at three voltages: 7 kV, 9.5 kV, and 12 kV. Electrospinning parameters were: 22 gauge needle, 0.05 mL min^{-1}, 55 % relative humidity, 50°C heat jacket.

At each time point, all electrospinning was complete within 20 minutes and voltages were tested in the same order to minimise the effects of viscosity increase with time. The separation between needle and collector plate was adjusted for each voltage at each time point in order to obtain successfully electrospun fibres. The separation distance used: 15 cm, 20 cm, or 25 cm, was noted. All fibres were dried at 25°C room temperature overnight.

Determining the electrospinning viscosity range

The electrospinning viscosity range was determined after assessing the bonding and structure of the 70G CF185 fibres produced. Fibres electrospun within the electrospinning viscosity range were distinct fibres (not fused to form a porous sheet). A quick test to check if fibres were fused was to see if the fibres could be removed from the aluminium collector plate as fused fibres adhered to the surface.

The bonding within the fibres electrospun at increasing viscosities were analysed using FTIR analysis, FT/IR-4100, JASCO with ATR PR0450-S stage (NITech, Japan). FTIR was run in absorption mode between 600-4000 cm^{-1} at a resolution of 0.9 cm^{-1}. Once background analysis was complete, the sample was placed over the beam and secured in place for testing.

Between samples, the surface was cleaned with ethanol. All spectra were normalised to the gelatin amide I band at 1640 cm^{-1}.

SEM was used to assess the fibre structure at increasing viscosities. SEM images were obtained using the JEOL JCM 6000 (Nagoya, Japan), with voltage set to 5 kV and working distance of 20 cm. Samples were coated with amorphous osmium, Neoc Meiwafosis, Japan, Ox coater. From these SEM images, the fibre diameters were measured using ImageJ software.

6.2.4 Electrospinning high C-factor hybrids

The CF185 electrospinning study established the electrospinning viscosity range, applied voltage, and needle-collector plate separation required for electrospinning silica-gelatin hybrids based on low C-factor hybrid fibres, 70G CF185. The finalised electrospinning parameters were brought forward to this study where higher C-factor hybrids were investigated.

The electrospun 70G CF185 BG-gelatin hybrids electrospun by Gao *et al.* showed fibre fusion and decrease in fibre width after just 12 h in PBS. To avoid rapid dissolution rates, the C-factor in this hybrid composition, 70G, was increased to CF250, CF500 and CF750. The improvements in bonding within the fibres and the types of fibre structures achievable were assessed. CF500 was selected as it was found to be a C-factor that induced a high degree of crosslinking without being in excess in the crosslinking study in section 4.2.4, Figure 21. CF250 was selected as it was between CF500 and the already established composition of 70G CF185 which produced distinct, unfused fibres. Song *et al.* showed CF740 to reduce the dissolution of 100G fibres, though unfused fibres were not attainable (Song *et al.*, 2008b). CF750 was therefore tested despite the results obtained via the crosslinking study, with the aim to maximise functionalisation.

Hybrid preparation

The compositions analysed were all 70G hybrids with C-Factors of 250, 500 and 750. The Electrospinning hybrid method was followed as shown schematically in Figure 42.

Time point protocol

For the new compositions it was important to redefine the electrospinning viscosity range. The process of measuring the viscosity and electrospinning the solutions at intervals was repeated for the 70G: CF250, CF500, and CF750 hybrids.

During the solution-aging period, 3 mL samples were removed at ~1 h intervals and placed in a 5 mL syringe. The viscosity of the solution was measured and the solutions were electrospun for up to 30 minutes. The process was repeated until solutions were too viscous for electrospinning.

To measure the viscosity of the hybrid solutions, an Anton Paar Modular Compact Rheometer, MCR 102 (NITech) was used. Conditions were: solvent trap, 40°C, 50 points, 2 s intervals, frequency 20 rad s^{-1}. The mean viscosity was calculated and standard deviations were negligible.

To electrospin, the parameters used were: a 22 gauge stainless steel 18-8 hypodermic needle, 0.05 mL min^{-1} flow rate (FP-W-100, Melquest, Japan), 55 % humidity, 50°C syringe heating jacket. As determined by the preliminary study, 9.5 kV and 20 cm needle-collector separation were used and viscosities of 37-60 cP were known to produce distinct 2D fibre mats using the 70G CF185 composition.

SEM and FTIR were used to analyse the fibre formation and chemistry at increasing viscosities as described in the CF185 electrospinning study.

Determining the 2D and 3D electrospinning viscosity range

As well as producing distinct, unfused, high C-factor fibres, a secondary aim was to produce cotton wool-like fibres by electrospinning in a high humidity environment. It was predicted that long stable fibres would form when the effects of humidity and viscosity reached a critical point (De Vrieze *et al.*, 2009).

For each composition, the viscosity range where the hybrid solutions formed 2D mats and 3D cotton wool-like fibres were determined after viewing the fibres in SEM to assess the fibre structure.

Calculating methanol release

The volume of methanol released was calculated using the amount of GPTMS added, the M_r of GPTMS (236.3 Da), the M_r of Methanol (32.04 Da), the ratio of GPTMS to methanol molecules released (3) and the density of methanol (0.792 g mL^{-1}).

6.2.5 Evaluation of high C-factor hybrid composition

Thermal analysis was used to compare the composition of electrospun cotton wool-like hybrid fibres of composition 70G: CF250, CF500, CF750, to hybrids with the same composition but produced using the HF-free 3D printing method, and functionalised gelatin samples. The mass percent of organic and inorganic components of the samples were compared.

Hybrids of composition 70G: CF250, CF500, CF750 and 78G CF500 were made using the HF-free hybrid method following the monolith route as described in section 4.2.3: Silica-gelatin HF-free hybrid method. The functionalised gelatin samples of composition: 100G CF250, 100G CF500, and 100G CF750 were made following the same method however the TEOS part of the method was omitted. Both the hybrids and functionalised gelatin solutions were solution-aged on the hotplate until gelled, then were transferred into sealed containers for further aging and freeze drying as described in the HF-free hybrid method.

Electrospun fibres of composition 70G: CF250, CF500, CF750 were produced according to section 6.2.1: Electrospinning hybrid method. To electrospin, the parameters used were: a 22 gauge stainless steel 18-8 hypodermic needle, 0.05 mL min^{-1} flow rate (FP-W-100, Melquest, Japan), 55 % humidity, 50°C syringe heating jacket, 9.5 kV, and 20 cm needle-collector separation. The hybrids were electrospun within the cotton wool-like viscosity range: 60-80 cP for CF250 and CF500, 60-100 cP for CF750.

From the TGA results obtained from the functionalised gelatin plots, the number of moles of GPTMS was estimated from the resultant inorganic (GPTMS inorganic M_r = 76 Da). This was used to estimate the mass of the organic portion of GPTMS (M_r = 115 Da) and the remaining organic mass loss was attributed to gelatin (M_r = 87.5 kDa), so the C-factor could be calculated. From the TGA results of the HF-free 3D printing samples, the total mass percentage of organic was calculated. This information along with the C-factor was used to calculate the mass contributions from gelatin, organic GPTMS, inorganic GPTMS, and TEOS. The gelatin to silica ratio (TEOS contributions only) was then calculated. The results were then compared to the mass percentage of organic content of the electrospun fibres to assess where the changes in organic content may have originated.

To analyse the 70G: CF250, CF500, CF750 hybrids produced using the electrospinning and HF-free 3D printing method, and the functionalised gelatin samples, TGA and DSC was performed using a Netzsch STA 449C under the following conditions: 21°C to 800°C, ramp rate of 10 K min^{-1}, air flow rate 50 mL min^{-1}, platinum crucible, n = 3.

6.2.6 Silica network condensation of fibres

The cotton wool-like 70G hybrid fibres with CF250, CF500 and CF750 were analysed using ^{29}Si MAS NMR to observe the changes in the silica network that resulted from increasing the C-factor.

^{29}Si MAS NMR was performed at NITech using a JNM-ECA600 with 600 MHz spectrometer. Parameters were: 20 s, cumulated number: 2048, analysis time: ≈ 12.5 h.

From the ^{29}Si MAS NMR spectra, the relative peak areas were resolved by deconvolution using OriginPro software and the network condensation was calculated using Equation 12: where Q^n is the abundance of Q^n species and T^n is the abundance of T^n species.

6.2.7 Dissolution

The soluble silica and gelatin release were monitored in a dissolution study comparing the 3D cotton wool silica-gelatin hybrid fibres with increasing C-factor. The 70G hybrid fibres with CF250, CF500, and CF750 were compared over a one week period. The one week period was selected as it was a common dissolution timeframe in the literature due to rapid dissolution of electrospun fibres (Gao *et al.*, 2013a, Song *et al.*, 2008b, Tonda-Turo *et al.*, 2013).

In the study, 15 mg of cotton wool-like fibres were immersed in 10 mL of TRIS (n = 3), and stored in an incubator shaker at 37°C for 1 week. Time points were performed after: 0, 1, 2, 4, 8, 24, 48, 72, and 168 h of immersion. At the given time points, the pH was measured and 0.7 mL of solution was removed and centrifuged. From this centrifuged solution, samples for ICP and BCA assay (n = 3) were taken. Samples for ICP and BCA were not taken directly from the sample to avoid fibres entering ICP or BCA samples. The removed 0.7 mL solution was replenished with fresh TRIS solution.

For ICP, 0.5 mL of solution was removed and added to 9.5 mL of 1M HNO_3. The solutions were filtered using a Minisat 0.2 µm syringe filter (Satorius stedim biotech, Germany) to remove gelatin from the solutions as polymers are not compatible with ICP analysis. The concentration of silicon was measured at the end of the study using ICP-Atomic emission spectroscopy (ICP-AES, ICPS-7510, Shimadzu, Japan). Silicon standards were prepared: 0, 2, 5, 20, 40 µg mL^{-1}, to produce a calibration curve which was measured at the beginning of the sequence of the dissolution samples. To determine the silicon release during dissolution, ICP results were multiplied by 20 to account for the nitric acid dilution.

For the BCA assay (Pierce BCA Protein Assay kit), 25 µl (n = 3) of the solution was placed into 96-well plates for each sample at each time point. 200 µl of working reagent (bicinchoninic acid) was added to each well and shaken for 30 s. The microplate was then incubated for 4 h before reading the absorption values at 562 nm using a microplate reader (SpectraMax M5). BCA standards: 0, 2.5, 5, 26, 62.5, 125, 250 µg mL^{-1}, were produced using 1 mg mL^{-1} gelatin solution and measured alongside each time point to produce a calibration curve. Additional time points for BCA assay analysis at 96 h and 120 h were required due to experimental errors at the 72 h time point.

After the dissolution study the mass of the fibres was measured to calculate mass loss, and FTIR spectra and SEM images were obtained to compare the chemical bonding and fibre structure before and after dissolution. The SEM and FTIR methods were the same as

previously described, however, to observe the fibres after dissolution they were first dried at room temperature.

6.2.8 Cell attachment and viability

Cell work was performed by Dr Siwei Li on silica-gelatin electrospun cotton wool-likescaffolds with composition 7G CF500 and 70G CF750. All cell culture reagents were obtained from Invitrogen and Sigma-Aldrich UK unless specified otherwise. ATDC5 murine chondrogenic cell line (ATCC, UK) was culture expanded in basal DMEM supplemented with 5 % (v/v) FCS (foetal calf serum), 100 unit mL^{-1} penicillin, 100 µg mL^{-1} streptomycin and 1× ITS liquid supplement (10 µg mL^{-1} insulin, 5.5 µg mL^{-1} transferrin and 5 ng mL^{-1} selenite premix). Cultures were maintained in humidified atmosphere at 37°C, 5 % CO_2 and 21 % O_2. Upon confluence, cells were passaged using 500 µg mL^{-1} trypsin-EDTA (ethylene diamine tetra-acetic acid).

Firstly, cell viability was visualised using a LIVE/DEAD® Viability/Cytotoxicity Kit (ThermoFisher, UK) following manufacturer's instructions. A 3-day cell attachment study was performed using ATDC5 cell lines, on the electrospun fibres.

To prepare the samples, the 70G CF500 and 70G CF750 electrospun fibres were divided into 2 mg aliquots and sterilised with 70 % ethanol. Following washing with a copious amount of PBS, each sample was transferred to a sterile 15 mL centrifuge tube and preconditioned for 30 minutes in serum-free media in humidified atmosphere at 37°C, 5 % CO_2 and 21 % O_2. Each sample was centrifuged at 400× g in order to create a compact fibre network prior to cell seeding.

Cells were harvested and suspended in basal media. In the fibre attachment study, less cells were used than in the 3D printed scaffold study as the fibre scaffold were more compact. 5 mL of cell suspension containing 5×10^5 were added to each centrifuge tube containing the fibres and incubated in a humidified atmosphere at 37°C, 5 % CO_2 and 21 % O_2 for 2 h, with gentle agitation every 30 minutes to allow for diffusion and well distributed cell adhesion. Cell-seeded scaffolds were collected on day 3 and analysed by viewing under SEM. Samples were coated in 2 nm gold and viewed under a JEOL JSM 6010 SEM in normal scanning mode, accelerating voltage 20 kV, 15 cm working distance, spot size 50, and x2000 magnification.

6.3 Results and Discussion

To begin, 70G CF185 fibres were electrospun to establish the electrospinning method for silica-gelatin hybrids. The C-factor was then increased to CF250, CF500 and CF750 and the dependence of viscosity with time was monitored and the viscosity range for 2D and 3D cotton wool-like fibres was determined. The mechanism for cotton wool-like formation was discussed, the composition investigated. The condensation of the network was evaluated and suitability for hosting chondrocytes was then evaluated *in vitro*.

6.3.1 CF185 electrospinning study

In this preliminary study, the fibre formation dependency on viscosity, and the viscosity dependence on time was investigated for 70G CF185 hybrids. The C-factor value of 185 was used as a starting point to electrospin silica-gelatin-GPTMS hybrids based on papers by Song *et al.* (Song *et al.*, 2008b), Fong *et al.* (Fong *et al.*, 1999) and Gao *et al.* (Gao *et al.*, 2013a) in order to establish the electrospinning process. SEM images and FTIR were used to characterise the fibres formed.

Electrospinning 70F CF185

The viscosity evolution over time of the 70G CF185 and 100G CF185 solutions are plotted in Figure 44. Over a solution-aging period of 8 h, the viscosity of the 70G CF185 solution increased from 34 cP to 190 cP, whereas the 100G CF185 solution remained at ~33 cP. The stable viscosity of functionalised gelatin arose from the lack of condensation reactions between silanol groups when in solution (Tonda-Turo *et al.*, 2013). When TEOS was added to the solution, the viscosity increase was caused by the sol-gel network forming bridging crosslinks between functionalised gelatin molecules.

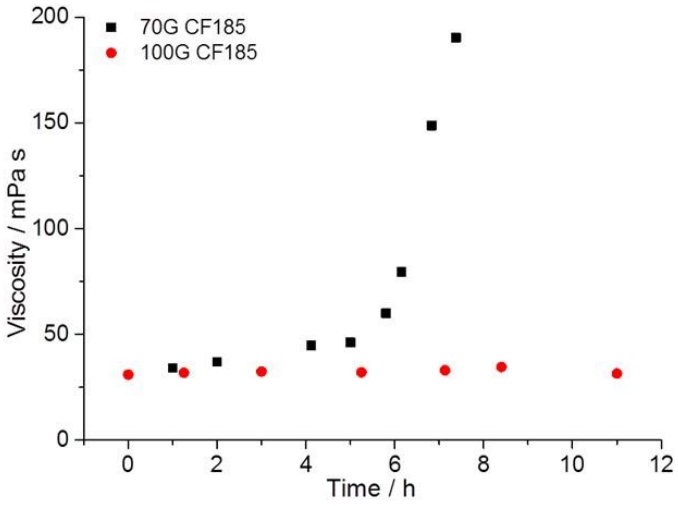

Figure 44. Viscosity measurements over time of 70G CF185 solutions and 100G CF185 solutions.

The 70G CF185 solutions were electrospun regularly during the solution-aging process to assess the fibre formation at increasing viscosities. As the viscosity of the 70G CF185 solution increased from 37 mPa to 79 mPa, fibres were produced using applied voltages of 7 kV, 9.5 kV and 12 kV between the needle and collector. Fibres produced at 7 kV and 9.5 kV had a similar structure and fibre diameter at all viscosities tested. Representative images are shown in Figure 45.

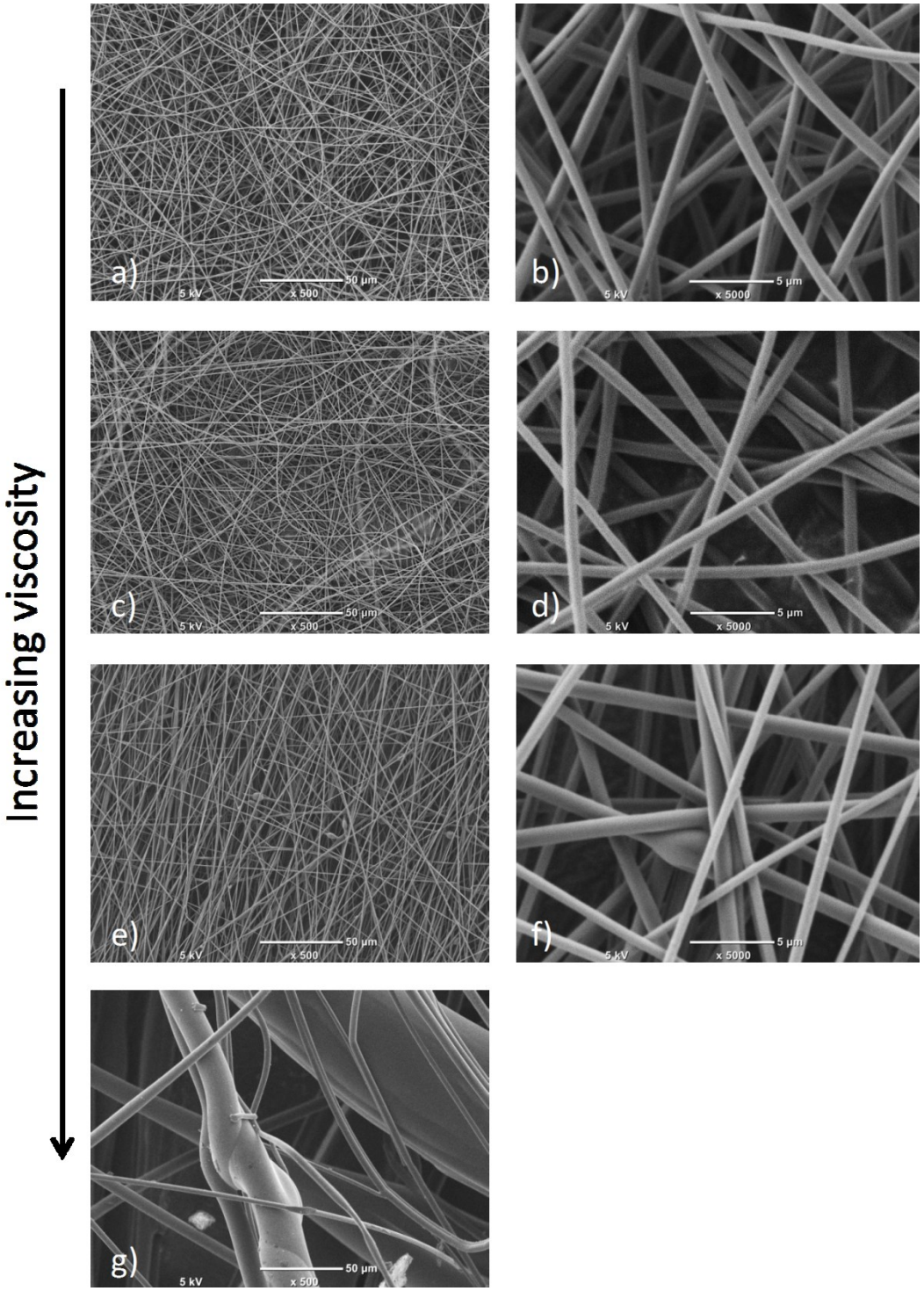

Figure 45. SEM images of electrospun 70G CF185 silica-gelatin hybrid. Images a) to g) represent fibres electrospun at 7 kV and 9.5 kV. The images represent fibres formed with the following viscosities: a) and b) 37 cP, c) and d) 46 cP, e) and f) 60 cP and g) 79 cP.

An applied voltage of 12 kV was also tested and the resultant fibres were similar for all viscosities where electrospinning of the 70G CF185 hybrid was possible, i.e. from 37-60 cP. Representative images of the fibres obtained at 12 kV are shown in Figure 46. The increased

applied voltage caused detrimental effects of fusion and increased fibre thickness. The higher voltage increased the speed of the fibre jets and prevented total evaporation of the solvent before reaching the collector plate.

The higher applied voltage of 12 kV had no effect on the already poor structure of the hybrid solutions with a viscosity of 79 cP, Figure 45g. This indicated that the viscosity had a much more important role in fibre formation than the voltage applied.

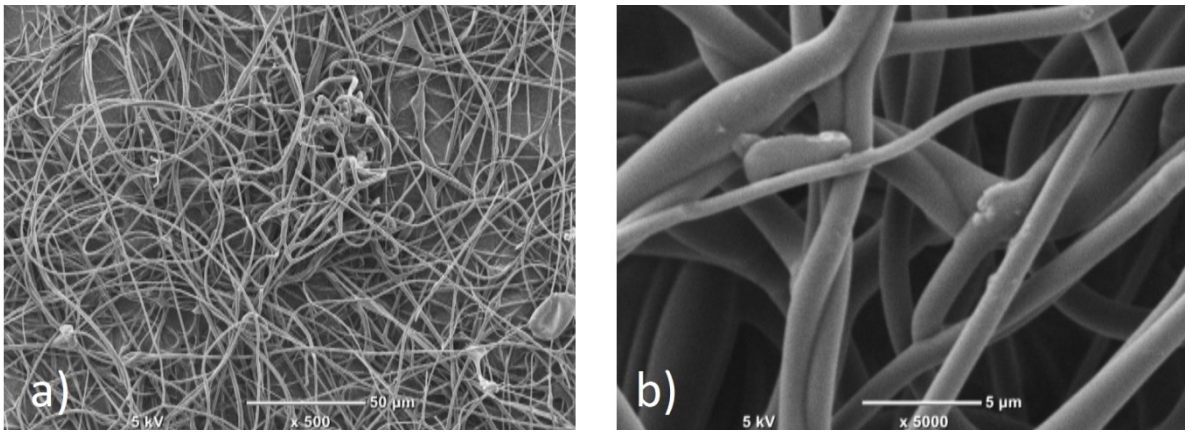

Figure 46. SEM images of CF185 fibres spun at 12 kV representative of 40 cP-60 cP solutions.

In Table 11, the fibre diameters of the electrospun fibres as shown in Figure 45 are presented. Fibres electrospun with an applied voltage of 9.5 kV and viscosity of 37-46 cP had similar fibre formation with mean diameters between 0.75 µm and 0.79 µm and standard deviations of ± 0.1 µm. When electrospinning 60 cP solutions, the standard deviation of the fibre diameters approximately doubled, to ± 0.21 µm, and some beading was observed. The next set of fibres electrospun with a viscosity of 79 cP, produced a range of fibre diameters; 8.5 µm ± 6.4 µm were clearly distinguishable to the eye and formed cobweb like structures. Electrospinning at this viscosity was problematic as gelling frequently occurred in the nozzle and fibres were released in bursts.

Table 11. Mean fibre diameters and standard deviations in µm of 70G CF185 fibres electrospun at increasing viscosities and voltages.

Viscosity /cP	Applied voltage /kV	Fibre diameters /µm
37	9.5	0.75 ± 0.12
46	9.5	0.79 ± 0.10
60	9.5	0.81 ± 0.21
79	9.5	8.5 ± 6.4
40 - 60	12	1.5 ± 0.5

The fibres electrospun within the viscosity range 37-46 cP, at an applied voltage of 12 kV, had approximately double the mean fibre diameter obtained using 9.5 kV. The mean diameter and standard deviation were 1.51 µm ± 0.53 µm.

The optimal applied voltage for electrospinning 70G CF185 was therefore 9.5 kV and the ideal viscosity range was found to be 37-46 cP for this 70G CF185 composition. The fibres produced had a diameter of ~0.8 µm, which is larger than the CF185 functionalised gelatin fibres obtained by Song *et al.*, 0.1-0.6 µm, and 70G CF185 hybrid fibres produced by Gao *et al.,* 192 ± 8 nm (Gao *et al.*, 2013a). The larger fibre diameter reduced the surface area and therefore had the potential to reduce the dissolution rate whilst still providing small contacts for cells.

Compared to the viscosities of functionalised gelatin solutions electrospun by Ren *et al.*, ~65000 cP (Ren *et al.*, 2010), the hybrid electrospinning values, <50 cP, were very small. Values were closer to the viscosities required by Poologasundarampillai *et al.* to electrospin sol-gels into cotton wool-like fibres, 560 - 950 cP, (Poologasundarampillai *et al.*, 2014a).

During electrospinning, the separation between needle and plate was adjusted to achieve continuous flow of fibres. The optimum distance for CF185 fibres using viscosity values between 37-60 cP, with 7-9.5 kV applied voltage, was 20 cm. To achieve (semi)continuous flow at 79 cP and to electrospin at 12 kV, the distance had to be increased to 30 cm. At smaller separations than those noted, continuous fibre formation was not possible due to erratic bursts of fibres leading to voltage drops. At higher separations, fibres did not reach the collector. A needle-collector distance of 20 cm and applied voltage of 9.5 kV were chosen as the electrospinning parameters to create optimal fibres as seen in Figure 47.

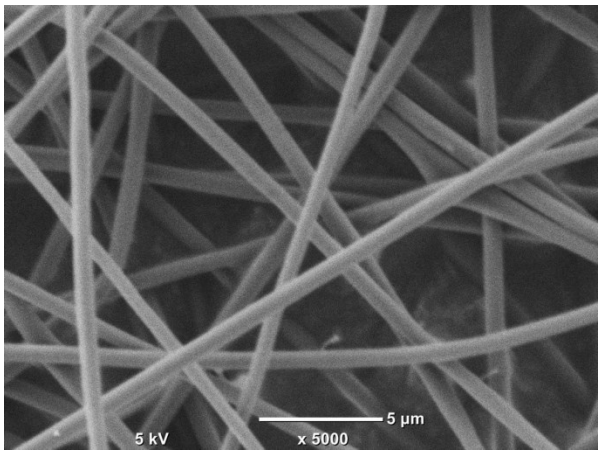

Figure 47. Optimal 70G CF185 electrospun fibres with 0.79 ± 0.10 µm fibre width, electrospun using: 22 gauge stainless steel needle, 0.05 mL min^{-1} flow rate, 55 % relative humidity, 50°C heat jacket , applied voltage 9.5 kV, and needle-collector distance 20 cm, 37-60 cP viscosity.

Chemical bonding of fibres

FTIR was used to analyse the bonding present in the fibres. In the functionalisation study conducted for 3D printing (section 4.2.2: Functionalisation study), functionalisation times of 3 h and 14 h did not have substantial impact on the GPTMS incorporation, so it was assumed the amount of GPTMS attached to gelatin molecules was constant over the 5 h period of 70G CF185 solution-aging, which followed 3 h of functionalisation.

Figure 48 presents FTIR spectra of the 70G CF185 fibres electrospun with increasing solution viscosities, 37-110 cP, as a result of increasing solution-aging time,1-5 h. Bands at 1200 cm^{-1} (Si-C band), and 910 cm^{-1} (oxirane and GPTMS Si-OH) were attributed to GPTMS as determined in section 4.3.1, Figure 18. The bands at 1040 cm^{-1} and 790 cm^{-1} were assigned to the Si-O-Si asymmetric and symmetric bands respectively. Bands at 1640 cm^{-1} (Amide I), 1540 cm^{-1} (Amide II), 1450 cm^{-1} (Amide III) were all attributed to gelatin. The band at 958 cm^{-1} was assigned to asymmetric stretching of Si-OH from hydrolysed TEOS which was not fully condensed (Gao *et al*., 2013a). The spectra were normalized to Amide I.

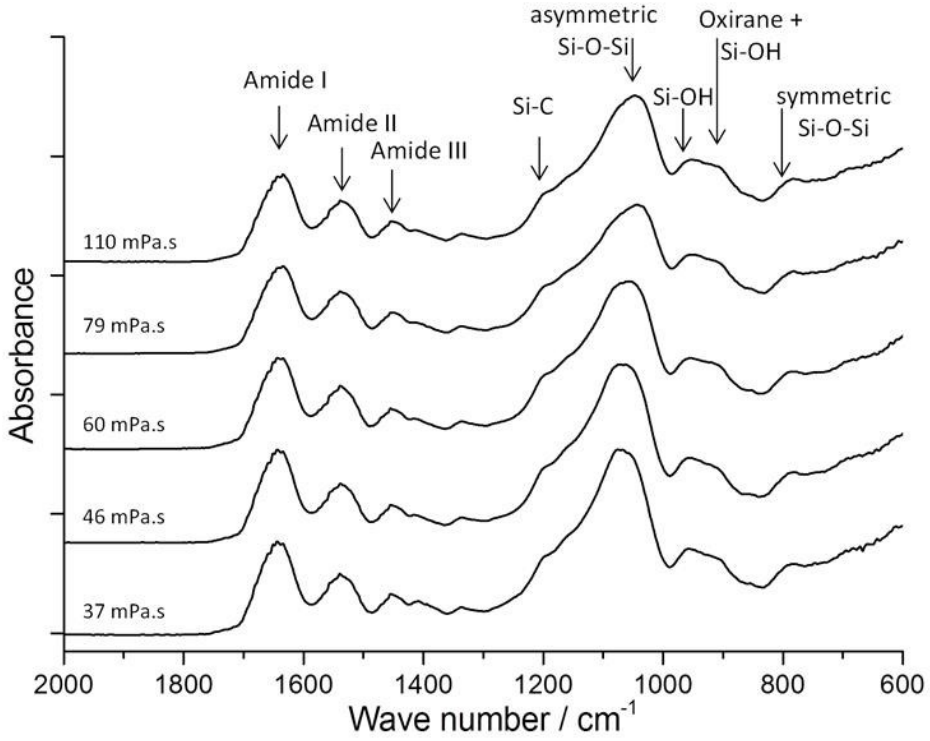

Figure 48. FTIR of 70G CF185 electrospun samples spun with increasing viscosity values due to increased solution-aging between 1 - 5 h.

The Si-C band of GTPMS did not vary in intensity compared to the gelatin amide bands as viscosity increased, indicating the amount of GPTMS attached was stable over the 5 h solution-aging period as assumed.

As the viscosity of the solutions increased, FTIR spectra in Figure 48 showed a decrease in the asymmetric Si-O-Si band relative to the amide bands. The symmetric Si-O-Si band increased only slightly relative to the amide bands. The Si-OH (from TEOS) band, and oxirane + Si-OH (GPTMS) band also increased relative to the amide bands. The changes in band intensity suggested the Si-O-Si content reduced while Si-OH contributions increased in the electrospun fibres as the viscosity of the solutions electrospun increased.

6.3.2 Electrospinning high C-factor hybrids

For the application of cartilage tissue regeneration, a low dissolution rate of fibres is very important as scaffolds must provide a stable environment for cells to attach, proliferate and generate ECM. The 100G CF740 functionalised gelatin fibres electrospun by Song *et al.* (Song *et al.*, 2008b) suggested there was opportunity to improve dissolution rates through increasing C-factor. However, the fibres obtained had a poor structure, so the electrospinning process and material composition had to be adapted to produce distinct, unfused fibres.

In this experiment: 70G CF250, 70G CF500, and 70G CF750, where synthesised and electrospun at regular intervals whilst the viscosity of the solution was investigated with time. The aim was to produce distinct fibres and reduce dissolution.

Viscosity dependency on time

Figure 49 shows how the viscosity of the three hybrids increased with solution-aging time. The points correspond to multiple batches of solution tested over a month long period. The viscosity developed in two stages. The first stage was a slow steady increase marked on the plot and the second stage was a sharp increase in the viscosity-time gradient. The gradient of the first and second stage appears similar regardless of the C-factor, however the onset time of the second stage increased with C-factor. As GPTMS is a crosslinking agent, it was expected that higher C-factors would induce a faster viscosity increase, however Figure 49 showed the opposite.

The gelatin content for each composition was 70G and hydrolysed TEOS was present in the solutions from 0 h on the graph. The only difference in the solutions was the amount of GPTMS added to the system. The delayed onset of the inflection point in the graph was therefore related to GPTMS content. Identifying why the C-factor affected the inflection point and what was causing the inflection point was required.

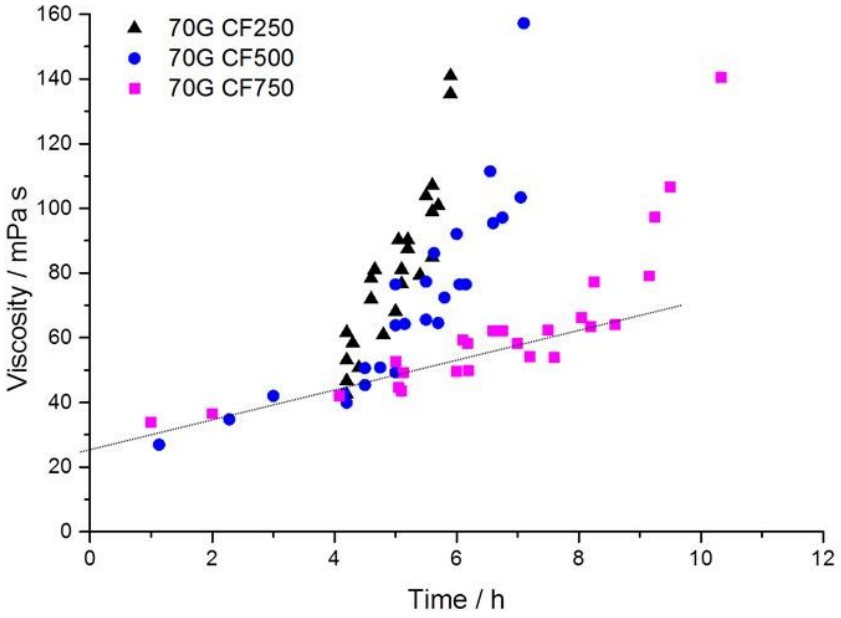

Figure 49. Viscosity measurements of all 70G hybrids: CF250, CF500, CF750 with increasing solution-aging time.

The viscosity of the hybrids increased due to crosslinks formed by bridging of functionalised GPTMS by the sol-gel network. When no TEOS was introduced, no viscosity increase was observed, as seen in Figure 44. Here, the initial slow steady increase with time was attributed to the network crosslinking due to sol-gel network condensation. The inflection point was consistent with phase separation of a crosslinked network in a solvent. Polymers crosslinked in the presence of a diluent eventually phase separate to form a gel phase and liquid phase due to the crosslinks limiting the maximum degree of swelling of the network. A critical crosslinking density is reached when the swollen network can no longer absorb the diluent (Dusek, 1971). During the solution-aging period of the silica-gelatin hybrid, the inflection point indicated when the system reached this critical point and began to separate into two phases. Similar viscosity behaviour was shown by Norton *et al.* at a critical amount of PVA addition to gellan gum. The viscosity of the solution became dependent on a second, higher linear gradient. This was due to the gellan polymer being forced into becoming a filler phase due to the PVA occupying the majority of the space (Norton *et al.*, 2014). In the electrospinning method, phase separation may be enhanced by the use of ethanol, a non-polar solvent, which reduces the gelatin solubility.

The time to reach the inflection point increased with C-factor due to the increased amount of methanol solvent present due to GPTMS hydrolysis. During functionalisation, the GPTMS oxirane end reacted with gelatin through nucleophilic attack from carboxylic groups of the polymer. At the other end of the GPTMS molecule, hydrolysis released three methanol

molecules per GPTMS molecule. Therefore, at higher C-factors, the amount of solvent in the hybrid solution increased due to increased methanol release. At CF750, the amount of GPTMS added to gelatin was substantial (11.42 g) which was added to 56 mL of gelatin solution and released 5.87 mL of methanol, whereas CF250 fibres released one third the amount of methanol.

The CF750 inflection point was delayed compared to the CF250 and CF500 hybrids. The prediction for this was that excess GPTMS in the hybrid system was further increasing the amount of solvent in the hybrid solution as hybrids were held in closed containers during solution aging. Whether GPTMS was in excess or not was confirmed in the composition evaluation of electrospun fibres (section 6.3.4).

Comparison with 3D printing solutions

The composition compatibility study conducted for the 3D printing method shows various similarities in how the gelation of the solutions developed. The study in section 4.3.5: Composition compatibility study, compared the solution-aging times and printing windows for hybrids with increased gelatin content. The C-factor was maintained at CF500, however with increased gelatin content came increased solvent as the amount of GPTMS increased with the gelatin content. As the 3D printed solutions were contained within a covered beaker and later a syringe, there was no opportunity for the additional solvent to escape despite the low volatility of methanol. The increased gelation rate may therefore have been affected by the solvent increase as well as the reduction in TEOS.

70G CF500 was examined in both the composition compatibility study for 3D printing and here for electrospinning. The 'printing window' began after 5 h of solution-aging, and the inflection point occurred here at 5 h also. This indicated that ethanol lowered the viscosity of solutions, as after 5 h the hybrid was a solution when using the electrospinning method, but a gel when using the 3D printing method.

High C-factor fibre structures

Electrospinning of the 70G hybrid solutions with C-factors of 250, 500, and 750 produced distinct fibres with various structures. Figure 50 presents SEM images of typical electrospun fibre structures produced at increasing viscosity. Table 12 presents the fibre diameters of these structures.

Fibres formed at low viscosities, less than 50 cP, are shown in Figure 50a, d, g and are representative of the 2D structures formed by each hybrid. CF250 hybrid solutions formed

distinct fibres as previously seen when electrospinning CF185, whereas CF500 and CF750 fibres fused together and were not improved by adjusting the viscosity. The fusion occurred due to low solvent evaporation rates at 55 % humidity (De Vrieze *et al.*, 2009). Fusion of electrospun CF500 and CF750 fibres but not lower C-factor fibres was due to the increased solvent volumes at higher C-factors. The 2D fibres structures were similar to what was achieved by Song *et al.* (Song *et al.*, 2008b), distinct fibres at low C-factors 100G CF185 and 100G CF370, and fused fibres at 100G CF740.

The 2D structures were formed at increasing viscosities until the solutions reached the 3D cotton wool-like viscosity range: 60-80 cP for CF250 and CF500, 60-100 cP for CF750. The cotton wool-like fibres are shown in Figure 50b, e, h. The mean fibre diameter increased as C-factor of the hybrids increased, to: 1.35 µm, 1.51 µm, 1.60 µm, for CF250, CF500 and CF750 respectively, while the standard deviation was similar, ~0.5 µm (Table 12).

3D fusion fibres are fibres with a cotton wool-like structure but with some fusion between fibres. Fusion of CF500 and CF750 cotton wool-like fibres was observed towards the higher end of the 3D cotton wool-like viscosity range, as seen in Figure 50f, i. The resulting 3D fused material appeared like cotton wool but the mean fibre diameters were ~0.5 µm larger when viewed under SEM. Although the SEM images of CF250 do not show 3D fused fibres, the fusion structure is expected, though unfortunately not imaged here.

As the viscosity increased further above cotton wool-like range, the amount of fibre fusion and fibre width increased, eventually resulting in gelation within the nozzle and erratic bursts of cobweb-like fibres as seen for the 70G CF185 composition, Figure 45g.

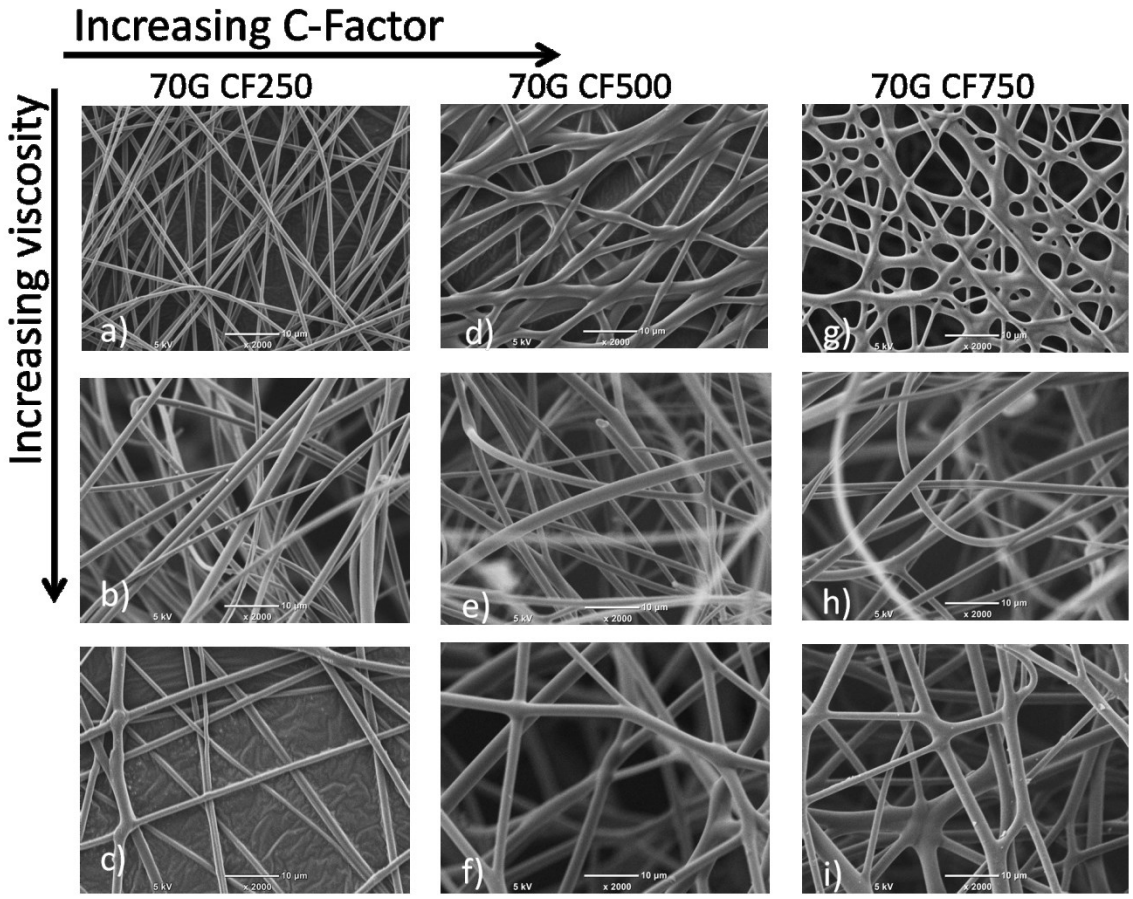

Figure 50. SEM images of electrospun 70G hybrid fibres with increasing C-Factor and viscosity. A), B), C) CF250, D), E), F) CF500 and G), H), I) CF750. With increasing viscosity the structures achievable changes: A), D) and G) show fibre mats electrospun from viscosities of 44, 45 and 49 cP respectively, B), E) and H) show cotton wool-like structures electrospun from viscosities of 72, 66 and 64 cP respectively and C) F) and I) show fibre fusion electrospun from viscosities of 81, 76 and 65 cP respectively. Scale bar is 10 µm.

Table 12. Fibre diameters of 2D mats, 3D cotton wool-like fibres and 3D fused fibres as shown in Figure 50.

Type of fibre	Mean fibre diameters ± standard deviation /µm		
	CF 250	CF 500	CF 750
2D fibres	0.88 ± 0.18	-	-
3D cotton wool-like	1.35 ± 0.51	1.51 ± 0.54	1.60 ± 0.50
3D fusion	-	2.21 ± 0.56	2.09 ± 0.76

6.3.3 Cotton wool-like silica-gelatin hybrid structures

Figure 51 shows the difference in 2D and 3D cotton wool-like fibres as seen in bulk. The 2D fibres were flat sheets whereas the cotton wool-like structures were thicker, voluminous and although still sheets, they no longer laid flat and had a voluminous nature. Within the 3D cotton wool-like electrospinning viscosity range, sections of the electrospun sample formed this conformable cotton wool-like material.

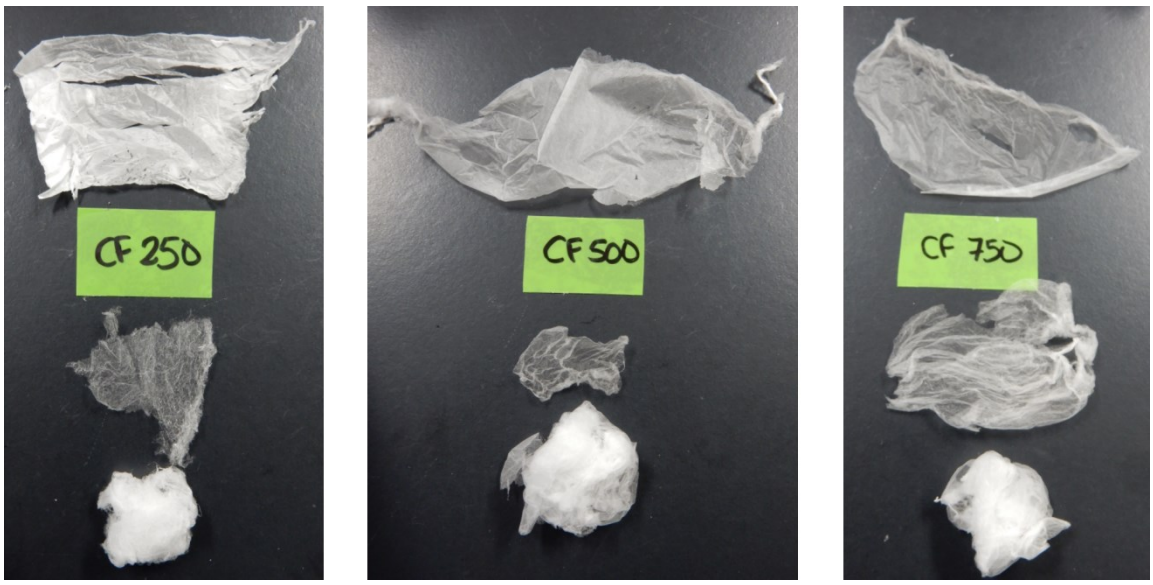

Figure 51. Photographs of 70G fibre structures formed with C-factors of a) 250, b) 500 and c) 750. The fibre sheets at the top represent 2D fibres formed at low viscosities. The bottom images show 3D cotton wool-like fibre structures laid out flat (middle) and balled up like cotton wool (bottom).

Cotton wool-like fibre structures from sol-gel solutions was previously attributed to accelerating Ca^{+2} in the sol (Poologasundarampillai *et al.*, 2014a), however no Ca^{+2} was present here. The formation of the 3D structure was attributed to the high humidity which allowed a slow solvent evaporation rate and highly elongated fibres to form. How these fibres attached to the collector and dried was vital to the formation of the 3D structure. The collector was a shoe box with aluminium foil lining the inside of the box, and ejected fibres were attracted to the collector edges. As demonstrated in the schematic in Figure 52, for a 3D structure to form, when the tip of the fibre jet was attached to the top edge, the remaining length was suspended between the top edge, the back surface and the base edge. Fibres that were attracted to the side edges were suspended between the side edge contact point and the base of the electrospinning chamber. The length of the fibre jet therefore needed to very long (due to humidity), strong (due to crosslinking/viscosity), and stable (a balance between the

two), to support the 3D fibre arrangement. Below the 3D viscosity range, the solutions were not crosslinked enough to sustain the formation of such long, stable fibres.

Figure 52. Cross-section schematic of electrospun fibres attached to collector.

Whilst the fibres were in suspension, it was essential that fibres did not touch each other or lie flat against the aluminium surface as they dried. Even within the 3D viscosity range, 2D fibre structures formed across the collector surface as the fibres lay flat across the back surface. Fibres that came into contact when suspended formed the 3D fusion structure. The prevalence of the 3D fusion structure at higher viscosities is likely due to the increased fibre diameters and therefore increased weight reducing the stability of the suspended fibre arrangement.

Relationship with viscosity-time graph

The 3D cotton wool-like viscosity ranges for all three compositions were in the second stage of the viscosity-time relationship, after the inflection point, where it is predicted that phase separation occurred. With 70G CF185 hybrids, electrospinning in this stage resulted in fused, erratic, non-uniform fibre formation. For the higher C-factor hybrids examined in this experiment, the change in gradient indicated the start of cotton wool-like fibre formation. As CF185 solutions did not form the cotton wool morphology, it was assumed a cut-off C-factor value existed between 250 and 185 where cotton wool-like formation was no longer possible due to low crosslinking of the hybrid resulting in less stable fibres.

Chemical bonding of fibres

The FTIR spectra presented in Figure 53 compares cotton wool-like fibres (60-80 cPa) to 2D sheets (40-60 cPa) made with 70G hybrids with C-factors: 250, 500, and 750. Comparing the spectra, all compositions and viscosities that produced distinct fibres during electrospinning

had similar relative band intensities to the amine I band: 2D CF250, 3D CF250, 3D CF500 and 3D CF750.

CF250 fibres produced spectra with no changes in the relative band intensities between 2D and 3D cotton wool-like fibres. The band ratios of the 2D and 3D CF250 spectra were comparable to the 3D cotton wool-like fibres formed by CF500 and CF750 (with the exception of a band at 950 cm^{-1}in CF250). This corresponded to the ability of CF250 solutions to form distinct 2D fibres at low viscosities rather than fused 2D fibre sheets as were seen for CF500 and CF750.

The band at 950 cm^{-1} was observed in both CF185 and CF250 hybrid fibre spectra and is associated with Si-OH (Gao *et al.*, 2013a). The 950 cm^{-1} band was not present in the hydrolysed GPTMS spectra, Figure 18, therefore the 950 cm^{-1} band was assigned to Si-OH from unreacted hydrolysed TEOS. The CF185 and CF250 hybrid solutions had less crosslinking potential and shorter solution-aging times before electrospinning took place compared to the CF500 and CF750 hybrid fibres. Both factors would have lowered the resultant connectivity of the silica network and increased the Si-OH contribution.

The compositions and viscosity combinations that did not produce distinct fibres were 2D CF500 and 2D CF750. The spectra for these fibres showed an increase in the relative intensity of the asymmetric Si-O-Si band compared to the distinct 3D cotton wool-like fibres with the same composition. This suggested that CF500 and CF750 fibres at low viscosities had a larger Si-O-Si conent, as was seen for the 70G CF185 fibres. The increased levels of silica may have been incorporated into the fibre jet as uncondensed molecules and condensed during drying. At higher viscosities, phase separation would have begun to remove unreacted species to the solvent phase and hence reduce the TEOS incorporation in the fibres.

Both resultant spectra of the CF500 and CF750 hybrid fibres were similar though there was a very slight increase in asymmetrical Si-O-Si for CF750 fibres. This implied that the amount of silica incorporated in the hybrid fibres had only marginally increased despite the 50 % increase in C-factor. This correlated to the findings of the crosslinking index study (section 4.3.3) which suggested a plateau in the crosslinking was reached between CF500 and CF750 (though results are based on 78G compositions using the HF-free method, not 70G). This supports the viscosity findings that some of the additional GPTMS in 70G CF750 compositions may have acted to increase the solvent volume.

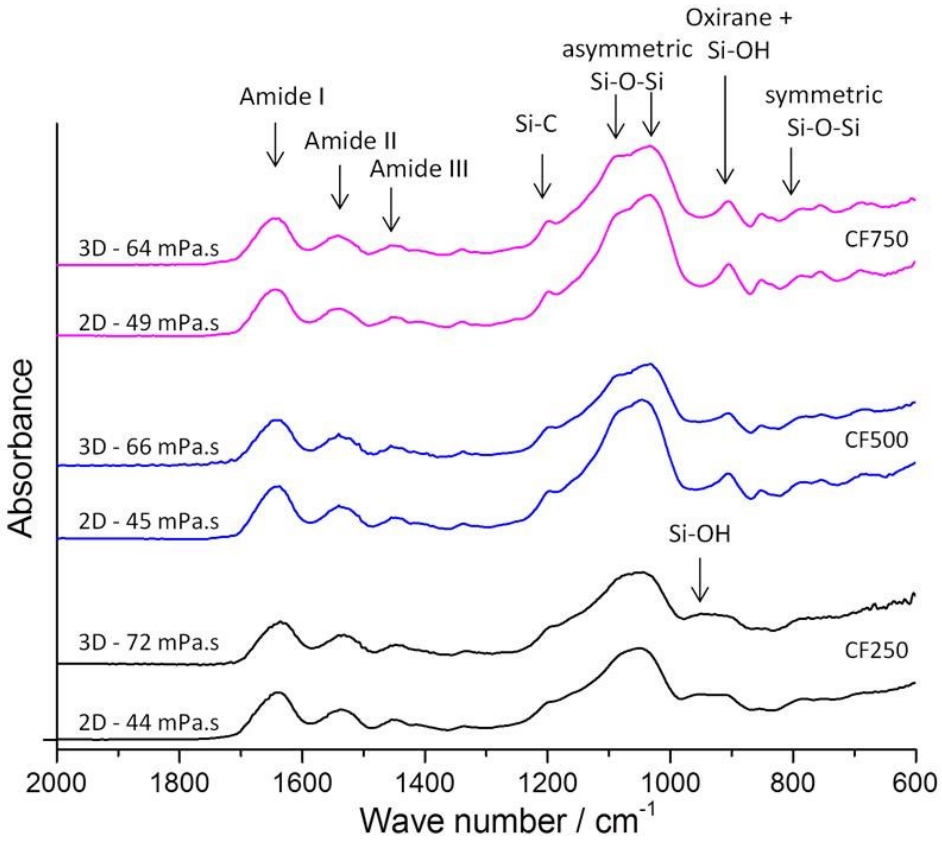

Figure 53. FTIR spectra of 70G hybrid fibres with increasing C-Factor produced by electrospinning. 3D cotton wool-like fibres (60-80 cPa) are compared to 2D sheets (40-60 cPa).

6.3.4 Evaluation of high C-factor hybrid composition

To break down the hybrid composition, three types of sample with C-factors: 250, 500, and 750, were thermally analysed:

1- Functionalised gelatin (100G) samples produced using the 3D printing method;
2- Hybrid samples produced using the 3D printing method;
3- Cotton wool-like electrospun samples.

Functionalised gelatin samples produced using the HF-free 3D printing method were analysed to calculate the number of moles of GPTMS and hence the C-factor from the remaining inorganic mass % which remained after heating the hybrids to 750°C, as seen in Table 13. All samples were homogeneous. The CF250 and CF500 samples both show C-factors very similar to the predicted value, however as predicted, CF750 was not attainable. The C-factor was actually ~CF630, which is still a substantial increase in GPTMS inclusion over CF500.

Table 13. Moles of GPTMS and gelatin, and C-factor, as calculated from the remaining inorganic after TGA of functionalised gelatin samples: CF250, CF500, CF750.

Functionalised gelatin composition	Inorganic (GPTMS) /% of functionalised gelatin	GPTMS /moles	Gelatin /moles x10^{-4}	C-factor
CF250	14	0.18	7.40	249
CF500	21	0.27	5.48	492
CF750	23	0.30	4.82	628

Thermal analysis of the hybrids produced using the 3D printing method resulted in 66 % organic for each composition examined: 70G CF250, 70G CF500, and 70G CF750. Samples were homogeneous. The organic component of GPTMS also accounts for 66 % of total hydrolysed GPTMS molecule. Knowing the total organic, the C-factor, and the molecular mass of gelatin, organic GPTMS, and inorganic GPTMS, the contributions of each component were identified, and the ratio of gelatin to silica (from TEOS contributions only) was calculated. The estimated values are shown in Table 14.

The values for the 78G CF500 3D printed hybrid were also assessed to check the method with a different G composition. All estimations resulted in composition values very close, with <3 % difference in G composition to those predicted. This was expected considering the long aging times used in the 3D printing method eliminating the presence of unreacted small molecules though condensation and removing solvent by freeze-drying.

Table 14. Percentage mass contributions of each hybrid component as calculated from the total percentage of organic of the hybrids produced using the HF-free 3D printing method and the C-factor for hybrids with composition 70G: CF250, CF500, CF750.

Designed composition	3D printing method organic content /%	Percentage contributions of each hybrid component to the total mass				Estimated Composition
		GPTMS organic /%	Gelatin /%	GPTMS inorganic /%	TEOS /%	
70G CF250	66	16	50	11	23	68G CF249
70G CF500	66	26	40	17	17	70G CF492
70G CF750	66	30	36	20	14	72G CF628
78G CF500	70	27	43	18	12	78G CF482

The TGA plots of the cotton wool-like hybrid fibres were also analysed to determine the total mass percentage of organic content. Rather than 66 % for each composition, the percentage of organic content was 62 %, 68 %, and 67 %, for 70G fibres with CF250, CF500 and CF750 respectively. As the GPTMS contributes to 66 % organic, the fluctuation in total organic content was due to changes in the amount of gelatin and TEOS incorporated into the fibres.

When electrospinning, there is opportunity for gelatin, GPTMS, and hydrolysed TEOS to be lost from the final fibre composition as droplets of solution which fall from the needle. This is typical of electrospinning and these droplets may have contained unreacted components of the solution, or excess homogeneous solution if the flow rate was too high. The former option is more likely considering the phase separation of the solutions.

Figure 54 plots the mass percentage of each component, gelatin, GPTMS organic, GPTMS inorganic and TEOS of the 70G hybrids. The total organic content of the 3D printed hybrids is marked at 66 % and the total organic content of the electrospun hybrids in laid over the graph in green.

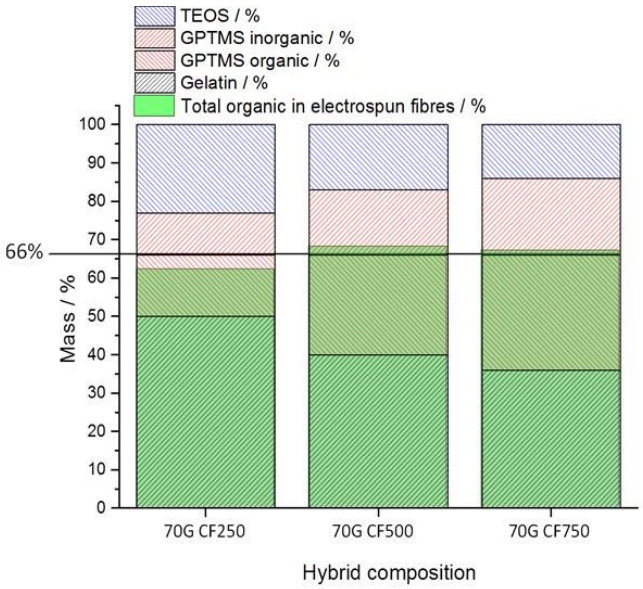

Figure 54. Chart showing the % mass contributions of gelatin, TEOS, inorganic GPTMS, and organic GPTMS of hybrids produced using the HF-free 3D printing method, and the total mass % of organic in electrospun fibres of the same composition.

From this comparison, the amount of gelatin and silica lost during electrospinning cannot be measured. However, by comparing the DSC plots of hybrids prepared using the 3D printing and electrospinning method in Figure 55, some clues were revealed. 70G CF500 TGA and DSC plots was used as an example as all composition showed a similar result. The electrospun hybrid plot has a peak at 340°C indicating the oxidation and thermal degradation of GPTMS and no high temperature gelatin degradation peak (oxidation of glycine) at ~600°C. Therefore, the amount of gelatin incorporated into the fibres was small compared to the amount incorporated when 3D printing.

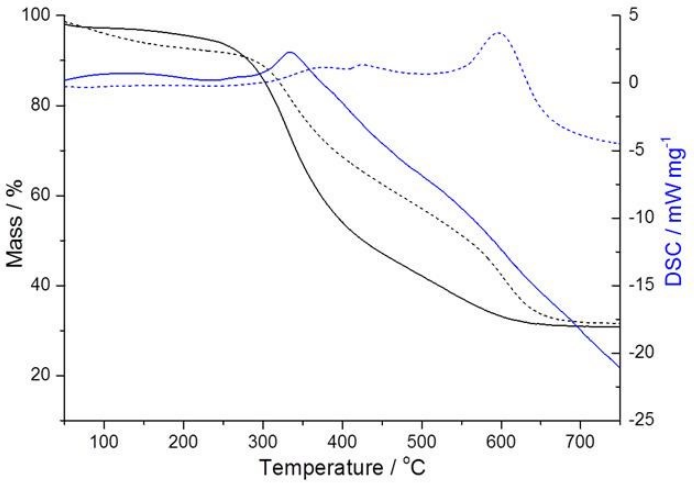

Figure 55. Thermal analysis of 70G CF500 hybrid. Solid lines indicate hybrid prepared by electrospinning, dashed lines indicate hybrid prepared by 3D printing method.

Due to the shorter aging times when electrospinning, the silica network condensation of the solutions were predicted to be low, particularly at low C-factors. The DSC plots and organic content of the fibres suggest both silica and gelatin were lost from during the electrospinning process. For the CF500 and CF750 hybrids, if less gelatin was incorporated when electrospinning, then less TEOS must also have been incorporated in order to maintain the 68 % and 67 % organic content. The CF250 hybrid must have lost more gelatin than silica.

These results are all based on the assumption that the C-factor of the functionalised gelatin samples were the same as the C-factor of the hybrid samples as expected from the functionalisation study, and that 1 GPTMS molecule contributes one SiO_3 unit of organic (76 Da). This is not the standard value for calculating moles of GPTMS organic as it is generally assumed that 1 mole of GPTMS produces 1 mole of $SiO_{1.5}$. Using the molecular weight of this organic unit (52 Da) results in a C-factor much larger than predicted, CF1082 for the CF500 sample, which is not possible as the GPTMS addition was 500x the molar amount of gelatin added, and it is again impossible that 50 % of the gelatin was lost during freeze drying.

6.3.5 Silica network condensation of fibres

The viscosity of the electrospun solutions was dependent on the crosslinking induced by condensation of the silica-gelatin hybrid network. Therefore, shorter solution-aging times were required compared to 3D printing which implied lower silica network condensation of the solutions during electrospinning, however further condensation was expected during solvent evaporation (Tonda-Turo *et al.*, 2013). The silica network condensation of 3D cotton wool-like fibres of composition 70G: 250, 500, and 750, were investigated by ^{29}Si MAS NMR. The T structure relates to the GPTMS connectivity, and Q structure relates to the TEOS connectivity. The NMR data is presented in Table 15, the NMR patterns are shown in Figure 56.

Table 15. T structure, Q structure, and degree of condensation quantified by ^{29}Si MAS NMR for 3D cotton wool-like electrospun 70G hybrids with varying C-factor: 250, 500 and 750.

			CF250 (3D)	CF500 (3D)	CF750 (3D)
T^1	δ_{iso}	[ppm]]	-49.5	-48.4	-49.8
	I	[%]	11.4	1.5	1.2
T^2	δ_{iso}	[ppm]	-56.5	-57.2	-57.5
	I	[%]	13.2	18.8	18.9
T^3	δ_{iso}	[ppm]	-65.0	-66.0	-66.2
	I	[%]	15.3	31.1	43.2
Q^2	δ_{iso}	[ppm]	-92.1	-92.4	-92.1
	I	[%]	6.3	4.7	0.1
Q^3	δ_{iso}	[ppm]	-101.1	-101.2	-101.4
	I	[%]	21.6	11.9	8.5
Q^4	δ_{iso}	[ppm]	-110.5	-110.4	-110.9
	I	[%]	32.3	32.1	28.2
D_c	[%]		**64.3**	**75.5**	**81.1**

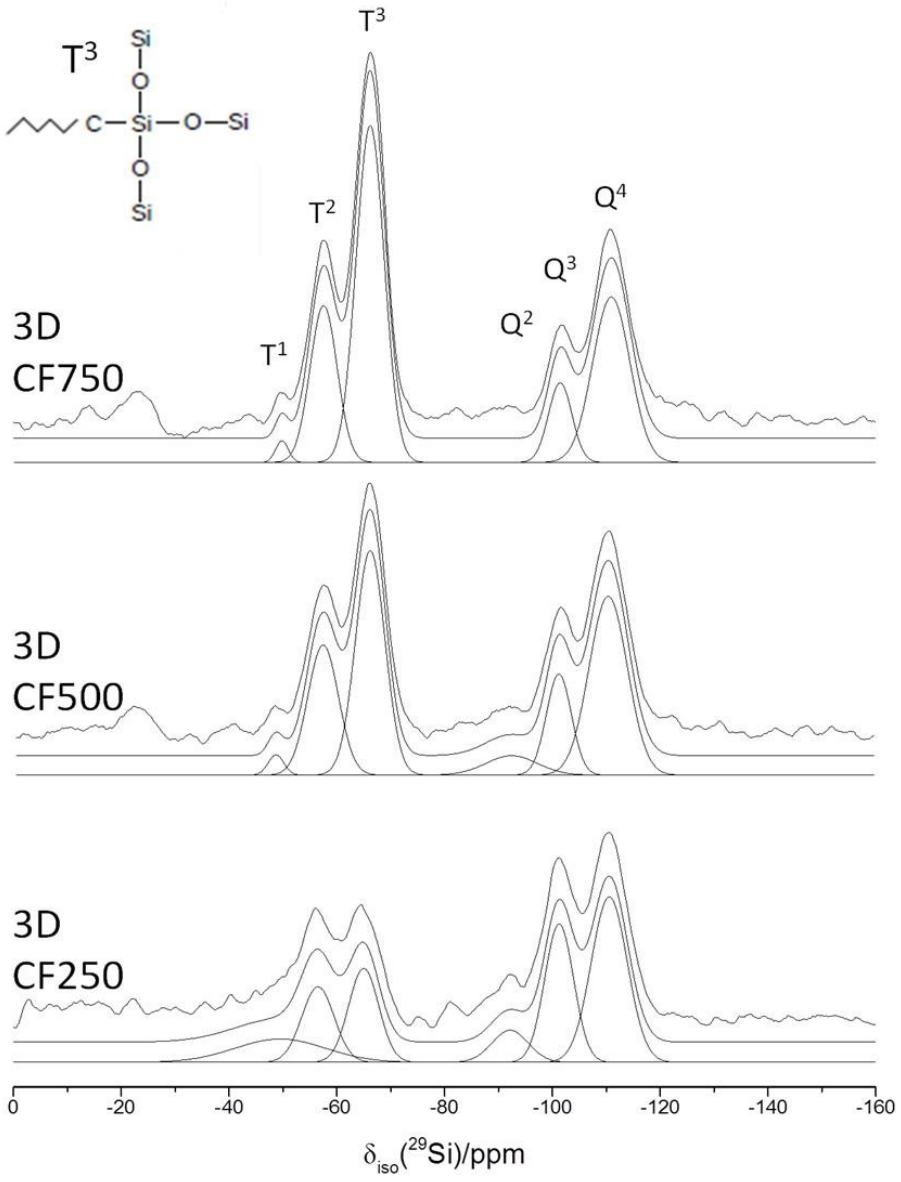

Figure 56. ^{29}Si MAS NMR spectra for 3D cotton wool-like electrospun silica-gelatin 70G hybrids comparing C-factors: CF250, CF500, CF750.

As C-factor increased, the % of Si-OH groups available for condensation increased due to the increased numbers of GPTMS molecules providing Si-OH groups while the contribution of Si-OH groups from TEOS remained constant. Therefore, with increasing C-factor, the contribution of the T structure was expected to increase and Q was expected to decrease.

Figure 57 was produced to visualise the distribution of individual species presented in Table 15. The distribution of the T species and Q species for each composition were compared to identify the most condensed T structure and Q structure.

The T structure was where the most substantial change in distribution was observed. CF250 fibres had a fairly even distribution of T^1, T^2, and T^3, compared to CF500 and CF750 fibres

which had a larger percentage of T^2 and T^3 compared to T^1. For example, CF250 fibres had 11.4 % T^1 and 15.3 % T^3, whereas CF750 fibres had 1.2 % T^1 and 43.2 % T^3. The percentage of T^3 species increased almost linearly with C-factor. The higher percentage of higher order T species indicated a more condensed T structure in higher C-factor hybrid fibres.

The overall Q species contributions from CF250, CF500, and CF750 fibres did decrease with increasing C-factor, 60.2 %, 48.7 % and 36.8 % respectively; however the Q^4 contributions were similar, with 32.3 %, 32.1 % and 28.2 % contributions from CF250, CF500 and CF750 fibres respectively. Also important was the reduction in Q^2 presence in CF750 fibres which was 0.1 % compared to 6.3 % and 4.7 % for CF250 and CF500 fibres respectively. Therefore, CF750 fibres had the most condensed Q structure as 77 % of the Q structure was attributed to Q^4, compared to 66 % for CF500 and 54 % in the CF250 hybrid fibres.

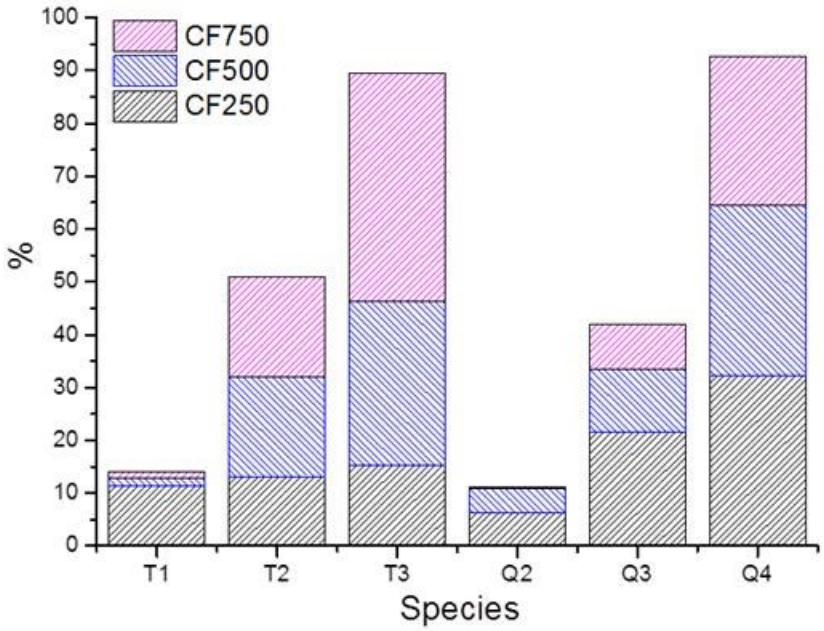

Figure 57. T and Q structure plotted to demonstrate trends in distribution of species.

Overall, the degree of condensation, D_c, of the hybrids, was highest for CF750 with a value of 81.1%. CF500 had a value of 74.5 % and CF250 had a value of 64.3 %. The solid state NMR results showed the T structure increased relative to the Q structure in the electrospun fibres, indicating improved functionalisation regardless of a reduced aging time compared to 3D printing. This is as expected from the functionalisation study in section 4.3.1 and evaluation of high C-factor compositions, Figure 54. Determining that 70G CF250 fibres had the lowest connectivity was not unexpected as FTIR results showed an additional Si-OH band that was not observed for CF500 or CF750 hybrid fibres.

6.3.6 Dissolution study

The dissolution properties of the silica-gelatin hybrid fibres were characterised by a 1 week dissolution study in TRIS. The release of gelatin and soluble silica from the cotton wool-like fibres produced from 70G CF250, 70G CF500, and 70G CF750 hybrid solutions are shown in Figure 58. Comparing these results to the dissolution results for the 3D printed scaffolds, Figure 36, involves comparing lots of variables, some unknown, including: gelatin content, GPTMS content, silica (from TEOS), surface area and some known, including: network condensation and designed composition.

The gelatin had a similar release trend for all compositions. At the end of the one-week study, CF250 showed the lowest concentration of gelatin released and none of the fibres had reached a plateau in the release. This correlates to the finding that 70G CF250 fibres had the lowest organic content. Comparing the gelatin release of the fibres to that of 3D printed scaffolds, the release trend was similar despite the predicted increase in surface area of the fibres. Considering the gelatin release as a percentage of the total organic of the hybrids, 70G electrospun fibres released ~2.0 % for all C-factors whereas the 3D printed scaffolds, 78G CF500, released ~1.4 % after one week. The gelatin release was half that of 30G CF500 foams produced by Mahony *et al.,* and with the fibres, the surface area of the fibres was larger than that of the foams (Mahony *et al.*, 2010), hence gelatin is more stable in the fibres than the foams.

The silicon detection showed marked differences between the different compositions. CF250 hybrid fibres released 42 μg mL^{-1} of Si in the first 8 h whereas CF500 and CF750 hybrid fibres released less than 5 μg mL^{-1} of Si. This correlated with the FTIR and solid state NMR findings that CF250 had a high percentage of T and Q species in low orders. After 24 h, CF250 dissolution began to slow. CF500 showed a similar release curve to CF250 however the initial rate of release for CF500 was delayed and levelling off took place at 72 h. CF750 showed a very different trend in dissolution. Instead of rapid initial release leading to a plateau of Si concentration, the release was gradual and slow, only 17 μg mL^{-1} of Si was detected at 72 h for CF750, compared to 61 μg mL^{-1} and 73 μg mL^{-1} for CF500 and CF750 respectively. This correlated to the solid state NMR results that CF750 had almost no Q^2 species, hence reducing dissolution. At the 1 week time point, CF250 showed the highest release of 94 μg mL^{-1} while CF500 and CF750 were lower, ~60 μg mL^{-1}. Considering the total inorganic content at each composition, the Si release is equivalent to 17 % loss for CF250 fibres and 13 % for CF500 and CF750 fibres. The reduced soluble silica release at higher C-factors correlates to the overall improved connectivity of the T structure with increased C-factor.

The 3D printed scaffolds, 78G CF500, lost ~18 % of the silicon at the one week time point. The reduced soluble silica release of the fibres could be due to the origin of the silica in the silica network, as cleavage of the ester bond to release GPTMS requires a higher activation energy than hydrolysis of the silica network; 56 kcal mol^{-1} compared to 49, 33 and 23 kcal $mol^{-1}$for Q^4, Q^3, and Q^2 respectively (Pelmenschikov *et al.*, 2000).

The overall mass loss was measured to be 37 % (CF250), 34 % (CF500) and 33 % (CF750) for the electrospun 70G hybrids after one week in TRIS, hence additional mass was lost as silica was released in the form of soluble silica or GPTMS.

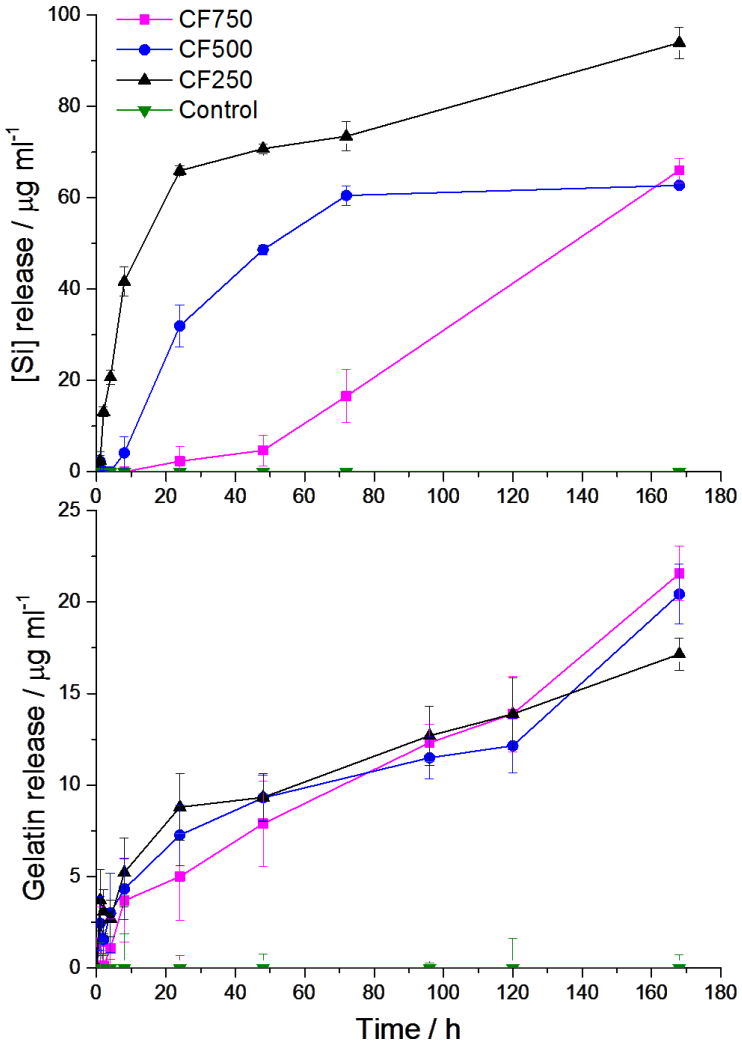

Figure 58. Results of dissolution in TRIS for fibres made with 70G and CF250, 500 and 750. Over a one week period the Si release and gelatin release was investigated as shown in a) and b) respectively.

In general, the gelatin and silica release trend during dissolution was very similar for both scaffold types (see Figure 36). Both showed non-congruent degradation, high Si release and low gelatin release when compared to the foams produced by Mahony *et al.*

Post-dissolution fibres

After one week of soaking in TRIS, the fibres were filtered, dried, and viewed under SEM. The fibres appeared to have softened and distorted but did not reduce in diameter. The mean fibre diameters in μm were 1.58 ± 0.36, 1.33 ± 0.43 and 1.15 ± 0.48 for CF250, CF500 and CF750 respectively. Comparing these to the fibre diameters before dissolution, the diameters were in the same range when errors were considered. The reduction in fibre diameter was therefore negligible, which is an important improvement in comparison to papers using similar compositions (Gao *et al.*, 2013a, Song *et al.*, 2008b, Tonda-Turo *et al.*, 2013).

Whist suspended in TRIS, the fibres would have softened due to loss of silica content however the fibre diameters (volumes) were maintained by the low gelatin release of ~2 %. Softening due to loss of silica was also observed for the 3D printed scaffolds after one week soaking, and resulted in a 95 % loss of compressive strength. Despite the distortion of the CF750 fibres, the structure looks like a flattened version of a mix of 3D cotton wool-like fibres and 3D fused fibres. The CF500 and CF250 fibres appear to show increased levels of fusion that occurred during the soaking and drying process, however this is not entirely clear as the fibres may have been fused before soaking.

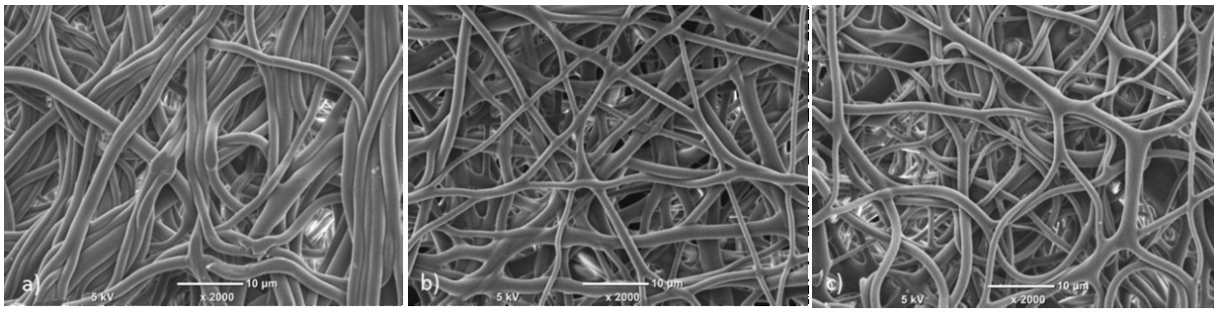

Figure 59. SEM of fibres after 1 week soaking in TRIS solution: a) CF250 sheet-structure fibres, b) CF500 cotton wool-like fibres and c) CF750 cotton wool-like fibres.

Post-dissolution chemical bonding of fibres

FTIR data in Figure 60 shows the change in spectra of the fibres after the one week dissolution study in TRIS. The bands were normalised against the gelatin amide bands. Gelatin reduced during dissolution, but as the gelatin release was similar for all compositions the data was still comparable.

For all compositions there was a reduction in the Si-C band at 1200 cm^{-1} and Si-OH/oxirane band at 900 cm^{-1} relative to the gelatin amide I band. The reduction in these bands indicated a loss of GPTMS relative to gelatin for all compositions. This could be due to cleavage of the ester or the loss of self-hydrolysed species.

The asymmetric bands for Si-O-Si: 1040 cm^{-1} and 1090 cm^{-1}, and symmetric band at 790 cm^{-1}, reduced for CF250 and CF500, however the band showed less reduction in intensity for CF750 fibres. This correlated to the solid state NMR results where a high proportion of well-connected GPTMS molecules and low proportion of Q^2 species were observed for CF750 hybrid fibres compared to lower C-factor fibres.

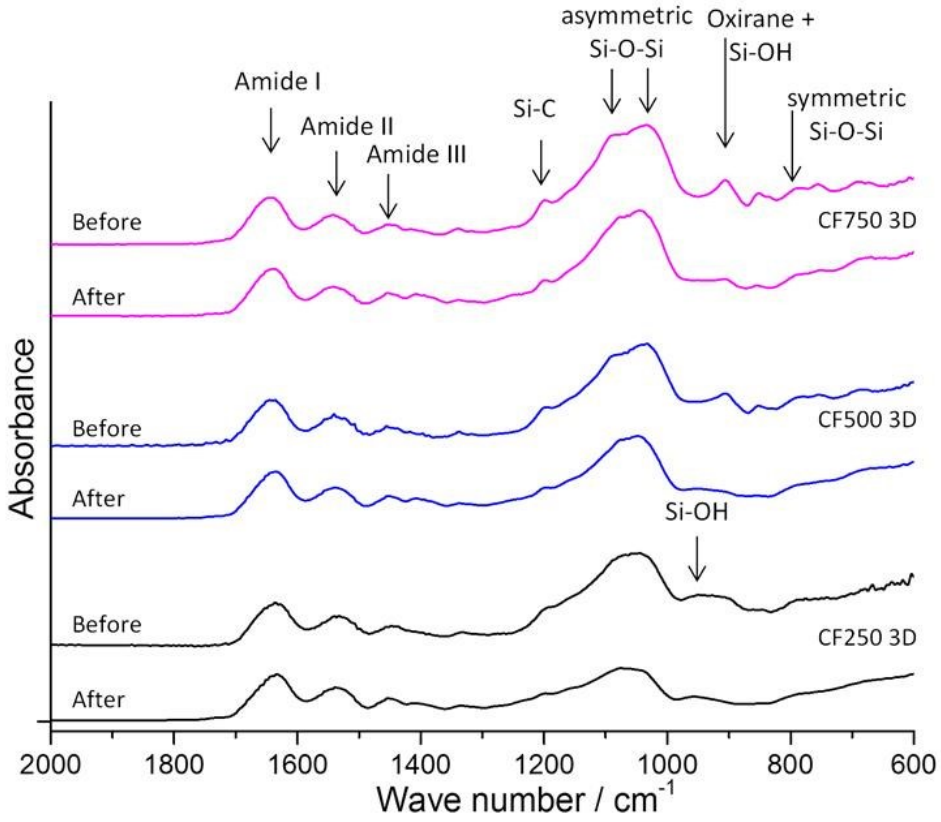

Figure 60. FTIR spectra of 70G hybrid: CF250, CF500 and CF750 fibres before and after one week dissolution study in TRIS.

6.3.7 Cell attachment and viability

The fibres were designed for use in the superficial zone of the cartilage tissue scaffold so the cell attachment, morphology and viability were assessed of 70G CF500 and 70G CF750 fibres. The 70G CF250 electrospun fibres were not examined due to the reduced stability of the fibres in TRIS making them less appropriate for the application.

The SEM images of individual cells on the fibres in Figure 61 show that cells readily attached to the fibres in the 3-day attachment study. The cells maintained a spherical morphology, even when attached to various fibres as seen in image b.

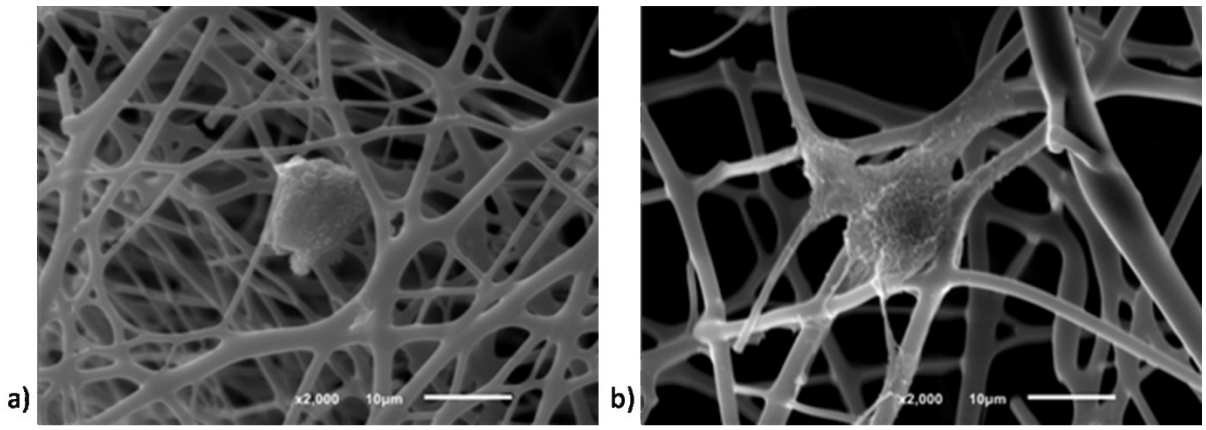

Figure 61. SEM image of the spherical morphology of the ATDC5 chondrocytes attached to: a) 70G CF500; and b) 70G CF750 fibres.

The fusion observed of the fibres is unlikely to be due to fusion during the cell study. The fibres used for the cell work were 3D fusion fibres as the fibre volume produced was limited.

The confocal images of the LIVE/DEAD assay in Figure 61 demonstrated that the composition and structure were not cytotoxic to cells as no dead (red) cells were observed after 7 days. The cells generally appeared to maintain the spherical morphology expected of hyaline cartilage. Again, the fibre structure seen is not ideal and beading is observed, however this has not been detrimental to the results. The out of focus regions of Figure 61b are due to the presence of fibres above the cells, where the microscope is focused.

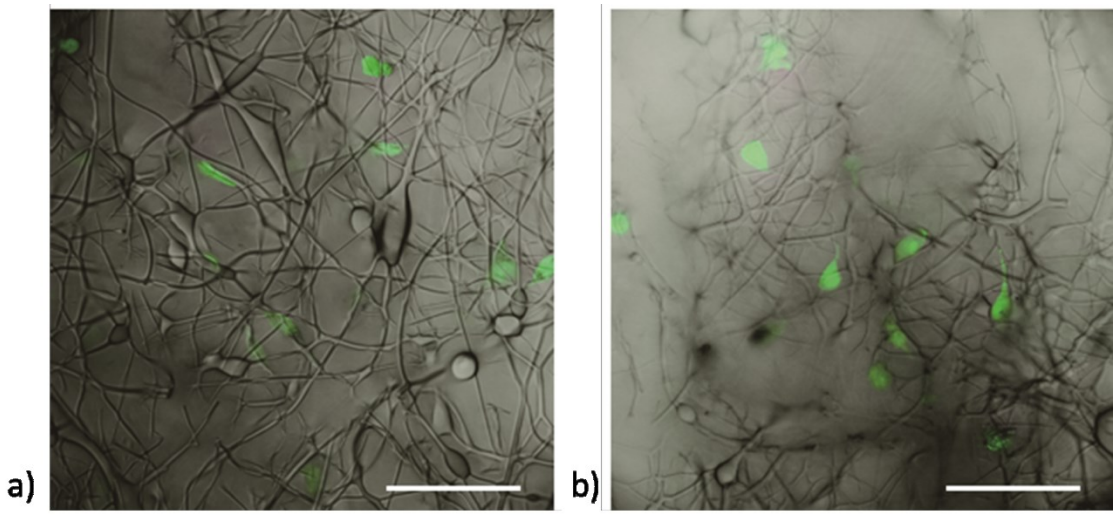

Figure 62. *In vitro* toxicity evaluation by a LIVE/DEAD assay of a) 70G CF500 fibres and b) 70G CF750 fibres, using calcein AM for staining of the live cells (green) and ethidium homodimer-1 for staining the nuclei of dead cells (red). Scale bar is 100 µm.

Overall, the fibres are small compared to cells, and individual cells are hosted on individual and fused fibres. The spacing between fibres is expected to allow for 3D regeneration of the superficial zone, however a cartilaginous matrix study is required to fully assess whether these fibres would increase the cell and ECM density in the superficial layer of the scaffold. Current results are promising as cell viability is high and chondrocytes remain spherical when attached to the fibres.

6.4 Summary

This chapter presented a new method for electrospinning silica-gelatin hybrids functionalised by GPTMS directly from sol. 3D cotton wool-like structures of ~1.5 µm diameter fibres from the hybrid solutions: 70G CF250, 70G CF500, 70G CF750, were produced. The electrospinning parameters used to obtain these cotton wool-like fibres were: applied voltage of 9.5 kV, needle collector separation of 20 cm, flow rate of 0.05 mL min^{-1}, 22 gauge stainless steel needle, humidity of 55 %, and syringe temperature of 50°C. The material parameters required to obtain these cotton wool-like fibres were: 60-80 cP viscosity for CF250 and CF500, 60-100 cP viscosity for CF750. To form the cotton wool-like-like structure the high humidity and requisite viscosity were essential along with preventing the fibres from coming into contact with each other and the collector surface. 2D fibre mats of distinct fibres were also formed using silica-gelatin hybrid compositions of 70G CF185 and 70G CF250.

To achieve distinct cotton wool-like fibres with high C-factors, the first consideration was the requisite viscosity. The viscosity-time plot showed an inflection point. As the crosslinking in the network reached a critical point, the solvent and gel began to phase separate, increasing the viscosity at a higher rate. The onset time of the inflection point increased with C-factor due to the increased amount of solvent present.

The thermal analysis of hybrids with increasing C-factor showed that a C-factor of CF750 was not attainable when using the 3D printing method and 70G hybrids. A C-factor of 630 was achieved which still offered a considerable increase in functionalisation compared to CF500 hybrids for which a C-factor of 492 was estimated. During the electrospinning process, the gelatin and TEOS content were reduced compared to when 3D printing. This was apparent from the missing gelatin degradation peak at ~600°C peak in the DSC plot of the electrospun fibres. The organic portion of GPTMS represents 66 % by mass, therefore to maintain the total organic content observed for the fibres, 60 %, 67 %, and 68 % for 70G: CF250, CF500, and CF750 respectively, TEOS must also have been lost as solvent or in droplets when exiting the needle.

The silica network connectivity, D_c, of the hybrids, increased with increasing C-factor. The D_c improved from 64.3 % to 75.5 %, to 81.1 % for the increasing C-factor hybrid fibres due to the increased functionalisation, solvent content which increased solution-aging times, and the solvent evaporation period where GPTMS and sol-gel condensation occurred when electrospinning.

In the dissolution study, CF750 showed reduced Si release and a more linear release trend compared to the other compositions which showed initial rapid release and reached a plateau after 3 days. In total there was 17 % Si release as a percentage of the total inorganic content from CF250 fibres, and 13 % loss from CF500 and CF750 fibres. The gelatin release for all compositions was similar, ~2 %, with linear release observed. SEM images after this one week study indicated increased fusion of the CF250 and CF500 hybrid fibres but this was less apparent in CF750 hybrid fibres. FTIR data comparing the composition before and after dissolution again confirmed CF750 to have a more stable silica network.

The 70G CF750 composition proved to be the most promising due to reduced dissolution in TRIS and highest D_c. The cell attachment study showed that chondrocytes seeded on the fibres retained the spherical morphology typical of hyaline cartilage and no cell death was induced.

CHAPTER 7. CONCLUDING REMARKS

Silica-gelatin sol-gel hybrids were developed as new biomaterial inks for 3D printing and electrospinning in order to create a zonal scaffold for cartilage regeneration. The most important finding was that Class II hybrids were compatible with 3D printing when using the HF-free method developed here and when monitoring the gelation rate of the hybrid material. Another novel aspect of this work was the ability to form cotton wool-like fibre structures from the hybrid material. The high C-factor solutions formed distinct fibres with excellent volume stability after 1 week soaking in TRIS.

Compared to prior work, the 3D printed scaffolds have improved mechanical properties over the foamed silica-gelatin hybrid scaffolds by Mahony *et al.* (Mahony *et al.*, 2010). In comparison to the 3D printed BG-gelatin Class I hybrids produced by Gao *et al.*, the scaffolds here have smaller channel and strut width, as well as reduced swelling. The electrospun fibres produced are more volumetrically stable in TRIS than other gelatin-GPTMS based fibres (Tonda-Turo *et al.*, 2013, Ren *et al.*, 2010, Gao *et al.*, 2013a) and distinct fibres were formed using high C-factor compositions which was not previously observed (Song *et al.*, 2008b).

The main limitation of these techniques to create a cartilage tissue scaffold is the limited time window for 3D printing and electrospinning due to the continuing network condensation and crosslinking of the hybrid material. Secondary limitations include the strut width during 3D printing and shift in strut arrangement during scaffold aging. To reduce strut width, the concentration of the hybrid gel could be increased but this would affect the network condensation rate, and reducing the aging time would limit the final silica network condensation.

I believe the scaffold developed in this work is clinically relevant due to the high bioactivity of the material, direct cell infiltration channels, and volume stability. The mechanical properties when wet are compatible with native tissue and low swelling allows for direct implantation of the scaffold into the defect site.

7.1 Summary of results

The primary objective was to adapt the silica-gelatin hybrid process to produce a highly condensed sol-gel network without the use of HF, but with GPTMS as the coupling agent. The functionalisation and aging conditions were investigated and the conditions selected for 3D printing were 3 h functionalisation at 40°C, and 1 week scaffold-aging at room temperature before drying. To electrospin, the method replaced 40 % of water with ethanol during the 3 h functionalisation to increase the volatility of the solvent when electrospinning. In both cases, the condensation of the sol-gel network increased the viscosity of the hybrids over time and had to be monitored to determine a suitable viscosity window for 3D printing and electrospinning. The hybrid composition for 3D printing, 78G CF500, was selected due to its high gelatin content, efficient crosslinking, and suitable gelation rate. The minimum strut separation achieved was 1 mm; the limiting factor was the width of the strut deposited when extruded through the smallest compatible nozzle with lowest compatible deposition rate and print speed. The hybrid compositions which produced cotton wool-like fibres at 55 % humidity were 70G hybrids with CF250, CF500 and CF750, and ~1.5 µm fibre diameters were measured.

The drying method was critical for both fabrication methods. 3D printed scaffolds had controllable strut width and separation when dried via critical point drying, but had shrunken, spindle-like struts when freeze-dried. In both cases, dried scaffolds had dense walls running vertically across the scaffold which provided additional compressive strength but retained large interconnects between the walls to allow for efficient cell infiltration and diffusion. Scaffolds 3D printed with 1 mm strut separation resulted in scaffolds with ~160 µm strut width and ~200 µm channels, the desired channel width for 3D printed cartilage tissue scaffolds. The fibres were dried at room temperature overnight, however to maintain the cotton wool-like structure, fibre-fibre and fibre-collector contacts were minimised by using a collector that fibres could essentially hang from.

In both cases, the degree of condensation of the hybrids was measured. Comparing 78G CF500 3D printed hybrids to 78G CF500 foamed hybrids (using HF), the D_c values were 90.4 % and 94.2 % respectively, and hence the revised hybrid method maintained high network condensation. The electrospun fibres with 70G and increasing C-factors produced hybrids with increasing D_c values with improvements arising from the T structure. CF250, CF500 and CF750 had D_c values 64.3 %, 75.5 %, and 81.1 % respectively.

The stability of the 3D printed scaffolds and electrospun fibres in TRIS were measured over a one month period for 3D printed scaffolds, and a one week period for the fibres. At the end of the 3D printed scaffold study, ~25 % of the total silica content was detected (as silicon), and the gelatin released was ~3 % of the total organic content. The CF500 and CF750 fibres released ~13 % of the total silica content as Si, and the gelatin released was ~2 % of the total organic content. The CF250 fibres released slightly more silicon, ~17 %. This low gelatin release resulted in stable structures in terms of volume, however mechanical properties were affected by the loss of inorganic. If the silicon was lost in the form of $Si(OH)_4$, the mass of soluble silica lost is 3.4x the mass of silicon detected, and the mass loss is greater, 6.8x, when Si is lost through hydrolysis of the GPTMS ester bond. After one week soaking in TRIS, the FD 3D printed scaffolds lost 90 % of their compressive strength and Young's modulus. When wet, the CPD scaffolds had a compressive strength of 1.3 MPa for CPD scaffolds with 200 μm channel width which is an order of magnitude lower than the compressive strength of hyaline cartilage ~30 MPa. A positive outcome from the loss of inorganic was a non-linear compressive response from the CPD scaffolds and a Young's modulus comparable to native ECM, 0.5-1 MPa.

In both scaffolds, chondrocytes showed excellent cell attachment in 3 days and a 28-day cartilaginous matrix formation study on the 3D printed scaffolds showed uniform distribution of healthy hyaline cartilage throughout using one quarter of the cells required for ACI. This study was not performed on the electrospun fibres, however the spherical morphology of cells when attached to the fibres was very promising.

Overall, development of a method to produce silica-gelatin-GPTMS hybrids, with a high degree of network condensation, but avoiding rapid gelation, was successful. The compositions were tailored for the 3D printing and electrospinning process and the desired channel width and fibre width were obtained. The dissolution study showed excellent volume stability of the hybrids and the loss of inorganic resulted in a Young's modulus in the range of native ECM, but was detrimental to compressive strength.

7.2 Further work

To improve and establish the viability of this cartilage tissue scaffold, there are various avenues to explore. Firstly, a cartilaginous matrix study should be performed on the electrospun layer to assess whether the formation of a superficial zone is possible. Current results show cell attachment and spherical morphology of chondrocytes, but cell density and native hyaline ECM formation is yet to be observed.

The stability of the dual layer must be assessed in *in vivo* conditions. By implanting the scaffolds into the articular joints of cadavers, whether the fibres are retained on top of the 3D printed scaffold when natural articular motions occur could be assessed. The first idea to stabilize the layers is to place the 3D printed scaffold with the fibres on top and centrifuge whilst suspended in medium to create mechanical linkages. If not stable, the alternative option is to use glue; gelatin-GPTMS glue would be the starting point. Once stable, the compatibility of the electrospun layer as a conformable, low friction surface must be evaluated by assessing any damage to the opposing layer of hyaline cartilage in the joint.

The section of the scaffold designed to integrate with subchondral bone could be improved by calcium inclusion to stimulate HCA nucleation on the surface. Calcium salts used to make bioactive glass do not incorporate into sol-gel hybrids due to the low-temperature processing route. Alternatively, calcium alkoxides may be introduced to the sol-gel process however they are highly reactive with water and hydroxyl groups and would therefore affect the 3D printing process (Poologasundarampillai *et al.*, 2014b). It may be possible to add the calcium alkoxide solution to the hybrid as it is extruded from the nozzle, or post-printing.

To assess the potential of the scaffold as a cell-free, AMIC implant, the scaffolds require testing *in vivo* using an osteochondral rabbit model. Ideally, the high bioactivity of the scaffold would stimulate stem cells released from the bone marrow to regenerate hyaline cartilage without the need for pre-selecting or pre-seeding the cells onto the scaffold. Depending on the speed and strength of the scaffold fixation with subchondral bone, additional fixation of the scaffold with the surround cartilage may be required using fibrin glue or alternatives.

REFERENCES

AHMED, T. A. E. & HINCKE, M. T. 2010. Strategies for articular cartilage lesion repair and functional restoration. *Tissue Engineering Part B-Reviews,* 16**,** 305-329.

AKIZUKI, S., MOW, V. C., MULLER, F., PITA, J. C., HOWELL, D. S. & MANICOURT, D. H. 1986. Tensile properties of human knee-joint cartilage: 1. Influence of ionic conditions, weight bearing, and fibrillation on the tensile modulus. *Journal of Orthopaedic Research,* 4**,** 379-392.

ALLEN, J. L., COOKE, M. E. & ALLISTON, T. 2012. ECM stiffness primes the TGF beta pathway to promote chondrocyte differentiation. *Molecular Biology of the Cell,* 23**,** 3731-3742.

ALLO, B. A., RIZKALLA, A. S. & MEQUANINT, K. 2010. Synthesis and alectrospinning of epsilon-polycaprolactone-bioactive glass hybrid biomaterials via a sol-gel process. *Langmuir,* 26**,** 18340-18348.

ARORA, A., KOTHARI, A. & KATTI, D. S. 2015. Pore orientation mediated control of mechanical behavior of scaffolds and its application in cartilage-mimetic scaffold design. *Journal of the Mechanical Behavior of Biomedical Materials,* 51**,** 169-183.

BENYA, P. D. & SHAFFER, J. D. 1982. Dedifferentiated chondrocytes re-express the differentiated collagen phenotype when cultured in agarose gels. *Cell,* 30**,** 215-224.

BHARDWAJ, N. & KUNDU, S. C. 2010. Electrospinning: A fascinating fiber fabrication technique. *Biotechnology Advances,* 28**,** 325-347.

BIAN, L., FONG, J. V., LIMA, E. G., STOKER, A. M., ATESHIAN, G. A., COOK, J. L. & HUNG, C. T. 2010. Dynamic mechanical loading enhances functional properties of tissue-engineered cartilage using mature canine chondrocytes. *Tissue Engineering Part A,* 16**,** 1781-1790.

BIGI, A., COJAZZI, G., PANZAVOLTA, S., ROVERI, N. & RUBINI, K. 2002. Stabilization of gelatin films by crosslinking with genipin. *Biomaterials,* 23**,** 4827-4832.

BIGI, A., COJAZZI, G., PANZAVOLTA, S., RUBINI, K. & ROVERI, N. 2001. Mechanical and thermal properties of gelatin films at different degrees of glutaraldehyde crosslinking. *Biomaterials,* 22**,** 763-768.

BILLIET, T., GEVAERT, E., DE SCHRYVER, T., CORNELISSEN, M. & DUBUEL, P. 2013. The 3D printing of gelatin methacrylamide cell-laden tissue-engineered constructs with high cell viability *Biomaterials,* 31**,** 49-62.

BORAL, S., GUPTA, A. N. & BOHIDAR, H. B. 2006. Swelling and de-swelling kinetics of gelatin hydrogels in ethanol-water marginal solvent. *International Journal of Biological Macromolecules,* 39**,** 240-249.

BOSCHETTI, F., PENNATI, G., GERVASO, F., PERETTI, G. M. & DUBINI, G. 2004. Biomechanical properties of human articular cartilage under compressive loads. *Biorheology,* 41**,** 159-166.

BRINKER, C. J. 1988. Hydrolysis and condensation of silicates- effects on structure. *Journal of Non-Crystalline Solids,* 100**,** 31-50.

BRYANT, S. J. & ANSETH, K. S. 2003. Controlling the spatial distribution of ECM components in degradable PEG hydrogels for tissue engineering cartilage. *Journal of Biomedical Materials Research Part A,* 64A**,** 70-79.

CAI, Y., LI, J., POH, C. K., TAN, H. C., THIAN, E. S., FUH, J. Y. H., SUN, J., TAY, B. Y. & WANG, W. 2013. Collagen grafted 3D polycaprolactone scaffolds for enhanced cartilage regeneration. *Journal of Materials Chemistry B,* 1**,** 5971-5976.

CESARIO, M. R., MACEDO, D. A., OLIVEIRA, R. M. P. B., PIMENTEL, P. M., MOREIRA, R. L. & MELO, D. M. A. 2011. The synthesis, thermal stability, crystal structure and spectroscopic study of $La_{0.80}Sr_{0.20}MnO_3$ powder obtained by the modified Pechini's method. *Journal of Ceramic Processing Research,* 12**,** 102-105.

CHEN, H.-C., JAO, W.-C. & YANG, M.-C. 2009. Characterization of gelatin nanofibers electrospun using ethanol/formic acid/water as a solvent. *Polymers for Advanced Technologies,* 20**,** 98-103.

CHEN, Y., DONG, K., LIU, Z. & XU, F. 2012. Double network hydrogel with high mechanical strength: Performance, progress and future perspective. *Science China-Technological Sciences,* 55**,** 2241-2254.

CHEN, Z. C. C., EKAPUTRA, A. K., GAUTHAMAN, K., ADAIKAN, P. G., YU, H. & HUTMACHER, D. W. 2008. In vitro and in vivo analysis of co-electrospun scaffolds made of medical grade poly(epsilon-caprolactone) and porcine collagen. *Journal of Biomaterials Science-Polymer Edition,* 19**,** 693-707.

CHERNEY, L. T. 1999. Structure of Taylor cone-jets: limit of low flow rates. *Journal of Fluid Mechanics,* 378**,** 167-197.

CHUNG, C., BEECHAM, M., MAUCK, R. L. & BURDICK, J. A. 2009. The influence of degradation characteristics of hyaluronic acid hydrogels on in vitro neocartilage formation by mesenchymal stem cells. *Biomaterials,* 30**,** 4287-4296.

CHUNG, C. & BURDICK, J. A. 2008. Engineering cartilage tissue. *Advanced Drug Delivery Reviews,* 60**,** 243-262.

COHEN, D. L., MALONE, E., LIPSON, H. & BONASSAR, L. J. 2006. Direct freeform fabrication of seeded hydrogels in arbitrary geometries. *Tissue Engineering,* 12**,** 1325-1335.

CORREIA, D. M., PADRAO, J., RODRIGUES, L. R., DOURADO, F., LANCEROS-MENDEZ, S. & SENCADAS, V. 2013. Thermal and hydrolytic degradation of electrospun fish gelatin membranes. *Polymer Testing,* 32**,** 995-1000.

CUI, X., BREITENKAMP, K., FINN, M. G., LOTZ, M. & D'LIMA, D. D. 2012. Direct human cartilage repair using three-dimensional bioprinting technology. *Tissue Engineering Part A,* 18**,** 1304-1312.

DE VRIEZE, S., VAN CAMP, T., NELVIG, A., HAGSTROM, B., WESTBROEK, P. & DE CLERCK, K. 2009. The effect of temperature and humidity on electrospinning. *Journal of Materials Science,* 44**,** 1357-1362.

DURAN, A., SERNA, C., FORNES, V. & NAVARRO, J. M. F. 1986. Structural considerations about SiO_2 glasses prepared by sol-gel. *Journal of Non-Crystalline Solids,* 82**,** 69-77.

DUSEK, K. 1971. Phase separation in ternary systems induced by crosslinking. *Chemicke Zvesti,* 25**,** 184-189.

EDELSTEN, L., JEFFREY, J. E., BURGIN, L. V. & ASPDEN, R. M. 2010. Viscoelastic deformation of articular cartilage during impact loading. *Soft Matter,* 6**,** 5206-5212.

EGLIN, D., MORTISEN, D. & ALINI, M. 2009. Degradation of synthetic polymeric scaffolds for bone and cartilage tissue repairs. *Soft Matter,* 5**,** 938-947.

EISENBACK, J. D. 1986. A comparison of techniques useful for preparing nematodes for scanning electron-microscopy. *Journal of Nematology,* 18**,** 479-487.

EMANS, P. J., JANSEN, E. J. P., VAN IERSEL, D., WELTING, T. J. M., WOODFIELD, T. B. F., BULSTRA, S. K., RIESLE, J., VAN RHIJN, L. W. & KUIJER, R. 2013. Tissue-engineered constructs: the effect of scaffold architecture in osteochondral repair. *Journal of Tissue Engineering and Regenerative Medicine,* 7**,** 751-756.

FAN, H., HU, Y., ZHANG, C., LI, X., LV, R., QIN, L. & ZHU, R. 2006. Cartilage regeneration using mesenchymal stem cells and a PLGA-gelatin/chondroitin/hyaluronate hybrid scaffold. *Biomaterials,* 27**,** 4573-4580.

FARRIS, S., SONG, J. & HUANG, Q. 2010. Alternative reaction mechanism for the cross-linking of gelatin with glutaraldehyde. *Journal of Agricultural and Food Chemistry,* 58, 998-1003.
FONG, H., CHUN, I. & RENEKER, D. H. 1999. Beaded nanofibers formed during electrospinning. *Polymer,* 40, 4585-4592.
FORTIER, L. A., BARKER, J. U., STRAUSS, E. J., MCCARREL, T. M. & COLE, B. J. 2011. The role of growth factors in cartilage repair. *Clinical Orthopaedics and Related Research,* 469, 2706-2715.
FREED, L. E., VUNJAKNOVAKOVIC, G., BIRON, R. J., EAGLES, D. B., LESNOY, D. C., BARLOW, S. K. & LANGER, R. 1994. Biodegradable polymer scaffolds for tissue engineering. *Bio-Technology,* 12, 689-693.
FU, Q., SAIZ, E. & TOMSIA, A. P. 2011. Direct ink writing of highly porous and strong glass scaffolds for load-bearing bone defects repair and regeneration. *Acta Biomaterialia,* 7, 3547-3554.
FURUKAWA, T., EYRE, D. R., KOIDE, S. & GLIMCHER, M. J. 1980. Biochemical-studies on repair cartilage resurfacing experimental defects in the rabbit knee. *Journal of Bone and Joint Surgery-American Volume,* 62, 79-89.
GABRIELLI, L., RUSSO, L., POVEDA, A., JONES, J. R., NICOTRA, F., JIMENEZ-BARBERO, J. & CIPOLLA, L. 2013. Epoxide opening versus silica condensation during sol-gel hybrid biomaterial synthesis. *Chemistry - A European Journal,* 19, 7856-7864.
GAO, C., GAO, Q., LI, Y., RAHAMAN, M. N., TERAMOTO, A. & ABE, K. 2013a. In vitro evaluation of electrospun gelatin-bioactive glass hybrid scaffolds for bone regeneration. *Journal of Applied Polymer Science,* 127, 2588-2599.
GAO, C., RAHAMAN, M. N., GAO, Q., TERAMOTO, A. & ABE, K. 2013b. Robotic deposition and in vitro characterization of 3D gelatin-bioactive glass hybrid scaffolds for biomedical applications. *Journal of Biomedical Materials Research Part A,* 101A, 2027-2037.
GEIGER, B., BERSHADSKY, A., PANKOV, R. & YAMADA, K. M. 2001. Transmembrane extracellular matrix-cytoskeleton crosstalk. *Nature Reviews Molecular Cell Biology,* 2, 793-805.
GENES, N. G., ROWLEY, J. A., MOONEY, D. J. & BONASSAR, L. J. 2004. Effect of substrate mechanics on chondrocyte adhesion to modified alginate surfaces. *Archives of Biochemistry and Biophysics,* 422, 161-167.
GIANNITELLI, S. M., ACCOTO, D., TROMBETTA, M. & RAINER, A. 2014. Current trends in the design of scaffolds for computer-aided tissue engineering. *Acta Biomaterialia,* 10, 580-594.
GOBBI, A., NUNAG, P. & MALINOWSKI, K. 2005. Treatment of full thickness chondral lesions of the knee with microfracture in a group of athletes. *Knee Surgery Sports Traumatology Arthroscopy,* 13, 213-221.
GONG, J. P., KATSUYAMA, Y., KUROKAWA, T. & OSADA, Y. 2003. Double-network hydrogels with extremely high mechanical strength. *Advanced Materials,* 15, 1155-1158.
GORE, G. 1869. XXXIII.-On hydrofluoric acid. *Journal of the Chemical Society,* 22, 368-406.
HENCH, L. L. & POLAK, J. M. 2002. Third-generation biomedical materials. *Science,* 295, 1014-1017.
HENCH, L. L. & WILSON, J. 1993. An Introduction to Bioceramics. *Wold Scientific Publishing Co. Pta. Ltd.* Singapore.
HIDAKA, C., CHENG, C., ALEXANDRE, D., BHARGAVA, M. & TORZILLI, P. A. 2006. Maturational differences in superficial and deep zone articular chondrocytes. *Cell and Tissue Research,* 323, 127-135.

HOCH, E., SCHUH, C., HIRTH, T., TOVAR, G. E. M. & BORCHERS, K. 2012. Stiff gelatin hydrogels can be photo-chemically synthesized from low viscous gelatin solutions using molecularly functionalized gelatin with a high degree of methacrylation. *Journal of Materials Science-Materials in Medicine,* 23, 2607-2617.
HOHMAN, M. M., SHIN, M., RUTLEDGE, G. & BRENNER, M. P. 2001. Electrospinning and electrically forced jets. II. Applications. *Physics of Fluids,* 13, 2221-2236.
HOLLISTER, S. J. 2005. Porous scaffold design for tissue engineering. *Nature Materials,* 4, 518-524.
HONG, S., SYCKS, D., CHAN, H. F., LIN, S., LOPEZ, G. P., GUILAK, F., LEONG, K. W. & ZHAO, X. 2015. 3D printing of highly stretchable and tough hydrogels into complex, cellularized structures. *Advanced Materials,* 27, 4035-4040.
HOSHIKAWA, A., NAKAYAMA, Y., MATSUDA, T., ODA, H., NAKAMURA, K. & MABUCHI, K. 2006. Encapsulation of chondrocytes in photopolymerizable styrenated gelatin for cartilage tissue engineering. *Tissue Engineering,* 12, 2333-2341.
HOSOYA, K., OHTSUKI, C., KAWAI, T., KAMITAKAHARA, M., OGATA, S., MIYAZAKI, T. & TANIHARA, M. 2004. A novel covalently crosslinked gel of alginate and silane with the ability to form bone-like apatite. *Journal of Biomedical Materials Research Part A,* 71A, 596-601.
HUANG, J.-J., YANG, S.-R., CHU, I. M., BREY, E. M., HSIAO, H.-Y. & CHENG, M.-H. 2013. A comparative study of the chondrogenic potential between synthetic and natural scaffolds in an in vivo bioreactor. *Science and Technology of Advanced Materials,* 14.
HUANG, J. I., KAZMI, N., DURBHAKULA, M. M., HERING, T. M., YOO, J. U. & JOHNSTONE, B. 2005. Chondrogenic potential of progenitor cells derived from human bone marrow and adipose tissue: A patient-matched comparison. *Journal of Orthopaedic Research,* 23, 1383-1389.
HUNT, N. C. & GROVER, L. M. 2010. Cell encapsulation using biopolymer gels for regenerative medicine. *Biotechnology Letters,* 32, 733-742.
HUNZIKER, E. B. 2002. Articular cartilage repair: basic science and clinical progress. A review of the current status and prospects. *Osteoarthritis and Cartilage,* 10, 432-463.
INNOCENZI, P., BRUSATIN, G., GUGLIELMI, M. & BERTANI, R. 1999. New synthetic route to (3-glycidoxypropyl)trimethoxysilane-base hybrid organic-inorganic materials. *Chemistry of Materials,* 11, 1672-1679.
JAKUS, A. E., RUTZ, A. L. & SHAH, R. N. 2016. Advancing the field of 3D biomaterial printing. *Biomedical materials (Bristol, England),* 11, 014102-014102.
JERMAN, I., VUK, A. S., KOZELJ, M., SVEGL, F. & OREL, B. 2011. Influence of amino functionalised PUSS additive on the corrosion properties of (3-glycidoxypropyl)trimethoxysilane coatings on AA 2024 alloy. *Progress in Organic Coatings,* 72, 334-342.
JOHNSON, L. L. 1986. Arthroscopic abrasion arthroplasty historical and pathological perspective present status. *Arthroscopy,* 2, 54-69.
JONES, J. R. 2013. Review of bioactive glass: from Hench to hybrids. *Acta biomaterialia,* 9, 4457-86.
JURVELIN, J. S., BUSCHMANN, M. D. & HUNZIKER, E. B. 1997. Optical and mechanical determination of Poisson's ratio of adult bovine humeral articular cartilage. *Journal of Biomechanics,* 30, 235-241.
KASUGA, T., OBATA, A., MAEDA, H., OTA, Y., YAO, X. & ORIBE, K. 2012. Siloxane-poly(lactic acid)-vaterite composites with 3D cotton-like structure. *Journal of Materials Science-Materials in Medicine,* 23, 2349-2357.
KAWANISHI, M., OURA, A., FURUKAWA, K., FUKUBAYASHI, T., NAKAMURA, K., TATEISHI, T. & USHIDA, T. 2007. Redifferentiation of dedifferentiated bovine articular chondrocytes enhanced by cyclic hydrostatic pressure under a gas-controlled system. *Tissue Engineering,* 13, 957-964.

KELLY, D. J. & PRENDERGAST, P. J. 2006. Prediction of the optimal mechanical properties for a scaffold used in osteochondral defect repair. *Tissue Engineering,* 12, 2509-2519.
KERIN, A. J., WISNOM, M. R. & ADAMS, M. A. 1998. The compressive strength of articular cartilage. *Proceedings of the Institution of Mechanical Engineers Part H-Journal of Engineering in Medicine,* 212, 273-280.
KI, C. S., BAEK, D. H., GANG, K. D., LEE, K. H., UM, I. C. & PARK, Y. H. 2005. Characterization of gelatin nanofiber prepared from gelatin-formic acid solution. *Polymer,* 46, 5094-5102.
KIM, G. & KIM, Y. 2013. Collagen/alginate scaffolds comprising core (PCL)–shell (collagen/alginate) struts for hard tissue regeneration: fabrication, characterisation, and cellular activities. *Journal of Materials Chemistry.*
KIM, T. K., SHARMA, B., WILLIAMS, C. G., RUFFNER, M. A., MALIK, A., MCFARLAND, E. G. & ELISSEEFF, J. H. 2003. Experimental model for cartilage tissue engineering to regenerate the zonal organization of articular cartilage. *Osteoarthritis and Cartilage,* 11, 653-664.
KIM, Y. B., LEE, H., YANG, G.-H., CHOI, C. H., LEE, D., HWANG, H., JUNG, W.-K., YOON, H. & KIM, G. H. 2016. Mechanically reinforced cell-laden scaffolds formed using alginate-based bioink printed onto the surface of a PCL/alginate mesh structure for regeneration of hard tissue. *Journal of Colloid and Interface Science,* 461, 359-368.
KIRCHMAJER, D. M. & PANHUIS, M. I. H. 2014. Robust biopolymer based ionic-covalent entanglement hydrogels with reversible mechanical behaviour. *Journal of Materials Chemistry B,* 2, 4694-4702.
KLEIN, T. J., MALDA, J., SAH, R. L. & HUTMACHER, D. W. 2009. Tissue engineering of articular cartilage with biomimetic zones. *Tissue Engineering Part B-Reviews,* 15, 143-157.
KNUTSEN, G., DROGSET, J. O., ENGEBRETSEN, L., GRONTVEDT, T., ISAKSEN, V., LUDVIGSEN, T. C., ROBERTS, S., SOLHEIM, E., STRAND, T. & JOHANSEN, O. 2007. A Randomized trial comparing autologous chondrocyte implantation with microfracture. *Journal of Bone and Joint Surgery-American Volume,* 89A, 2105-2112.
KOEBEL, M. M. 2011. *Aerogels Handbook*, Springer-Verlag New York.
KOHN, D. H. & ROSSELLO, R. A. 2010. Cell communication and tissue engineering. *Communicative & Integrative Biology,* 3, 53-56.
KREUZ, P. C., STEINWACHS, M. R., ERGGELET, C., KRAUSE, S. J., KONRAD, G., UHL, M. & SUEDKAMP, N. 2006. Results after microfracture of full-thickness chondral defects in different compartments in the knee. *Osteoarthritis and Cartilage,* 14, 1119-1125.
KUNDU, J., SHIM, J.-H., JANG, J., KIM, S.-W. & CHO, D.-W. 2015. An additive manufacturing-based PCL-alginate-chondrocyte bioprinted scaffold for cartilage tissue engineering. *Journal of Tissue Engineering and Regenerative Medicine,* 9, 1286-1297.
KUO, C. K. & MA, P. X. 2001. Ionically crosslinked alginate hydrogels as scaffolds for tissue engineering: Part 1. Structure, gelation rate and mechanical properties. *Biomaterials,* 22, 511-521.
LAI, J.-Y., MA, D. H.-K., LAI, M.-H., LI, Y.-T., CHANG, R.-J. & CHEN, L.-M. 2013. Characterization of cross-linked porous gelatin carriers and their interaction with corneal endothelium: biopolymer concentration effect. *Plos One,* 8.
LANGELIER, E., SUETTERLIN, R., HOEMANN, C. D., AEBI, U. & BUSCHMANN, M. D. 2000. The chondrocyte cytoskeleton in mature articular cartilage: structure and distribution of actin, tubulin, and vimentin filaments. *Journal of Histochemistry & Cytochemistry,* 48, 1307-1320.
LANGER, R. & VACANTI, J. P. 1993. Tissue engineering. *Science,* 260, 920-926.
LI, D. & XIA, Y. N. 2004. Electrospinning of nanofibers: Reinventing the wheel? *Advanced Materials,* 16, 1151-1170.

LI, W.-J., JIANG, Y. J. & TUAN, R. S. 2006. Chondrocyte phenotype in engineered fibrous matrix is regulated by fiber size. *Tissue Engineering,* 12, 1775-1785.
LIEN, S. M., KO, L. Y. & HUANG, T. J. 2009. Effect of pore size on ECM secretion and cell growth in gelatin scaffold for articular cartilage tissue engineering. *Acta Biomaterialia,* 5, 670-679.
LIN, S., IONESCU, C., PIKE, K. J., SMITH, M. E. & JONES, J. R. 2009. Nanostructure evolution and calcium distribution in sol-gel derived bioactive glass. *Journal of Materials Chemistry,* 19, 1276-1282.
LITTLE, C. J., BAWOLIN, N. K. & CHEN, X. 2011. Mechanical properties of natural cartilage and tissue-engineered constructs. *Tissue Engineering Part B-Reviews,* 17, 213-227.
LIU, Y. L., SU, Y. H. & LAI, J. Y. 2004. In situ crosslinking of chitosan and formation of chitosan–silica hybrid membranes with using g-glycidoxypropyltrimethoxysilane as a crosslinking agent. *Polymer,* 45, 6831-6837.
LU, H., KO, Y.-G., KAWAZOE, N. & CHEN, G. 2010. Cartilage tissue engineering using funnel-like collagen sponges prepared with embossing ice particulate templates. *Biomaterials,* 31, 5825-5835.
MACKAY, A. M., BECK, S. C., MURPHY, J. M., BARRY, F. P., CHICHESTER, C. O. & PITTENGER, M. F. 1998. Chondrogenic differentiation of cultured human mesenchymal stem cells from marrow. *Tissue Engineering,* 4, 415-428.
MAEDA, H., KASUGA, T. & HENCH, L. L. 2006. Preparation of poly(L-lactic acid)-polysiloxane-calcium carbonate hybrid membranes for guided bone regeneration. *Biomaterials,* 27, 1216-1222.
MAHONY, O. 2010. *Silica - natural polymer hybrid materials for human tissue regeneration.* PhD Thesis, Imperial College London.
MAHONY, O. & JONES, J. R. 2008. Porous bioactive nanostructured scaffolds for bone regeneration: a sol-gel solution. *Nanomedicine,* 3, 233-245.
MAHONY, O., TSIGKOU, O., IONESCU, C., MINELLI, C., LING, L., HANLY, R., SMITH, M. E., STEVENS, M. M. & JONES, J. R. 2010. Silica-gelatin hybrids with tailorable degradation and mechanical properties for tissue regeneration. *Advanced Functional Materials,* 20, 3835–3845.
MAHONY, O., YUE, S., TURDEAN-IONESCU, C., HANNA, J. V., SMITH, M. E., LEE, P. D. & JONES, J. R. 2014. Silica-gelatin hybrids for tissue regeneration: inter-relationships between the process variables. *Journal of Sol-Gel Science and Technology,* 69, 288-298.
MAKRIS, E. A., GOMOLL, A. H., MALIZOS, K. N., HU, J. C. & ATHANASIOU, K. A. 2015. Repair and tissue engineering techniques for articular cartilage. *Nature Reviews Rheumatology,* 11, 21-34.
MALDA, J., WOODFIELD, T. B. F., VAN DER VLOODT, F., WILSON, C., MARTENS, D. E., TRAMPER, J., VAN BLITTERSWIJK, C. A. & RIESLE, J. 2005. The effect of PEGT/PBT scaffold architecture on the composition of tissue engineered cartilage. *Biomaterials,* 26, 63-72.
MALDONADO, M. & NAM, J. 2013. The role of changes in extracellular matrix of cartilage in the presence of inflammation on the pathology of osteoarthritis. *Biomed Research International,* 2013, 1-10.
MANDAL, B. B., PARK, S.-H., GIL, E. S. & KAPLAN, D. L. 2011. Multilayered silk scaffolds for meniscus tissue engineering. *Biomaterials,* 32, 639-651.
MANNOOR, M. S., JIANG, Z., JAMES, T., KONG, Y. L., MALATESTA, K. A., SOBOYEJO, W. O., VERMA, N., GRACIAS, D. H. & MCALPINE, M. C. 2013. 3D printed bionic ears. *Nano Letters,* 13, 2634-2639.
MAQUET, V., BOCCACCINI, A. R., PRAVATA, L., NOTINGHER, I. & JEROME, R. 2004. Porous poly(alpha-hydroxyacid)/Bioglass composite scaffolds for bone tissue engineering. I: preparation and in vitro characterisation. *Biomaterials,* 25, 4185-4194.

MARELLI, B., GHEZZI, C. E., MOHN, D., STARK, W. J., BARRALET, J. E., BOCCACCINI, A. R. & NAZHAT, S. N. 2011. Accelerated mineralization of dense collagen-nano bioactive glass hybrid gels increases scaffold stiffness and regulates osteoblastic function. *Biomaterials,* 32**,** 8915-8926.

MCCULLEN, S. D., AUTEFAGE, H., CALLANAN, A., GENTLEMAN, E. & STEVENS, M. M. 2012. Anisotropic fibrous scaffolds for articular cartilage regeneration. *Tissue Engineering Part A,* 18**,** 2073-2083.

MMWR 2007. National and state medical expenditures and lost earnings attributable to arthritis and other rheumatic conditions. *MMWR MORB MORTAL weekly,* 56**,** 4.

MOUTOS, F. T., FREED, L. E. & GUILAK, F. 2007. A biomimetic three-dimensional woven composite scaffold for functional tissue engineering of cartilage. *Nature Materials,* 6**,** 162-167.

MOW, V. C., RATCLIFFE, A. & POOLE, A. R. 1992. Cartilage and diarthrodial joints as paradigms for hierarchial materials and structures. *Biomaterials,* 13**,** 67-97.

MOZAFARI, M., RABIEE, M., AZAMI, M. & MALEKNIA, S. 2010. Biomimetic formation of apatite on the surface of porous gelatin/bioactive glass nanocomposite scaffolds. *Applied Surface Science,* 257**,** 1740-1749.

MUZZARELLI, R. A. A., GRECO, F., BUSILACCHI, A., SOLLAZZO, V. & GIGANTE, A. 2012. Chitosan, hyaluronan and chondroitin sulfate in tissue engineering for cartilage regeneration: A review. *Carbohydrate Polymers,* 89**,** 723-739.

NORTON, A. B., HANCOCKS, R. D. & GROVER, L. M. 2014. Poly (vinyl alcohol) modification of low acyl gellan hydrogels for applications in tissue regeneration. *Food Hydrocolloids,* 42**,** 373-377.

NOVAK, B. M. 1993. Hybrid nanocomposite materials - between inorganic glass and organic polymers. *Advanced Materials,* 5**,** 422-433.

NUERNBERGER, S., CYRAN, N., ALBRECHT, C., REDL, H., VECSEI, V. & MARLOVITS, S. 2011. The influence of scaffold architecture on chondrocyte distribution and behavior in matrix-associated chondrocyte transplantation grafts. *Biomaterials,* 32**,** 1032-1040.

O'BRIEN, F. J., HARLEY, B. A., YANNAS, I. V. & GIBSON, L. 2004. Influence of freezing rate on pore structure in freeze-dried collagen-GAG scaffolds. *Biomaterials,* 25**,** 1077-1086.

O'BRIEN, F. J., HARLEY, B. A., YANNAS, I. V. & GIBSON, L. J. 2005. The effect of pore size on cell adhesion in collagen-GAG scaffolds. *Biomaterials,* 26**,** 433-441.

OBATA, A., OZASA, H., KASUGA, T. & JONES, J. R. 2013. Cotton wool-like poly(lactic acid)/vaterite composite scaffolds releasing soluble silica for bone tissue engineering. *Journal of Materials Science-Materials in Medicine,* 24**,** 1649-1658.

ORTH, P., REY-RICO, A., VENKATESAN, J. K., MADRY, H. & CUCCHIARINI, M. 2014. Current perspectives in stem cell research for knee cartilage repair. *Stem cells and cloning : advances and applications,* 7**,** 1-17.

OZEKI, M. & TABATA, Y. 2005. In vivo degradability of hydrogels prepared from different gelatins by various cross-linking methods. *Journal of Biomaterials Science-Polymer Edition,* 16**,** 549-561.

PELMENSCHIKOV, A., STRANDH, H., PETTERSSON, L. G. M. & LESZCZYNSKI, J. 2000. Lattice resistance to hydrolysis of Si-O-Si bonds of silicate minerals: Ab initio calculations of a single water attack onto the (001) and (111) beta-cristobalite surfaces. *Journal of Physical Chemistry B,* 104**,** 5779-5783.

POOLOGASUNDARAMPILLAI, G., WANG, D., LI, S., NAKAMURA, J., BRADLEY, R., LEE, P. D., STEVENS, M. M., MCPHAIL, D. S., KASUGA, T. & JONES, J. R. 2014a. Cotton-wool-like bioactive glasses for bone regeneration. *Acta Biomaterialia,* 10**,** 3733-3746.

POOLOGASUNDARAMPILLAI, G., YU, B., JONES, J. R. & KASUGA, T. 2011. Electrospun silica/PLLA hybrid materials for skeletal regeneration. *Soft Matter,* 7**,** 10241-10251.

POOLOGASUNDARAMPILLAI, G., YU, B., TSIGKOU, O., WANG, D., ROMER, F., BHAKHRI, V., GIULIANI, F., STEVENS, M. M., MCPHAIL, D. S., SMITH, M. E., HANNA, J. V. & JONES, J. R. 2014b. Poly(gamma-glutamic acid)/silica hybrids with calcium incorporated in the silica network by use of a calcium alkoxide precursor. *Chemistry-a European Journal,* 20, 8149-8160.

REISSIS, D., QUEN OAK, T., COOPER, N. C., CARASCO, C. F., GAMIE, Z., MANTALARIS, A. & TSIRIDIS, E. 2016. Current clinical evidence for the use of mesenchymal stem cells in articular cartilage repair. *Expert Opinion on Biological Therapy,* 16, 535-557.

REN, L., TSURU, K., HAYAKAWA, S. & OSAKA, A. 2001a. Incorporation of Ca^{2+} ions in gelatin-siloxane hybrids through a sol-gel process. *Journal of the Ceramic Society of Japan,* 109, 406-411.

REN, L., TSURU, K., HAYAKAWA, S. & OSAKA, A. 2001b. Synthesis and characterization of gelatin-siloxane hybrids derived through sol-gel procedure. *Journal of Sol-Gel Science and Technology,* 21.

REN, L., TSURU, K., HAYAKAWA, S. & OSAKA, A. 2002. Novel approach to fabricate porous gelatin-siloxane hybrids for bone tissue engineering. *Biomaterials,* 23, 4765-4773.

REN, L., WANG, J., YANG, F.-Y., WANG, L., WANG, D., WANG, T.-X. & TIAN, M.-M. 2010. Fabrication of gelatin-siloxane fibrous mats via sol-gel and electrospinning procedure and its application for bone tissue engineering. *Materials Science & Engineering C-Materials for Biological Applications,* 30, 437-444.

RENDERS, G. A. P., MULDER, L., VAN RUIJVEN, L. J. & VAN EIJDEN, T. M. G. J. 2007. Porosity of human mandibular condylar bone. *Journal of Anatomy,* 210, 239-248.

REPO, R. U. & FINLAY, J. B. 1977. Survival of articular-cartilage after controlled impact. *Journal of Bone and Joint Surgery-American Volume,* 59, 1068-1076.

REZWAN, K., CHEN, Q. Z., BLAKER, J. J. & BOCCACCINI, A. R. 2006. Biodegradable and bioactive porous polymer/inorganic composite scaffolds for bone tissue engineering. *Biomaterials,* 27, 3413-3431.

RHEE, S. H., CHOI, J. Y. & KIM, H. M. 2002. Preparation of a bioactive and degradable poly(epsilon-caprolactone)/silica hybrid through a sol-gel method. *Biomaterials,* 23, 4915-4921.

ROWLEY, J. A., MADLAMBAYAN, G. & MOONEY, D. J. 1999. Alginate hydrogels as synthetic extracellular matrix materials. *Biomaterials,* 20, 45-53.

SCHUURMAN, W., KHRISTOV, V., POT, M. W., VAN WEEREN, P. R., DHERT, W. J. A. & MALDA, J. 2011. Bioprinting of hybrid tissue constructs with tailorable mechanical properties. *Biofabrication,* 3.

SEMPLE, J. L., WOOLRIDGE, N. & LUMSDEN, C. J. 2005. In vitro, in vivo, in silico: Computational systems in tissue engineering and regenerative medicine. *Tissue Engineering,* 11, 341-356.

SHIRAZI, A. N., FATHI, A., SUAREZ, F. G., WANG, Y., MAITZ, P. K. & DEHGHANI, F. 2016. A novel strategy for softening gelatin-bioactive-glass hybrids. *Acs Applied Materials & Interfaces,* 8, 1676-1686.

SKOTAK, M., NORIEGA, S., LARSEN, G. & SUBRAMANIAN, A. 2010. Electrospun cross-linked gelatin fibers with controlled diameter: The effect of matrix stiffness on proliferative and biosynthetic activity of chondrocytes cultured in vitro. *Journal of Biomedical Materials Research Part A,* 95A, 828-836.

SOBRAL, J. M., CARIDADE, S. G., SOUSA, R. A., MANO, J. F. & REIS, R. L. 2011. Three-dimensional plotted scaffolds with controlled pore size gradients: Effect of scaffold geometry on mechanical performance and cell seeding efficiency. *Acta Biomaterialia,* 7, 1009-1018.

SOLCHAGA, L. A., TEMENOFF, J. S., GAO, J. Z., MIKOS, A. G., CAPLAN, A. I. & GOLDBERG, V. M. 2005. Repair of osteochondral defects with hyaluronan- and polyester-based scaffolds. *Osteoarthritis and Cartilage,* 13**,** 297-309.

SONG, J.-H., KIM, H.-E. & KIM, H.-W. 2008a. Production of electrospun gelatin nanofiber by water-based co-solvent approach. *Journal of Materials Science-Materials in Medicine,* 19**,** 95-102.

SONG, J. H., YOON, B. H., KIM, H. E. & KIM, H. W. 2008b. Bioactive and degradable hybridized nanofibers of gelatin-siloxane for bone regeneration. *Journal of Biomedical Materials Research Part A,* 84A**,** 875-884.

SPILLER, K. L., MAHER, S. A. & LOWMAN, A. M. 2011. Hydrogels for the repair of articular cartilage defects. *Tissue Engineering Part B-Reviews,* 17**,** 281-299.

STANDARDIZATION, I. O. F. 2009. ISO 10993-1:2009. *Biological evaluation of medical devices -Part 1: Evaluation and testing within a risk management process.*

STEELE, J. A. M., MCCULLEN, S. D., CALLANAN, A., AUTEFAGE, H., ACCARDI, M. A., DINI, D. & STEVENS, M. M. 2014. Combinatorial scaffold morphologies for zonal articular cartilage engineering. *Acta Biomaterialia,* 10**,** 2065-2075.

STEVENS, M. M. & GEORGE, J. H. 2005. Exploring and engineering the cell surface interface. *Science,* 310**,** 1135-1138.

STOKES, D. G., LIU, G., COIMBRA, I. B., PIERA-VELAZQUEZ, S., CROWL, R. M. & JIMENEZ, S. A. 2002. Assessment of the gene expression profile of differentiated and dedifferentiated human fetal chondrocytes by microarray analysis. *Arthritis and Rheumatism,* 46**,** 404-419.

SUN, B., LONG, Y.-Z., YU, F., LI, M.-M., ZHANG, H.-D., LI, W.-J. & XU, T.-X. 2012a. Self-assembly of a three-dimensional fibrous polymer sponge by electrospinning. *Nanoscale,* 4**,** 2134-2137.

SUN, B., LONG, Y. Z., ZHANG, H. D., LI, M. M., DUVAIL, J. L., JIANG, X. Y. & YIN, H. L. 2014. Advances in three-dimensional nanofibrous macrostructures via electrospinning. *Progress in Polymer Science,* 39**,** 862-890.

SUN, J.-Y., ZHAO, X., ILLEPERUMA, W. R. K., CHAUDHURI, O., OH, K. H., MOONEY, D. J., VLASSAK, J. J. & SUO, Z. 2012b. Highly stretchable and tough hydrogels. *Nature,* 489**,** 133-136.

TANAKA, Y., YAMAOKA, H., NISHIZAWA, S., NAGATA, S., OGASAWARA, T., ASAWA, Y., FUJIHARA, Y., TAKATO, T. & HOSHI, K. 2010. The optimization of porous polymeric scaffolds for chondrocyte/atelocollagen based tissue-engineered cartilage. *Biomaterials,* 31**,** 4506-4516.

TEMENOFF, J. S. & MIKOS, A. G. 2000. Review: tissue engineering for regeneration of articular cartilage. *Biomaterials,* 21**,** 431-440.

TONDA-TURO, C., CIPRIANI, E., GNAVI, S., CHIONO, V., MATTU, C., GENTILE, P., PERROTEAU, I., ZANETTI, M. & CIARDELLI, G. 2013. Cross linked gelatin nanofibres: preparation, characterisation and in vitro studies using glial-like cells. *Materials Science & Engineering C-Materials for Biological Applications,* 33**,** 2723-2735.

TONDA-TURO, C., GENTILE, P., SARACINO, S., CHIONO, V., NANDAGIRI, V. K., MUZIO, G., CANUTO, R. A. & CIARDELLI, G. 2011. Comparative analysis of gelatin scaffolds crosslinked by genipin and silane coupling agent. *International Journal of Biological Macromolecules,* 49**,** 700-706.

TRIPATANASUWAN, S., ZHONG, Z. & RENEKER, D. H. 2007. Effect of evaporation and solidification of the charged jet in electrospinning of poly(ethylene oxide) aqueous solution. *Polymer,* 48**,** 5742-5746.

VALLIANT, E. M. & JONES, J. R. 2011. Softening bioactive glass for bone regeneration: sol-gel hybrid materials. *Soft Matter,* 7**,** 5083-5095.

VERZIJL, N., DEGROOT, J., THORPE, S. R., BANK, R. A., SHAW, J. N., LYONS, T. J., BIJLSMA, J. W. J., LAFEBER, F., BAYNES, J. W. & TEKOPPELE, J. M. 2000. Effect

of collagen turnover on the accumulation of advanced glycation end products. *Journal of Biological Chemistry,* 275, 39027-39031.
VUNJAK-NOVAKOVIC, G., OBRADOVIC, B., MARTIN, I., BURSAC, P. M., LANGER, R. & FREED, L. E. 1998. Dynamic cell seeding of polymer scaffolds for cartilage tissue engineering. *Biotechnology Progress,* 14, 193-202.
WAGNER, D. R., LINDSEY, D. P., LI, K. W., TUMMALA, P., CHANDRAN, S. E., SMITH, R. L., LONGAKER, M. T., CARTER, D. R. & BEAUPRE, G. S. 2008. Hydrostatic pressure enhances chondrogenic differentiation of human bone marrow stromal cells in osteochondrogenic medium. *Annals of Biomedical Engineering,* 36, 813-820.
WANG, Y., ZHANG, W., YUAN, J. & SHEN, J. 2016. Differences in cytocompatibility between collagen, gelatin and keratin. *Materials Science & Engineering C-Materials for Biological Applications,* 59, 30-34.
WEIBEL, G. L. & OBER, C. K. 2003. An overview of supercritical CO_2 applications in microelectronics processing. *Microelectronic Engineering,* 65, 145-152.
WOODFIELD, T. B. F., MALDA, J., DE WIJN, J., PETERS, F., RIESLE, J. & VAN BLITTERSWIJK, C. A. 2004. Design of porous scaffolds for cartilage tissue engineering using a three-dimensional fiber-deposition technique. *Biomaterials,* 25, 4149-4161.
WOODFIELD, T. B. F., VAN BLITTERSWIJK, C. A., DE WIJN, J., SIMS, T. J., HOLLANDER, A. P. & RIESLE, J. 2005. Polymer scaffolds fabricated with pore-size gradients as a model for studying the zonal organization within tissue-engineered cartilage constructs. *Tissue Engineering,* 11, 1297-1311.
YAMAOKA, H., ASATO, H., OGASAWARA, T., NISHIZAWA, S., TAKAHASHI, T., NAKATSUKA, T., KOSHIMA, I., NAKAMURA, K., KAWAGUCHI, H., CHUNG, U. I., TAKATO, T. & HOSHI, K. 2006. Cartilage tissue engineering chondrocytes embedded in using human auricular different hydrogel materials. *Journal of Biomedical Materials Research Part A,* 78A, 1-11.
YUN, H.-S., KIM, S.-E. & HYEON, Y.-T. 2007. Design and preparation of bioactive glasses with hierarchical pore networks. *Chemical Communications,* 1, 2139-2141.
ZHANG, C. X., YUAN, X. Y., WU, L. L., HAN, Y. & SHENG, J. 2005. Study on morphology of electrospun poly(vinyl alcohol) mats. *European Polymer Journal,* 41, 423-432.
ZHANG, L., HU, J. & ATHANASIOU, K. A. 2009. The role of tissue engineering in articular cartilage repair and regeneration. *Critical reviews in biomedical engineering,* 37, 1-57.
ZHANG, Y., VENUGOPAL, J. R., EL-TURKI, A., RAMAKRISHNA, S., SU, B. & LIM, C. T. 2008. Electrospun biomimetic nanocomposite nanofibers of hydroxyapatite/chitosan for bone tissue engineering. *Biomaterials,* 29, 4314-4322.

APPENDIX

JOHN WILEY AND SONS LICENSE
TERMS AND CONDITIONS
Apr 11, 2016

This Agreement between maria nelson ("You") and John Wiley and Sons ("John Wiley and Sons") consists of your license details and the terms and conditions provided by John Wiley and Sons and Copyright Clearance Center.

License Number	3834761372128
License date	Mar 23, 2016
Licensed Content Publisher	John Wiley and Sons
Licensed Content Publication	Journal of Biomedical Materials Research
Licensed Content Title	Bioactive and degradable hybridized nanofibers of gelatin–siloxane for bone regeneration
Licensed Content Author	Ju-Ha Song,Byung-Ho Yoon,Hyoun-Ee Kim,Hae-Won Kim
Licensed Content Date	Jul 23, 2007
Pages	10
Type of use	Dissertation/Thesis
Requestor type	University/Academic
Format	Print and electronic
Portion	Figure/table
Number of figures/tables	1
Original Wiley figure/table number(s)	4
Will you be translating?	No
Title of your thesis / dissertation	3D silica-gelatin hybrid scaffolds for tissue regeneration
Expected completion date	Apr 2016
Expected size (number of pages)	170
Requestor	Maria Nelson

JOHN WILEY AND SONS LICENSE
TERMS AND CONDITIONS

This Agreement between maria nelson ("You") and John Wiley and Sons ("John Wiley and Sons") consists of your license details and the terms and conditions provided by John Wiley and Sons and Copyright Clearance Center.

License Number	3842630231823
License date	Apr 05, 2016
Licensed Content Publisher	John Wiley and Sons
Licensed Content Publication	Advanced Functional Materials
Licensed Content Title	Silica-Gelatin Hybrids with Tailorable Degradation and Mechanical Properties for Tissue Regeneration
Licensed Content Author	Oliver Mahony,Olga Tsigkou,Claudia Ionescu,Caterina Minelli,Lowell Ling,Ruth Hanly,Mark E. Smith,Molly M. Stevens,Julian R. Jones
Licensed Content Date	Aug 23, 2010
Pages	11
Type of use	Dissertation/Thesis
Requestor type	University/Academic
Format	Print and electronic
Portion	Figure/table
Number of figures/tables	1
Original Wiley figure/table number(s)	6
Will you be translating?	No
Title of your thesis / dissertation	3D silica-gelatin hybrid scaffolds for tissue regeneration
Expected completion date	Apr 2016
Expected size (number of pages)	170
Requestor	Maria Nelson